Severin Klever

High-Bandwidth Current-Probing Techniques for the Dynamic Characterization of Wide-Bandgap Semiconductor Devices

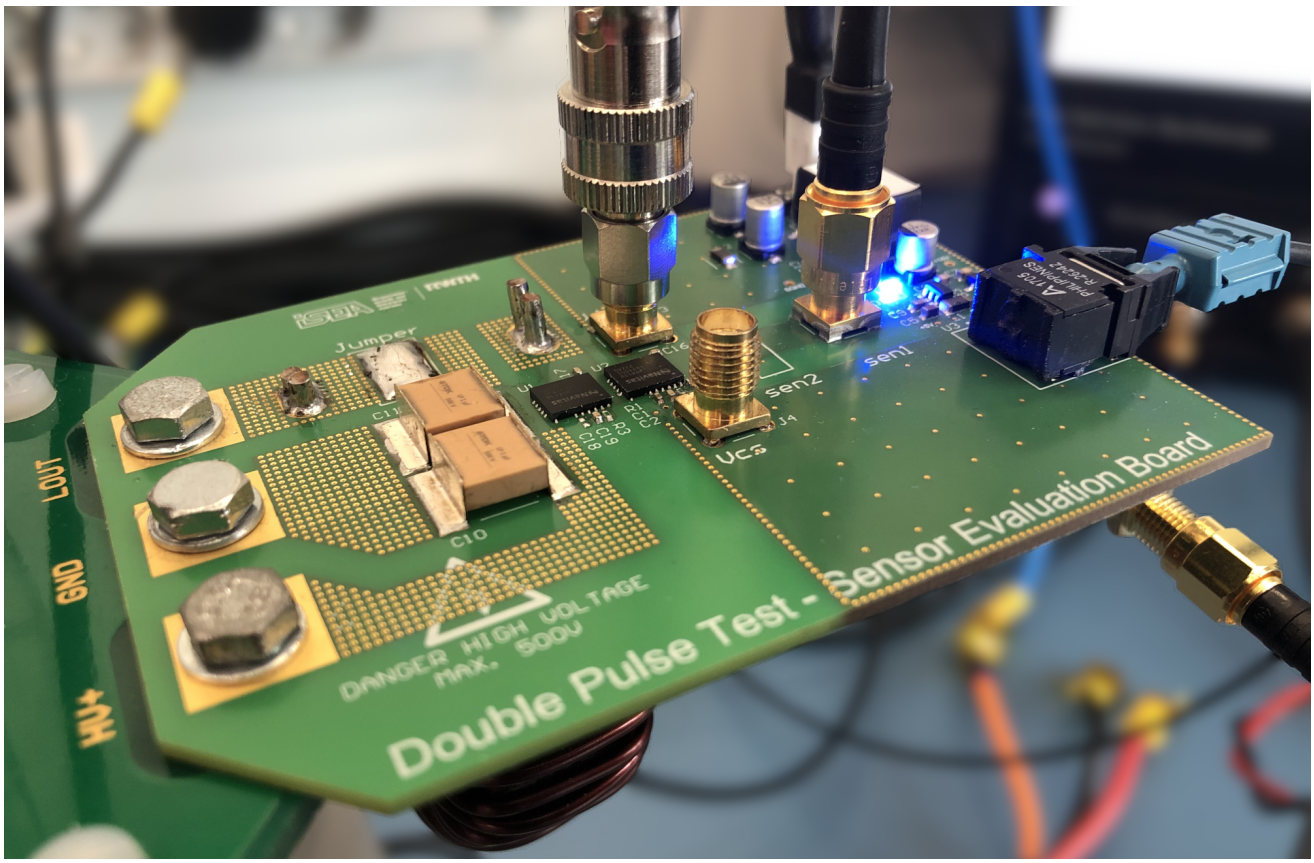

Aachener Beiträge des ISEA Band 192

High-Bandwidth Current-Probing Techniques for the Dynamic Characterization of Wide-Bandgap Semiconductor Devices

Von der Fakultät für Elektrotechnik und Informationstechnik der Rheinisch-Westfälischen Technischen Hochschule Aachen zur Erlangung des akademischen Grades eines Doktors der Ingenieurwissenschaften genehmigte Dissertation

vorgelegt von
Severin Klever, M.Sc.
aus Langenfeld (Rhld.)

Berichter:
Univ.-Prof. Dr. ir. Dr. h. c. Rik W. De Doncker
Prof. Dr. Deepakraj M. Divan

Tag der mündlichen Prüfung: 30. Januar 2025

AACHENER BEITRÄGE DES ISEA
Vol. 192

Editor:
Univ.-Prof. Dr. ir. Dr. h. c. Rik W. De Doncker
Director of the Institute for Power Electronics and Electrical Drives (ISEA)
RWTH Aachen University

ISSN 1437-675X

Institute for Power Electronics and Electrical Drives (ISEA)
RWTH Aachen University
Campus-Boulevard 89 ▪ 52074 Aachen ▪ Germany
Tel: +49 (0)241 80-96920
Fax: +49 (0)241 80-92203
post@isea.rwth-aachen.de

Vorwort

Diese Dissertation entstand im Rahmen meiner Tätigkeit als wissenschaftlicher Mitarbeiter am Institut für Stromrichtertechnik und elektrische Antriebe (ISEA) der RWTH Aachen University. Zunächst möchte ich mich herzlich bei Professor De Doncker für die Möglichkeit der Promotion und das mir entgegengebrachte Vertrauen bedanken. Neben der fachlichen Unterstützung habe ich vor allem das exzellente Forschungsumfeld am ISEA geschätzt. Dieses ermöglichte nicht nur spannende Industrieprojekte und Lehrtätigkeiten, sondern ließ auch ausreichend Freiraum für meine eigene Forschung. Mein herzlicher Dank gilt zudem Professor Divan vom Georgia Institute of Technology für die Übernahme des Koreferats sowie für die investierte Zeit und die wertvollen fachlichen Impulse.

Ein großes Dankeschön gilt dem gesamten ISEA, dessen angenehme Arbeitsatmosphäre entscheidend zu meinen Ergebnissen beigetragen hat. Dies schließt alle unterstützenden Abteilungen ein, wie das Sekretariat, die Verwaltung, IT und Werkstätten, die stets einen reibungslosen Ablauf gewährleistet haben. Zudem möchte ich mich bei meinen ehemaligen Kolleginnen und Kollegen aus der LE- und RPE-Gruppe bedanken. Ich habe die hohe Hilfsbereitschaft und den Zusammenhalt im Team sehr geschätzt – sowohl im Arbeitsalltag als auch bei zahlreichen sozialen Events und gemeinsamen Konferenzbesuchen. Ich bin zuversichtlich, dass diese Kultur auch in Zukunft fortgeführt wird.

Während der Finalisierung meiner Dissertation haben mich einige Kollegen durch wertvolle fachliche Diskussionen und Anregungen besonders unterstützt. An dieser Stelle danke ich Alireza, André, Carsten, Laurids, Lukas und Tianlong. Zusätzlich danke ich Anne, Laurids und Tobias für die Unterstützung bei der Vorbereitung des öffentlichen Teils meiner Verteidigung. Darüber hinaus haben auch zahlreiche Studierende durch ihr Engagement bei studentischen Projekten und Abschlussarbeiten einen wichtigen Beitrag geleistet. Ich möchte hier vor allem Anton, Jan, Martí, Mert, Otmane und Thomas erwähnen.

Abschließend möchte ich denjenigen danken, die mich außerhalb des Instituts auf meinem Weg begleitet und unterstützt haben. Mein größter Dank gilt meinen Eltern Gaby und Heinz, die mich stets gefördert haben und mir immer zur Seite standen. Ebenso danke ich meinen Freunden, die mich nicht nur mit Ablenkung versorgt, sondern mich auch zum Durchhalten motiviert haben. Ein ganz besonderes Dankeschön geht an meine Partnerin Jasmin, die immer für mich da war und ist.

Düsseldorf, im März 2025 *Severin Klever*

Acknowledgment

The research conducted within the scope of this thesis was supported by the research training group “Integrated Energy Supply Modules for Roadbound E-Mobility” (mobilEM) (GRK 1856) of the German Research Foundation (DFG).

Abstract

Motivation, Goal and Task of this Dissertation A key trend in the field of power electronics is the continuous increase in efficiency and power densities. This is particularly relevant in mobile applications such as traction drives, electric aviation and consumer electronics. The use of the wide-bandgap semiconductor materials Silicon carbide (SiC) and Gallium nitride (GaN), which are characterized by their high switching speeds, plays a key role in this context. To improve the performance of a power electronic system and to optimize it with regard to safety and reliability, it is essential to precisely characterize the semiconductor devices used. Among the dynamic characteristics, the switching energies are particularly relevant as they are strongly dependent on the selected operating point and the topology. The switching energies can be determined in the double-pulse test and require the simultaneous measurement of the drain-source current and the drain-source voltage of the device under test. Suitable measuring equipment such as the recently developed optically-isolated differential probes are available for voltage measurement. However, it has been observed that the techniques used for current measurement are unsuitable for fast-switching wide-bandgap (WBG) devices. Common state-of-the-art solutions, such as coaxial shunts and Rogowski coils, have either too high parasitic inductance or too low bandwidth, which leads to incorrect measurement results. The aim of this work is to maximize the measurement accuracy for turn-off and turn-on switching energies. To achieve this, a better understanding of the sources of error and their influence on measurement accuracy is required. Subsequently, novel concepts will be developed and implemented. The research focuses on both resistive and inductive current sensors, with the aim of demonstrating their suitability through experimental validation.

Major Scientific Contributions The first step involved investigating which sources of error influence the measurement of switching energies, and how significant these effects are. By simulating multiple configurations for the double-pulse test, the sensitivity of individual measurement parameters for different classes of wide-bandgap semiconductors was estimated. The results indicated that measurement errors exceeding 10% are to be expected when incorrect probes are selected. These are primarily caused by the parasitic inductance of the current sensor and the input capacitance of the voltage probe, which both influence the switching behavior and must therefore be minimized. Furthermore, a reduction in measurement accuracy results from the limited bandwidths of the probes, for which device-specific recommendations with a lower limit of 500 MHz have been derived. Another highly relevant factor is the incorrect deskewing, which describes the time offset between current and voltage measurement. Even a waveform offset of a

few hundred picoseconds can significantly distort the results. Therefore, it is essential to have precise knowledge of the transmission characteristics of the measuring equipment used to compensate for this error in post-processing. It has been shown that among the various classes of WBG semiconductors, low-voltage GaN devices are particularly susceptible to measurement errors. Subsequently, existing approaches to current measurement were discussed, and two novel concepts for measuring the drain-source current i_{ds} were developed. With regard to resistive current measurement, a compact shunt resistor based on radially arranged thin-film resistors is presented. The arrangement is characterized by a usable frequency range from dc to 2.17 GHz and a parasitic inductance of less than 100 pH. The inductive measurement technology presented is a current sensor based on a planar pick-up coil embedded in a multilayer circuit board. This technology enables current measurement up to 2.66 GHz by processing the induced voltage. Both measurement methods were validated experimentally. For this purpose, a low-inductance switching cell with fast-switching GaN devices was designed and its switching behavior was characterized in double-pulse tests. The comparison between both measurement methods with each other and with simulation results has proven that the radial shunt resistor is the most effective approach for characterizing fast-switching WBG semiconductor devices. In addition to the excellent performance, the straightforward assembly technology is also a decisive advantage over alternative solutions.

Contents

1 Introduction

Before presenting the research results of this thesis, a brief categorization of the topic is provided. First, Section 1.1 presents the general motivation of this research project, which is the widespread adoption of new semiconductor technologies and the necessity to characterize their switching behavior. Subsequently, the objective of this thesis is outlined in detail in Section 1.2, which sets a focus on highly-dynamic current-probing techniques. Finally, the structure of this thesis is presented in Section 1.3.

1.1 Motivation and Background

The electrification of the transport sector and the decentralization of the energy sector have driven the widespread use of power electronic systems. This trend is encouraged by the global goal of reducing carbon dioxide emissions. Components made from semiconductor materials are an essential part of all these systems. In the past decade, the materials Silicon carbide (SiC) and Gallium nitride (GaN) have become established as alternatives to the previously used Silicon (Si). SiC and GaN are referred to as wide-bandgap (WBG) semiconductors due to their higher bandgap, which is a characteristic of the respective atoms. Compared to Si devices, WBG devices offer several advantages, which have been crucial in increasing efficiency and power density. Mass production and optimized manufacturing processes have reduced the cost of WBG devices, making them popular in many fields of application. Fig. 1.1 classifies exemplary applications for different semiconductor technologies according to switching frequency and nominal power [1]. The switching frequency is an essential characteristic of a power electronic system, enabling more compact designs and dynamic control. SiC is particularly suitable for high-power applications, traditionally dominated by insulated-gate bipolar transistors (IGBTs) and metal-oxide semiconductor field-effect transistors (MOSFETs) made from Si. These include grid applications, wind turbines, railway applications, and central photovoltaic plants. In fast-switching applications, SiC is found in industrial systems, electric traction drives, and household applications such as heat pumps, washing machines, and household photovoltaic systems. GaN devices are most common in applications that use very high switching frequencies at lower power, with the high-electron-mobility transistor (HEMT) being established as the preferred device [2]. Common applications include data centers and consumer electronics such as chargers and personal computers. In the field of electromobility, both SiC and GaN technologies compete and can be used for traction drives, stationary or mobile battery chargers and on-board dc-dc converters [3].

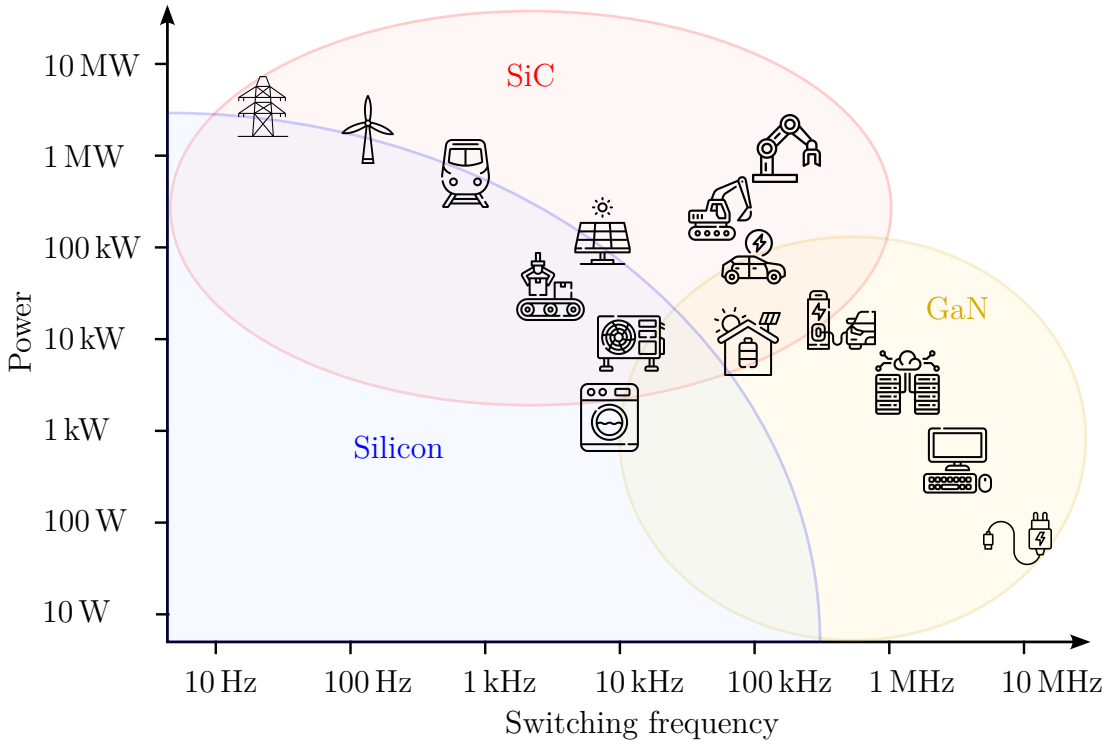

Figure 1.1: Fields of application for WBG semiconductor devices [4]
icon source: `https://www.flaticon.com/`

The WBG materials GaN and SiC will likely stay in focus in the future. In addition, new semiconductor materials may become significant for producing power electronic components. Promising candidates are the ultrawide-bandgap (UWBG) semiconductor materials diamond, cubic Boron nitride (c-BN) and Alimunum nitride (AlN) [7]. To evaluate the potential of these materials, their key characteristics are compared. Figure 1.2a shows a radar chart with the key material properties of different semiconductors [5]. The diagram shows the bandgap E_g, the breakdown field strength E_{bd}, the electron saturation velocity v_{sat}, the thermal conductivity λ and the melting point T_{max}. The WBG semiconductors SiC and GaN show very similar performance and perform better than Si in all categories. GaN has a slightly higher breakdown field strength and electron velocity, but lower thermal conductivity than SiC. The UWBG semiconductors diamond, c-BN and AlN show even better material properties in almost all categories [8]. In Fig. 1.2b the electrical characteristics on-resistance and breakdown voltage resulting from the material properties are compared . When dimensioning a semiconductor device, a trade-off must be made between these values, which are both proportional to the channel length. This results in the contour lines of constant BFOM values, which make the physical limit of the technology visible and is plotted for unipolar vertical devices [6]. It can be seen that the UWBG semiconductors enable a considerable potential for improvement compared to WBG semiconductors. It is therefore likely that UWBG devices will become a trend in the future and play an important role alongside other device-specific trends such as intelligent gate drivers and monolithic integration of components [9], [10].

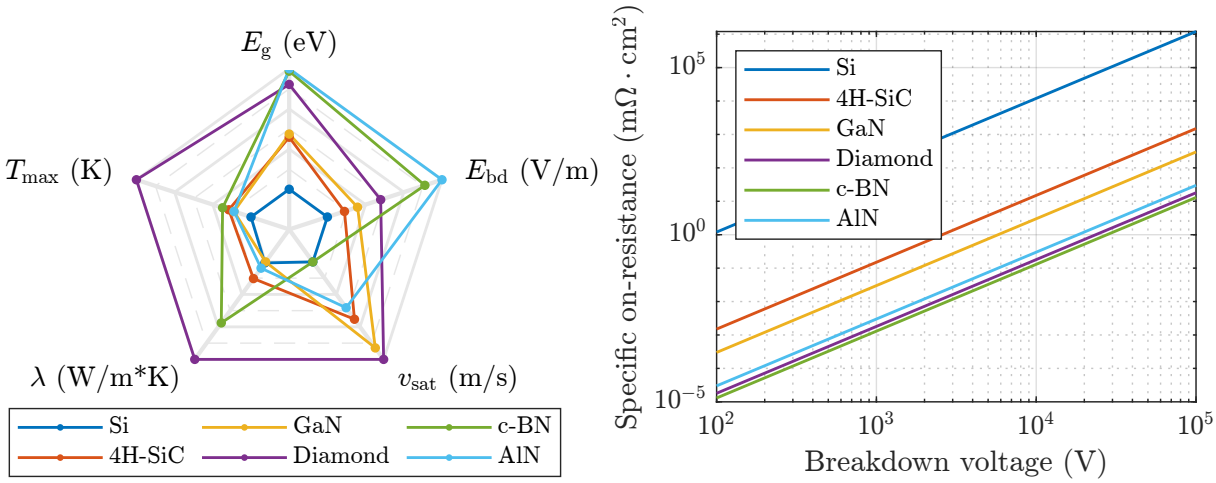

(a) Radar chart of material properties [5]

(b) Contour lines of constant Baliga Figure of Merit (BFOM) values for unipolar vertical devices [6]

Figure 1.2: Comparison of present and future technologies for power semiconductor devices

1.2 Research Objectives and Statement of Novelty

Due to the widespread use of WBG semiconductor devices, there is a high demand for their dynamic characterization, as a recent survey has shown [11]. This work aims to improve the measurement accuracy in this task, which is a significant challenge due to the very fast-switching transients of SiC and GaN devices. Further development towards UWBG devices would increase this challenge even more. In particular, the measurement of switching energies E_{off} and E_{on} in the double-pulse test (DPT) is very challenging and significant measurement errors are expected, which are mainly caused by non-ideal probes [12]. To enhance the measurement accuracy, it is essential to identify the parameters that have the most significant influence on the results. Previous publications have mainly focused on the measurement errors of individual current and voltage transients or do not offer a holistic approach for deriving the requirements for measuring switching energies. Consequently, the initial step is to identify which parameters have the most significant impact on the measurement accuracy for E_{off} and E_{on} and how these parameters interact with each other. This is achieved in this work by simulating DPTs with WBG devices and statistically evaluating the results.

One of the most significant challenges in dynamic characterization is the measurement of the drain-source current, which offers a significant opportunity for improvement [13], [14]. Coaxial shunts are still used in several publications, as they have been the best available option for a considerable period of time. However, with fast-switching devices such as HEMTs, their parasitic inductance is too high and affects the switching behavior. For this reason, there is a continuous search for new technologies that can be classified into resistive and inductive measurement techniques [15]. This work evaluates existing

concepts and presents two novel designs for current sensors that enable precise measurement while minimizing the influence on the switching behavior. The results are a radial shunt resistor consisting of discrete thin-film resistors and a planar pick-up coil embedded into a printed circuit board (PCB). For both techniques, very high bandwidths of over 2 GHz and parasitic inductances in the range of 100 pH could be validated. In this way, two straightforward tools are provided that significantly reduce the issue of drain-source current measurement of WBG devices.

1.3 Outline of this Thesis

After providing an introduction to the research topic in this chapter, the structure of this thesis is presented by explaining the contents of the five main chapters.

Chapter 2: Fundamentals on the Characterization of WBG Semiconductor Devices
The first part of Chapter 2 summarizes the various electrical properties of power transistors. Besides the static and dynamic characteristics, there are also characteristics that are specific to WBG devices such as the dynamic on-resistance of GaN HEMTs. Afterwards, the DPT is introduced, which enables measuring the switching energies E_{off} and E_{on} in hard-switching operation. In addition to the topology, state-of-the-art probes as well as alternatives to the DPT are reviewed. Particularly with fast-switching WBG devices, this test is susceptible to measurement errors that are caused by bandwidth limitations of probes, parasitic elements or incorrect deskewing. These sources of error and their effects are discussed in the last part of Chapter 2.

Chapter 3: Evaluation of the Measurement Accuracy in Double Pulse Tests
In the third chapter, the measurement accuracy in DPT is systematically investigated. First, the methodology is presented, which is based on the simulation of DPTs including the sources of error described previously. Using a design of experiments (DoE) with a large number of different measurement setups, the switching behavior of four different WBG devices is analyzed. It is shown that bandwidths, parasitics and incorrect deskewing can significantly reduce the measurement accuracy and errors above 10 % are possible. In particular, the measurement of the drain-source current needs to be optimized.

Chapter 4: Design of an Advanced Resistive Current Sensor
Chapter 4 focuses on the design of an advanced resistive current sensor. The motivation is the fact that conventional coaxial shunts have a relatively high parasitic inductance, which is unsuitable for fast-switching WBG devices. After providing an overview on existing concepts, a novel design is presented. It is based on the circular arrangement of discrete thin-film resistors. The transfer function of the design is analyzed in detail, using

both simulations and the measurement of prototypes. In addition, the thermal limits and options for extending the bandwidth are discussed. The novel design achieves an inductance below 100 pF and a bandwidth of 2.17 GHz.

Chapter 5: Design of an Advanced Inductive Current Sensor
Chapter 5 focuses on the design of an advanced inductive current sensor. This is motivated by the fact that conventional Rogowski coils have a relatively low bandwidth, which is unsuitable for fast-switching WBG devices. After a review of existing concepts, a novel design based on a planar pick-up coil embedded in an inner layer of a circuit board is presented. The geometry of the design is optimized by comparing different variants via simulation. Material properties and the dimensioning of a damping resistor are also taken into account. A bandwidth of 2.66 GHz is validated in the measurement of prototypes.

Chapter 6: Proof of Concept
In Chapter 6, the radial shunt resistor from Chapter 4 and the inductive sensor from Chapter 5 are applied in DPTs as a proof of concept. For this purpose, an evaluation board is designed with GaN HEMTs of which the drain-source current can be measured via both concepts. As a further reference, the board, including all parasitic elements, is simulated to evaluate the measurement of E_{off} and E_{on}. It is determined that the radial shunt resistor, in particular, provides highly accurate results and is, therefore, the optimal choice for measuring the drain-source current of WBG devices.

Chapter 7: Conclusions and Outlook
In the last chapter, the contributions of this thesis are highlighted and the previous chapters are summarized. Finally, an outlook is given on further research to improve the dynamic characterization of fast-switching WBG semiconductor devices.

2 Fundamentals on the Characterization of WBG Semiconductor Devices

This chapter summarizes the fundamentals of the characterization of WBG semidonductor devices. First, Section 2.1 defines the various electrical characteristics that are relevant for the design and operation of a power electronic system. This is followed by Section 2.2, which discusses the DPT in more detail. This test is a standardized measurement method for dynamic characterization and enables measuring switching energies in hard-switching operation. Section 2.3 deals with the error sources that arise in DPTs and presents the impact on the switching transients. Finally, Section 2.4 provides a brief conclusion about the contents of this chapter.

2.1 Electrical Characteristics of Semiconductor Devices

When characterizing semiconductor devices, a distinction can be made between static and dynamic characteristics. One of the most important static characteristics is the output characteristic of a semiconductor, which is presented in Section 2.1.1. The dynamic characteristics presented in Section 2.1.2 include the switching energies, the switching times and various charge quantities. These variables have in common that they influence the switching behavior and that their determination requires a measurement in the time domain. In addition, there are special characteristics of WBG semiconductors such as the dynamic on-resistance, which are described in Section 2.1.3. Besides the electrical characteristics, there are other characteristics such as the thermal impedance Z_{th}, which are not covered by this thesis.

2.1.1 Static Characteristics

One of the main specifications of a transistor is its output characteristic. It describes the relationship between the drain current i_{ds} and the drain-source voltage v_{ds} as a function of the gate-source voltage v_{gs} for static operating points [16]. Figure 2.1a gives an overview of the output characteristics of a power MOSFET in the forward direction. The operation takes place in one of four regions, of which the ohmic region and the blocking region are the most relevant for operation as a power electronic switch. A similar characteristic is

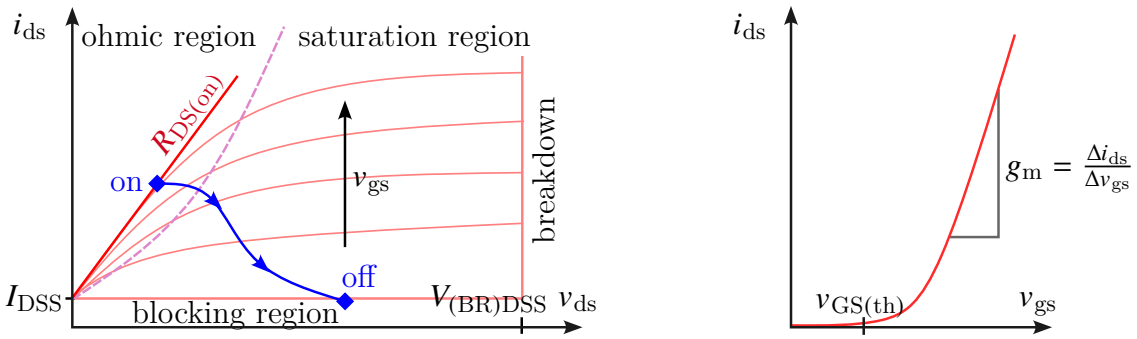

(a) Output characteristic with switching trajectory

(b) Transfer characteristic

Figure 2.1: Static characteristics of a power MOSFET

defined for bipolar devices such as IGBTs, but the saturation region is referred to as the linear region or active region, as the term saturation is used for the area that corresponds to the ohmic region of a MOSFET. If the gate source voltage v_{gs} is lower than the threshold voltage $v_{GS(th)}$, the transistor is in the blocking region and will conduct just a minimal current I_{DSS}. If the voltage v_{gs} is sufficiently high, the transistor is operated in the ohmic region, which means that it is completely turned on and behaves like a resistor with the constant value $R_{DS(on)}$. The transition between these two operating points takes place by passing through the saturation region, as shown in Figure 2.1a. In the MOSFET saturation region, the current i_{ds} is strongly dependent on v_{gs} and the operation involves high losses, which is expressed as the switching loss defined in Section 2.1.2. The upper voltage limit of the transistor, which is marked as the breakdown voltage $V_{(BR)DSS}$ in the output characteristic, should not be exceeded to avoid destruction of the device.

In Fig. 2.1b, the transfer characteristic is shown, which relates directly to the output characteristic curve. It describes the relationship between the gate-source voltage v_{gs} and the maximum possible drain current i_{ds}. Once the threshold voltage $v_{GS(th)}$ is exceeded, i_{ds} starts to increase, with the gradient g_m corresponding to the transconductance of the transistor. The static characteristics described are measured using semiconductor curve tracers, which have precise measuring instruments and allow all relevant data to be recorded automatically. Since static operating points are measured during the test, any dynamic measurement parameters such as the bandwidth of the measuring equipment do not play a critical role.

2.1.2 Dynamic Characteristics

In addition to the static characteristics, there are dynamic characteristics of power semiconductors, which provide information about the switching behavior. Since both GaN HEMTs and SiC MOSFETs can be categorized as field-effect transistors (FETs), the dy-

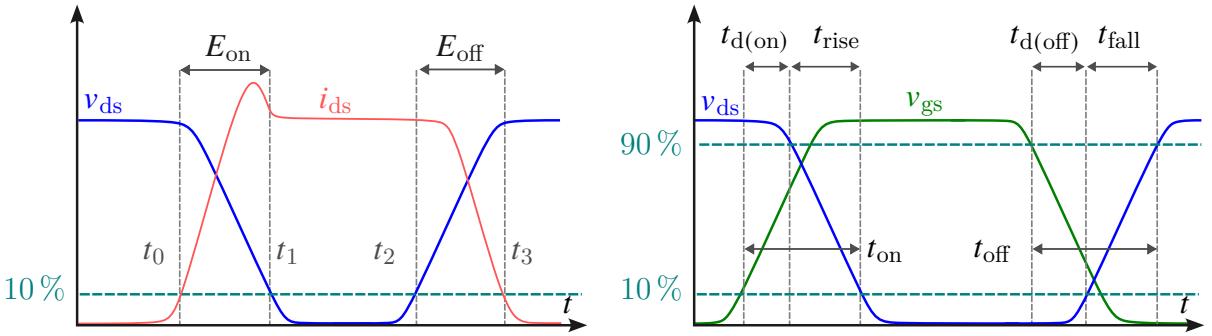

(a) Integral times for E_{on} and E_{off}

(b) Switching times

Figure 2.2: Definition of dynamic characteristics according to *IEC 60747-8* [17]

namic characteristics are defined according to the standard *IEC 60747-8* [17]. In contrast to the static characteristics, the measurement of the dynamic characteristics can be very challenging, as the associated transients must be recorded with high temporal resolution and can be influenced by parasitics. In this section, the most important dynamic characteristics from the data sheet of a power semiconductor are reviewed.

The switching energies E_{on} and E_{off} are two key characteristics for operating a transistor. The switching energies result from the overlap of current and voltage when switching between the turn-off and turn-on state and are dissipated as heat. As these switching losses are proportional to the switching frequency f_{sw}, they can contribute significantly to the overall losses with fast-switching topologies. The calculation is based on the integration of the instantaneous power loss p_{loss} according to Eq. (2.1) and Eq. (2.2), using the integration boundaries specified in Fig. 2.2a. The integration boundaries are defined via the 10 % limit of the drain-source voltage v_{ds} present during switching and the drain-source current i_{ds}. The switching energies are measured using the DPT with an inductive load, which is discussed in detail in Section 2.2 and is considered the main application of this thesis.

$$E_{on} = \int_{t_0}^{t_1} p_{loss}(t)\ \mathrm{d}t = \int_{t_0}^{t_1} v_{ds}(t) \cdot i_{ds}(t)\ \mathrm{d}t \tag{2.1}$$

$$E_{off} = \int_{t_2}^{t_3} p_{loss}(t)\ \mathrm{d}t = \int_{t_2}^{t_3} v_{ds}(t) \cdot i_{ds}(t)\ \mathrm{d}t \tag{2.2}$$

In addition to the switching energies, there are other dynamic characteristics, such as the switching times defined in Fig. 2.2b [16]. These are based on the relation of the drain-source voltage v_{ds} to the gate-source voltage v_{gs} during the switching events. The turn-on time t_{on} and the turn-off time t_{off} describe the duration of the respective switching event and use the respective 10 % limits of v_{ds} and v_{gs}. The two criteria turn-on delay $t_{d(on)}$ and turn-off delay $t_{d(off)}$ describe the delay with which the voltage v_{ds} reacts to a change in the gate-source voltage v_{gs}. The switching times also include the two rise times t_{rise} and t_{fall}, which correspond to the time required by v_{ds} to switch between 10 % and 90 %.

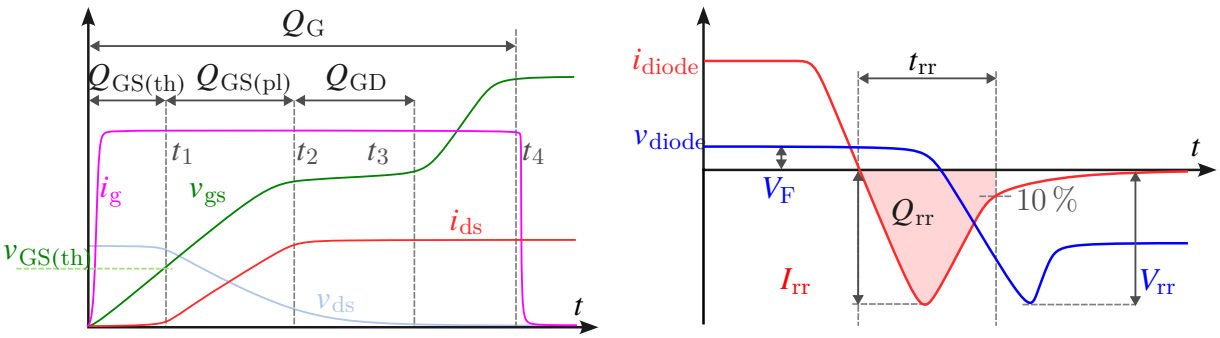

(a) Gate charges

(b) Body diode reverse characteristics

Figure 2.3: Definition of dynamic characteristics (continued)

It is important to note that t_{rise} is assigned to the falling edge of v_{ds}, as the current i_{ds} rises during the turn-on [17]. The switching times are measured in a defined measurement setup with a resistive load [17].

The dynamic characteristics also include several charge quantities that determine the behavior of the semiconductor. Their values are required, for example, to optimally dimension gate driver circuits. Figure 2.3a shows the time response of the gate-source voltage v_{gs} during the charging process of the gate capacitance with the constant current i_g. The total gate charge Q_G can be determined via the integration of i_g. This is divided into the threshold gate charge $Q_{GS(th)}$, which is required to charge the gate capacitance to the threshold voltage $v_{GS(th)}$, and the plateau gate charge $Q_{GS(pl)}$, which is required to increase the voltage v_{gs} to the Miller plateau. After the Miller plateau is reached, v_{gs} only increases further once the gate-drain charge Q_{GD} has been applied. Another dynamic charge quantity that occurs in MOSFETs is the reverse recovery charge Q_{rr} of the body diode. Figure 2.3b shows the behavior of the current i_{diode} when the body diode changes from the conducting to the blocking state. In this case, the recombination of the charge carriers leads to an opposite current peak I_{rr}, which extends over the period of the reverse recovery time t_{rr}. Like the switching times, the charge characteristics are measured in a defined measurement setup with a resistive load and require both a high temporal resolution and a sufficiently high vertical accuracy.

The capacitances of a transistor are also classified as dynamic characteristics, as they influence the dynamic behavior. Figure 2.4a shows the definition of the gate-source capacitance C_{GS}, the drain-source capacitance C_{DS} and the Miller capacitance C_{GD} [18]. A characteristic of these capacitances is that they are dependent on the drain-source voltage v_{ds}, as shown in Fig. 2.4b as an example. This illustration can be found in data sheets of power transistors and shows the behavior of the input capacitance C_{ISS}, the output capacitance C_{OSS} and the reverse transfer capacitance C_{RSS} and their respective definitions. In contrast to the other dynamic characteristics, the capacitances are not measured in the time domain. Instead, they are recorded by means of curve tracers that use a small-signal ac analysis with a dc bias.

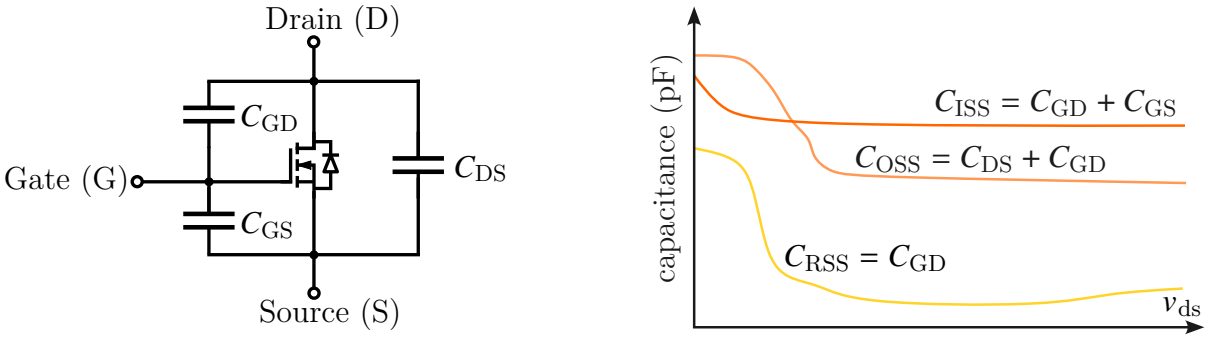

(a) Capacitance definition

(b) Exemplary capacitance curves

Figure 2.4: Dynamic capacitances

2.1.3 Characteristics Specific to WBG Semiconductor Devices

The previous sections refer only to the conventional characteristics, which are mostly independent of the respective transistor technology and are mentioned in common data sheets. For WBG semiconductor devices, further characteristics have been observed, like the dynamic on-resistance $R_{DS(on)}$ and the hysteresis of the output capacitance C_{OSS}. These effects can influence the conduction and switching losses of a converter and thus its overall efficiency.

Figure 2.5a shows the effect of the dynamic on-resistance [19]. The effect is caused by electron trapping effects and depends on the preconditioning of the device under test (DUT). Initially, the DUT is turned on and the value of $R_{DS(on)}$ is at a static level. Subsequently, the device is switched off for the period t_1 to t_2, which is referred to as trapping time. After the device is turned on again, an increased value of $R_{DS(on)}$ can be measured, whereby the increase in resistance depends on the trapping time and the dc bias voltage, which is given as V_1 and V_2. During the detrapping time, the dynamic value of $R_{DS(on)}$ gradually approaches its static value again. The dynamic on-resistance of GaN devices can strongly influence the efficiency of a converter, as the conduction losses are increased by up to 35 % [20]. The measurement of the dynamic $R_{DS(on)}$ can be performed in the DPT or similar topologies, using a clamping circuit to measure the forward voltage drop in the on-state of the DUT with sufficiently high accuracy [21], [22].

The C_{OSS} hysteresis is another specific effect that is observed in Si superjunction MOSFETs and also occurs in WBG devices [23], [24]. This effect describes the dependency of the output capacitance C_{OSS} on the voltage history and the current value of the drain-source voltage v_{ds}. Figure 2.5b shows the charging and discharging process of the output capacitance affected by the hysteresis effect, whereby the hysteresis causes the energy loss $E_{OSS,H}$. Since $E_{OSS,H}$ is frequency-dependent, the switching behavior and switching losses may deviate from the expected values, especially at high switching frequencies. The measurement method using the Sawyer-Tower test is described in the recently published standard [25]. In addition to the C_{OSS} hysteresis, there are other effects, such as the

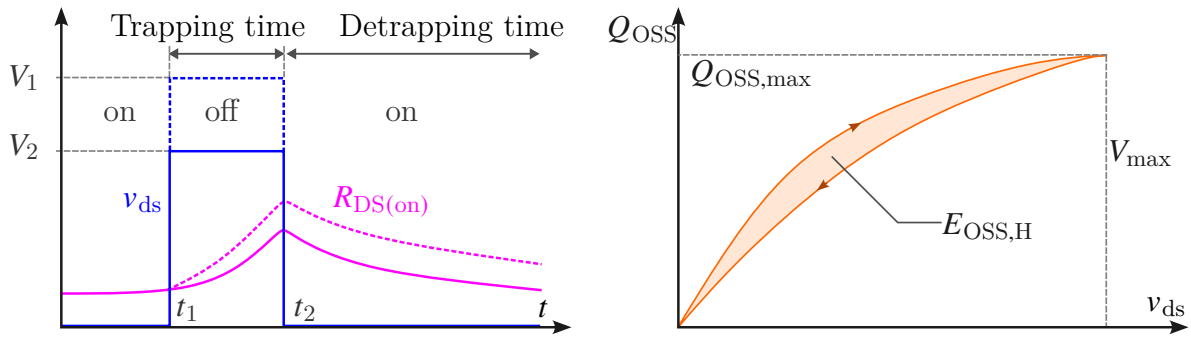

(a) Dynamic $R_{DS(on)}$ (b) Hysteresis of C_{OSS}

Figure 2.5: Dynamic effects of WBG semiconductor devices

threshold voltage hysteresis, which is described in [26] and [27] for SiC MOSFETs. In this case, the gate-source threshold voltage $v_{GS(th)}$ depends on the gate turn-off voltage and the duration in the turn-off state. In summary, the characteristics given in the data sheet never describe the dynamic behavior completely, especially for WBG semiconductor devices. An individual and exact characterization is therefore essential to optimize the performance of SiC and GaN devices.

2.2 Double-Pulse Testing

The double-pulse test (DPT) is one of the most important test methods for determining the dynamic characteristics of power semiconductor devices. First, the topology and operation of the DPT is presented in Section 2.2.1. The test requires that current and voltage are measured with high precision during the switching event. Section 2.2.2 therefore shows various state-of-the-art voltage probes and compares their properties with each other. An analogous overview is given in Section 2.2.3 for state-of-the-art current probes, which are based on different measurement principles. Finally, Section 2.2.4 compares the DPT with alternative methods for determining switching losses. These are calorimetric measurements and efficiency measurements in continuous converter operation.

2.2.1 Topology and Operation

The DPT is based on the topology shown in Fig. 2.6b and makes it possible to measure the hard-switching operation of a power semiconductor device [13]. The central element is the DUT, which forms a half-bridge circuit consisting of two transistors whose switching behavior is to be investigated. In parallel to this is the dc-link capacitor C_{DC}, which is charged to the voltage V_{sw}. The switching node of the half-bridge is connected to the potential V_{sw} via the load inductance L_{load}. During the test, the upper transistor is

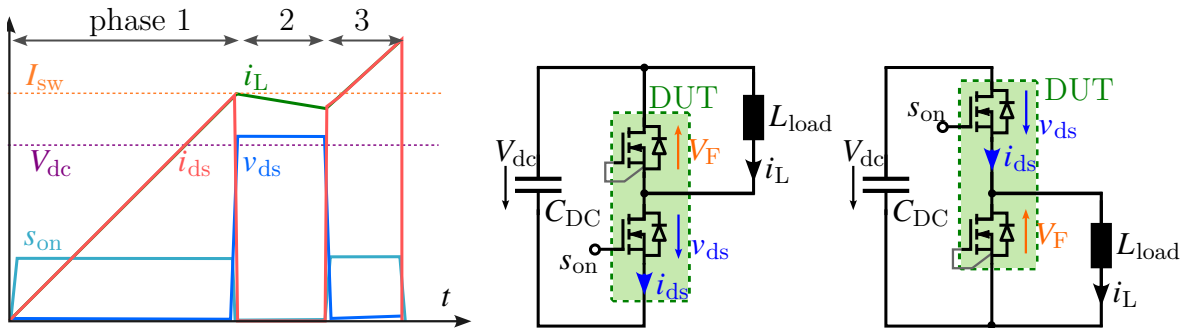

(a) Test sequence (b) Conventional circuit (c) High-side circuit

Figure 2.6: Double-Pulse Testing

permanently turned off and is operated in the reverse direction. Figure 2.6a shows the time sequence of the test, which is characterized by two successive pulses of the drive signal s_{on} and can be divided into three phases.

Phase 1 In the first pulse, the low-side switch is turned on for a predefined time, which causes the current i_L to increase according to Eq. (2.3). When the current i_L has reached the desired value I_{sw}, the low-side switch is turned off and the turn-off event can be recorded by simultaneously measuring the two transients v_{ds} and i_{ds}.

$$i_L(t) = \frac{V_{sw}}{L_{load}} \cdot t \tag{2.3}$$

Phase 2 The low-side switch is completely turned off and the current i_L has commutated into the freewheeling path via the reverse-conducting high-side switch. Due to energy preservation, i_L remains at an almost constant level and only drops slowly according to Eq. (2.4). The voltage at the switching node increases to $v_{ds} = V_{sw} + V_F$, where V_F corresponds to the forward voltage drop of the body diode of the high-side transistor.

$$i_L(t) = I_{sw} \cdot \left(1 - \frac{V_F}{L_{load}} \cdot t\right) \tag{2.4}$$

Phase 3 As soon as the turn-off switching event is completed, the low-side switch is turned on again. This causes the current i_L to commutate back into the lower path and the turn-on switching event can be recorded. The voltage drops to $v_{ds} = R_{DS(on)} \cdot i_L$, where $R_{DS(on)}$ corresponds to the drain-source on resistance of the low-side transistor. Once the turn-on event is completed, the low-side switch is turned off again, which represents the end of the experiment.

In the case of fast-switching WBG devices, the entire DPT is completed within a time window in the order of typically a few microseconds. As a result, the junction tempera-

ture T_j, which is another important operating parameter, can be assumed to be constant during the test. For the DPT to be carried out successfully, careful selection and dimensioning of the components L_{load} and C_{DC} is required, which is discussed in more detail in Section 3.1.2. In addition, with regard to WBG devices, it is essential that the parasitic elements of the switching cell are minimized and that the measuring devices for the drain-source current i_{ds} and the drain-source voltage v_{ds} meet the requirements.

Figure 2.6c shows an alternative topology for the DPT, in which the load inductance L_{load} is connected to the ground potential. Instead of the low-side switch, the switching behavior of the high-side switch can be investigated using the same sequence as Fig. 2.6a. In this variant, the low-side switch stays permanently turned off an acts as the free-wheeling path during phase 2. This variant is required if the two transistors have different switching behavior, which is particularly the case with asymmetrically designed power modules [28]. Another topology for the DPT was presented in [29]. By adding additional switches and a separate voltage source for the magnetization of L_{load}, it is possible to control the test voltage and current independently of each other. This increases flexibility and safety, as the dc link capacitor is decoupled, making this variant attractive for stationary test bench setups. A similar topology was also used in [30] to measure IGBTs under zero-voltage switching (ZVS) conditions. Both examples show that the DPT can be adapted to different requirements and is therefore an essential tool for dynamic characterization.

2.2.2 State-of-the-Art Voltage Probes

This section provides a brief overview of state-of-the-art voltage probes. The selection of the probe to measure the drain-source voltage v_{ds} is crucial for a successful DPT. The most important properties of the different probing techniques are introduced and a brief evaluation for the application with fast-switching WBG semiconductor devices is given.

Passive probes These probes represent the simplest type of voltage measurement and are included with most oscilloscopes. The measuring principle is based on a resistive and capacitive voltage divider, which is formed with the 1 MΩ input of the oscilloscope. The voltage is measured against the ground potential with a division ratio of typically 10:1 or 100:1. With regard to the characterization of fast-switching WBG devices, it must be considered that the bandwidth of a passive probe is typically limited to 500 MHz and that the relatively high input impedance of the probe can affect the switching behavior [31]. In Fig. 6.8b the design and measurement principle of a high-impedance passive probe is discussed in more detail. A special type are low-impedance passive probes, which are terminated on the output side with 50 Ω. hey achieve significantly higher bandwidths at the cost of lower nominal voltages.

Active probes (single-ended) Probes of this group contain active electronic components such as amplifiers and require an external power supply. [32] The advantage is a high input impedance, which results in a low impact on the circuit to be measured. In addition, very high bandwidths of over 10 GHz can be achieved, whereby a low nominal voltage must be taken into account as a trade-off. The area of application therefore lies in the measurement of high-frequency signals with low amplitude, which makes this type of probe rather unsuitable for the characterization of power electronic devices in the DPT.

Active probes (differential) These probes form a sub-category of active probes and are characterized by differential measurement of the input voltage with high common mode rejection ratio (CMRR). This makes them suitable for measuring floating signals and therefore very versatile. Differential probes are very common in power electronics and achieve bandwidths of several 100 MHz at nominal voltages up to the kilovolt range. With regard to the characterization of fast-switching WBG devices, a drawback of conventional differential probes is that the CMRR decreases at high frequencies, as there is typically no galvanic isolation, making the measurement susceptible to noise [33].

Optically-isolated probes A special class of differential probes are optically isolated probes. These are characterized by an optical transmission technology with laser diodes, resulting in a high CMRR, which is also maintained at high frequencies. The design enables measuring voltages up to the kilovolt range with a simultaneously high bandwidth of up to 1 GHz and low susceptibility to noise. With regard to the characterization of WBG semiconductors, optically-isolated probes are considered to be the most suitable solution, but also the most cost-intensive type of probes.

In addition to the aforementioned characteristics, there are several other parameters for characterizing a voltage probe [34]. With regard to DPT with WBG devices, the criteria of bandwidth and input capacitance are particularly significant [35]. The detailed requirements are device-specific and are discussed in Chapter 3. Figure 2.7 classifies several commercially-available voltage probes according to these criteria. In addition, the type of probe and the nominal voltage are indicated. It is noticeable that passive probes with high impedance do not exceed a bandwidth of 1 GHz and also have a relatively high input capacitance. The same applies to the group of high-voltage (HV) differential probes, which have the highest voltage rating but are limited in their bandwidth. Higher bandwidths are achieved by low-voltage (LV) differential probes, which, however, are usually not suitable for DPT due to their low voltage rating. This limitation also applies to the two groups of single-ended active probes and low-impedance passive probes, which achieve the best performance in terms of bandwidth and input capacitance, but only offer low voltage ratings. The group of optically-isolated probes is positioned in the middle of the diagram. Most models have a bandwidth of 1 GHz with an input capacitance of a few picofarads. As high voltages can be measured, these probes are ideally suited for DPTs with fast-switching WBG semiconductor devices, if they are used properly [36].

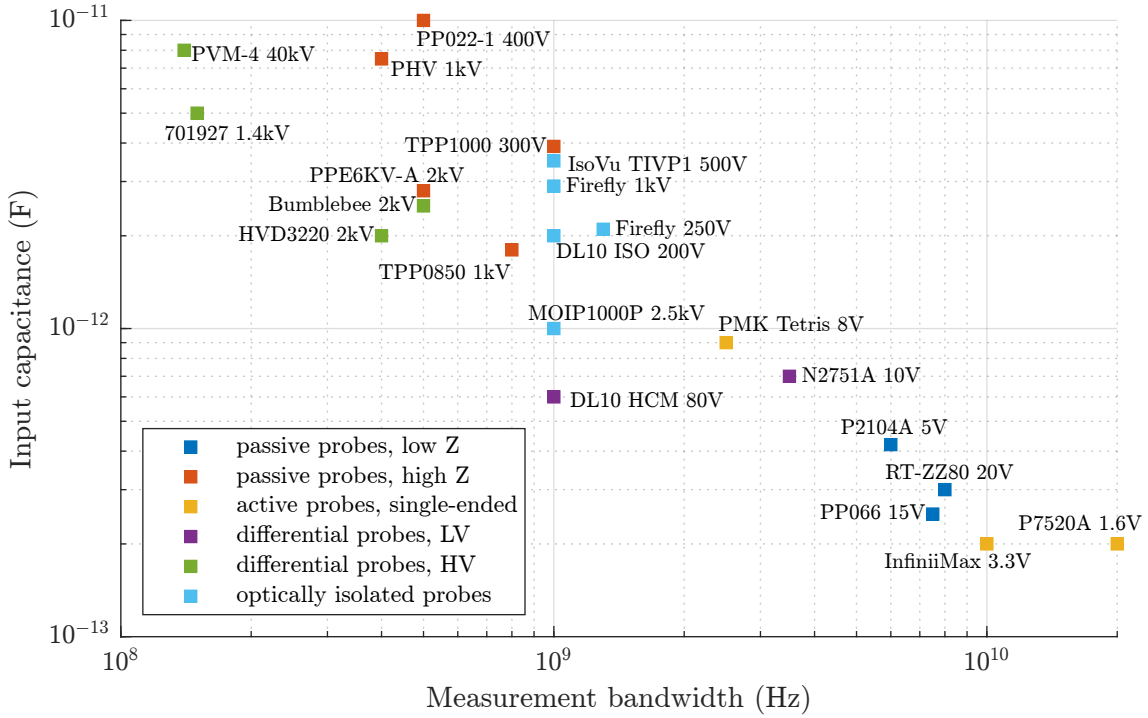

Figure 2.7: Classification of commercially-available voltage probes

2.2.3 State-of-the-Art Current Probes

This section provides a brief overview of state-of-the-art current probes. It presents only measurement methods that are commercially available and offer relatively high bandwidth, making them suitable for measuring fast transients. In addition to the measurement principles presented, there are other solutions such as Hall-effect sensors or magnetoresistive current sensors, but these have significantly lower bandwidths and are therefore irrelevant for the dynamic characterization of WBG semiconductor devices [15], [37].

Clamp-on current probes Current clamps are the most convenient type of current measurement. Their advantage is that no interruption of the current-carrying conductor is necessary, and they can measure both dc and ac currents. The measuring principle of a current clamp usually combines a Hall-effect sensor for the lower frequency range and an inductive current measurement for the high-frequency range [38]. Current clamps are available for a wide range of applications, but since they are designed for measuring cable-guided currents, they are only suitable for characterizing semiconductor devices to a limited extent [39]. An exemplary model is the current clamp *N7026A* from *Keysight Technologies*, which has a bandwidth of 150 MHz and a rated current of 30 A.

Closed-core current transformers Current transformers with a closed magnetic core offer better performance than clamp-on current probes in terms of bandwidth. As this is a purely inductive type of current measurement, the current sensing is limited to ac currents. The main disadvantage is the relatively large geometric expansion, which makes this type of current measurement unsuitable for characterizing semiconductor devices. An exemplary model is the current transformer *6585* from *Pearson Electronics Inc.*, which enables a bandwidth of 250 MHz at a rated current of 500 A.

Rogowski coils Rogowski coils are another solution for inductive current measurement. In contrast to current transformers, Rogowski coils do not have a magnetic core, which leads to better flexibility and enables higher currents since no saturation can occur [40]. An exemplary model is the Rogowski coil *Mini50HF* from *PEM Ltd.*, which offers a bandwidth of 50 MHz at a rated current of up to 3 kA. The suitability of Rogowski coils for characterizing semiconductor devices depends on the availability of sufficient space and the adequacy of the bandwidth for the intended application [41].

Shunt resistors Shunt resistors are an alternative to the previously mentioned current probes. A shunt resistor is inserted directly into the circuit and enables resistive current measurement by acquiring the voltage drop that is proportional to the current. This allows both dc and ac currents to be measured with high precision. The general disadvantages are the lack of galvanic isolation and the ohmic losses in the resistor. A special type of shunt resistor is the coaxial shunt, which is described in detail in Section 4.1.1. An exemplary model is the coaxial shunt *SDN-414-10* from *T&M Research Products, Inc.*, which enables a bandwidth of 2 GHz. Shunts are suitable for the characterization of semiconductor devices, but the parasitic inductance can affect the switching behavior, which is particularly relevant for very fast switching WBG devices [42], [43].

Optical current measurement Another type of current measurement are fibre-optic current sensors (FOCSs). These are sensors that use the Faraday effect, which describes the rotation of the polarization plane of an electromagnetic wave as a function of a magnetic field. This measurement technology was originally developed for low-frequency applications in the high-voltage grid [44]. In [45] it is investigated to what extent the method is also suitable for DPT. By now, commercial solutions achieve bandwidths of up to 150 MHz [46]. As the measuring principle is completely non-invasive, it offers considerable potential for future measuring equipment.

This overview has shown that there are various concepts for current measurement. With regard to the characterization of fast-switching WBG semiconductor devices, however, there are only a few viable options. Only coaxial shunts achieve bandwidths in the gigahertz region, but they can lead to a distortion of the switching behavior due to their parasitic inductance. Rogowski coils enable a non-invasive measurement but do not achieve

a sufficiently high bandwidth. The same applies to FOCSs. Therefore, various new concepts are being researched, and extensive efforts are being made to maximize bandwidth while minimizing measurement impact. In Section 5.1, advanced inductive measurement techniques are discussed, which can be seen as an improvement over conventional Rogowski coils. In Section 4.1.2, advanced concepts for resistive current measurement are presented, representing an alternative to conventional coaxial shunts.

2.2.4 Alternatives to the Double Pulse Test

In addition to the DPT, there are other methods for determining the switching losses of power semiconductor devices. The most straightforward approach is the efficiency measurement, in which a power converter is operated at a resistive or active power sink. This method has been employed in several studies, including [47] and [48]. A measurement of the input power p_{in} and output power p_{out} allows the overall system efficiency to be determined for different operating points. Despite the high precision achievable with power meters, the measurement of the overall efficiency always includes all loss mechanisms within the converter. In addition to switching losses, conduction losses, driver losses, capacitor losses, and magnetic losses in inductors must be considered. Extracting switching losses is a challenging task that is often only partially achievable [49]. By varying the switching frequency f_{sw} of the pulse-width modulation (PWM), it is possible to extract frequency-dependent losses. It is possible to determine the influence of temperature by waiting until a thermal steady-state is reached. This increases the time required for the procedure. The advantage of this method is that it is simple to implement and provides results that correspond to the real application.

Another alternative are calorimetric measurements. The total power loss of a semiconductor is determined indirectly by measuring temperature changes in a thermally defined environment. In conventional calorimeters, the DUT is located in a thermally insulated chamber [50]. By measuring the temperature increase ΔT in steady state, the dissipated power loss p_{loss} can be derived after prior calibration via a reference heater. In another method, the power loss p_{loss} is determined by measuring temperature and flow rate of a cooling medium [51]. A disadvantage of conventional methods is that temperature changes have to be measured over periods of 30 min to several hours [52]. To overcome this drawback, transient calorimetric methods were developed. In [53], the change in temperature over time is evaluated, which makes it possible to measure the power loss without the system being in a steady state. A similar approach is pursued in [54]. Using a previous calibration measurement, the thermal impedance Z_{th} of the system can be used to determine the power loss of the DUT for different operating points. The calibration method presented in [55] also takes into account the conduction losses and driver losses, so that a high level of agreement with the electrical measurement in the DPT is achieved. Overall, a calorimetric measurement has the advantage that it is not limited to the hard-switching operation of the DUT, as is the case with the standard DPT topologies that are shown in Fig. 2.6.

Table 2.1: Comparison of test methods for measuring switching losses

	DPT	Calorimetric measurement	Efficiency measurement
Measurement principle	direct measurement of transients	indirect measurement via dissipated heat	measurement of input and output power
Measured quantities	v_{ds}, i_{ds}	ΔT	p_{in}, p_{out}
Derived quantities	E_{on}, E_{off} and t_{off}, t_{on}, t_{rise}, ...	p_{loss}	p_{loss}
Duration	transient	transient or steady-state	steady-state
Excitation	two single pulses	continuous PWM	continuous PWM
Heat sink	not required	thermally isolated DUT or heatsink with defined Z_{th}	regular cooling
Electrical load	inductive load	power sink (active or resistive)	power sink (active or resistive)
Operation mode	hard switching	hard switching and soft switching	hard switching and soft switching
Challenges	measuring transients, parasititcs elements	complex calibration	breakdown of loss mechanisms

Table 2.1 compares both methods presented to the DPT. The DPT is characterized by the fact that the switching behavior can be evaluated directly and switching energies and other dynamic characteristics such as t_{on}, t_{off} and t_{rise} are directly accessible. For this reason, the DPT is an irreplaceable method. The other methods are limited to measuring the total switching losses, which need to be separated from other loss mechanisms. Another advantage of the DPT over the other methods is the short time required and the relatively simple measurement setup, which does not require a heatsink, power sink and calibration. However, the DPT places high demands on the electrical measuring equipment, is susceptible to parasitic influences and is limited to hard-switching operation if the standard topology is used. For a complete evaluation of the performance of WBG semiconductor devices, a combination of the different methods can be useful to precisely determine the overall efficiency.

2.3 Sources of Error

This section identifies four main sources of error that influence the measurement accuracy in DPTs. First of all, the limited bandwidth of the probes is addressed in Section 2.3.1. In Section 2.3.2 the parasitic properties of probes and their influence on the switching transients are discussed. Another effect is the misalignment of the investigated waveforms, which causes the deskewing error that is explained in Section 2.3.1. Subsequently, Section 2.3.4 shows the relevant metrics when selecting a suitable oscilloscope for characterizing WBG semiconductor devices. Finally, Section 2.3.5 examines the definition and composition of switching energies in more detail, which are not a conventional measurement error but can also lead to deviations.

2.3.1 Bandwidth Limitation of Probes

A fundamental characteristic of every voltage and current probe is the bandwidth. For low-pass filters the bandwidth is another term for the 3 dB cutoff frequency f_c. It describes the frequency at which the frequency components of the input signal are attenuated by more than 3 dB [56]. The bandwidth also determines how quickly a system reacts to a change in the input signal and what minimum rise time t_{rise} can be measured with a probe. Equation (2.5) shows a common rule of thumb, which provides a correlation between the minimum-measurable rise time and the 3 dB cutoff frequency of a system with low-pass characteristics [57]. The origin of Eq. (2.5) is based on the step response of an first-order RC low-pass filter and can be found in Appendix A.1. It becomes clear that this is only a general approximation and thus not valid for systems of a different order.

$$t_{rise} = \frac{0.35}{f_c} \tag{2.5}$$

Figure 2.8a shows the bode diagram for a first-order low-pass filter for different bandwidths f_c. The magnitude response shows a typical drop of -20 dB per decade starting at f_c. The influence of this filter on a signal is shown in Fig. 2.8b using a switching transient as an example. The waveform v_{ds} was taken from the simulation of a 100 V GaN device presented later in Section 3.1.2. The response becomes considerably less steep as the cutoff frequency decreases and the measured rise time increases. This is caused by the fact that the filter not only changes the amplitude of the signal components, but also distorts their phase shift. This is referred to as amplitude and phase error. The phase of the filter is also shown in Fig. 2.8a and begins to fall before f_c is reached and approaches a value of -90°. The non-linear phase response has the effect that certain frequency components appear delayed [58]. This can be expressed via the group delay τ_g, which is defined as the

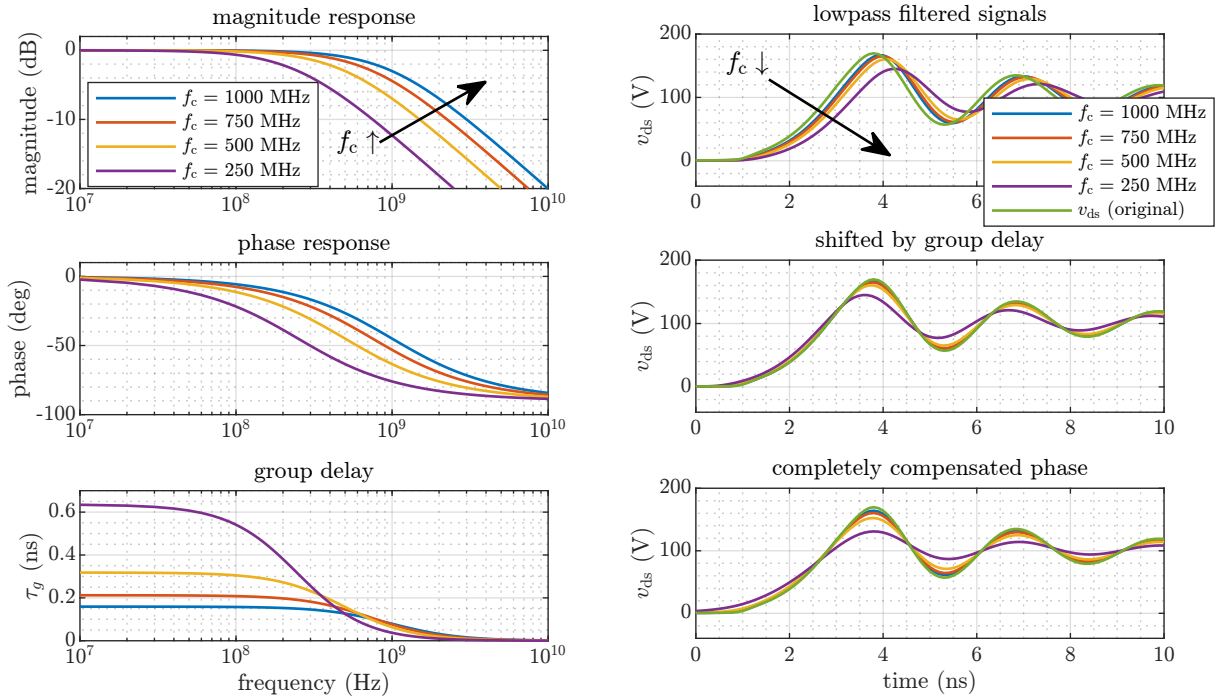

(a) Bode diagram including group delay τ_g

(b) Simulated switching transients in time domain

Figure 2.8: Examplary first-order lowpass filter and its impact on the v_{ds} switching transient of a 100 V GaN device

negative derivative of the phase ϕ by the angular frequency ω as shown in Eq. (2.6).

$$\tau_g = -\frac{d\phi}{d\omega} \tag{2.6}$$

The group delay is shown in the lower subplot of Fig. 2.8a. It has a constant value for low frequencies and converges to zero at high frequencies. If the group delay of a system is known, it can be compensated by shifting the signal by the low-frequency value of τ_g. This correction is shown in the second subplot of Fig. 2.8b and it is possible to partially correct the distortion caused by filtering. This correction is important in DPT with WBG semiconductor devices and is discussed in more detail in Section 2.3.3. If the phase response of a system is known exactly, it is possible to compensate the distortion completely, which is shown in the lower subplot of Fig. 2.8b. In this case, only the amplitude error is visible. However, this is difficult to realize in the real application as it requires an high-accurate modeling [59].

In addition to the rise time t_{rise}, the settling time T_s is another parameter for the transient response of a system. It was defined for operational amplifiers as the time required for the output to reach and steady within a given tolerance band [60]. In the context of high-frequency probes, T_s is typically not specified in datasheets, suggesting that it is either negligible or not considered a limiting factor in practical applications.

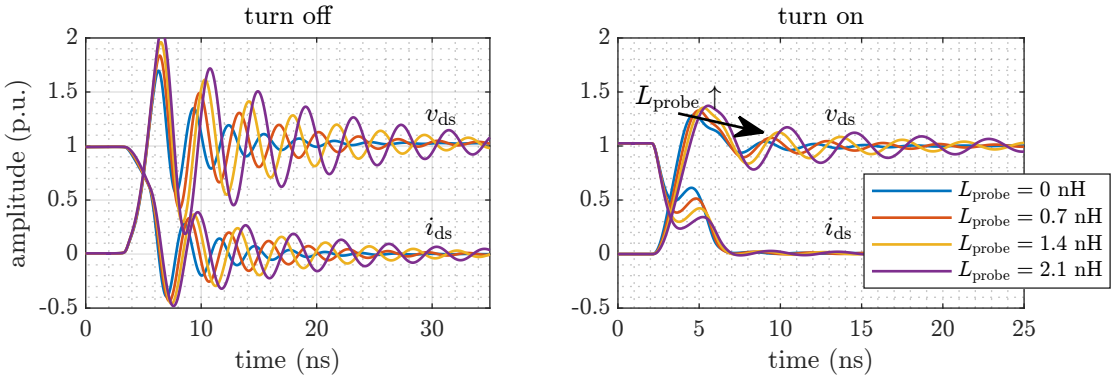

(a) Influence of probe inductance L_{probe}

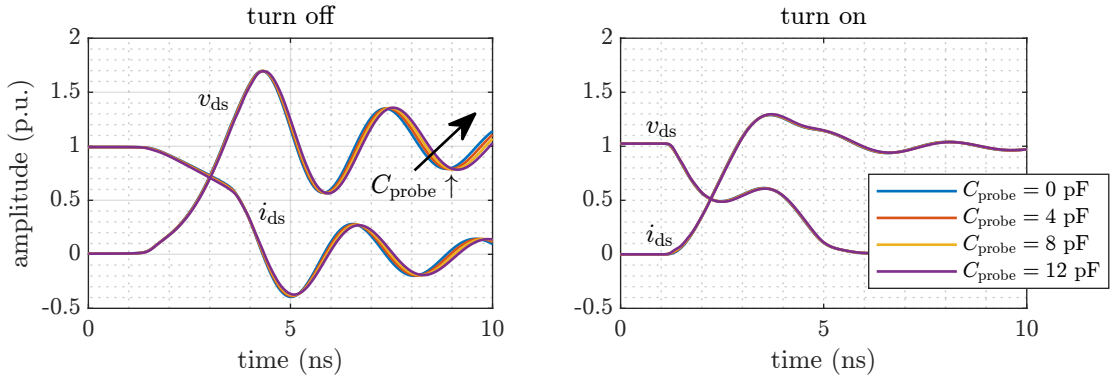

(b) Influence of probe capacitance C_{probe}

Figure 2.9: Examplary influence of probe parasitics to switching transients of a 100 V GaN device with normalized waveforms

2.3.2 Parasitics of Probes

In addition to the low-pass characteristics, probes have further characteristics that reduce the measurement accuracy. In most cases, a non-invasive measurement of electrical quantities is not possible. The reason for this are parasitic properties of the respective probes [12]. With regard to the drain-source voltage measurement v_{ds}, this is the input capacitance of the voltage probe, which is connected in parallel to the output capacitance of the DUT [35]. A typical passive probe has an input capacitance of 10 pF [61]. In terms of current measurement, the parasitic inductance of the current sensor is connected in series with the DUT [42]. A prominent example is the coaxial shunt, which adds a parasitic inductance of at least 2 nH. When designing switching cells with WBG semiconductor devices, the power loop inductance L_{loop} is a decisive criterion, which has an impact on the overall performance and must therefore be minimized [62]. Fast-switching GaN applications in particular react sensitively to an increase in L_{loop} [63].

To demonstrate the influence of probe parasitics on the switching behavior, Fig. 2.9 shows simulated switching transients of v_{ds} and i_{ds} for different probe setups using the example of a 100 V GaN device. The waveforms were generated with the simulation setup presented

in Section 3.1.2 and the y-axes were normalized to the corresponding values I_{sw} and V_{sw}. Figure 2.9a shows the change in the switching transients by introducing an additional inductance L_{probe}. In particular, the amplitude and frequency of oscillations caused by switching are affected. In Fig. 2.9b the influence of an additional capacitance C_{probe} on the switching behavior is shown. This is less significant and only leads to a slight change in the oscillation at turn-off. The reason for this is that the simulated DUT has a comparatively high output capacitance of $C_{OSS} = 110\,\text{pF}$ [64]. Devices with a higher rated voltage typically have a lower output capacitance, so a greater effect can be expected in this case.

2.3.3 Misalignment of Waveforms (Deskewing Error)

The measurement of the switching energies in DPT requires the drain-source current i_{ds} and the drain-source voltage v_{ds} to be measured simultaneously. To ensure a correct instantaneous power loss $p_{loss}(t) = i_{ds}(t) \cdot v_{ds}(t)$, both waveforms must be precisely aligned in time. The correction of the time offset, which is caused by the different propagation times, is called deskewing [13]. The total group delay of a measurement line consists of two parts. The first part is caused by the low-pass characteristic of the probe and the second part by the propagation delay of the cable. Figure 2.10 shows the effect of insufficient deskewing on the switching-energy measurement of a 100 V GaN device. As an example, switching transients were used that were generated with the simulation setup presented in Section 3.1.2. The y-axes were normalized to the corresponding values I_{sw} and V_{sw}. Figure 2.10a shows the effect of a positive offset of Δt between v_{ds} and i_{ds}. In this case, the overlapping area of current and voltage at turn-off is reduced, which decreases the measured turn-off switching energy E_{off}. For the turn-on event, the opposite effect takes place and the misalignment causes an increase in the overlapping area, which increases p_{loss} and therefore also E_{on}. Figure 2.10b shows the opposite case. With a negative time offset, the overlap at turn-off is increased, which means that E_{off} also increases. At the same time, the overlap is reduced during the turn-on, so that p_{loss} decreases and thus also the integral E_{on}.

As the later simulations show, improper deskewing can have a very strong effect on the measurement accuracy of E_{off} and E_{on}. There are various methods to successfully perform the deskewing, with deskewing fixtures such as [65] being the most straighforward option. However, most commercial deskewing fixtures are limited to use with current clamps or Rogowski coils and do not have the precision required for WBG applications [66]. In other publications, deskewing is performed in post-processing by aligning known characteristics of the waveforms [67], [68]. Another method based on step-response measurements is shown in Section 6.2.1. Under real conditions, complete compensation of the error caused by different signal propagation times is almost impossible, since the group delay of a non-ideal measurement line is frequency-dependent, as shown in Section 2.3.1.

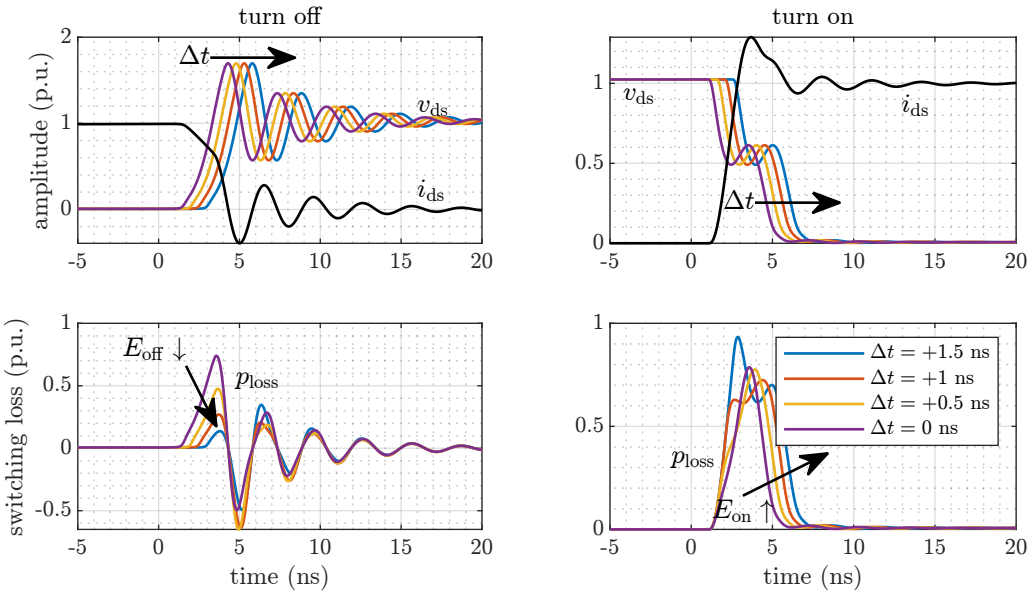

(a) Positive offset between v_{ds} and i_{ds}

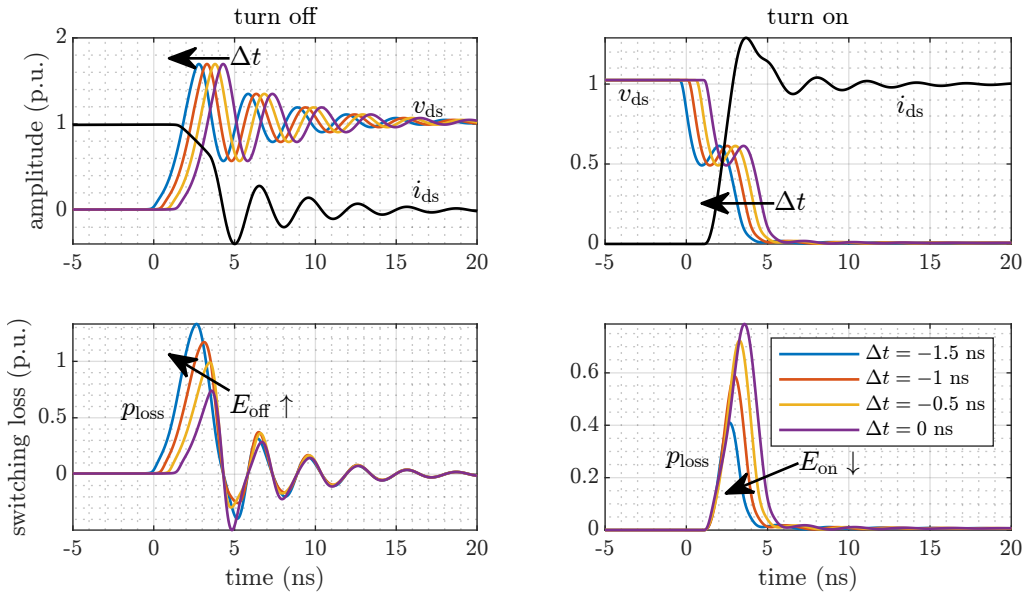

(b) Negative offset between v_{ds} and i_{ds}

Figure 2.10: Examplary influence of insufficient deskewing on the switching energy of a 100 V GaN device

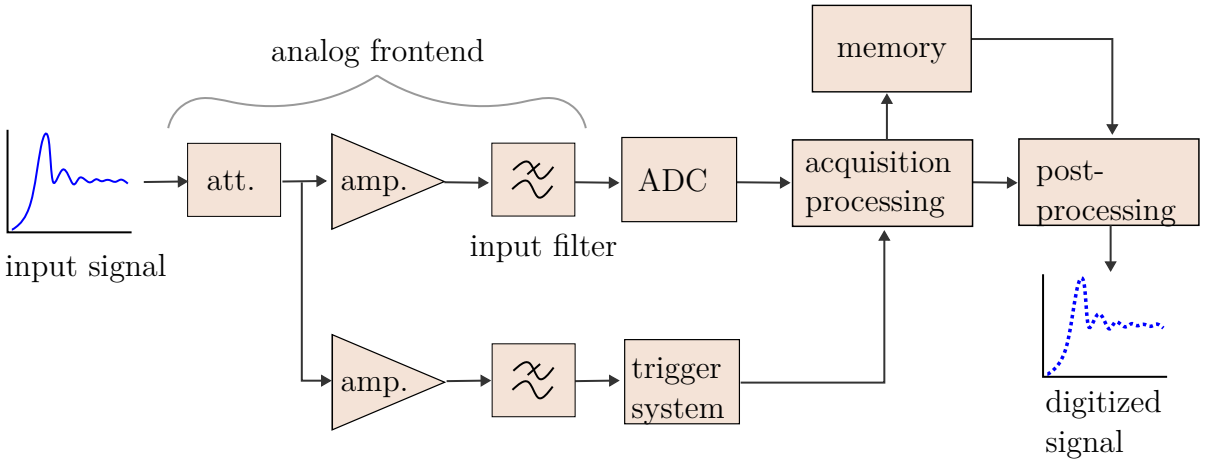

Figure 2.11: Block diagram of a digital storage oscilloscope (DSO)

2.3.4 Limitations of Oscilloscopes

The key component in a measurement setup is the oscilloscope, which is another potential source of error. In this section, the main limitations of an digital storage oscilloscope (DSO) are presented, which mainly relate to the vertical and horizontal resolution. Both characteristics are not specific to the DPT, but apply generally to all use cases of an oscilloscope.

Figure 2.11 shows the structure of a DSO [69]. The block diagram shown in Fig. 2.11 is implemented multiple times in parallel, which gives oscilloscopes typically four or eight independent channels. The left part of the figure shows the analog frontend, which consists of an attenuator, amplifier and filter stage. The input attenuator and amplifier condition the input signal to match the operating range of the analog-to-digial converter (ADC) in terms of amplitude. The input filter removes high-frequency components in the input signal that can lead to aliasing effects and defines the bandwidth of the oscilloscope. In parallel, there exists an analog trigger circuit which triggers the acquisition process for selected events. Depending on the architecture, the trigger ciruit can also be implemented behind the ADC as a digital trigger. The signal is quantized into digital values via the ADC by sampling it at a constant sampling frequency f_s, which is typically expressed in the unit $^{\mathrm{GS}}/_{\mathrm{s}}$. Finally, the sampled values are transferred to a processor and stored in memory for further post-processing and visualization. The memory depth limits the maximum time window that can be recorded. Since the switching events in the DPT take place in a very small time window of significantly less than 1 µs, the memory depth is not a problem with modern DSOs. For sampling, the Nyquist theorem Eq. (2.7) applies, which describes that the maximum observable frequency f_max is less than half the sampling frequency. Using methods such as *interleaved sampling* [70], the sampling frequency f_s can be increased for periodic input signals or by connecting several ADCs in parallel.

$$f_\mathrm{max} < \frac{f_\mathrm{s}}{2} \tag{2.7}$$

Modern DSOs achieve bandwidths beyond 10 GHz, so that the horizontal resolution is not a bottleneck in the characterization of WBG power semiconductors. When using oscilloscopes and probes with a rather low bandwidth, the relationship from Eq. (2.8) must be taken into account. It describes how the measured rise time $t_{\mathrm{rise,meas}}$ is reduced by concatenating several low-pass systems so that the rise time recorded by the oscilloscope is reduced, even if it corresponds exactly to the rise time of the signal $t_{\mathrm{rise,signal}}$ [12], [57].

$$t_{\mathrm{rise,meas}} = \sqrt{{t_{\mathrm{rise,scope}}}^2 + {t_{\mathrm{rise,probe}}}^2 + {t_{\mathrm{rise,signal}}}^2} \tag{2.8}$$

It is therefore important to ensure that the rise time of the oscilloscope used is always shorter than the rise time of the probes used, and that these in turn have a shorter rise time than the signal that is to be measured.

In addition to the horizontal resolution, the accuracy of a DSO is also limited by its vertical resolution, which is mainly defined by the number of bits [71]. In an ideal observation, the smallest voltage difference ΔV that can be digitally recorded is given by Equation (2.9) where n is the number of bits and V_{max} the upper voltage limit of the ADC.

$$\Delta V = \frac{V_{\mathrm{max}}}{2^n} \tag{2.9}$$

With modern oscilloscopes, a resolution of 12 bit has been established, from which 4096 different voltage levels can be distinguished. In practice, however, this resolution is reduced, as the individual levels can overlap due to the signal-to-noise ratio (SNR). For this reason, there is a specification for the effective number of bits (ENOB) that takes these effects into account and specifies the actual resolution. For example, the oscilloscope *Waverunner 8208HD* has a nominal resolution of 12 bit and a ENOB of 8.4 bit [72]. With conventional DPTs, the vertical resolution is not critical, but it becomes a problem if it is necessary to measure the precise voltage drop of a device when it is turned on, as is the case when measuring the dynamic $R_{\mathrm{DS(on)}}$ of GaN devices [21]. In this case, an additional clamping circuit is required to block the voltage V_{sw} in the turn-off state. Another application where a very high vertical resolution is required is the detection of zero-voltage crossing for soft-switching devices. This requires special solutions, such as the circuit patented in [73].

Besides the effects described, there are other sources of error. However, these sources of error are very application-specific and cannot be modeled in general. For example, oscilloscopes may suffer from a dc offset over time, which must be compensated for by regular calibration [74]. Another challenge can be electromagnetic interference (EMI), which leads to common-mode or differential-mode currents that are caused by inductive or capacitive couplings. To avoid these, a uniform grounding concept must be ensured and, if necessary, the use of countermeasures such as ferrite cores, optically-isolated probes and galvanically-isolated voltage sources [68], [75].

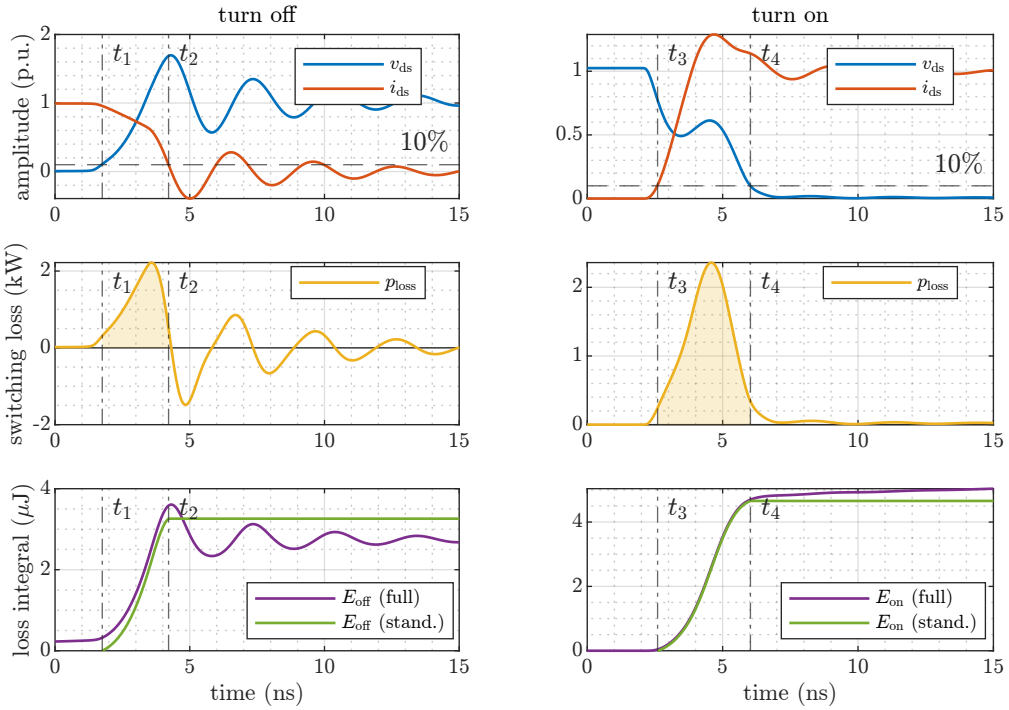

Figure 2.12: Examplary influence of the integral boundaries on E_{off} and E_{on} of a GaN device at 100 V and 30 A

2.3.5 Definition of Switching Energies

As shown in Section 2.1.2, the switching energies for MOSFETs and HEMTs are defined via the standard *IEC 60747-8*. Accordingly, the integral is calculated via the power loss p_{loss} between 10 % of the switching voltage and 10 % of the switching current (see Fig. 2.2a). For fast-switching WBG devices in particular, the switching event is often associated with oscillations, which occur after the 10 % threshold is reached and contribute to the switching losses that actually occur. Figure 2.12 shows an exemplary turn-off and turn-on event. The switching transients are simulated for a 100 V GaN devices from Section 3.1.2. It can be observed that the integration via the *IEC* standard leads to a higher turn-off energy E_{off} compared to the energies resulting from the calculation of the full integral. In the case of the turn-on, a larger value results for E_{on} when the full integral is calculated, as the transition to the conduction losses is gradual. This deviation does not represent a measurement error in the conventional definition, but must be taken into account depending on the application.

A further deviation between the measured and actual energies results from the electrical properties of the semiconductor device. For this purpose, a more detailed view on the switching process of a Si or SiC MOSFET and a GaN HEMT is required [76], [77], [78]. Figure 2.13 shows the turn-on switching process of the low-side transistor S_{LS}. As can be seen in Fig. 2.13a, there is a relatively high current overshoot during the turn-on of the MOSFET. This is caused by the high-side transistor S_{HS}. If a parasitic turn-on can

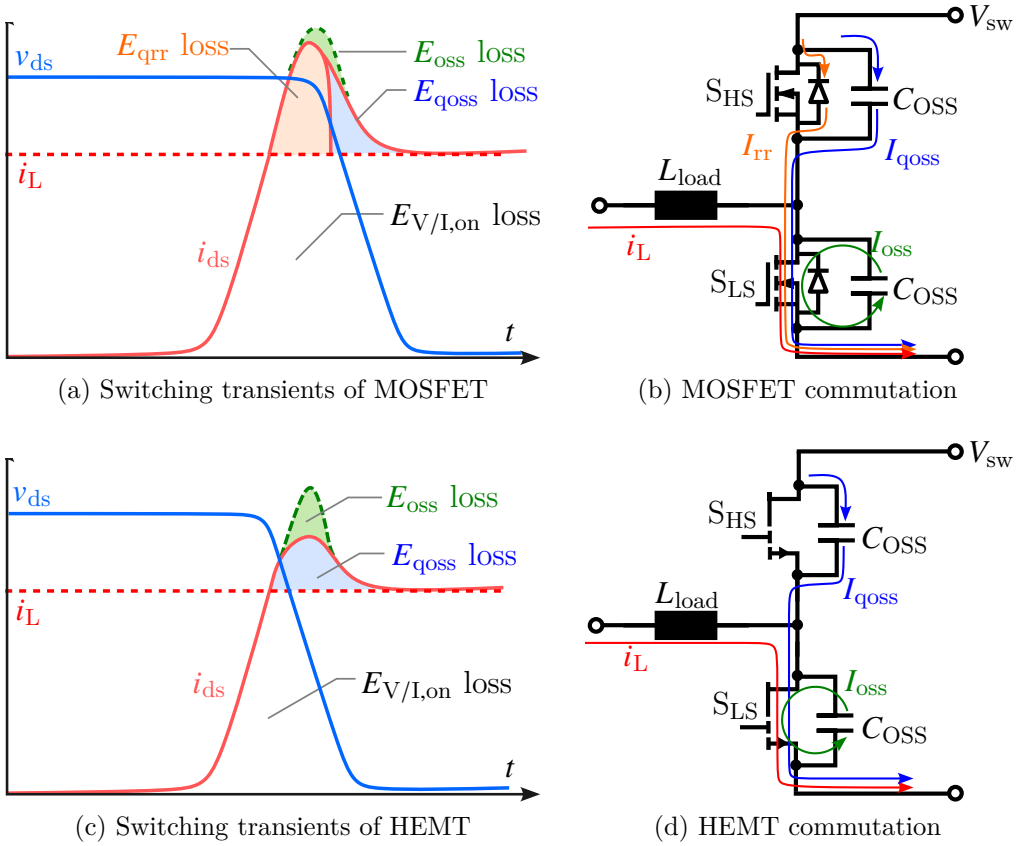

(a) Switching transients of MOSFET (b) MOSFET commutation

(c) Switching transients of HEMT (d) HEMT commutation

Figure 2.13: Breakdown of the loss mechanisms at turn-on of S_{LS}

be excluded, the overshoot is composed of the reverse recovery current I_{rr} from the body diode and the displacement current I_{qoss}, which is caused by the charging of the output capacitance C_{OSS} of S_{HS}, as illustrated in Fig. 2.13b. The total energy measured during turn-on therefore corresponds to $E_{on} = E_{V/I,on}+E_{qrr}+E_{qoss}$, where E_{qrr} is the energy caused by I_{rr} and E_{qoss} is the energy caused by I_{qoss}. The $E_{V/I,on}$ component corresponds to the actual intrinsic switching losses of S_{LS} that are caused by the overlap of i_{ds} and v_{ds} during the transition. In addition, there is another loss component E_{oss}, which corresponds to the energy stored in the output capacitance C_{OSS} of S_{LS}, that is dissipated as heat during the turn-on. However, the resulting current I_{oss} cannot be measured externally and is not part of i_{ds}, so the E_{oss} component cannot be measured during turn-on. This effect is reversed when S_{LS} is turned off. When the current i_{ds} of S_{LS} commutates to S_{HS}, the output capacitance C_{OSS} of S_{LS} is charged to the voltage V_{sw}. In this case, the energy $E_{off} = E_{V/I,off} + E_{oss}$ is measured externally, but the E_{oss} component is not converted into heat but stored in the capacitance.

Figure 2.13c and Fig. 2.13d show the turn-on switching transients and the representation of the commutation for a GaN HEMT. An important distinction between MOSFETs and HEMTs is that the latter do not have an intrinsic body diode. Consequently, there is no reverse-recovery effect in HEMTs, which would influence commutation in a hard-switching

half-bridge topology. This results in the energy E_{oss} having a greater contribution to the total turn-on energy E_{on}. With very fast-switching devices, there can therefore be a considerable deviation between the measured energies E_{on} and E_{off} and the actual heat dissipation during turn-on and turn-off. The total energy $E_{sw} = E_{off} + E_{on}$ is not influenced by the effect described, so a separation is only necessary if the individual energy components are relevant. Table 2.2 summarizes this information for a HEMT. The two quantities E_{oss} and E_{qoss} are highly dependent on the voltage V_{sw}, so that E_{oss} is typically greater than $E_{V/I,off}$ for high voltages [79]. The energy E_{oss} stored in the output capacitance is typically specified in the data sheet.

Overall, switching energies are very dependent on the definition and the exact measurement methodology and the calculation method should always be specified, as required by the standard *JEP187* [80], for example. There are also special cases such as cascode devices, which combine a GaN HEMT with a Si MOSFET. Depending on the internal structure, these may have a different loss distribution and therefore require individual consideration [81].

Table 2.2: Loss distribution of a GaN HEMT

	turn-off (E_{off})	turn-on (E_{on})
external measured energy	$E_{V/I,off}$ +E_{oss}	$E_{V/I,on}$ + E_{qoss}
intrinsic dissipated energy	$E_{V/I,off}$	$E_{V/I,on}$ + E_{qoss} +E_{oss}

2.4 Conclusion

In this chapter, the fundamental knowledge about the characterization of WBG semiconductors was reviewed. Firstly, the electrical characteristics of semiconductor devices were explained in Section 2.1. These can be divided into static characteristics, dynamic characteristics and specific characteristics of WBG devices. The most important static characteristic is the output characteristic, which is defined for each transistor and represents its individual operating points. The dynamic characteristics include the switching energies E_{on} and E_{off}, which can be measured in the DPT, which is the focus of this work. The characteristics specific to WBG devices are the dynamic on-resistance and the hysteresis of the output capacitance. These are typically not specified in the data sheets but can influence the performance of a converter. Section 2.2 described how the DPT works and which measurement techniques are available for measuring voltage and current. In terms of voltage measurement, optically-isolated probes provide the best performance for the dynamic characterization of fast-switching WBG devices. With regard to current

measurement techniques, there is a limited selection of commercially-available solutions that can be used for dynamic characterization. Depending on the application, a choice must be made between Rogowski coils and shunt resistors. Finally, the potential sources of measurement errors in the DPT were discussed in Section 2.3. These are the bandwidth limitation of probes, the parasitic properties of probes, deskewing and limitations of the oscilloscope used. In addition, the definition of switching energies is crucial to obtain consistent results. Although the calculation of E_{on} and E_{off} is consistently defined in the standard *IEC 60747-8*, the actual losses caused by switching may deviate from these values in practice.

3 Evaluation of the Measurement Accuracy in Double Pulse Tests

This chapter investigates the measurement accuracy to be expected in DPTs and evaluates the factors that determine the measurement error. Section 3.1 presents the methodology used to systematically investigate the measurement error, which is caused by the mechanisms that were described in Section 2.3. The chosen method involves simulating a large number of DPTs with different WBG semiconductor devices and the evaluation of the accuracy in relation to the measurement parameters. In Section 3.2 the results are presented and the significance of the different parameters is evaluated. Section 3.3 concludes this chapter and summarizes the most important findings.

3.1 Methodology

This section presents the methodology that is used to analyze the sensitivity of different measurement parameters on the characterization results in the DPT. First of all, Section 3.1.1 presents a selection of semiconductor devices that serve as examples for characterization. The simulation model, which is implemented in the software *Simulink Simscape*, is presented in Section 3.1.2. This is a replication of the DPT, which takes into account all sources of error presented previously. A parameter sweep has been carried out according to a DoE presented in Section 3.1.3. In this way, a large dataset is created which can be used to perform a sensitivity analysis. The results will be evaluated in Section 3.2.

3.1.1 Selection of Devices Under Test

For the analysis of the measurement accuracy, four different WBG semiconductor switches were selected as DUTs. These cover the two technologies SiC and GaN, as well as typical voltage levels for the respective technology. For GaN the voltage classes 100 V and 650 V were selected and for SiC the voltage classes 750 V and 1.2 kV. This work therefore represents a continuation of the study presented in [82], which only examined a 650 V GaN. In terms of current, the devices range between $I_\mathrm{D} = 24\,\mathrm{A} \ldots 38\,\mathrm{A}$, which allows the comparison at similar current levels. Table 3.1 shows an overview of the selected devices

Table 3.1: Characteristics of selected DUTs

	A	B	C	D	
Type	GaN HEMT	GaN HEMT	SiC MOSFET	SiC MOSFET	SiC SBD
Device	*GS61004B*	*GS66508T*	*SCT4045DW7*	*SCT4062KW7*	*SCS210KE2*
V_{DS}	100 V	650 V	750 V	1200 V	1200 V
$R_{DS(on)}$	16 mΩ	50 mΩ	45 mΩ	62 mΩ	-
I_D	38 A	30 A	31 A	24 A	10 A
I_{max}	60 A	48 A	61 A	52 A	170 A
Q_{rr}	0 nC	0 nC	89 nC	105 nC	34 nC
$V_{GS,on}$	6 V	6 V	18 V	18 V	-
$R_{G,on}$	10 Ω	10 Ω	4.7 Ω	4.7 Ω	-
$R_{G,off}$	2 Ω	2 Ω	4.7 Ω	4.7 Ω	-
Ref.	[64]	[84]	[85]	[86]	[87]

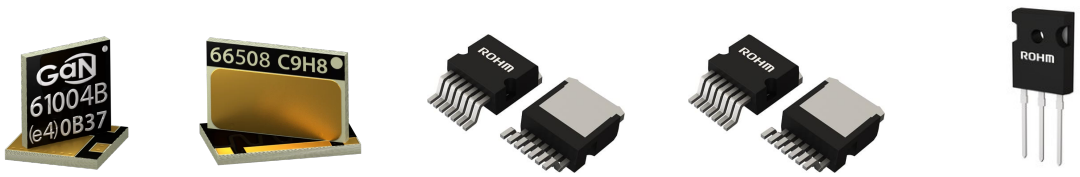

(a) *GS61004B* (GaNPX) (b) *GS66508T* (GaNPX) (c) *SCT4045DW7* (TO-263-7L) (d) *SCT4062KW7* (TO-263-7L) (e) *SCS210KE2* (TO-247N)

Figure 3.1: Packages of selected devices under test (sizes are not true to scale)
external image sources: `https://gansystems.com/gan-transistors`, `https://www.rohm.com/products/sic-power-devices`

labeled as A, B, C and D and lists their most important characteristics. In addition to the nominal drain-source voltage V_{DS} and the nominal drain current I_D, these are the drain-source resistance $R_{DS(on)}$ and the maximum permissible drain current I_{max}.

Another parameter that is relevant for hard-switching operation is the reverse recovery charge Q_{rr}. In contrast to the two SiC devices, the GaN devices do not have a reverse recovery charge. Since this parameter has a negative effect on the switching performance of the half-bridge topology under investigation, an additional component is added for the SiC devices [83]. This is the Schottky barrier diode (SBD), also listed in Table 3.1, which is used in the following simulation models instead of the high side switch S_{HS} and has a significantly lower charge than the intrinsic body diode of the SiC MOSFETs.

Table 3.1 also lists the relevant operation parameters that are recommended in the data sheets. These are the gate turn-on voltage $V_{GS,on}$ and the two external gate resistors $R_{G,on}$ and $R_{G,off}$. All devices are turned off with a gate-source voltage of $v_{gs} = 0\,V$. In the following simulations, the components are operated according to the manufacturer's recommendations [88], [89]. Figure 3.1 shows the packaging of all devices. It can be seen

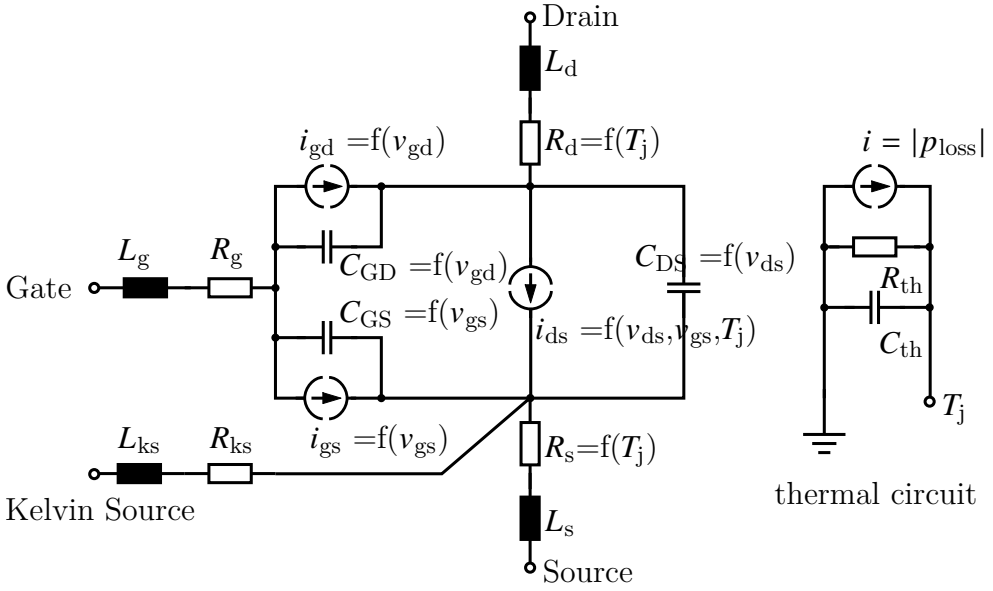

Figure 3.2: Behavioral model of a GaN HEMT

that the GaN components are already designed with a very low inductance introduced by the package, while the SiC components have wired packages with increased leakage inductance.

For the selected DUT, *LTSpice* simulation models are available, which are provided by the manufacturers *Rohm Semiconductor* and *GaN Systems, Inc.* unencrypted and can therefore be converted into the *Simulink Simscape* syntax. The toolbox *Simscape* is more suitable than the stand-alone solution *LTSpice*, as it is integrated into *MATLAB* and can efficiently implement an automated and parameter-driven analysis. The simulation models are in the form of behavioral models, which model the devices as subcircuits that behave externally as the devices would in reality. It has been shown that this type of modeling is very accurate and enables a simulation of the switching transients over the entire operating range [90], [91], [92].

The structure of such a model is described in [93] for the GaN devices and is illustrated in Fig. 3.2. The SiC models follow a similar structure [94]. In both cases, the individual elements of the model are defined using analytical equations, as described in [95], for example. The drain-source current I_D is modeled as a controlled current source that is dependent on the temperature T_j, the drain-source voltage v_{ds} and the gate-source voltage v_{gs}. Additional current sources describe the gate-drain leakage current i_{gd} and the gate-source leakage current i_{gs}. The model also includes the voltage-dependent capacitances C_{GD}, C_{GS} and C_{DS} within the semiconductor. Further modeled parasitic elements are the inductances and resistances of the package, which relate to the gate (g), drain (d), source (s) and kelvin source (ks) contacts. The models also contain a thermal equivalent circuit diagram, which consists of a multi-stage Cauer model [96]. This allows the junction temperature T_j, the case temperature T_c and the ambient temperature T_{amb} to

be individually utilized. Here, C_{th} describes the thermal capacity of the component and R_{th} the corresponding thermal resistance, which is specified in $^{\mathrm{K}}/_{\mathrm{W}}$. The losses are modeled via a current source, which is controlled via the instantaneous power loss p_{loss}. In Fig. 3.2, the thermal equivalent circuit diagram is only shown in a simplified form, as the junction temperature T_{j} is assumed to be constant in the simulations carried out in this chapter. This assumption is made because it is assumed that a DPT with a very short pulse duration is isothermal.

3.1.2 Double Pulse Simulation Setup

Figure 3.3 shows the circuit implemented in *Simulink Simscape* to simulate the switching behavior including the influence of the measurement parameters using a solver with variable step size. The central element of the DPTs are the DUTs connected in half-bridge configuration, which were introduced in Table 3.1. While the high-side switch $\mathrm{S_{HS}}$ is permanently turned off, the low-side switch $\mathrm{S_{LS}}$ is controlled via a gate driver implemented as an ideal voltage source. The two gate resistors $R_{\mathrm{G,off}}$ and $R_{\mathrm{G,on}}$ are dimensioned according to Table 3.1. Due to the rather small external gate resistors selected, oscillations caused by steep switching transients are expected. For the GaN devices, a snubber circuit is added to the drain contact of the upper device with $C_{\mathrm{sn}} = 10\,\mathrm{nF}$ and $R_{\mathrm{sn}} = 10\,\Omega$ according to the recommendation given in [97]. Further elements are the power loop inductance defined as $L_{\mathrm{loop}} = 2\,\mathrm{nH}$ and the equivalent series resistance (ESR) of the switching cell $R_{\mathrm{s}} = 1\,\mathrm{m\Omega}$. In addition, the parasitics of the probes are modeled, which are marked red in Fig. 3.3. The capacitor C_{probe} models the input capacitance of the voltage probe for measuring the drain-source voltage v_{ds} and L_{probe} the parasitic inductance of the current sensor for measuring the drain-source current i_{ds}. The value of both elements is variable and part of the parameter setup. The simulated values of v_{ds} and i_{ds} are filtered via low-pass filters to model the bandwidth limitation of the measuring equipment. In addition, a time shift is applied to simulate the deskewing error. In this way, the simulation allows the actual values v_{ds} and i_{ds} and the values v_{meas} and i_{meas} influenced by the measurement to be compared with each other. Other elements are the dc-link capacitor C_{DC}, which is charged to V_{sw}, and the load inductance L_{load}. Both variables are individually adapted to the operating point, which will be discussed in more detail below. In a real DPT setup, the pulse duration t_{ramp} would be varied for a known inductance value L_{load} to achieve the desired current I_{sw}. In a simulation, it is possible to keep the pulse duration t_{ramp} constant and set the desired current exactly by varying the value L_{load} via Eq. (3.1) [98].

$$L_{\mathrm{load}} = t_{\mathrm{ramp}} \cdot \frac{V_{\mathrm{sw}}}{I_{\mathrm{sw}}} \tag{3.1}$$

This has the advantage that the number of data points is reduced and a efficient evaluation is possible, as the times of the turn-off and turn-on events are uniform across all simulations. The model implemented assumes a constant pulse duration of $t_{\mathrm{ramp}} = 1.7\,\mu\mathrm{s}$, as this value leads to realistic setups over the entire operating range, as the following cal-

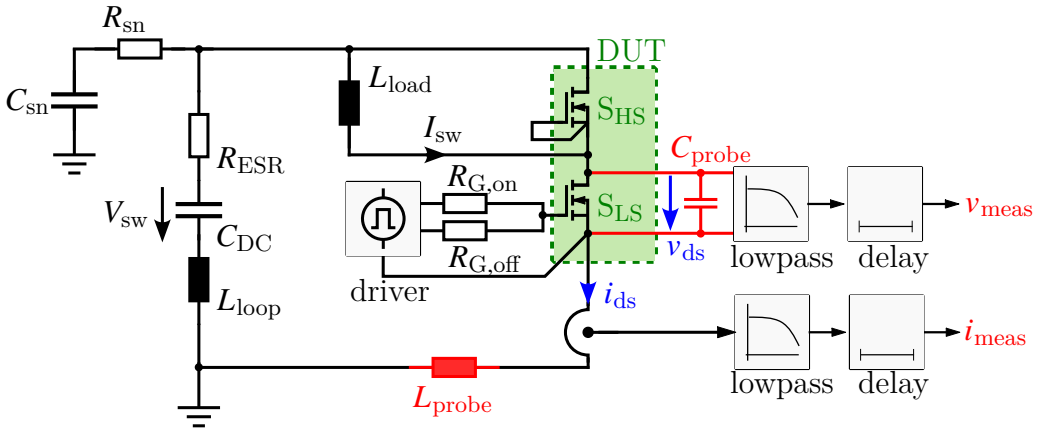

Figure 3.3: Schematic representation of the DPT simulation model

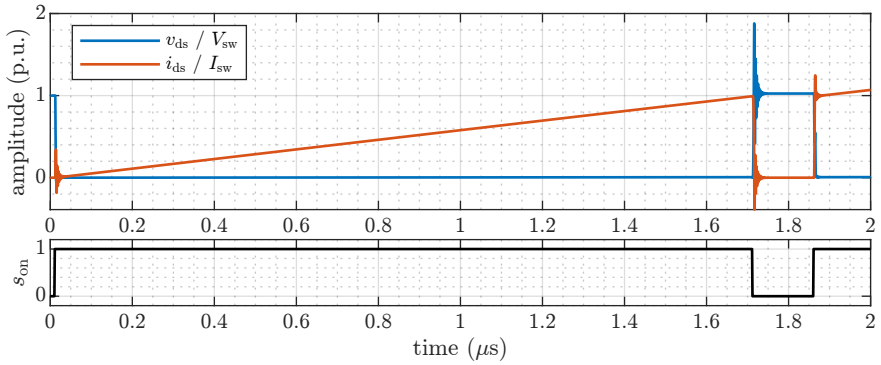

Figure 3.4: Example for simulated DPT waveforms with t_{ramp} = 1.7 µs and t_{break} = 150 ns

culations will show. A constant time of t_{break} = 150 ns is assumed for the turn-off period between the first and second pulse. Figure 3.4 shows the pattern of the DPT, which is completed after 2 µs.

In a real test environment, the DUT is not connected directly to a voltage source for safety reasons, and instead the entire energy is taken from the capacitor C_{DC}. The capacitor must be dimensioned to be still sufficiently charged after magnetizing the inductance L_{load} during the first pulse. The dimensioning of C_{DC} is carried out as described in [28] using the energy balance $\Delta E_L = \Delta E_C$. Here, ΔE_L describes the energy required for magnetization, which can be expressed via Eq. (3.2). The condition is set that the capacitor is charged to V_{sw} at the start of the experiment and that the voltage is 99 % of its initial value after the desired current I_{sw} has been reached. This corresponds to an energy change ΔE_C which can be expressed via Eq. (3.3).

$$\Delta E_L = \frac{1}{2} L_{load} {I_{sw}}^2 = \frac{1}{2} t_{ramp} V_{sw} I_{sw} \tag{3.2}$$

$$\Delta E_C = \frac{1}{2} C_{DC} ({V_{sw}}^2 - (0.99 V_{sw})^2) = \frac{0.0199}{2} C_{DC} {V_{sw}}^2 \tag{3.3}$$

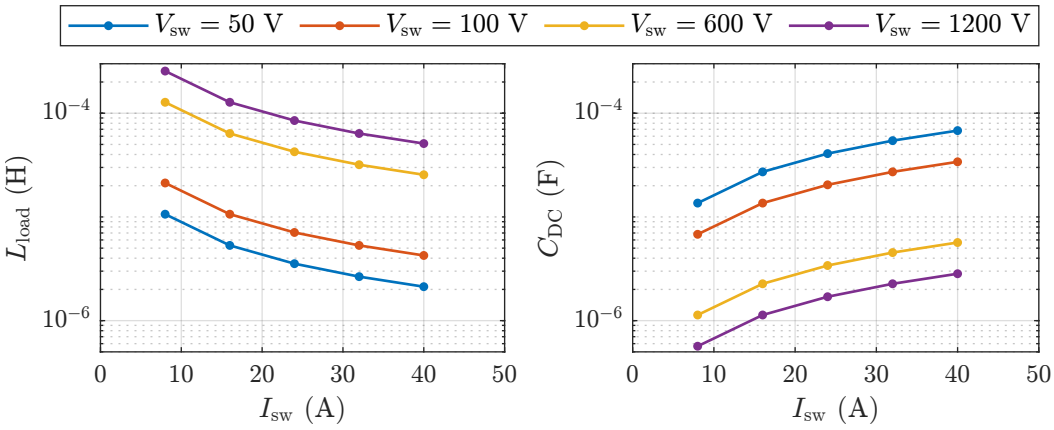

Figure 3.5: Dimensioning of L_{load} and C_{DC} as a function of I_{sw} and V_{sw} (t_{ramp} = 1.7 µs)

$$\Leftrightarrow C_{DC} = \frac{t_{ramp} I_{sw}}{0.0199 V_{sw}} \approx 50 \cdot \frac{t_{ramp} I_{sw}}{V_{sw}} \tag{3.4}$$

Both equations can be combined to calculate the required capacitance of the dc-link capacitor C_{DC}, which is shown in Eq. (3.4). Figure 3.5 shows the resulting values for L_{load} and C_{DC} at a ramp time of t_{ramp} = 1.7 µs and different settings of V_{sw} and I_{sw}. The caluclated inductance values are in the range L_{load} = 1.06 µH ... 254 µH and the calculated capacitances in the range C_{DC} = 0.57 µF ... 70.4 µF.

For the dimensioning of L_{load} and C_{DC}, it was previously assumed that the time constant $\tau = \frac{L_{load}}{R_s}$ is long enough for the ramp to be linear and that the desired current I_{sw} is set precisely via Eq. (3.1). With small inductance values or a large value for R_s, it can happen that τ comes close to t_{ramp}. As a result, the current i_{ds} no longer increases linearly and I_{sw} is not reached after the expected time. In this case, the ESR of the circuit must be estimated, which is made up of various components. In addition to the $R_{DS(on)}$ of the DUT, the resistance values of the capacitors and the inductor contribute to the total ESR. As these are frequency-dependent, a suitable value for R_s can only be estimated and the value for L_{load} can then be calculated via the equations given in Appendix A.2.

3.1.3 Design of Experiments

Using the circuit shown in Fig. 3.3, various DPTs can be simulated to evaluate the effects of different measurement setups. The analysis is based on the Design of Experiments (DoE) method, which is a systematic approach to planning, performing and evaluating experiments and allows investigating the influences of multiple factors on one or more target variables [99]. As the individual experiments are not time-critical, a full-factorial design is implemented.Table 3.2 shows all parameters relevant for the simulation and their settings.

Table 3.2: DoE parameter configuration

	parameter	symbol	lower limit	upper limit	steps
1	switching voltage	V_{sw}	$0.55V_{\mathrm{DS}}$	$1\ V_{\mathrm{DS}}$	4
2	switching current	I_{sw}	10 A	40 A	4
3	junction temperature	T_{j}	−40 °C	125 °C	4
4	current probe inductance	L_{probe}	0 nH	2.1 nH	4
5	voltage probe capacitance	C_{probe}	0 pF	12 pF	4
6	cutoff frequency, voltage	$f_{\mathrm{c,v}}$	0.5 GHz	2.9 GHz	7
7	cutoff frequency, current	$f_{\mathrm{c,i}}$	0.5 GHz	2.9 GHz	7
8	deskewing error	t_{skew}	−200 ps	200 ps	5

Parameters (1)-(3) The first three parameters describe the operating point of the DUT, which are set to four equidistant levels between the lower limit and the upper limit. For the switching voltage V_{sw}, these limits are based on the rated voltage V_{DS} of the DUTs listed in Table 3.1. As semiconductor devices are usually operated close to the nominal voltage, a lower limit of 55 % of the nominal voltage was chosen. The switching current I_{sw} is set to allow permissible operating points for all DUTs. The junction temperature T_{j} is within the range specified for automotive applications [100].

Parameters (4)-(5) The following two parameters describe the parasitics of the measuring devices for current and voltage, which are also set to four different settings each. The maximum value of L_{probe} corresponds to a typical coaxial shunt [14] and the maximum value for C_{probe} corresponds to a typical passive probe [101]. Both parameters are thus orientated towards probes that exhibit rather disadvantageous parasitic properties. The lower limits correspond to ideal measuring devices.

Parameters (6)-(8) The last parameters are the dynamic properties of the measurement. For the two bandwidths $f_{\mathrm{c,i}}$ and $f_{\mathrm{c,v}}$, exemplary values are assumed that are in the range of current and future measuring devices (see Section 2.2.2, Section 4.1 and Section 5.1). The deskewing error between the two waveforms v_{ds} and i_{ds} is described by t_{skew}. It is assumed that the misalignment is within a range of $-200\,\mathrm{ps} \ldots 200\,\mathrm{ps}$. In practice, this would correspond to an offset of up to ±2 samples with a 10 GS oscilloscope. The simulation of the bandwidth limitation and the deskewing error takes place in the post-processing of the simulation data, which reduces the computational effort compared to modeling in the circuit simulator. Therefore, the number of steps is increased to seven and five respectively, which allows a more precise evaluation of these parameters.

Figure 3.6 shows how the total number of all simulations is composed. There are a total of 64 different operating points for each DUT. In addition, there are 16 different combinations

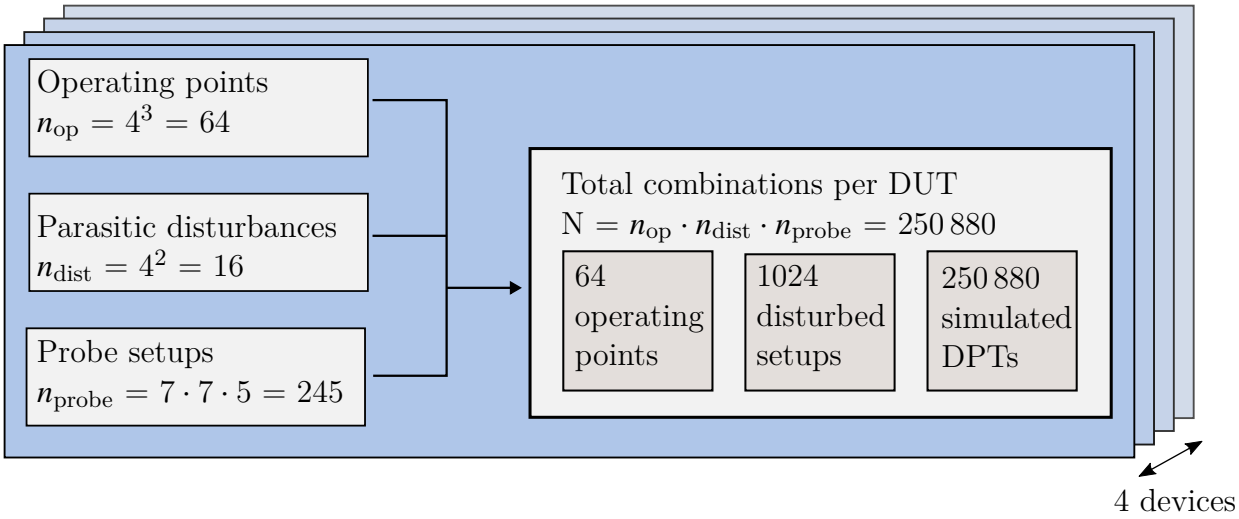

Figure 3.6: Visualization of the full-factorial DoE plan to analyze multiple combinations of measurement setups

for probe parasitics and 245 different combinations of probe setups. Combining these yields a full-factorial DoE plan with a total of 250 880 different settings for the simulation of the DPT per device.

To ensure that the simulation provides comprehensible results, the superimposed view of the switching transients shown in Fig. 3.7 is used. In this view, the number of steps for each parameter has been reduced to two so only the waveforms at which the lower and upper limits of the parameters are set are visible. The following can be observed:

- All switching events are fully completed in the time window of 100 ns used and all switching events take place between the normalized values 0 and 1. From this, it can be concluded that the simulation model was correctly dimensioned for all operating points and DUTs and the values I_{sw} and V_{sw} are reached. As was to be expected, the GaN devices switch significantly faster than the two SiC devices.

- All turn-on events show strong current overshoots of up to four times the rated current. This is mainly due to the fact that the turn-on resistors are relatively low. This operation is permissible because the focus of the investigation is on fast switching edges and negative consequences such as EMI or reliability are not relevant. Because the y-axis is normalized, overshoots are also more significant if the reference variable I_{sw} or V_{sw} is small. As an example, the overshoot of i_{ds} is partly caused by a capacitive discharge, independent of I_{sw} [78].

- The voltage overshoots during the turn-off events are in a moderate range of less than 1.2 V_{sw} on average. One exception is DUT A, which is the 100 V GaN device. This device is particularly susceptible to parasitic elements, such as the inductance of the current sensor L_{probe}.

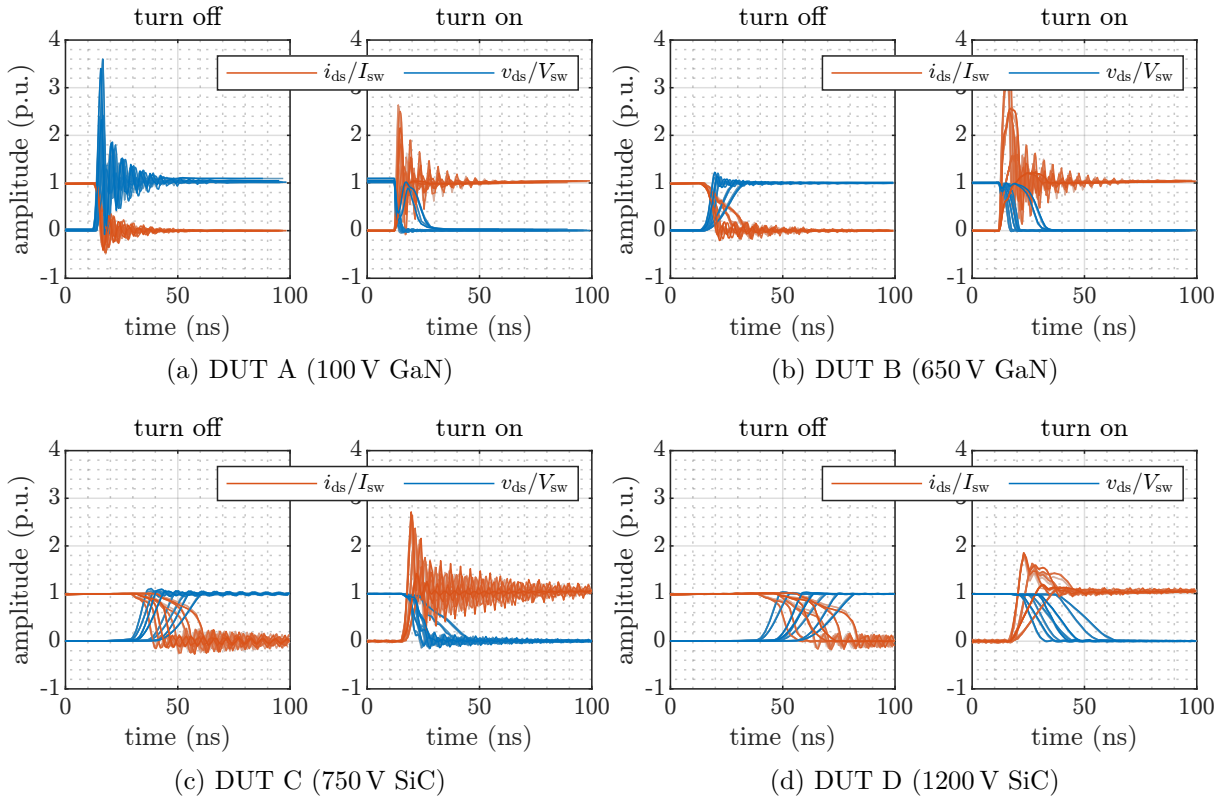

(a) DUT A (100 V GaN)

(b) DUT B (650 V GaN)

(c) DUT C (750 V SiC)

(d) DUT D (1200 V SiC)

Figure 3.7: Overlaid view of simulated switching transients (32 simulations per DUT)

3.2 Evaluation of the Simulation Results

Using the dataset created by 250 880 simulated DPT per device, it is possible to analyze the sensitivity of the measurement accuracy to the individual measurement parameters. First, the evaluation method is presented in Section 3.2.1, where the influence of the parameters I_{sw}, V_{sw} and T_j on the switching energies is shown as an example. The measurement of the turn-off switching energy E_{off} is analyzed in more detail in Section 3.2.2 and main-effect plots are used to show how the various measurement parameters influence the measurement accuracy. In Section 3.2.3, this procedure is applied correspondingly to the measurement of the turn-on switching energy E_{on}. Finally, Section 3.2.4 examines the measurement error of the total switching energy E_{sw} and what influence the selection of the integration boundaries has on the accuracy of the result.

3.2.1 Main Effects of the Switching Energies

For all following analyses, the complete integral of p_{loss} over the entire switching process is considered rather than the boundaries from the *IEC 60747-8* standard [17] (see Fig. 2.12). By reducing the switching event to the range between 10 % of V_{sw} and 10 %

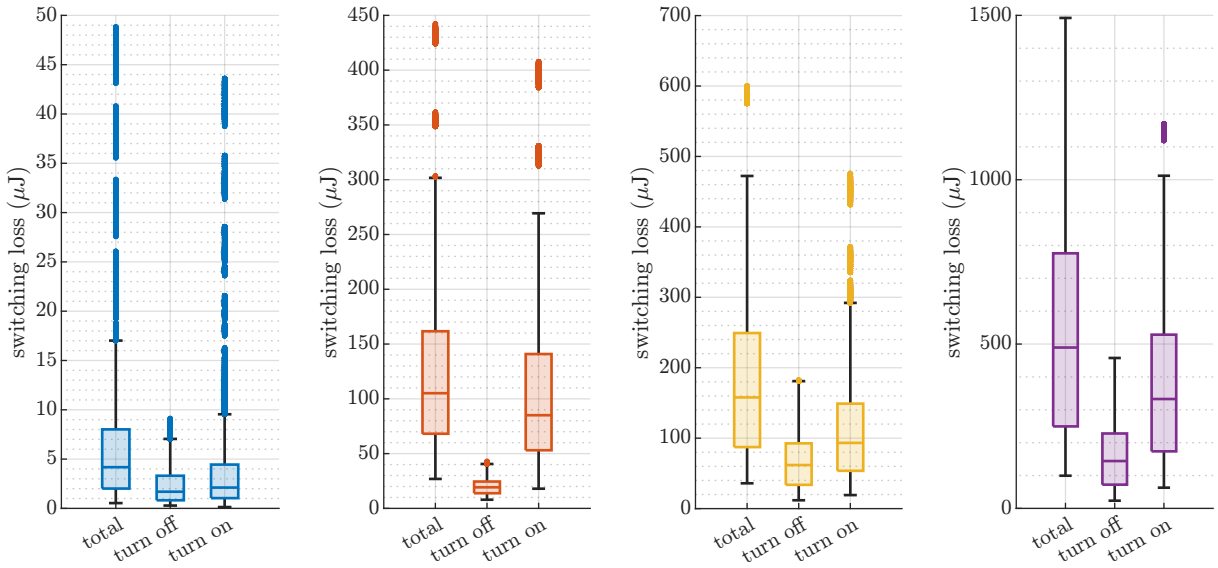

(a) DUT A (b) DUT B (c) DUT C (d) DUT D

Figure 3.8: Simulated distribution of all switching energies per DUT (N=250 880 per device)

of I_{sw}, information is lost and discontinuities occur in the error analysis. In Section 3.2.4 both methods for calculating the integral will be compared with each other. Figure 3.8 shows the distributions for the simulated switching energies of all DUTs using box plots. A box plot is a graphical representation of data that shows the distribution, median, quartiles and possible outliers of a data set [102]. The switching energies extend over a wide range and are therefore highly dependent on the operating point and the selected DUT. For each DUT, the turn-off energies represent a significantly lower proportion of the total energies compared to the turn-on energies. As expected, DUT A has the lowest energies overall, since it has the highest switching speed [64].

To investigate the influence of the input parameters on the results, the visualization with main-effect plots is chosen, which is a standardized diagram from the methodology DoE [99]. Figure 3.9a shows how the main effect of a single parameter is obtained. As an example, the influence of the switching current I_{sw} on the actual turn-off energies E_{off} of DUT A is investigated. The top subplot shows the histogram of the simulated E_{off} values over all $N = 250\,880$ simulations. The x-axis shows the simulated switching energy and the y-axis is normalized to the discrete probability density function (PDF) [103]. In addition, the mean value $\mu = 2.3\,\mu J$ is given. The histograms below show the distribution of E_{off} for subsets of the overall simulation dataset. All N simulations are grouped according to the value I_{sw}. This results in a total of four groups for the settings 10 A, 20 A, 30 A and 40 A, each containing $N/4 = 62\,720$ simulations. The different distributions reveal how increasing the parameter I_{sw} affects the resulting values for E_{off}. For the lowest setting the mean value of E_{off} is $\mu_{10A} = 0.6\,\mu J$ and at the highest setting of I_{sw} it has increased to $\mu_{40A} = 4.6\,\mu J$. The difference between the first and the last mean value is the main effect

of the factor I_{sw} on E_{off} [104]. Figure 3.9b will be discussed in Section 3.2.2 and shows that the method presented can also be applied to study the main effect of a measurement parameter to a measurement error.

In Fig. 3.10 a simplified representation of the main effects is shown for DUT A and C. The equivalent main effects of DUT B and D can be found in Fig. A.2 in Appendix A.3. Each subplot shows the influence of one operating point-defining parameter V_{sw}, I_{sw} and T_j on the simulated switching energies E_{off} and E_{on}. The dashed line shows the overall mean value μ, which is constant across all subplots. The value given in the center of each plot shows the main effect of the respective parameter. As this is formed from the difference between the first and last mean value, it is also expressed in the unit µJ. To improve readability, the value is shown without the unit. Several observations can be made based on these diagrams. For example, it is apparent that an increase in the voltage V_{sw} causes a almost linear increase in E_{off} and E_{on} for all DUTs. The influence of I_{sw} does not appear to be linear and has the strongest effect compared to the other parameters. The influence of T_j on the switching energies is device-specific. For DUT A, which is a 100 V GaN HEMT, T_j shows a strong effect on E_{on}, but almost no effect on E_{off}. This is a typical behavior that was confirmed by measurements in [105] and [106]. With DUT C, which is the 750 V SiC MOSFET, there is a positive influence of T_j on E_{off} and a negative influence on E_{on}. As explained in [107], this effect is caused by the fact that the turn-on threshold voltage $v_{GS(th)}$ decreases with increasing temperature. In addition to the evaluation of main effects, the DoE method also offers the possibility of investigating interactions between two or more parameters. However, no relevant interactions were identified in the context of this study, so that aspect is not discussed further.

3.2.2 Main Effects of the Measurement Error at Turn-Off

The actual objective of the simulation is to analyze the influence of the measurement parameters on the measurement accuracy of the switching energies. The actual values for the turn-off energy E_{off} and the turn-on energy E_{on} result from the two waveforms v_{ds} and i_{ds}, which, as shown in Fig. 3.3, were not manipulated by the measurement setup. The values $E_{off,meas}$ and $E_{on,meas}$, on the other hand, result from the waveforms v_{meas} and i_{meas} and are subject to the influence of the parameters L_{probe}, C_{probe}, $f_{c,v}$, $f_{c,i}$ and t_{skew}. The relative deviation corresponds to the two measurement errors ε_{off} and ε_{on}. These are calculated for each of the $N = 250\,880$ simulations performed per device according to Eq. (3.5) and Eq. (3.6).

$$\varepsilon_{off} = \frac{E_{off,meas} - E_{off}}{E_{off}} \tag{3.5}$$

$$\varepsilon_{on} = \frac{E_{on,meas} - E_{on}}{E_{on}} \tag{3.6}$$

Figure 3.9b shows how the measurement parameter L_{probe} affects the measurement error ε_{off} of DUT A using the same visualization that was used to show the influence of I_{sw}

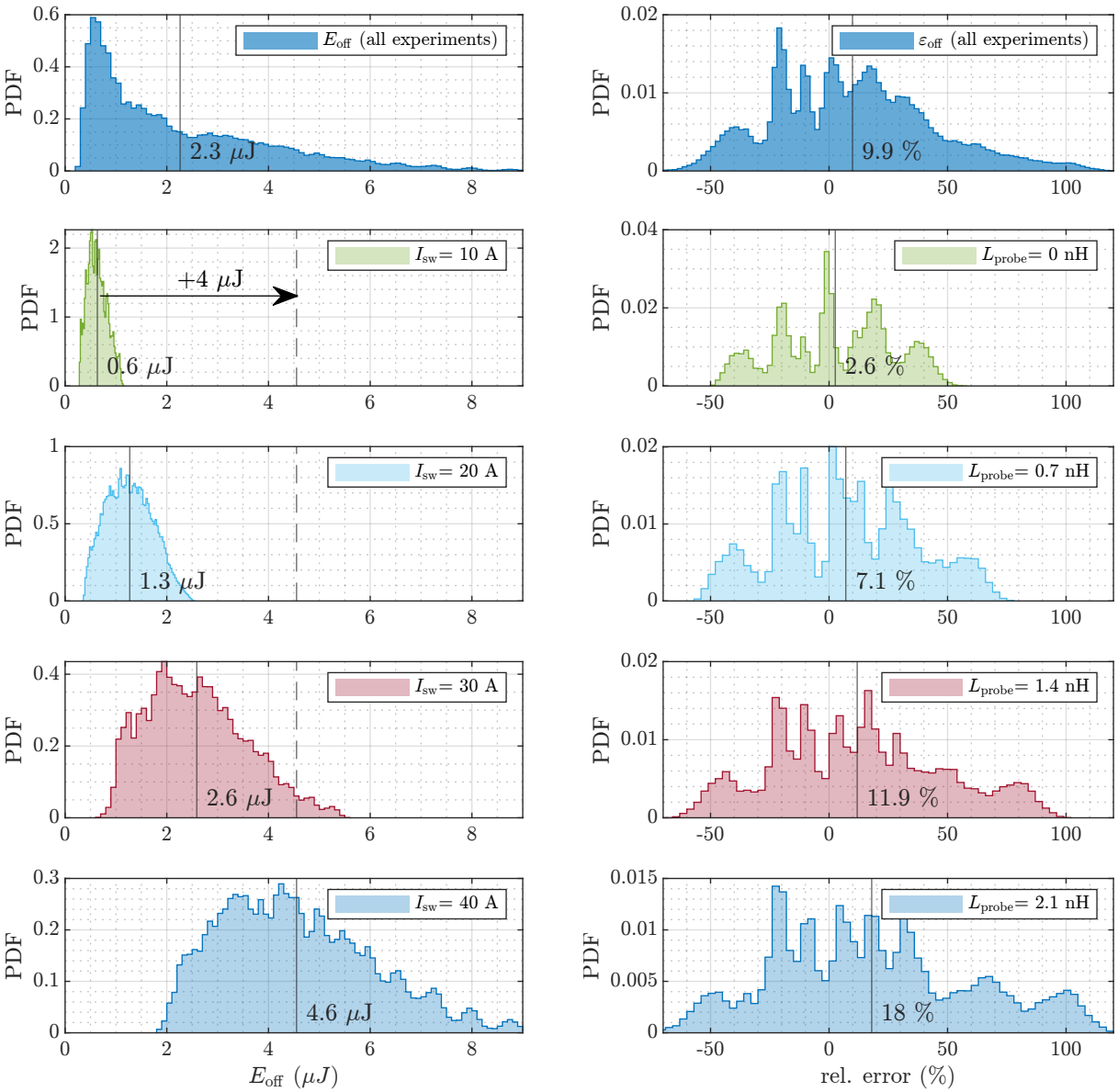

(a) Main effect of I_{sw} on E_{off}

(b) Main effect of L_{probe} on ε_{off}

Figure 3.9: Simulated example for understanding the main effect of I_{sw} on the turn-off energy E_{off} and the main effect of L_{probe} on the measurement error ε_{off} for DUT A (100 V GaN HEMT)

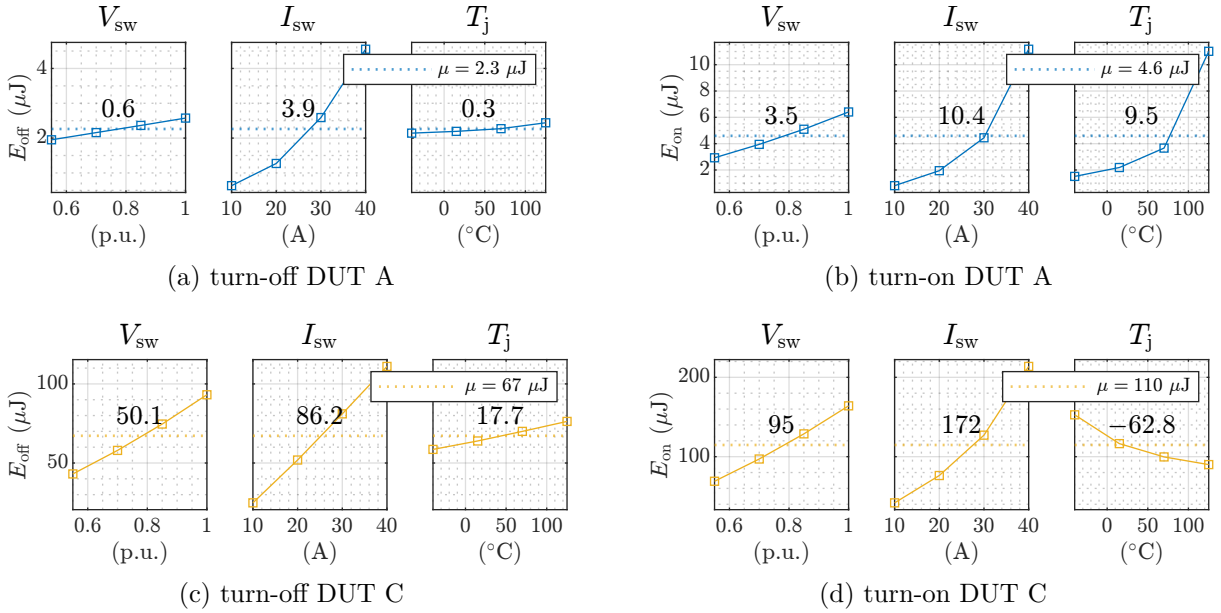

(a) turn-off DUT A

(b) turn-on DUT A

(c) turn-off DUT C

(d) turn-on DUT C

Figure 3.10: Simulated main effects of operating point parameters (V_{sw}, I_{sw}, T_j) on measured switching energies, showing E_{off} and E_{on} and their mean value μ

on E_{off}. The top subplot shows the overall distribution of the measurement error over all simulations performed. In this case, the relative error is plotted on the x-axis and the PDF on the y-axis. This reveals that ε_{off} extends over a wide range of values between approximately $-50\,\%$ and $100\,\%$. The mean value of each subplot will be used as a benchmark for a set of N simulations. It calculated using the equation Eq. (3.7) and introduced as the mean percentage error (MPE). In the example, the mean value of all simulations is $MPE = 9.9\,\%$.

$$MPE = \frac{1}{N} \cdot \sum_{i=1}^{N} \varepsilon_i \tag{3.7}$$

When all setups are grouped according to the variable L_{probe}, it can be seen that the MPE shifts upwards with increasing L_{probe}. The resulting main effect is defined as the percentage point (pp) difference between the first and last MPE. In the selected example this difference equals 15.4 pp. The limitation of this approach is that only mean values are evaluated. However, the objective is not the exact specification of a measurement error, but the evaluation of the significance of the individual parameters on the overall measurement accuracy. The distribution of all turn-off measurement errors is shown in Fig. 3.11. The evaluation shows that the value ε_{off} assumes the largest values for DUT A and has a significantly wider distribution compared to the other devices. The measurement errors of DUT B, C and D are less significant and have mean values close to $0\,\%$. In addition, the measurement error for the SiC devices C and D is lower and is in the range of $\pm 10\,\%$.

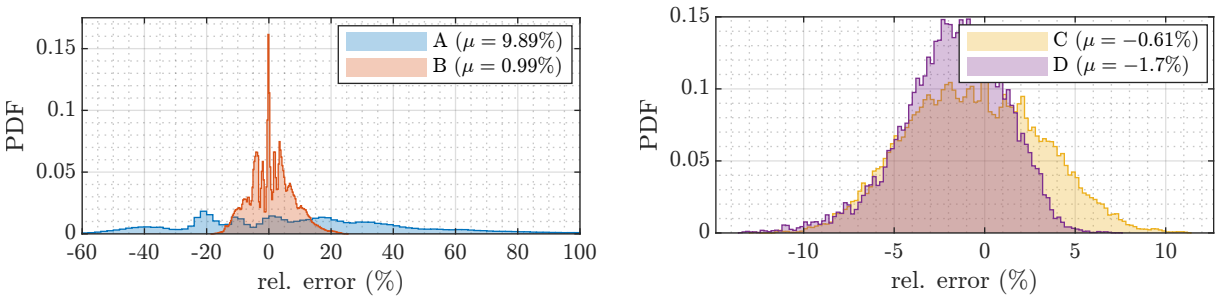

(a) GaN devices (b) SiC devices

Figure 3.11: Simulated distribution of the measurement error ε_{off} for all DUTs

Similar to Fig. 3.10, the main effects analysis is now extended to all measurement parameters and all DUTs. Figure 3.12 shows the main-effect diagram of each DUT for measuring the turn-off switching energy E_{off}. Using the MPE shown on the y-axis, various findings can be obtained from the dataset:

DUT A The parameter t_{skew} has the most significant effect on the measurement error ε_{off}. There is a difference of −82.9 pp between the minimum and maximum setting. The reason why the effect shows a zero crossing at about +50 ps is that the different sources of error overlap and coincidentally compensate for each other. In the case of an ideal measurement setup, the zero crossing would logically be at $t_{\text{skew}} = 0$ ps. The parameter L_{probe} has the second strongest effect. It increases the measurement error by up to 15.4 pp in the positive direction, which means that L_{probe} increases the measured energy $E_{\text{off,meas}}$. The effect of C_{probe} is less significant and has an effect in the opposite direction, which means that the value for $E_{\text{off,meas}}$ decreases with an increase in C_{probe}. This can be explained by the fact that the additional capacitance C_{probe} acts like a snubber capacitor that dampens the voltage overshoot [108]. With regard to the two bandwidths $f_{\text{c,v}}$ and $f_{\text{c,i}}$, it can be seen that the bandwidth of the current measurement $f_{\text{c,i}}$ has almost no effect on the error and it can therefore be concluded that the lower value of 500 MHz is sufficient for the measurement of i_{ds}. For the bandwidth $f_{\text{c,v}}$, there is a slight effect in the negative direction, which is particularly pronounced in the range between 500 MHz and 1.3 GHz. An increase in $f_{\text{c,v}}$ above this value shows almost no effect on the measurement error ε_{off}, from which it can be concluded that a bandwidth of approximately 1 GHz is sufficient for measuring v_{ds}.

DUT B With this device, the parameter t_{skew} again has the strongest influence on the ε_{off}, even if this effect is less pronounced than with DUT A, which is due to the longer switching event. It is noticeable that the two parasitics of the measuring devices L_{probe} and C_{probe} hardly influence the measurement error. The bandwidth $f_{\text{c,v}}$ of the voltage probe has almost zero influence on the measurement accuracy, from which it can be concluded that the lower value of 500 MHz is sufficient for the measurement of v_{ds}. The

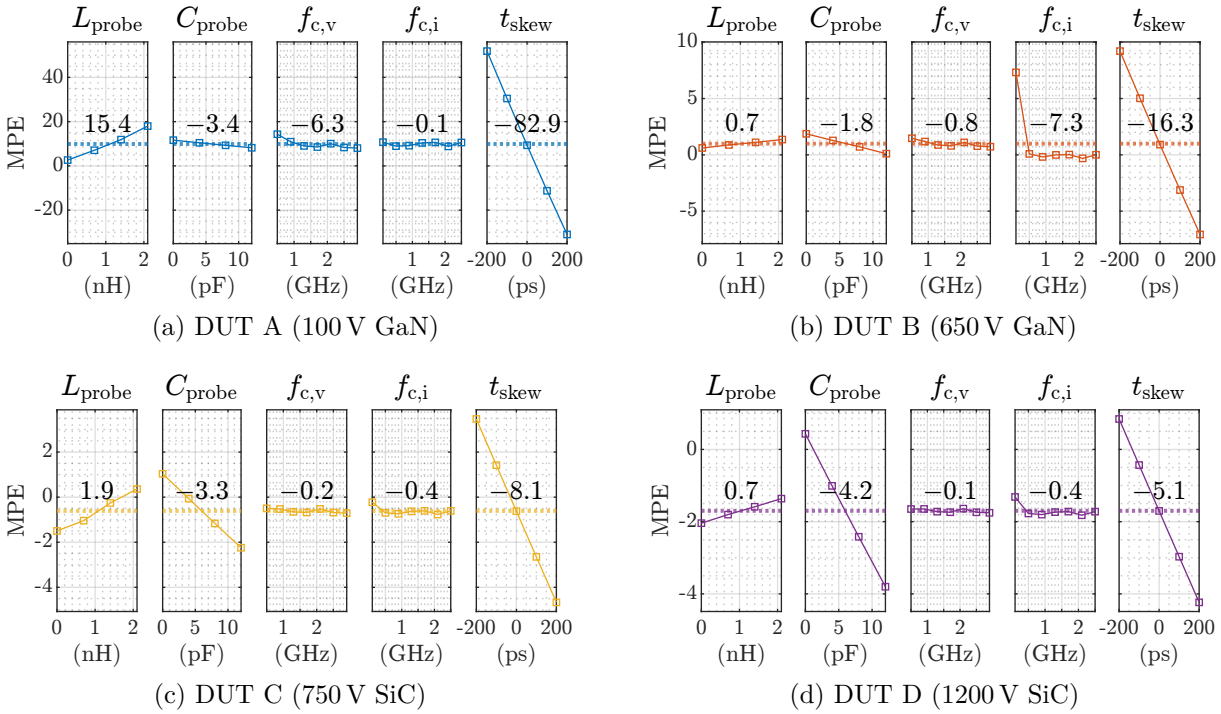

(a) DUT A (100 V GaN)

(b) DUT B (650 V GaN)

(c) DUT C (750 V SiC)

(d) DUT D (1200 V SiC)

Figure 3.12: Simulated main-effect diagrams of the relative error ε_{off} for E_{off} measurements

bandwidth $f_{\text{c,i}}$ of the current sensor shows a strong effect of −7.3 pp, which is particularly evident when 500 MHz is increased to 900 MHz. It can therefore be concluded that the characterization of DUT B requires a bandwidth of at least 900 MHz for the measurement of i_{ds}.

DUT C & DUT D Both SiC devices show a very similar behavior with regard to the sensitivity of the measurement error ε_{off}. As with the two GaN devices, the influence of t_{skew} on the measurement accuracy is the most significant. However, it is less severe compared to the GaN devices, which is due to the longer duration of the SiC switching events. The parasitics L_{probe} and C_{probe} show effects in the same directions as with DUT A and DUT B, with the difference being that C_{probe} has the stronger effect. This is caused by the higher operating voltage V_{sw} and the lower output capacitance C_{OSS} of the SiC MOSFETs. The two bandwidths for the measurement of v_{ds} and i_{ds} show almost no effect on the measurement error ε_{off}, which means that the lower limit of 500 MHz is sufficiently high in both cases.

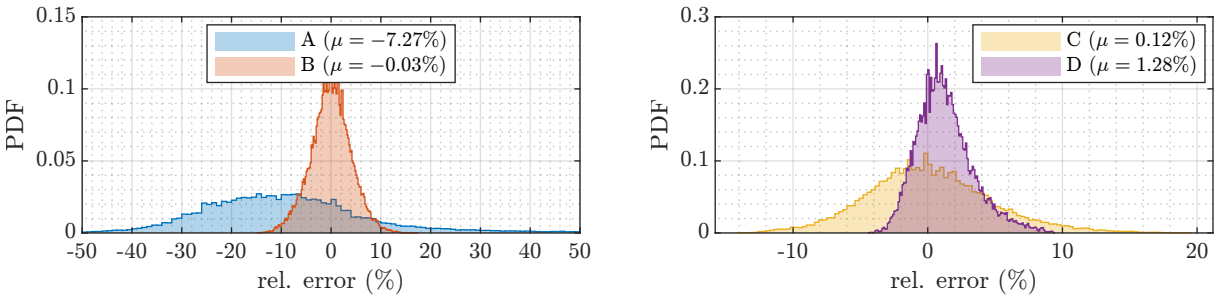

(a) GaN devices (b) SiC devices

Figure 3.13: Simulated distribution of the measurement error $\varepsilon_{\mathrm{on}}$ for all DUTs

3.2.3 Main Effects of the Measurement Error at Turn-On

The evaluation of the error for the measurement of the turn-on switching energy E_{on} is carried out using the same methodology as used in the previous section for E_{off}. Figure 3.13 shows the distribution of the measurement error $\varepsilon_{\mathrm{on}}$ calculated for each simulation performed according to Eq. (3.6). As in Fig. 3.11, DUT A has a widespread measurement error in the range of ±50 %. The measurement errors of DUT B and C are very similar to each other and are in the range of ±10 % with a mean value of almost zero. DUT D shows a slight positive shift in the measurement error. Figure 3.14 shows the main-effect diagrams of the relative error $\varepsilon_{\mathrm{on}}$ for all DUTs. As in the previous section, all simulation results are grouped according to a measurement parameter and the MPE for each group is mapped on the y-axis. The following statements can be made for the measurement of the turn-on switching energy:

DUT A The parameter $f_{\mathrm{c,i}}$ has the strongest influence on the measurement accuracy and shows an main effect of −31.9 pp. It is noticeable that the strongest influence occurs with the increase from 500 MHz to 900 MHz. From 1.3 GHz, $f_{\mathrm{c,i}}$ no longer influences the measurement error, which leads to the conclusion that this is the required bandwidth. The bandwidth of the voltage measurement $f_{\mathrm{c,v}}$, on the other hand, hardly influences the measurement error, so the lower value of 500 MHz is sufficient in this case. The parameter L_{probe} has the second strongest effect. An increase reduces the measured energy $E_{\mathrm{on,meas}}$ by −28.5 pp. The parameter C_{probe} only shows a weak effect in the positive direction. The deskewing error t_{skew} also has a strong effect, but it is only about a quarter as strong as when measuring E_{off}. As expected, the effect acts in the opposite direction in relation to the turn-off.

DUT B & DUT C The main effects of DUT B and C are very similar to each other, even if they involve the different technologies SiC and GaN, which are, however, in similar voltage classes. The parameter t_{skew} shows the strongest effect of approximately 9 pp with

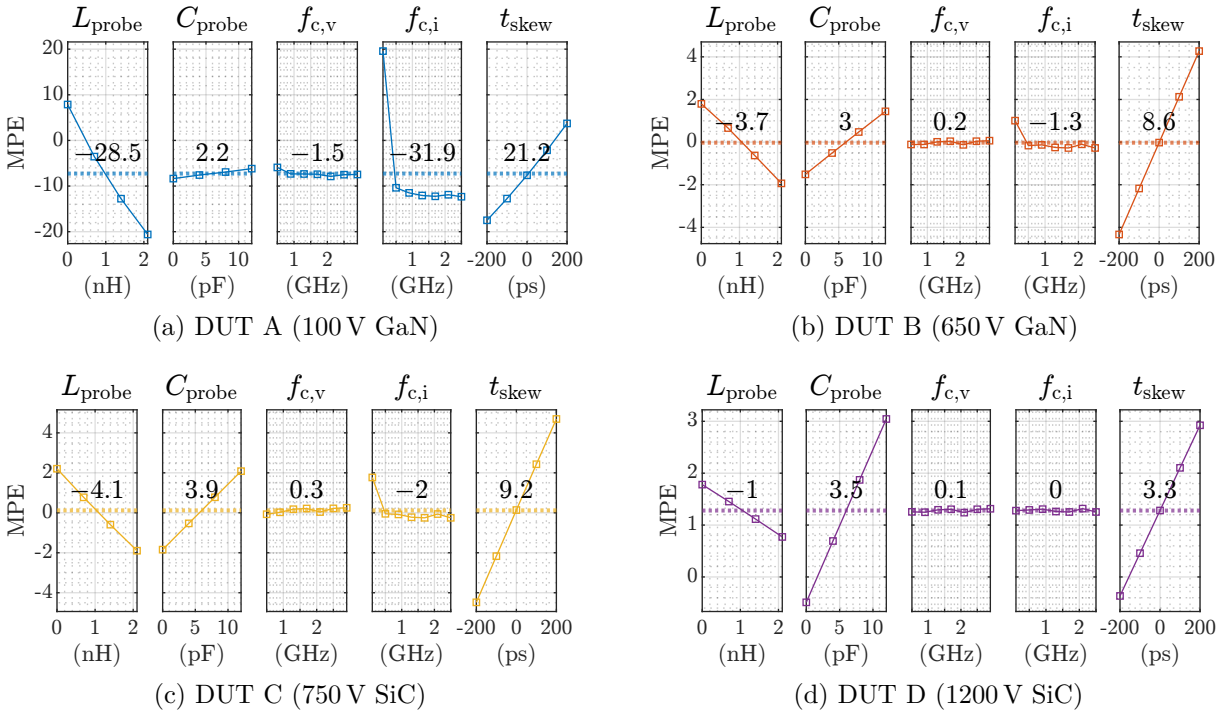

(a) DUT A (100 V GaN)

(b) DUT B (650 V GaN)

(c) DUT C (750 V SiC)

(d) DUT D (1200 V SiC)

Figure 3.14: Simulated main-effect diagrams of the relative error ε_{on} for E_{on} measurements

both DUTs in the positive direction. With regard to the bandwidths, $f_{c,v}$ has almost no influence on the measurement error. When $f_{c,i}$ is increased from 500 MHz to 900 MHz, an effect is visible, from which it can be concluded that 900 MHz is the required bandwidth for the correct measurement of E_{on}. Both parasitics L_{probe} and C_{probe} show effects that are very similar in strength but act in different directions. This means that L_{probe} reduces the measured value for $E_{on,meas}$, while C_{probe} increases the measured energy $E_{on,meas}$. By coincidence, it is possible that both effects overlap, resulting in a MPE of zero.

DUT D When characterizing DUT D, the parameter C_{probe} has the strongest influence on the measurement result. It increases the measurement error by 3.5 pp and is therefore even stronger than the influence of t_{skew}. The reason for this is the relatively small output capacitance of the component, which is C_{OSS} = 69 pF [85]. With regard to the bandwidths for the current and voltage measurement, there is no influence on the measurement accuracy, which means that 500 MHz is sufficiently high in both cases. The parameter L_{probe} shows a minor effect of −1 pp and is therefore the least significant compared to all other DUTs.

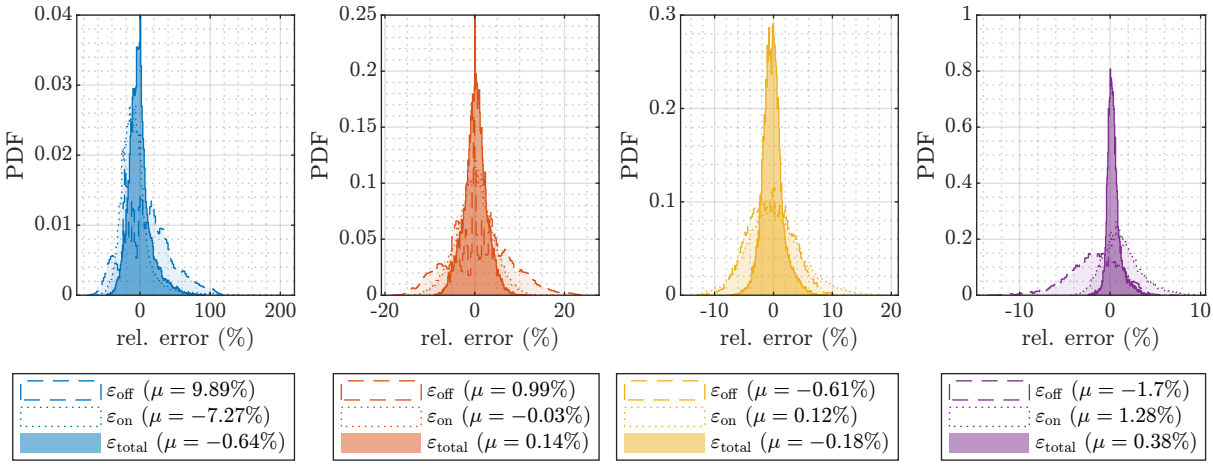

(a) DUT A (b) DUT B (c) DUT C (d) DUT D

Figure 3.15: Simulated distribution of the relative error ε_{total} for the total switching energy E_{sw} of each DUT

3.2.4 Influence of Superposition and Integral Definition

A separate determination of the switching energies at turn-off and turn-on is not always necessary and for some applications it is sufficient to know the total switching energy for a given operating point. To investigate the measurement accuracy in this situation, the two measurement errors ε_{off} and ε_{on} are superimposed to form the total measurement error ε_{total}, which can be calculated with Eq. (3.8).

$$\varepsilon_{total} = \frac{(E_{off,meas} + E_{on,meas}) - (E_{off} + E_{on})}{E_{off} + E_{on}} \tag{3.8}$$

The previous analysis revealed counteracting effects of individual parameters which can compensate for each other to a certain extent. In addition to the obvious influence of t_{skew}, this behavior can also be seen in the parasitics of the current and voltage probes. L_{probe} increases the measured turn-off energy $E_{off,meas}$ for all DUTs while simultaneously reducing the measured turn-on energy $E_{on,meas}$. With C_{probe} this is reversed and an increased value reduces $E_{off,meas}$ and simultaneously increases $E_{on,meas}$. Figure 3.15 shows the distribution of the individual measurement errors. In addition to ε_{off} and ε_{on} already shown in Fig. 3.11 and Fig. 3.13, the distribution of ε_{total} is depicted. The corresponding mean values μ are shown below each plot. For all devices, the superposition leads to the overall measurement error becoming smaller and results in mean values of close to zero, with ε_{total} having an approximately normal distribution. A comparison between the individual devices can therefore be made using the standard deviation σ. For DUT A, B, C and D these are $\sigma_A = 16.4\,\%$, $\sigma_B = 2.5\,\%$, $\sigma_C = 1.7\,\%$ and $\sigma_D = 0.8\,\%$. Accordingly, the 100 V GaN device is by far the most susceptible to measurement errors and the 1200 V SiC device is the least susceptible to measurement errors.

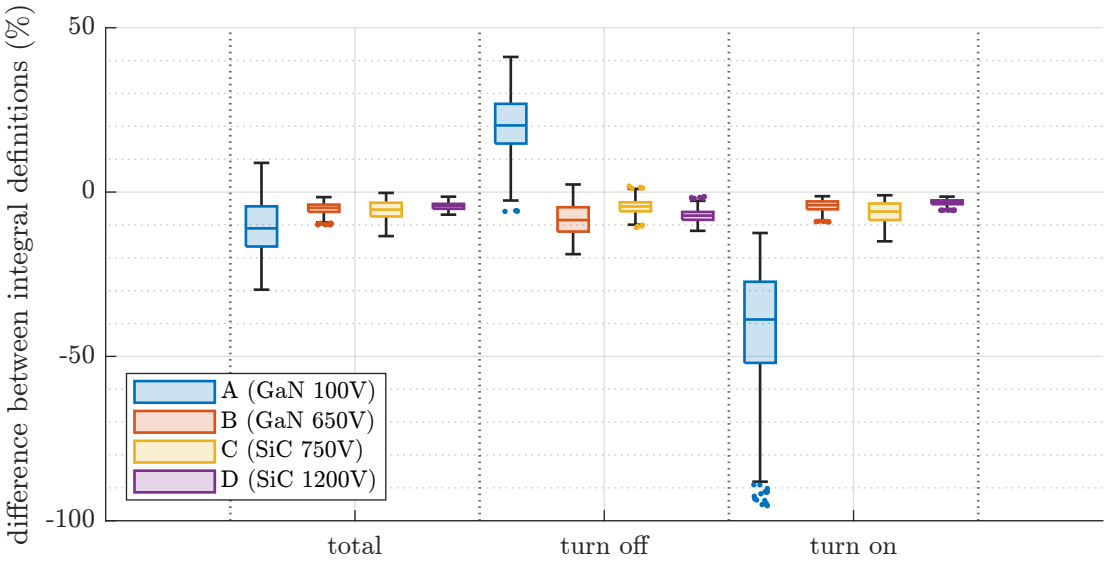

Figure 3.16: Simulated distribution of the difference between the integral definition for all DUTs

Finally, the impact of the definition of switching energies is evaluated. So far, all evaluations have been carried out using the full integral over the instantaneous power loss p_{loss}. In the definition from the standard *IEC 60747-8*, only the range between 10 % of V_{sw} and 10 % of I_{sw} is taken into account (see Fig. 2.12). This means that oscillations caused by switching are not included in the calculation of E_{off} and E_{on}. In Fig. 3.16 the relative deviation is shown, which results when $E_{\text{on,meas}}$ and $E_{\text{off,meas}}$ are calculated once according to the definition using the full integral and once using the boundaries from the *IEC* standard. Apart from DUT A, this deviation is in the range of approximately 0 % ... −10 %. Therefore, the switching energies according to the standard are lower than the losses that are actually caused by switching. However, it should be noted that the distinction between switching and conduction losses is not clearly defined when forming the complete integral.

Figure A.3 shows the distributions of the errors if the *IEC* standard is applied. Due to extremely fast turn-on switching events, a switching energy of $E_{\text{on}} = 0\,\mu\text{J}$ can result from the *IEC* standard and a corresponding error of $\varepsilon_{\text{on}} = -100\,\%$. This is the case if the 10 % limit of the falling voltage is reached before the 10 % limit of the rising current due to incorrect deskewing. Consequently, there is no continuous distribution for the total measurement error ε_{on} and evaluating the mean values μ is no longer appropriate. Therefore, an analysis via main-effect plots is distorted, which is the reason why the full integral was used in this study. A complete analysis would require evaluating the settling time T_{s} of the waveforms v_{ds} and i_{ds} to dynamically set the integration limits.

3.3 Conclusion

In this chapter, the answer was given to the question of how strongly the measurement accuracy of the switching energies E_{off} and E_{on} is influenced by individual measurement parameters. The relevant parameters are the parasitic inductance of the current sensor (L_{probe}), the parasitic capacitance of the voltage probe (C_{probe}), the two bandwidths $f_{\mathrm{c,v}}$ and $f_{\mathrm{c,i}}$, as well as the misalignment between the two waveforms v_{ds} and i_{ds}, which is expressed by the deskewing error t_{skew}. A simulation setup was introduced that uses the DoE method to model a large number of DPT with different settings for the operating point and the measurement setup. Using a total of 250 880 combinations for each of the four different WBG semiconductor devices, a data set was created to evaluate the sensitivity of the individual measurement parameters. The following findings were obtained on the basis of main-effect plots.

Probe Parasitics The parasitic elements L_{probe} and C_{probe} have a considerable impact on the measurement accuracy. The influence of L_{probe} is greatest for the 100 V GaN HEMT and changes the measurement error by up to 28.5 pp. The influence of C_{probe} in the case of the 1200 V SiC MOSFET most significant and affects the measurement error by up to 4.2 pp. The effects of these parameters act in different directions for both E_{off} and E_{on}, so that the resulting measurement errors compensate for each other by coincidence in some cases. Overall, care should be taken to minimize both parameters, with L_{probe} being the most prominent.

Measurement Bandwidth It has been shown that an extremely high bandwidth is not necessary for measuring the waveforms v_{ds} and i_{ds} with regard to the switching energies. In almost all scenarios, a voltage bandwidth of $f_{\mathrm{c,v}} = 500\,\mathrm{MHz}$ has proven to be sufficient. An exception is the measurement of E_{off} with the 100 V GaN HEMT, where 1.3 GHz is recommended. With regard to the bandwidth of the current measurement, a value of $f_{\mathrm{c,i}} = 900\,\mathrm{MHz}$ is recommended for the measurement of E_{off} and E_{on} and shows an increase in measurement accuracy for all DUTs. Therefore, this characteristic in particular should be taken into account when selecting suitable measuring equipment.

Deskewing The deskewing, which was expressed via the parameter t_{skew}, is by far the most critical measurement parameter. A mismatch of ±200 ps leads to a significant measurement error for all DUTs, which exceeds the error caused by the other measurement parameters. When the two variables E_{off} and E_{on} are combined to form the total switching energy E_{sw}, the influence of the deskewing is partially compensated, which is why the total error $\varepsilon_{\mathrm{total}}$ is always smaller than the errors of the individual variables $\varepsilon_{\mathrm{off}}$ and $\varepsilon_{\mathrm{on}}$. Another positive aspect is that the deskewing error is the only source of error that can be fully compensated for in post processing.

4 Design of an Advanced Resistive Current Sensor

This chapter focuses on the design of an advanced resistive current sensor. First, Section 4.1 gives an overview of existing concepts. This is followed by the presentation of a novel design in Section 4.2, which is a radial shunt resistor made up of discrete resistors. In Section 4.3, the transfer function of this shunt is analyzed in more detail and a method for improving the frequency response is presented. The thermal behavior of the shunt is analyzed in Section 4.4. After an outlook on possible improvements was given in Section 4.5, the most important findings about the new concept are summarized in Section 4.6.

4.1 Evaluation of Existing Concepts

Section 2.2.3 has already provided an brief overview of different solutions for current measurement in DPTs. In this section, the individual concepts for resistive current sensors are discussed in more detail. First of all, Section 4.1.1 deals with shunts made from *Manganin* foil. These are conventional coaxial shunts, which have been the state-of-the-art devices for a long time, and the so-called *M-shunts*. However, these devices are not suitable for the dynamic characterization of very fast-switching WBG semiconductor devices. For this reason, various new concepts have been developed in recent years. These concepts have in common, that discrete surface-mounted device (SMD) resistors are used to create structures with very high bandwidths and minimal parasitic inductances. Section 4.1.2 gives an overview about the most relevant designs for SMD shunts.

4.1.1 Shunts made from Manganin Foil

An early version of the coaxial shunt was introduced in 1991 for measuring transient currents with rise times of 25 ns in thyristor applications [109]. Meanwhile coaxial shunts are commercially distributed by *T&M Research Products Inc.* [110] and are recommended for a variety of applications [15], [37]. The coaxial shunt consists of an inner and an outer tube, which provides very good performance in terms of bandwidth and parasitic inductance [14]. Figure 4.1a shows the internal structure of a typical coaxial shunt. The

Table 4.1: Comparison of shunt resistors based on Manganin foil

Coaxial Shunts [110]

Variant	R_{shunt}	f_c	E_{max}
SDN-414-01	10 mΩ	0.4 GHz	6 J
SDN-414-025	25 mΩ	1.2 GHz	3 J
SDN-414-05	50 mΩ	2 GHz	2 J
SDN-414-10	100 mΩ	2 GHz	1 J

M-Shunts [115]

Variant	R_{shunt}	f_c	E_{max}
SCD25	25 mΩ	141 MHz	97 J
SCD50	25 mΩ	146 MHz	162 J
SCD75	25 mΩ	209 MHz	213 J
SCD100	25 mΩ	214 MHz	293 J

resistive element is a foil of the alloy *Manganin*. This material is used because of its low resistance temperature coefficient, good fabrication properties and long-term stability. Table 4.1 shows some exemplary devices, for which bandwidths up to $f_c = 2\,\text{GHz}$ are available.

Coaxial shunts are subject to closer examination in several publications. One of the main issues regarding the application with WBG devices is the parasitic inductance, which is in the range 2.2 nH ... 6.6 nH depending on the type of electrical connection [14], [111]. The parasitic inductance varies depending on the type of electrical contact, which, as shown in Fig. 4.1b, can be made either via a direct screw connection or via soldered pins. The main reason for the remaining parasitic inductance is the size of the component. As can be seen in Table 4.1, coaxial shunts achieve a very high thermal capacity E_{max}. However, for most WBG applications this is oversized and therefore there is potential for downsizing the component [112]. In addition, it was measured in [14] that the actual available bandwidth is limited to approximately 150 MHz and that there is a strong variance between individual samples.

A similar approach inspired by the conventional coaxial shunt is presented in [115]. The geometry is based on the hair-pin shunt presented in [116] and can be considered as a planar variant of the coaxial shunt. Figure 4.1c shows the cross-section of an *M-Shunt* and Table 4.1 lists some variants of *M-Shunts* on the right-hand side. The *M-Shunt* consists of a *Manganin* foil with a thickness of 50 µm. This means that, as with conventional coaxial

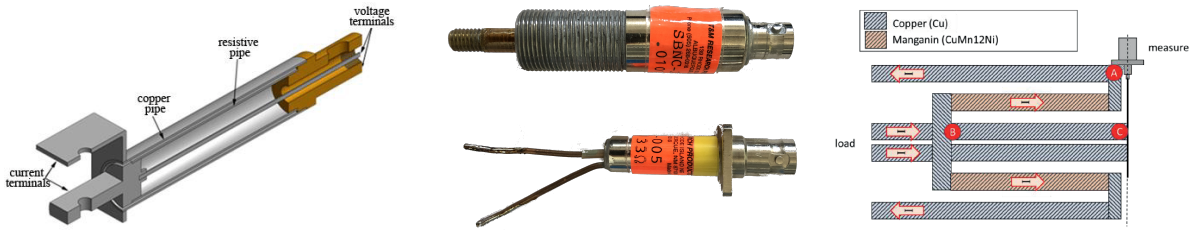

(a) Internal structure of coaxial shunt[113]

(b) Coaxial shunts with different connections

(c) Structure of M-Shunt[114]

Figure 4.1: Shunt resistors based on Manganin foil

shunts, the bandwidth is limited not only by the parasitic inductance but also by skin and proximity effects. Compared to the coaxial shunt, the bandwidth f_c is lower, but the thermal capacity E_{max} is significantly higher. Another advantage of this design is the lower parasitic inductance of approximately 1.1 nH [114].

Both the coaxial shunt and *M-Shunt* are recommended for applications with high currents, where a high thermal capacitance is required. However, their parasitic inductance of a few nanohenries is too high for the dynamic characterization of discrete WBG semiconductor devices. One possible application is the measurement of WBG power modules. Due to the intrinsic parasitic inductance of power modules, these are less susceptible to the additional inductance of a current sensor and typically exhibit a high nominal current [117].

4.1.2 SMD Shunt Resistors

Because of the disadvantages of conventional coaxial shunts mentioned in the previous section, multiple new concepts for resistive current measurement have been developed in recent years. All concepts have in common that discrete resistors are used instead of a foil made of *Manganin*. Through miniaturization and clever design of the geometry, shunt resistors can be constructed that achieve very high bandwidths with very low parasitic inductances. Both are essential requirements for the dynamic characterization of fast switching WBG semiconductor devices. The most relevant concepts are described below.

The simplest approach is a shunt resistor consisting of several SMD resistors connected in parallel. This concept is used in [120] in combination with a compensation network and a matching analog circuit to extend the bandwidth. In this way, a total bandwidth of 150 MHz was achieved and a parasitic inductance of 300 pF. The concept has also been successfully applied in [121], where an RC low-pass filter is used as a compensation network. However, no bandwidth was determined. In [118] the concept is taken up again

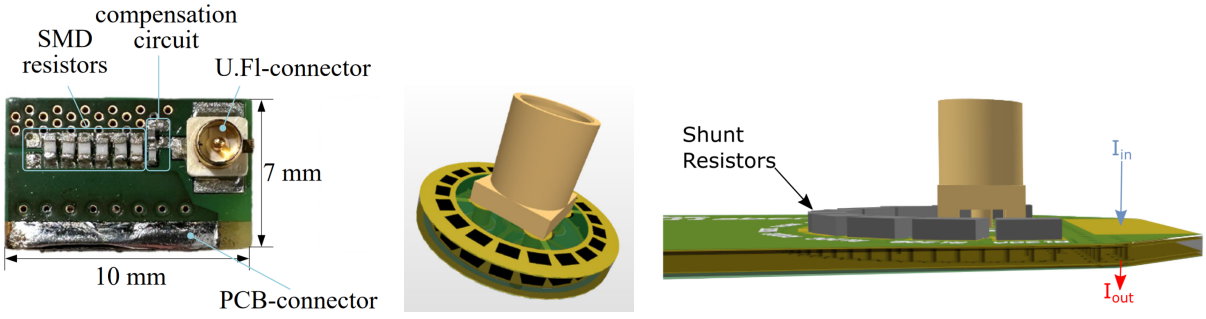

(a) Resistor array with compensation network [118]

(b) "SMD-CSR"[112]

(c) "Ultrafast Current Shunt"[119]

Figure 4.2: Presentation of SMD shunt concepts

and six resistors are arranged in an array, as shown in Fig. 4.2a. The bandwidth was increased to 734 MHz with a similar compensation network and the parasitic inductance was determined to be 452 pH. The two approaches are listed in Table 4.2.

The approach presented in [112] is a significant step forward as it is a miniaturized version of the coaxial shunt, called *SMDCSR*. The coaxial current flow is achieved by the vertical arrangement of discrete resistors as shown in Fig. 4.2b. Through this miniaturization, a bandwidth of up to 2.23 GHz was achieved with a very low inductance of 120 pH. Since the bandwidth also depends on the resistance value used, several variants have been implemented and are listed in Table 4.2. The design is patented by *Keysight Technologies, Inc.* [122]. In [123], the concept was replicated and the assembly technique was identified as a challenge because of the vertically placed SMD resistors.

Another high-bandwidth approach has been presented in [119]. The approach called *Ultra-Fast Current Shunt (UFCS)*, is based on a semicircular arrangement of multiple SMD resistors and is illustrated in Fig. 4.2c. As in [120], the bandwidth is maximized by a compensation network including analog electronics and a bandwidth of 1.55 GHz was achieved. The parasitic inductance depends on whether an insertable (*UFCS-I*) or an embedded solution (*UFCS-E*) is used. An additional parasitic inductance of only 20 pF is specified for the *UFCS-E* variant. Both variants are listed in Table 4.2. The challenge with this concept is to set up the compensation network and tune the analog circuit. The embedded version also requires a lot of space on the PCB that contain the DUT.

In [124] another new approach for a shunt was presented. In the *Impedance Matching Shunt (IM Shunt)* concept, the discrete shunt resistor is connected via a matched transmission line as shown in Fig. 4.3a. By matching the characteristic impedance, the effect of the parasitic inductance is compensated by the capacitance of the transmission line. The different variants of the *IM shunt* are listed in Table 4.2, where the ratio of line impedance to shunt impedance has been varied. A high bandwidth of 3 GHz was measured and a very low inductance of 100 pF is specified for the case of a perfectly matched line. The challenge with this concept is the assembly, which has to be very precise, needs sufficient space and is complicated by frequency-dependent material parameters.

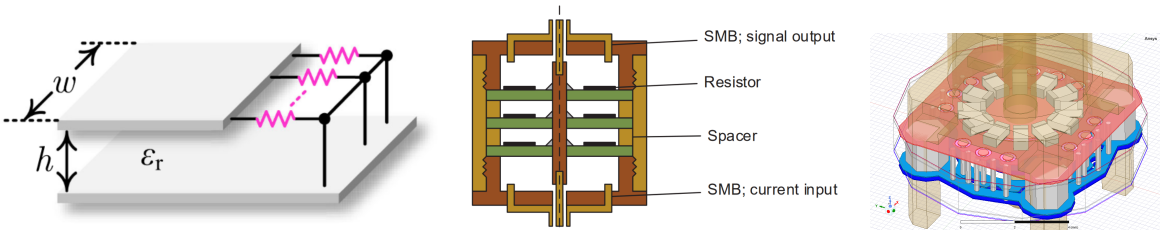

(a) "Impedance-Matching Shunt"[124]

(b) Radial shunt (stacked discs) [45]

(c) Radial shunt (4-layer)[125]

Figure 4.3: Presentation of SMD shunt concepts (continued)

Table 4.2: Comparison of concepts for high-bandwidth and low-inductive current shunts

	Concept	R_{shunt}	f_{c}	L_{shunt}	Reference
1	Resistor array with compensation	10 mΩ	0.150 GHz	300 pH	[120]
2	Resistor array with compensation	167 mΩ	0.734 GHz	452 pH	[118]
1	SMDCSR A	100 mΩ	0.528 GHz	220 pH	[112]
2	SMDCSR B	10 mΩ	0.125 GHz	120 pH	
3	SMDCSR C	110 mΩ	2.23 GHz	120 pH	
4	SMDCSR D	50 mΩ	1.63 GHz	120 pH	
5	UFCS-E (embedded)	100 mΩ	1.55 GHz	20 pH	[119]
6	UFCS-I (insertable)	100 mΩ	1.48 GHz	260 pH	
7	IM Shunt 1:1	100 mΩ	3 GHz	100 pH	[124]
8	IM Shunt 2:1	100 mΩ	0.457 GHz	100 pH	
9	IM Shunt 20:1	100 mΩ	0.135 GHz	350 pH	
12	Radial shunt (stacked discs)	100 mΩ	0.100 GHz	3.1 nH	[45]
13	Radial shunt (4-layer)	83.3 mΩ	1.26 GHz	86.7 pH	[125]
14	Radial shunt (2-layer)	83.3 mΩ	2.17 GHz	84.1 pH	this work

The other entries in Table 4.2 are classified as radial shunts, which are based on arrangements with radial current flow. A prototype for WBG devices was presented in [45]. As illustrated in Fig. 4.3b, several discs of PCBs with discrete resistors are stacked inside a single housing. The whole structure achieves an inductance of 3.1 nH with a bandwidth in the range of 100 MHz (see Table 4.2). A design from the author of this work is shown in Fig. 4.3c [125]. It follows a similar radial shunt layout but focuses on miniaturization. By placing the resistors directly underneath a coaxial connector on a 4-layer PCB, a bandwidth of 1.26 GHz was measured. In the following sections, the radial shunt is further optimized. A detailed description of the 2-layer design, which achieves a bandwidth of 2.17 GHz and a very low parasitic inductance of 84.1 pH, is given in the Section 4.2.

In Fig. 4.4 the concepts listed in Table 4.2 are plotted according to their measurement bandwidth and parasitic inductance. This shows that there are currently several favorites, with the concepts *UFCS-E*, *IM Shunt 1:1* and *Radial Shunt (2-layer)* currently being the best solutions. When selecting a suitable method, other criteria must also be considered. The complexity of the structure, the available space and the energy dissipated by the shunt can represent further limitations. A general disadvantage of comparing the different concepts is that the characterization and determination of the relevant properties f_{c} and L_{shunt} are not subject to a uniform methodology. Depending on the definition and type of measurement or simulation, different results may be obtained. The frequency dependence of the parasitic inductance is usually not specified and there are different ways to define the cutoff frequency, as shown in Section 4.3.

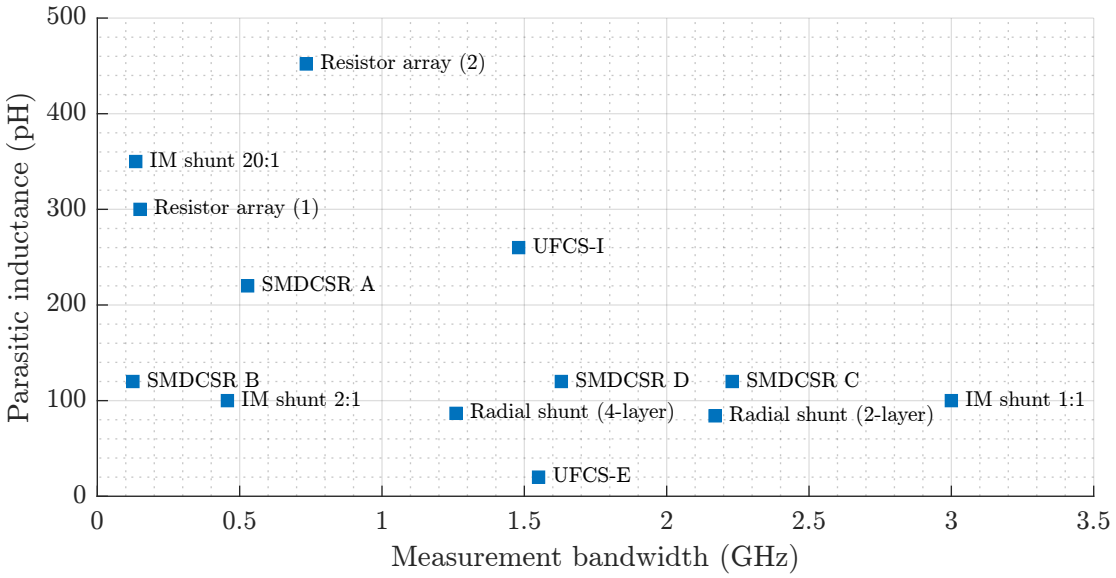

Figure 4.4: Comparison of evaluated concepts according to bandwidth and inductance

4.2 Introduction to a Radial Shunt Resistor

After a brief overview of existing solutions in the field of resistive current measurement, a novel design for a shunt resistor is presented in this section. The idea of a radial shunt with low inductance is already used in [126]. In this publication, however, the focus is not on maximizing the measurement bandwidth and the concept is only designed for currents up to 2 A. The concept is taken up again in [127], [128], where the voltage is accessed directly via a coaxial connector. This allowed measuring a rise time of 880 ps, which indicates that the concept is suitable for the characterization of WBG semiconductors. The radial shunt resistor presented in this thesis combines the features of coaxial current flow, short current loop, and a small footprint. The resistors of the shunt are placed directly underneath the coaxial connector, achieving an optimized variant of the concept described in [125]. In the Section 4.2.1, the structure is presented in more detail and in Section 4.2.2 its impedance and bandwidth are determined by simulation.

4.2.1 Low-Inductive Layout

The inductance L of a geometrical structure is defined by the ratio of the surface integral of the magnetic flux density $\vec{B}$ to the applied current i (4.1) [129]. To keep the parasitic inductance of a shunt low, it is therefore essential to minimize the area enclosed by the current, the so-called current loop area.

$$L = \frac{\phi}{i} = \oint_A \frac{\vec{B}}{i} \mathrm{d}\vec{A} \tag{4.1}$$

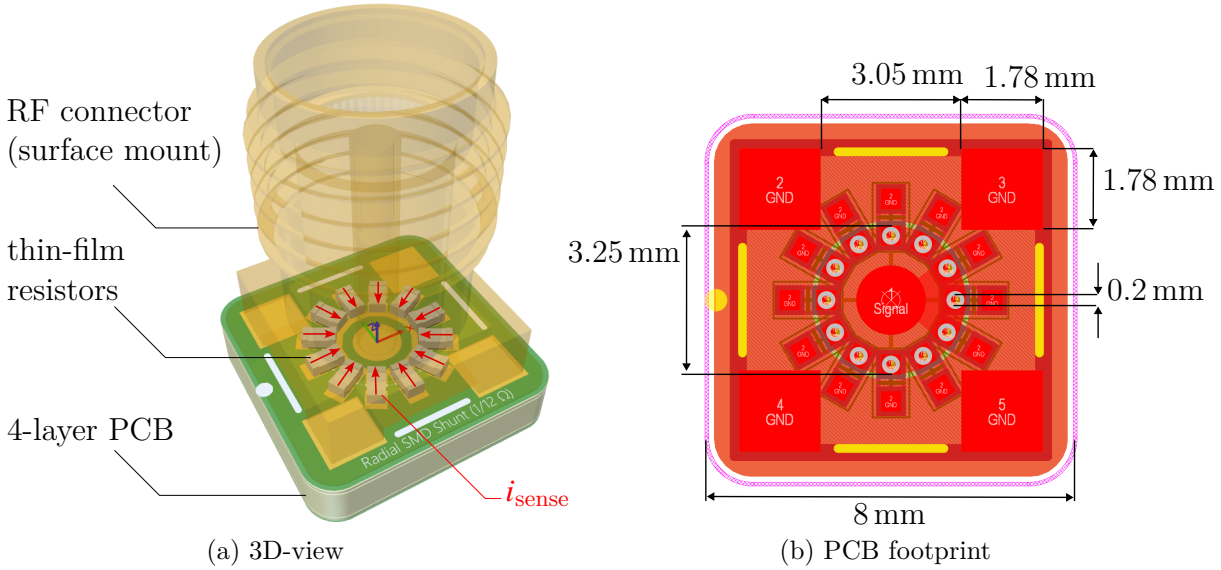

(a) 3D-view (b) PCB footprint

Figure 4.5: Design view of the radial shunt resistor with discrete thin-film resistors underneath a RF connector

Coaxial shunts make use of this principle by keeping the distance between the inner and outer conductor very small (see Fig. 4.1a). The coaxial arrangement also has the advantage that there is no leakage flux to the outside, as the geometry completely encloses the tangential magnetic field lines [14]. Nevertheless, coaxial shunts have an inductance of several nanohenries due to their overall size and connection to the DUT. Miniaturization is limited by the use of *Manganin* foil. There have been attempts to replicate the geometry using vertically placed SMD resistors, but this technique is relatively complex, as it cannot be realized using a regular assembly and soldering process. [112].

Therefore, a different approach is chosen in this work. A symmetrical and radial current flow i_{sense} is implemented via the circular arrangement of regular SMD resistors as shown in Fig. 4.5a. In contrast to the coaxial shunt, an analytical solution for the inductance is not obvious and requires complex calculations based on the Biot-Savart law [130], [131]. By placing the resistors on a 4-layer PCB, the distance between the forward and return current is minimized, since the distance between the top and first inner layer lies in the range of 100 µm. This principle is common with WBG semiconductors and is used in many low-inductance designs [132], [133] Another effect that limits the performance of a shunt in the high-frequency range is the skin effect. The skin effect causes an increase in resistance with increasing frequency, as the current is displaced to the conductor surface. It is therefore important to use thin-film resistors whose resistive films typically have a thickness in the range of 100 nm [134].

To implement the shunt, a total of 12 discrete thin-film resistors are arranged in a circle and connected in parallel. As a resistance value, 1 Ω was selected, resulting in a total shunt resistance of $R_{\text{shunt}} = 83.3\,\text{m}\Omega$. The dimensioning of the shunt resistance is always a trade-off between bandwidth and current carrying capacity. A higher resistance causes an

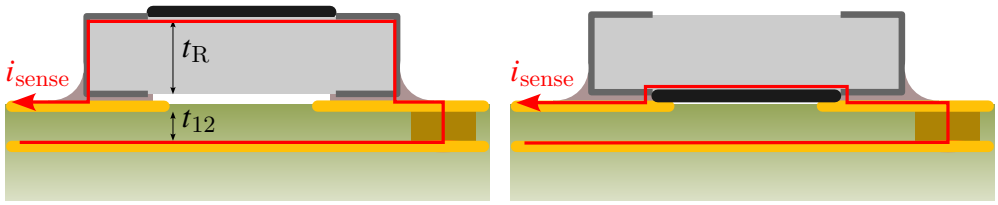

(a) regular placement (b) flipped placement

Figure 4.6: Current path dependend on resistor orientation [125]

increase in the 3 dB cutoff frequency, but at the same time increases the ohmic losses. The explanation of this relationship via a simplified equivalent circuit diagram can be found in [125]. Another requirement is the voltage tap across the shunt, which must be designed in such a way that no voltage can be induced in the measuring line. In the proposed design, this is achieved by placing a coaxial connector directly above the resistors, as shown in Fig. 4.5a. The use of discrete resistors in the *0402* package makes it possible to use a coaxial connector of the type SubMiniature version A (SMA) or SubMiniature version B (SMB) in terms of space. The proposed design can also be implemented with other types of resistors or connectors. Figure 4.5b shows the PCB footprint, which has external dimensions of 8 mm. Thus the structure is very compact and can be used on high-density PCBs. The copper plane consists of an inner and an outer section, with the inner section being a circle with a diameter of 3.25 mm. There are vias with a hole diameter of 200 µm located directly in the pads, allowing the current to pass through to the inner layer. Both blind and regular through-hole vias can be used.

Another characteristic is the reverse placement of the resistors. Figure 4.6 shows an image from [125] which illustrates this principle. In regular thin-film resistors, the resistive layer is located on a substrate, which makes up a large part of the component thickness and is required for mechanical stability [134]. The thickness of the selected *0402* resistor is $t_{\text{R}} = 350\,\mu\text{m}$ and is therefore greater than the prepreg between layers 1 and 2, which is $t_{12} = 140\,\mu\text{m}$. The current loop area of i_{sense} can therefore be reduced by placing the resistors in an upside-down position. With a similar design, the bandwidth was improved by almost 50 MHz [125].

4.2.2 Simulation of Bandwidth and Impedance

In a first step the presented design is simulated with the finite element method (FEM) software *ANSYS Q3D Extractor*. The structure is modeled as a conventional two-port system. As shown in Fig. 4.7a, the terminals of the shunt are defined as two differential pairs. The first pair consists of the current carrying traces of the PCB and the second pair consists of the pins of the coaxial connector. In addition to the modeling of the PCB, it is also necessary to model the thin-film resistors. Figure 4.7b shows the structure of a typical thin-film resistor in a *0402* package with a length of 1 mm and a width of 0.5 mm

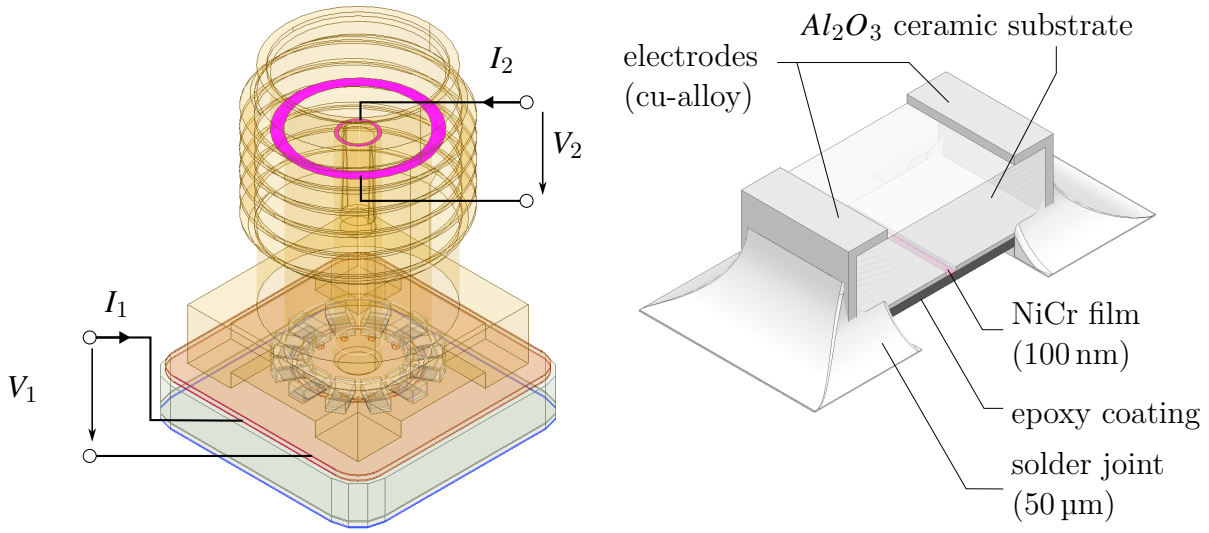

(a) Port definition

(b) Thin-film resistor model

Figure 4.7: Simulation model in *ANSYS Q3D Extractor*

[135]. The resistor is based on a Aluminum oxide (Al_2O_3) ceramic substrate, which is contacted by electrodes on the sides, which consist of a copper alloy [136]. The actual resistor is realized by a resistive layer of Nichrome (NiCr) with a typical thickness of 100 nm and is covered by an epoxy coating. The contact with the pads of the printed circuit board is realized by a solder connection for which a thickness of 50 µm was chosen [137].

The 2-port S-parameter matrix for each frequency is extracted from the simulation. The matrix is defined according to the conventional definition for S-parameters given in Eq. (4.2). Its entries describe the relationship between the vector of the incident waves $\vec{a}$ and the reflected wave $\vec{b}$, which are defined by the complex values for current and voltage at the respective port with the reference impedance $Z_0 = 50\,\Omega$ (see Eq. (4.3) and Eq. (4.4)) [56].

$$\begin{pmatrix} b_1 \\ b_2 \end{pmatrix} = \begin{pmatrix} S_{11} & S_{12} \\ S_{21} & S_{22} \end{pmatrix} \cdot \begin{pmatrix} a_1 \\ a_2 \end{pmatrix} \tag{4.2}$$

$$a_\mathrm{x} = \frac{1}{2}\left(\frac{V_\mathrm{x}}{\sqrt{Z_0}} + I_\mathrm{x}\sqrt{Z_0}\right) \tag{4.3}$$

$$b_\mathrm{x} = \frac{1}{2}\left(\frac{V_\mathrm{x}}{\sqrt{Z_0}} - I_\mathrm{x}\sqrt{Z_0}\right) \tag{4.4}$$

The S-parameters plotted in Fig. 4.8 describe the electrical behavior, but do not provide the actual transfer function of the shunt. To obtain the transfer function and to be able to make a statement about the bandwidth, the S-parameters are converted into Z-parameters. These are also called impedance parameters and are defined according to

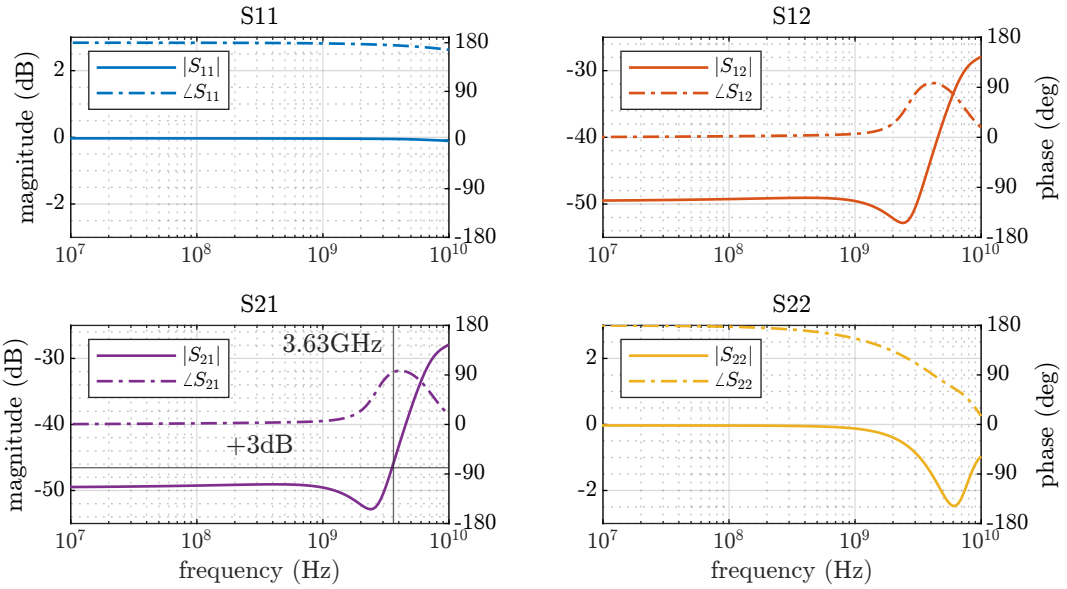

Figure 4.8: Simulated entries of S-parameter matrix by magnitude and phase

Eq. (4.5). The conversion is carried out using the formulas from Appendix A.4. The parameter Z_{21}, which is defined according to 4.6, describes the ratio of input current to output voltage of the shunt and thus corresponds to the desired transfer function. The condition $I_2 = 0\,\mathrm{A}$ is initially accepted as a valid approximation and discussed in Section 4.3.2.

$$\begin{pmatrix} V_1 \\ V_2 \end{pmatrix} = \begin{pmatrix} Z_{11} & Z_{12} \\ Z_{21} & Z_{22} \end{pmatrix} \cdot \begin{pmatrix} I_1 \\ I_2 \end{pmatrix} \tag{4.5}$$

$$Z_{21} = \left.\frac{V_2}{I_1}\right|_{I_2=0} \tag{4.6}$$

Figure 4.9 shows the simulated parameter Z_{21} as a Bode diagram. It can be seen that the transfer function has a very flat curve, with the expected dc value of 83.3 mΩ. For frequencies greater than 3.31 GHz, the magnitude of the transfer function deviates from this value by more than 3 dB and reaches an impedance of more than 118 mΩ. The phase initially shows a slightly increasing curve and moves in a range between −24° and 17°. In some publications, the bandwidth is determined using the S-parameter S_{21} [14], [119], [124]. However, this does not correspond to the desired transfer function of the shunt in practice. For the simulated geometry, the definition via S_{21} would result in a bandwidth of 3.63 GHz, which deviates from the actual value by 9.7 %.

In addition to the parameter Z_{21}, the input impedance of the shunt is also of relevance, as this is critical in terms of how the insertion of the shunt influences the switching behavior of the DUT to be measured. In a first step, the values R_{shunt} and L_{shunt} determined via *ANSYS Q3D Extractor* are plotted in Fig. 4.10a. These are frequency dependent, as the current distribution within the component changes due to the skin and proximity

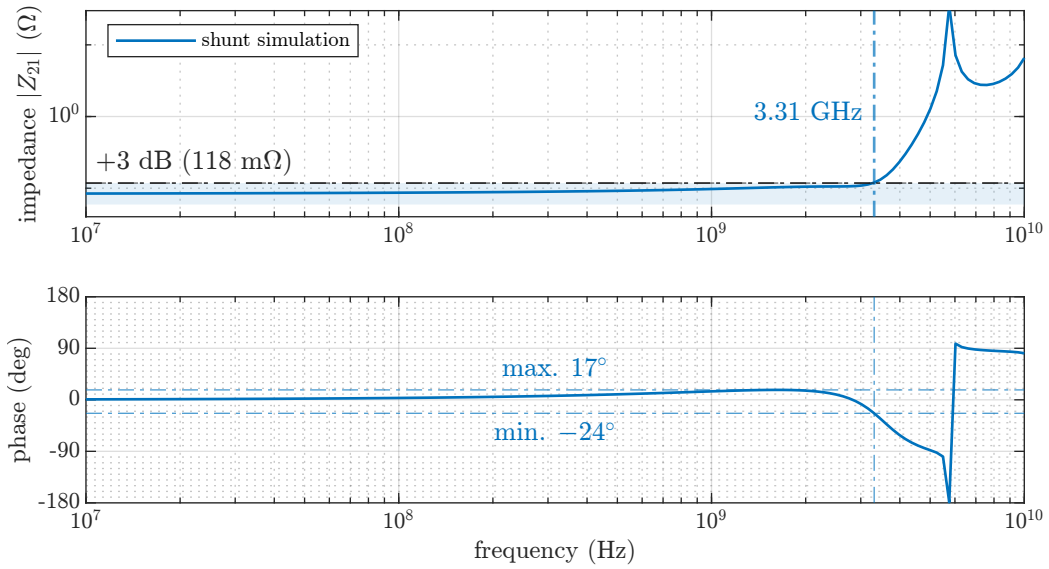

Figure 4.9: Bode diagram of the simulated transfer function Z_{21}

effect. It is observed that L_{shunt} decreases from initially 365 pH to 84.1 pH. The resistance increases continuously due to the skin effect starting at 83.3 mΩ for low frequencies. The input impedance Z_{in} can also be calculated using Z-parameters (Eq. (4.7)) [138]. In this equation, Z_{L} is the load at the output of the two-port network and is defined according to Eq. (4.8). In case of the shunt resistor, $Z_{\text{L}} = 50\,\Omega$ is selected, as this corresponds to the intended application with an oscilloscope.

$$Z_{\text{in}} = Z_{11} - \frac{Z_{12} \cdot Z_{21}}{Z_{22} + Z_{\text{L}}} \tag{4.7}$$

$$Z_{\text{L}} = -\frac{V_2}{I_2} \tag{4.8}$$

$$Z_{\text{in,fitted}} = R_{\text{shunt}} + \text{j}\omega L_{\text{shunt}} \tag{4.9}$$

Figure 4.10b shows the calculated curve of Z_{in} by magnitude and phase. It is noticeable that the input impedance has a curve that is characteristic for a series circuit combining a resistor and an inductor. It is therefore possible to approximate the impedance Z_{in} with a simplified model as derived in Eq. (4.9). The value of the resistive component is known and is $R_{\text{shunt}} = 83.3\,\text{m}\Omega$. The value $L_{\text{shunt}} = 84.1\,\text{pF}$ is selected for the inductance, which was determined at high frequencies. The curve of $Z_{\text{in,fitted}}$ is also displayed in Fig. 4.10b and shows high agreement with the simulated Z_{in} over the entire frequency range. The simplified model makes it possible to consider the impedance of the shunt resistor in circuit simulations, without having to model the frequency dependence of L_{shunt} and R_{shunt}.

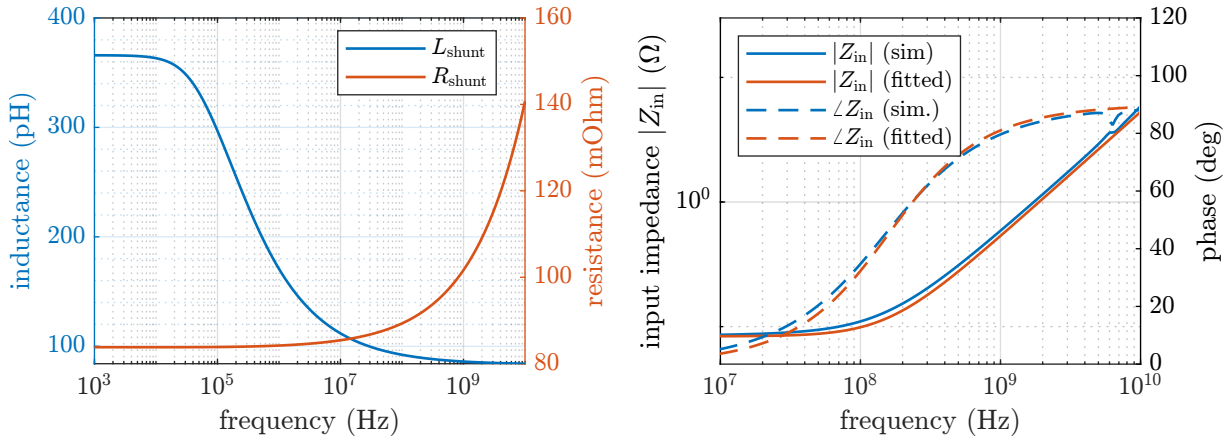

(a) Resistance and inductance

(b) Input impedance for $Z_{\text{L}} = 50\,\Omega$

Figure 4.10: Simulation results for the input impedance

4.3 Analysis and Improvement of the Transfer Characteristics

This section discusses the characterization of the transfer function of the radial shunt. First, the assembly of a prototype and its measurement in the frequency domain are presented in Section 4.3.1. Next, the influence of the entire measurement path consisting of cable and termination is analyzed in Section 4.3.2. Finally, in Section 4.3.3, a method is presented to increase the maximum bandwidth by using a digital filter.

4.3.1 Implementation of a Prototype

After the design has been designed and simulated, prototypes are built to test the design in the frequency domain. The previously presented shunt design is assembled twice on a PCB and is shown in Fig. 4.11a. The image on the left shows the shunt during assembly with the 12 reverse-placed thin-film resistors. An advantage of the design is that it allows a regular assembly with reflow soldering, which can also be automated. It is important that the coaxial connector is soldered in the same process as the resistors, since reheating could displace the tightly packed resistors. The measurement is performed using a two-port vector network analyzer (VNA), where port one is the current-conducting port of the shunt and port two is the signal output via the coaxial connector. This corresponds to the definition shown in Fig. 4.7a. To eliminate the influence of cables, connectors and PCB traces, de-embedding is required. For de-embedding the radial shunt, the PCB shown in Fig. 4.11b is used. It has been validated in [125] and allows a complete short-open-load-thru (SOLT) calibration.

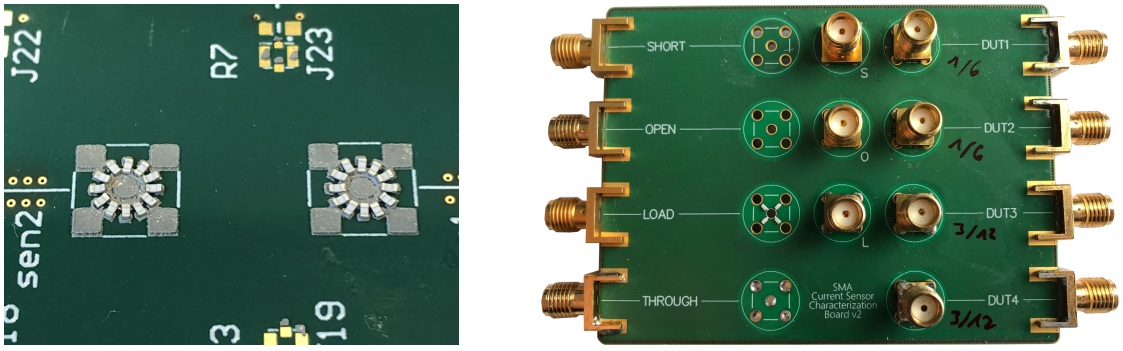

(a) View on shunt resistors during assembly

(b) View on the SOLT calibration board

Figure 4.11: Images of the PCBs used for measurement in the frequency domain

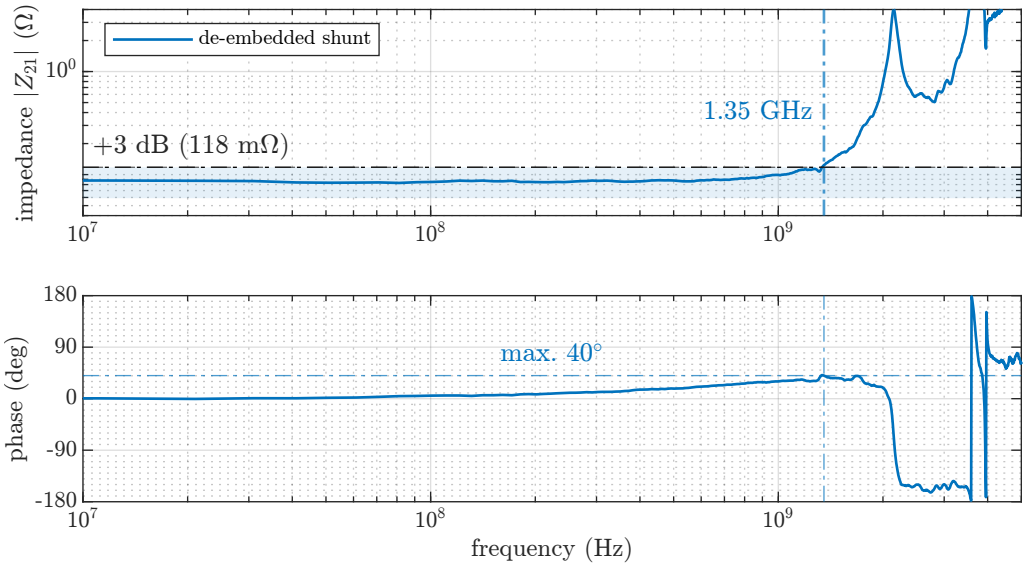

Figure 4.12: Measured Bode diagram Z_{21} of radial shunt with $R_{\text{shunt}} = 83.3\,\text{m}\Omega$

Figure 4.12 shows the frequency response of the parameter Z_{21} of the impedance matrix that was calculated from the S-parameter measurement. The initial value at 10 MHz is $Z_{21} = 85.2\,\text{m}\Omega$ and deviates by 2.3 % from the theoretical dc value, which is 83.3 mΩ. The cutoff frequency f_c is calculated via a deviation of 3 dB from the theoretical dc value and is located at 1.35 GHz. At this frequency there is a phase shift of 40°. As the frequency increases, the magnitude of the impedance increases and at 2.13 GHz a first resonance frequency is observed at which the impedance reaches $Z_{21} = 3.72\,\Omega$. This is caused by the parasitic capacity of the structure.

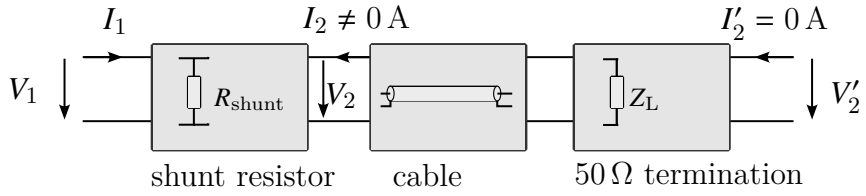

Figure 4.13: Complete measurement system

4.3.2 Influence of Cables and Termination

In the previous section, the impedance parameter Z_{21} was introduced as a transfer function to measure the current I_1 in relation to the voltage V_2. The definition of Z_{21} from Eq. (4.6) assumes that the current at the second terminal is zero. This assumption does not hold in practice, since the shunt is connected to an oscilloscope via a cable which leads to $I_2 \neq 0\,\mathrm{A}$. As with the calculation of the input impedance Z_{in}, the load at the output must be taken into account. The oscilloscope has an input impedance of $Z_{\mathrm{L}} = 50\,\Omega$, forming a current divider in parallel to R_{shunt}. In the following a method is presented to analyze the complete measuring system, which is illustrated in Fig. 4.13.

To obtain the complete transfer function of the measurement system, the T-parameters of the individual elements are used, which are defined according to 4.10 and can be calculated from the respective S-parameters. The T-parameters are defined in such a way that a matrix multiplication corresponds to cascading the individual systems and are therefore also called chain parameters. This makes it possible to calculate the total matrix of the system via Eq. (4.11), which can then be transformed back into S- or T-parameters. The formulas required for conversion are provided in Appendix A.4. The additional elements are modeled using the *RF Toolbox* from *MATLAB*, which allows to calculate the S-parameters of common circuits. The cable is modeled using the data sheet values of a *LMR-100A* coaxial cable with an characteristic impedance of 50 Ω and a length of 0.5 m [139]. An ideal termination resistance of $Z_{\mathrm{L}} = 50\,\Omega$ is assumed.

$$\begin{pmatrix} b_1 \\ a_1 \end{pmatrix} = \begin{pmatrix} T_{11} & T_{12} \\ T_{21} & T_{22} \end{pmatrix} \cdot \begin{pmatrix} a_2 \\ b_2 \end{pmatrix} \tag{4.10}$$

$$T_{\mathrm{total}} = T_{\mathrm{resistor}} \cdot T_{\mathrm{cable}} \cdot T_{\mathrm{termination}} \tag{4.11}$$

$$Z_{21}{}' = \left.\frac{V_2{}'}{I_2{}'}\right|_{I_2{}'=0} \tag{4.12}$$

The parameter Z_{21}' obtained from the cascaded matrix T_{total} is equal to the transfer function of the complete system (Eq. (4.12)). The assumption $I_2{}' = 0\,\mathrm{A}$ is valid now since the ADC after the 50 Ω termination is considered to be high-impedance. Figure 4.14 shows a comparison of the transfer functions in terms of magnitude and phase. It includes the case of the de-embedded shunt without termination as well as the terminated shunt with and without the influence of the coaxial cable. It is observed that the cutoff frequency

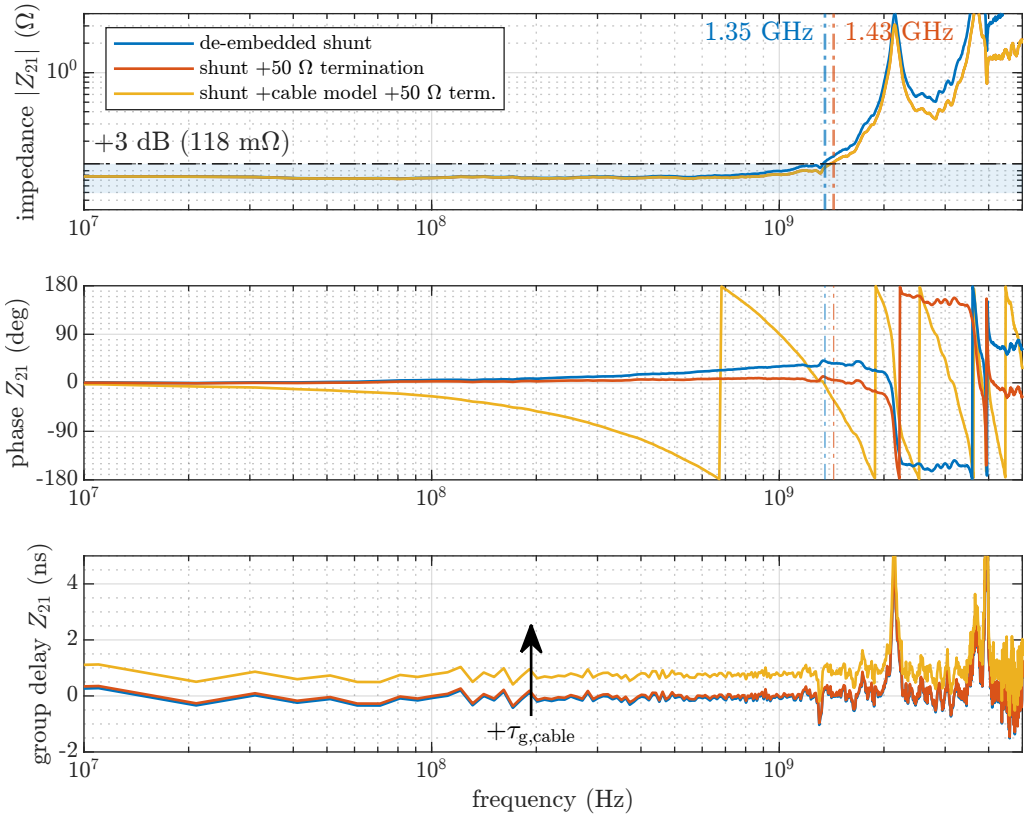

Figure 4.14: Influence of the measuring system consisting of cable and 50 Ω termination on the measured transfer function Z_{21}

f_c, which was defined by a deviation of 3 dB, is slightly increased by the termination resistance and now lies at 1.43 GHz. The presence of a cable between the shunt and termination resistor does not affect this result, since the attenuation of a short cable is negligible. Additionally, the termination resistance improves the phase response significantly, reducing its value from 40.3° to 4.98° at f_c. The first resonance at 2.13 GHz is not affected.

The insertion of the coaxial cable seems to have a large effect on the phase shift, which is caused by the length of the cable and the associated delay. According to [58], the differential time delay $\Delta\tau$ of a system is the difference between the phase delay τ_ϕ and the group delay τ_g (4.13), which was already introduced in Section 2.3.1.

$$\Delta\tau = \tau_\phi - \tau_g \tag{4.13}$$

The chosen coaxial cable has a defined time delay of $\Delta\tau = 1.54\,^{\mathrm{ns}}/_{\mathrm{m}}$. As this is a high-frequency cable suitable for lossless signal transmission up to 6 GHz, it is assumed that the phase delay for all frequencies is $\tau_\phi \approx 0$ ns and that the signal is therefore transmitted without any distortion. In this case, the time delay corresponds to the group delay

(4.14).

$$\Delta\tau = \tau_{\mathrm{g}}(\omega) \Rightarrow -\frac{\mathrm{d}\phi(\omega)}{\mathrm{d}\omega} = 1.54\,{}^{\mathrm{ns}}/_{\mathrm{m}} \cdot 0.5\,\mathrm{m} = 770\,\mathrm{ps} \tag{4.14}$$

In the lower plot of Fig. 4.14, the group delay of the complete system is plotted with and without the cable. It can be seen that the phase response caused by the cable corresponds to a constant increase in the group delay by $\Delta\tau$ and does not have any other effect on the transmission behavior. However, with regard to the deskewing issue described in Section 2.3.3, the time delay is relevant and must be compensated for accordingly. In summary, terminating the shunt with a $50\,\Omega$ resistor slightly improves the frequency response. Apart from adding a delay, the cable has no effect on the transfer function Z_{21} as long as it is a high-frequency cable characterized by a constant delay and negligible attenuation. In real applications, it is also recommended to use cables that do not show degradation due to aging [140].

4.3.3 Increasing the Bandwidth with Digital Filtering

The transfer function Z_{21} of the designed shunt has a certain characteristic, which has to be taken into account for applications with very short rise times. As can be seen in Fig. 4.14, the magnitude of Z_{21} increases, which leads to an upward break out from the 3 dB corridor. According to the conventional definition, frequencies above the cutoff frequency f_{c} are filtered out, which would correspond to a downward break out of the 3 dB corridor. In the case of the shunt, this means that frequency components above f_{c} are amplified by more than 3 dB compared to the dc gain, which is defined by $R_{\mathrm{shunt}} = 83.3\,\mathrm{m}\Omega$. This leads to the fact that input currents with high-frequency components appear distorted in the output signal. To counteract this characteristic, it is necessary to filter the output signal of the shunt accordingly. In the following, a method is presented to implement this in post-processing.

Figure 4.15 shows the transfer function Z_{21} obtained from the measurement data, which has a cutoff frequency of 1.43 GHz and a resonance frequency at 2.13 GHz. At the point of this resonance, the impedance of the shunt is $3.72\,\Omega$, which means that a corresponding frequency component in the input current causes a corresponding high output voltage. For this reason, a low-pass filter is designed to filter out the high-frequency components from the output signal. The filter is implemented as a digital finite impulse response (FIR) filter using the *Signal Processing Toolbox* from *MATLAB* [141]. The parameters have been designed according to the characteristics of the transfer function Z_{21} and are listed in Table 4.3.

The passband frequency is set equal to the cutoff frequency of Z_{21}, so that the 3 dB increase in Z_{21} is compensated by the decrease in the filter transfer function. The stopband frequency is set to the first resonance frequency of Z_{21}, since this is the frequency at which maximum attenuation is desired. To maintain the dc gain of the shunt, the passband ripple is set to a very small value, where 0.1 dB corresponds to a factor of 1.2 %. The last

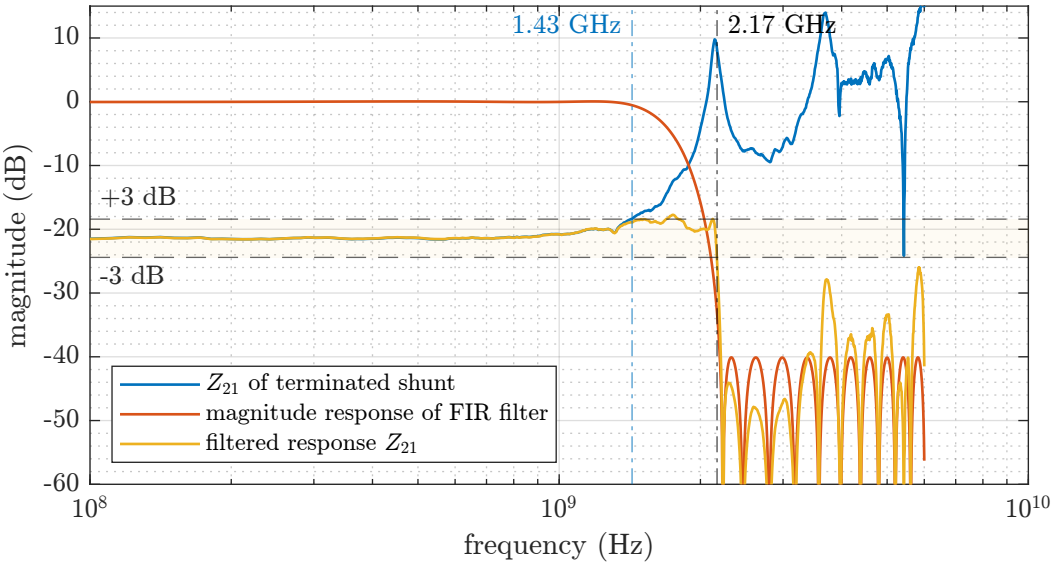

Figure 4.15: Application of the designed digital filter to the measured shunt transfer function Z_{21} (terminated with 50 Ω)

Table 4.3: Design parameters for FIR low-pass filter

filter parameter	value	design rule
passband frequency	1.3 GHz	close to 3 dB cutoff frequency of Z_{21}
stopband frequency	2.2 GHz	close to first resonance peak of Z_{21}
passband ripple	0.1 dB	set low as possible to maintain dc gain
stopband attenuation	40 dB	sufficiently high to damp all resonances of Z_{21}
sampling rate	10 GS/s	fit to sampling rate of oscilloscope

defining parameter of the filter is the stopband attenuation, which must be chosen so that all resonances in Z_{21} are attenuated by at least 3 dB below the dc gain. The calculated transfer function of the FIR filter is shown in Fig. 4.15 and the resulting overall transfer function for Z_{21}, which is obtained by multiplication of the two responses. It can be seen that the filter successfully attenuates all high-frequency components, so that the transfer function shows a true −3 dB cutoff frequency. Compared to the original cutoff frequency at 1.35 GHz, the cutoff frequency was increased to 2.17 GHz. By means of forward-backward filtering, it is possible to compensate for the nonlinear phase of the filter, so that the respective frequency components are only manipulated in their amplitude and no phase distortion is introduced [142]. Within *MATLAB* such zero-phase filtering is possible via the *filtfilt* function from the *Signal Processing Toolbox*.

After designing a digital filter to improve the frequency response, the next step is to determine its behavior in the time domain. Using the *RF Toolbox* of MATLAB, the complex transfer function Z_{21} is fitted to a rational function. This makes it possible to calculate the system response to any input signal in the time domain. In Appendix A.5,

the code for performing these calculations is given. Figure 4.16b shows the output voltage of the shunt for a total of four hypothetical input signals. The input signals have different rise times, which are in the range between $t_{\mathrm{rise}} = 207\,\mathrm{ps}$ and $t_{\mathrm{rise}} = 413\,\mathrm{ps}$ and thus have frequency components outside the linear range of Z_{21} and are hence causing disturbances. In Fig. 4.16a the spectrum of the input signal and the unfiltered output signal is shown for the example with $t_{\mathrm{rise}} = 207\,\mathrm{ps}$. It can be seen that the system response includes the expected amplification of the frequencies at 2.14 GHz and 3.68 GHz caused by the resonances in Z_{21}. In the time domain it is clearly visible that the distortion of the output voltage increases the shorter the rise time of the input signal is. If these output voltages are scaled with $R_{\mathrm{shunt}} = 83.3\,\mathrm{m\Omega}$, a significant measurement error would occur. Therefore, the calculated output voltages are filtered with the previously designed FIR low-pass filter. This results in a reconstruction of the input signal with a very accurate match for all examples. The only remaining artifact is a minor dip in the signal before the actual slope. The rise times of the reconstructed signals match those of the input signals except for a few picoseconds.

The presented procedure, at which the transfer function Z_{21} is compensated by a digital filter, can be extended as desired. The *MATLAB* function *yulewalk*, which applies the *Yule-Walker* algorithm, can be used to approximate a filter with a arbitrary transfer function [143]. If the transfer function of the entire measuring path is known exactly, a filter can be designed of which the transfer function is the inverse ${Z_{21}}^{-1}$. In this way, the bandwidth can be maximized and is theoretically only limited by the analog front end of the oscilloscope. A further prerequisite is that the high-frequency components of the input signal have not already been filtered out by the input impedance of the shunt. Due to this fact and the remaining measurement uncertainty in the high-frequency range of Z_{21}, the approach of the ${Z_{21}}^{-1}$ filter is not investigated further. By using a regular FIR low-pass filter a very high bandwidth of 2.17 GHz was achieved, which is sufficient for the intended application and outperforms previous measurement techniques.

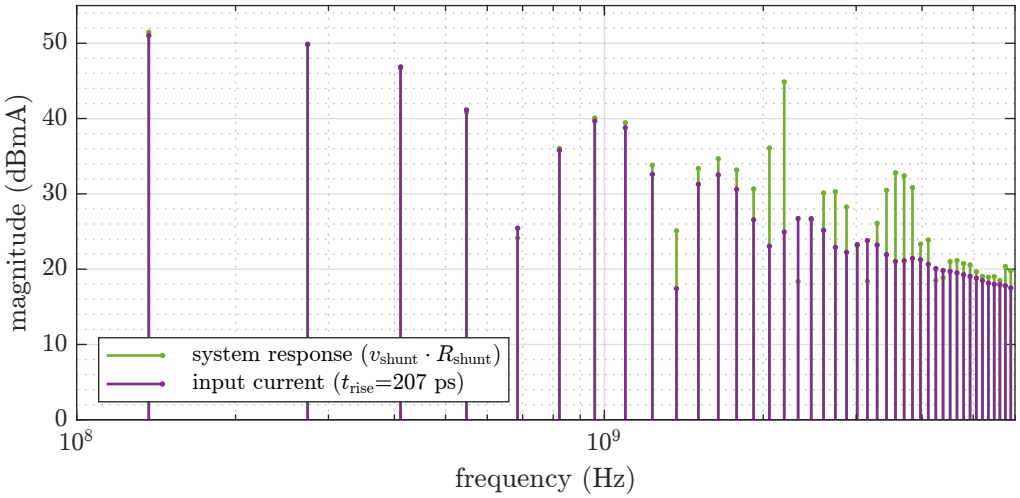

(a) Spectrum view for the case t_{rise} = 207 ps

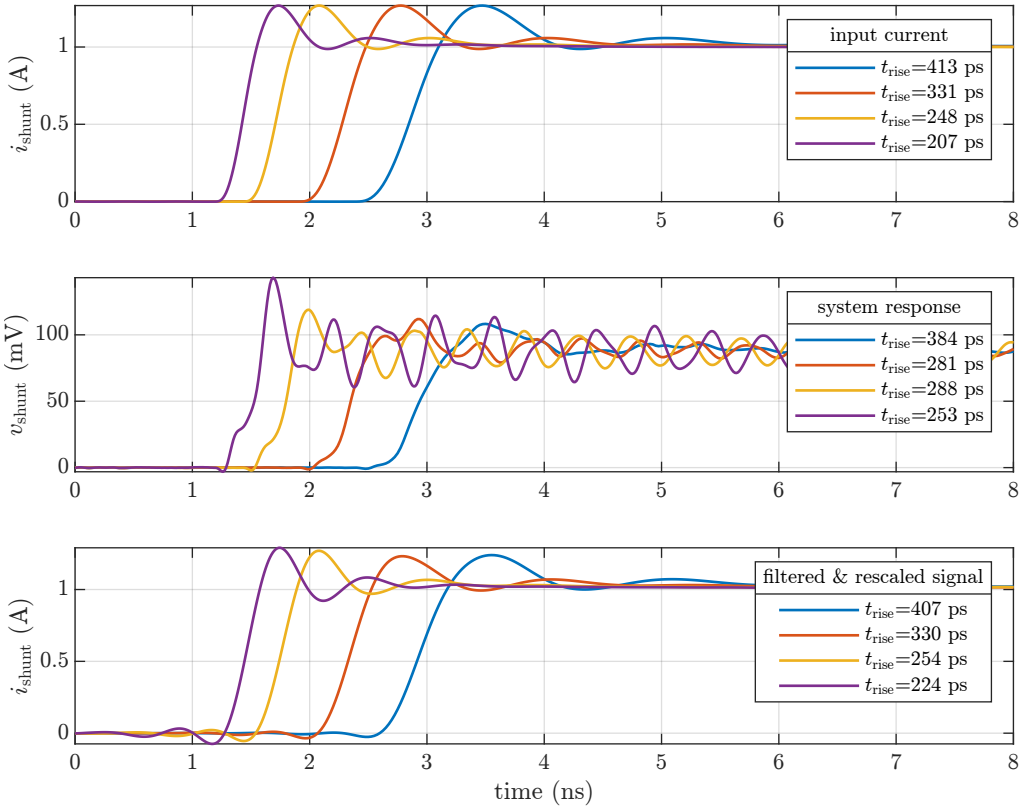

(b) Application of FIR filter in the time domain

Figure 4.16: Filtering of the response of Z_{21} for exemplary test signals with different rise times

4.4 Evaluation of the Thermal Capability

The main drawback of resistive current sensing is the thermal stress on the component, as the ohmic losses cause the resistors to heat up. This can lead to an increase in resistance and, in the worst case, damage the shunt resistor or other components. The thin-film resistors in the *0402* package used in the introduced design have a rated power of P_N = 62.5 mW each, which results in a very low nominal current of only 250 mA [134]. Due to the parallel connection of 12 resistors and very short pulse widths in DPTs, this nominal current can be exceeded significantly. To be able to estimate the maximum possible pulsed current, some fundamental considerations are presented in this section. Table 4.4 lists the required parameters for calculating the maximum thermal capability.

In addition to the rated power P_N, the manufacturer specifies a maximum overload voltage V_{max} in the data sheet [144]. This value describes the voltage withstand capability of the component which is exceeded at a current of I_{max} (see Eq. (4.15)).

$$I_{max} = \frac{V_{max}}{R_{shunt}} = 600\,\mathrm{A} \tag{4.15}$$

However, this value does not take into account the thermal limit of the component, which depends on the heating of the resistive element. The data sheet of a similar thin-film resistor gives a maximum allowable film temperature of T_{max} = 125 °C [145]. At ambient temperature of T_{amb} = 25 °C, this corresponds to a maximum allowable temperature rise of ΔT_{max} = 100 K. To relate this heating to the energy dissipated, the thermal capacity is evaluated. The resistive element is made of NiCr, which is an alloy of nickel and chromium. The specific heat capacities of these alloys vary between c_{NiCr} = 380 J/kg K ... 500 J/kg K [146]. The lower value is used in this study. The mass of the resistive film is m_{NiCr} = 4.38 µg according material declaration sheet provided by the manufacturer [147]. Since 12 resistors are in connected in parallel, the total mass of NiCr needs to be multiplied by 12 and therefore is 52.6 µg. With these values the energy E_{max} can be calculated that should

Table 4.4: Relevant parameters for calculating the maximum thermal capability

description	symbol	value
nominal power of *0402* package	P_N	62.5 mW
maximum overload voltage	V_{max}	50 V
total shunt resistance	R_{shunt}	83.3 mΩ
maximum film temperature	T_{max}	125 °C
ambient temperature	T_{amb}	25 °C
mass of NiCr (per resistor)	m_{NiCr}	4.38 µg
specific heat capacity of NiCr	c_{NiCr}	380 J/kg K ... 500 J/kg K
temperature coefficient of resistance (TCR)	α_R	2 ppm ... 50 ppm

not exceed the temperature rise $\Delta T_{\max}$ (see Eq. (4.16)). This calculation assumes that the thermal time constants within the package are so long that no thermal conduction occurs during the pulse and that all the energy is stored in the NiCr layer. This calculation also assumes that the total current is evenly distributed among all 12 resistors.

$$\Delta T = \frac{E_{\text{shunt}}}{12 \cdot m_{\text{NiCr}} \cdot c_{\text{NiCr}}} \Leftrightarrow E_{\max} = \Delta T_{\max} \cdot 12 \cdot m_{\text{NiCr}} \cdot c_{\text{NiCr}} = 2.0\,\text{mJ} \tag{4.16}$$

The theoretical value of $E_{\max} = 2\,\text{mJ}$ is relatively low at first glance and equals only 0.1 % of the energy rating of the commercial coaxial shunt *SDN-414-10* which has a similar resistance of 100 mΩ (see Table 4.1). For the application in the DPT the value $E_{\max}$ is less informative than the information which current profiles are allowed without damaging the component. The current i_{ds} in the DPT can be approximated by a ramp profile, which reaches the current I_{sw} after a duration t_{ramp} (4.17). The interval between the first and second pulse does not need to be modeled, since no current flows through the shunt resistor during this time, and the current level at turn-off of the DUT corresponds to the current level at turn-on in an ideal case. The energy dissipated in the shunt resistor can be calculated by the integral shown in Eq. (4.18). Rearranging this equation leads to Eq. (4.19), which gives the maximum allowed pulse duration t_{ramp} for a given amplitude I_{sw}.

$$i_{\text{ds}}(t) = \frac{I_{\text{sw}}}{t_{\text{ramp}}} \cdot t \tag{4.17}$$

$$E_{\text{shunt}}(t) = \int_0^t R_{\text{shunt}} \cdot i_{\text{ds}}(t)^2 \,\mathrm{d}t = \frac{R_{\text{shunt}} \cdot {I_{\text{sw}}}^2}{3 \cdot {t_{\text{ramp}}}^2} \cdot t^3 \tag{4.18}$$

$$\Leftrightarrow t_{\text{ramp}} = \frac{3 \cdot E_{\max}}{R_{\text{shunt}} \cdot {I_{\text{sw}}}^2} \tag{4.19}$$

With Eq. (4.19) and Eq. (4.17) different current profiles can be calculated with an energy dissipation of $E_{\max}$. Figure 4.17 shows several possible scenarios for a shunt with $R_{\text{shunt}} = 83.3\,\text{m}\Omega$. The higher the amplitude I_{sw}, the faster $T_{\max}$ is reached. The green dashed line marks the boundary of the safe operating area (SOA). DPTs with high currents require a steep $\mathrm{d}i/\mathrm{d}t$, which in turn requires a small load inductance L_{load} (see Section 3.1.2). For example, the current $I_{\text{sw}} = 100\,\text{A}$ requires a gradient of at least $\mathrm{d}i/\mathrm{d}t = 13.9\,\text{A}/\mu\text{s}$, which is a realistic value for a DPT with WBG semiconductor devices. Alternatively, it is also possible to increase the current capability by using resistors with a lower resistance value or using resistors in a larger package. However, both measures would result in a reduction of the measurement bandwidth and must be decided individually [125]. Another aspect that must be taken into account in practice is the maximum permissible voltage at the coaxial connector. The 50 Ω input of an oscilloscope usually has a voltage rating of 5 V, which for the case $R_{\text{shunt}} = 83.3\,\text{m}\Omega$ is reached at 60 A. A simple method to extend this range would be using an additional series resistor forming a voltage divider.

The calculations performed did not take into account the increasing resistance due to the

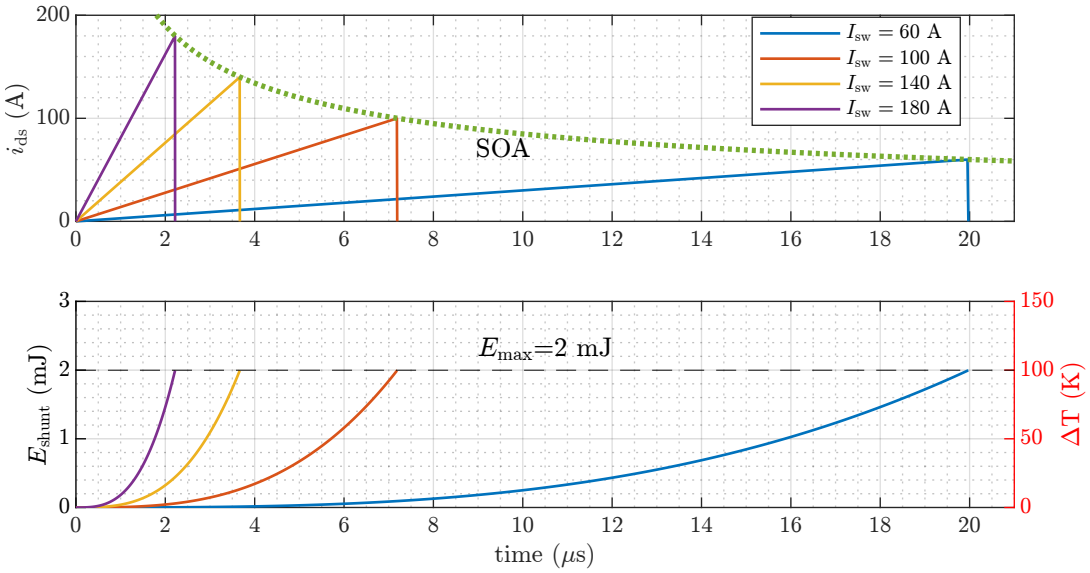

Figure 4.17: Exemplary current profiles and corresponding energy dissipation that do not exceed the maximum temperature limit (R_{shunt} =83.3 mΩ)

increase in temperature. To estimate this effect, the specific temperature coefficient of resistance (TCR) from the data sheet is used, which in the worst case corresponds to $\alpha_{\text{R}} = 50\,\text{ppm}$ [144]. According to Eq. (4.20), the resistance will rise by 0.5 %, which is within the manufacturing tolerance of the selected thin-film resistors and therefore does not have a significant influence on the results.

$$\Delta R_{max} = \alpha_{\text{R}} \cdot \Delta T_{max} \cdot R_{\text{shunt}} = 0.5\,\% \cdot R_{\text{shunt}} = 0.417\,\text{m}\Omega \tag{4.20}$$

The last consideration for the thermal capability refers to the minimum repetition period for a series of DPTs or multi-pulse applications. The minimum pulse period $t_{\text{period,min}}$ is estimated from the nominal power P_{N} and the maximum acceptable energy E_{max}. From Eq. (4.21) it follows that a pulse may occur every 2.67 ms. It should be noted that the power dissipation of the resistors may be reduced because they are located underneath the coaxial connector and the cooling through convection and radiation may be reduced. However, in a typical characterization setup, sufficient time can be provided between pulses so that this limit is not restrictive.

$$t_{\text{period,min}} > \frac{E_{\text{max}}}{P_{\text{N}}} = 2.67\,\text{ms} \tag{4.21}$$

4.5 Further Development

The presented design for a radial shunt resistor already shows very good performance in terms of bandwidth, parasitic inductance and thermal capability. The design still offers further potential for improvement, which is discussed in this section. Section 4.5.1 describes how the frequency response can be improved via a compensation network. Finally, Section 4.5.2 presents an assembly technique that can be used for further development.

4.5.1 Implementation of a Compensation Network

The measurements carried out in Section 4.3.1 have shown that the magnitude of the transfer function Z_{21} begins to increase strongly after the cutoff frequency is reached. The reason for this is the parasitic inductance of the shunt. Since high-frequency components in the input signal are excessively amplified, this leads to distortion in the output signal. To compensate for this characteristic, a method was introduced in Section 4.3.3, which attenuates these frequency components with a digital filter in post-processing. An alternative is to address this problem in hardware by implementing a compensation network [120]. In this section, two approaches for compensation networks are presented and evaluated.

The concepts from [118], [121] compensate the inductive component of the transfer function by a discrete RC low-pass filter. It has been shown that the construction of such a filter is impeded by the parasitics of the discrete components. Nevertheless, promising results were achieved in the frequency range up to 1 GHz. Figure 4.18a shows the structure of the resulting measurement system. An alternative to RC low-pass filters is presented in [148]. The transfer function of a shunt resistor is enhanced by a differential LR low-pass filter. An amplifier stage is added to the circuit to increase the CMRR and provide a defined 50 Ω output. In [119] this concept was tested successfully in DPTs with bandwidth of almost 1.6 GHz. Figure 4.18b shows the structure of the resulting measurement system.

First, the compensation network is designed as an RC low-pass filter which is connected in parallel to R_{shunt} (see Fig. 4.18a). As component values $R_1 = 10\,\Omega$ and $C_1 = 12\,\mathrm{pF}$ are chosen so that the cutoff frequency of the low-pass filter according to Eq. (4.22) corresponds to the cutoff frequency of the shunt transfer function Z_{21}.

$$f_{\mathrm{c}} = \frac{1}{2\pi \cdot R_1 C_1} = 1.33\,\mathrm{GHz} \tag{4.22}$$

Adding the series resistance R_1 changes the dc gain of the transfer function, since R_1 forms a voltage divider with the termination resistance $R_{\mathrm{T}} = 50\,\Omega$ of the oscilloscope. The new factor can be determined with Eq. (4.23) and is 69.3 mΩ. The modified value for the dc

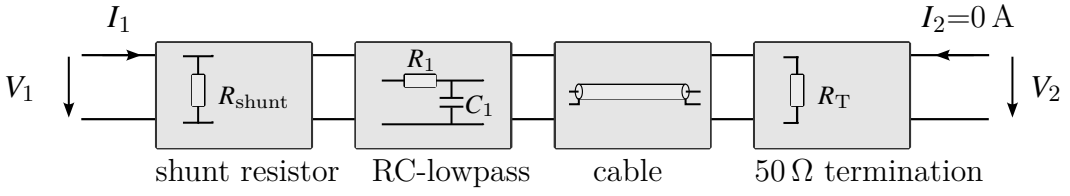

(a) RC low-pass filter

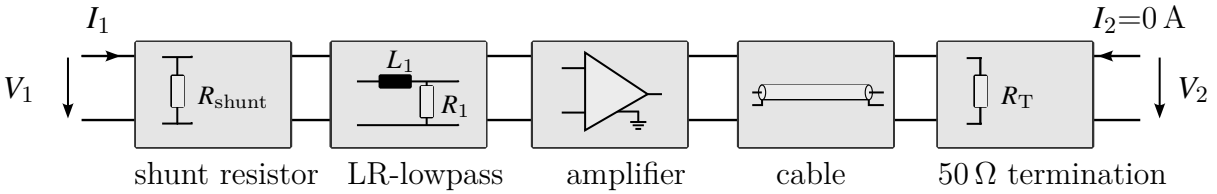

(b) LR low-pass filter and operational amplifier

Figure 4.18: Measurement system with added compensation network

gain means that the limit for the cutoff frequency of the whole system changes as well, where the new 3 dB impedance in this case is $69.3\,\text{m}\Omega \cdot 10^{\frac{3}{20}} = 98\,\text{m}\Omega$.

$$V_2 = V_1 \cdot \frac{R_\text{T}}{R_\text{T} + R_1} \approx I_1 \cdot R_\text{shunt} \cdot \frac{R_\text{T}}{R_\text{T} + R_1} = I_1 \cdot 69.4\,\text{m}\Omega \tag{4.23}$$

Before evaluating the effect of the RC low-pass filter, another option is considered, which is a LR low-pass filter. This filter is constructed according to Fig. 4.18b and is terminated with a high-impedance operational amplifier. The component values chosen are $R_1 = 75\,\Omega$ and $L_1 = 10\,\text{nH}$, resulting in a cutoff frequency of $f_\text{c} = 1.19\,\text{GHz}$ as calculated by Eq. (4.24).

$$f_\text{c} = \frac{R_1}{2\pi \cdot L_1} = 1.19\,\text{GHz} \tag{4.24}$$

As shown in Section 4.3.2, the total transfer function of any system can be calculated by concatenating individual T-parameter matrices. This method is applied to the two compensation networks so that the resulting total transfer functions Z_{21} can be analyzed. The measured S-parameters from Section 4.3.1 are used as a reference. Figure 4.19 shows the transfer function for the case of the RC low-pass filter and RL low-pass filter. The yellow colored corridor takes into account the ±3 dB deviation for the special case of the RC low-pass filter. It is observed that in both cases the compensation networks increase the 3 dB cutoff frequency. The RC compensation network achieves a bandwidth of 1.94 GHz, while the LR compensation network achieves a bandwidth of 1.72 GHz. At the resonance point, damping is not strong enough in either case, resulting in distortion with input signals that have very short rise times. It should be noted that the amplifier characteristics were not included in the calculation and likely have additional filtering characteristics. Additionally, the calculations do not include the influence of parasitic elements. The phase response of the RC low-pass filter shows a deviation of more than −90° for frequency components > 1 GHz, which is caused by the capacitance. The use of

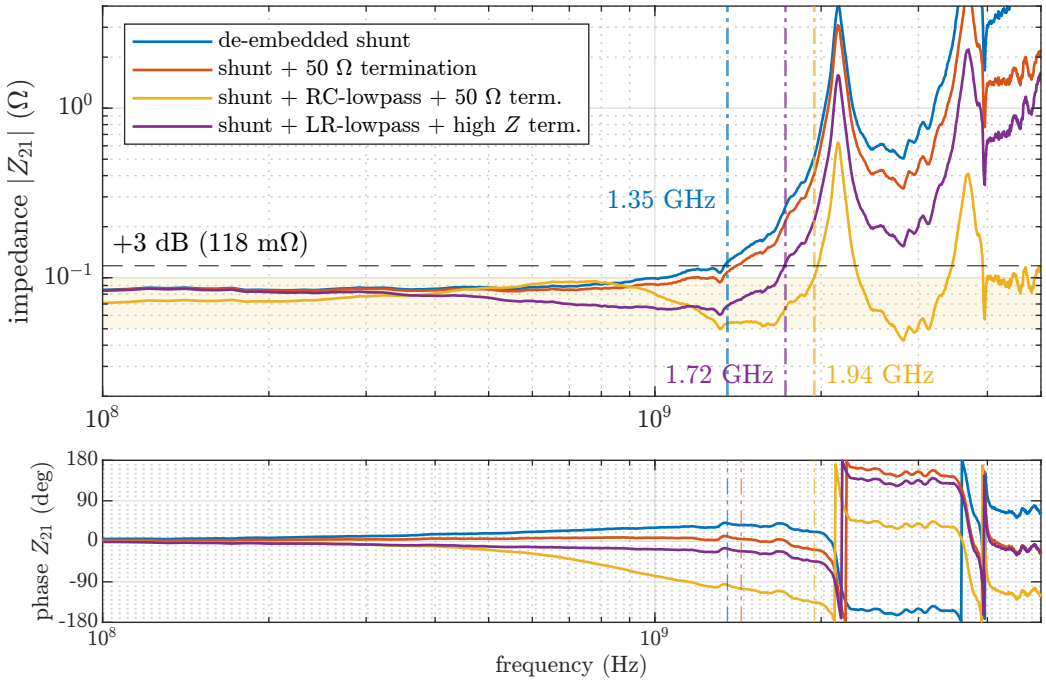

Figure 4.19: Bode diagram of Z_{21} including RC and LR compensation networks

a first-order RC low-pass filter as a compensation network is therefore not recommended without taking further correction for the phase. The LR low-pass filter seems more suitable, as the phase shows a very flat curve up to approximately 2 GHz. The disadvantage of the LR compensation network is the significantly more complex structure with analog electronics, since a direct 50 Ω termination of the LR filter is not feasible. Overall, no better performance was achieved with both tested approaches than with the digital FIR filter designed in Section 4.3.3. This achieved a bandwidth of 2.16 GHz without requiring any additional hardware.

4.5.2 Improvement of Assembly Technology

Another possible improvement is to replace the discrete resistors with a continuous surface. One way to achieve this goal is the use of technologies for implementing PCB-embedded resistors. Substrates such as *Ohmega* or *TCR*, which are distributed by *Quantic Electronics*, consist of a copper foil with an attached resistive layer (see Fig. 4.20a) [149], [150]. The resistive layer is made of NiCr or nickel-phosphorus (Ni-P) with a thickness in the range 100 nm ... 400 nm. Customized structures can be shaped by etching and laser trimming. These structures are in direct contact with the copper and are therefore perfectly connected in terms of both thermal and inductive behavior.

In [151] the design for a circular resistor with this technology is presented. Figure 4.20b shows the geometry which is defined by the inner radius r_1 and the outer radius r_2. The

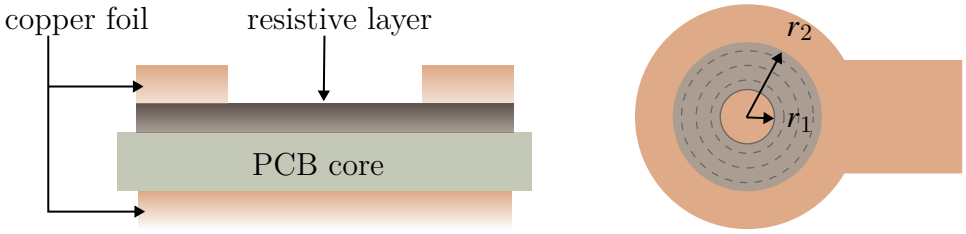

(a) Cross section of PCB stack with embedded resistive layer

(b) Geometry of a circular resistor

Figure 4.20: Design of a PCB-embedded resistor

resistance value R_{circ} can be calculated using Eq. (4.25). An infinitesimal element with the length dr and the width $2\pi r$ is integrated from the inner to the outer radius. the parameter R_{sheet} describes the sheet resistance of the resistive layer, whereas the lowest available sheet resistance of $R_{\text{sheet}} = 10\,\Omega/\text{sq}$ is selected. To place the resistor under the previously used coaxial connector, the outer radius is set to its largest possible value $r_2 = 2.0\,\text{mm}$. From equation Eq. (4.25) follows that a circular resistor with $R_{\text{shunt}} = 83.3\,\text{m}\Omega$ could be realized with $r_2 = 2\,\text{mm}$ and $r_1 = 1.89\,\text{mm}$.

$$R_{\text{circ}} = \int_{r_1}^{r_2} R_{\text{sheet}} \cdot \frac{\text{d}r}{2\pi r} = \frac{R_{\text{sheet}}}{2\pi} \cdot \ln\left(\frac{r_2}{r_1}\right) \tag{4.25}$$

The circular resistor is particularly suitable as a stand-alone component that needs to be connected to the DUT via external contacts, since it is expensive to integrate a resistive layer into each PCB to be measured. Due to the high complexity in terms of manufacturing and material supply, the embedded shunt approach was not pursued further in this work.

4.6 Conclusion

In this chapter an advanced design for a resistive current sensor was presented and analyzed. First, existing concepts were evaluated, and it was found that shunts with discrete SMD resistors are better suited for characterizing WBG semiconductor devices than conventional coaxial shunts. The design presented is based on a circular arrangement of thin-film resistors in a *0402* package, which are placed directly underneath a SMA-type coaxial connector. Using FEM, a very low parasitic inductance of 84.1 pF was established. The transfer function of the current sensor was characterized by measurements with a VNA. In combination with a matched FIR filter, a very high bandwidth of 2.17 GHz was achieved. The drawback of resistive current measurement is the thermal stress on the components. By means of analytical calculations, a SOA was defined, which enables DPTs of up to 100 A. Finally, possibilities for improvements were presented, which include the implementation of a compensation network and an embedded assembly technique. The concept of the radial SMD shunt is validated in DPTs with WBG devices in Chapter 6.

5 Design of an Advanced Inductive Current Sensor

This chapter presents the design of an advanced inductive current sensor. First, an overview of existing concepts for inductive current sensors is given in Section 5.1. This is followed by the presentation of a novel design in Section 5.2, which is a planar pick-up coil that is embedded into a PCB. After optimizing the geometry, the design is experimentally evaluated in Section 5.3 and a bandwidth of 2.33 GHz is measured. A conclusion about the most important findings is given in Section 5.4.

5.1 Evaluation of Existing Concepts

Section 2.2.3 has given a brief overview of various state-of-the-art solutions for current measurement in DPTs with WBG semiconductor devices. It was shown that the available commercial solutions do not meet the requirements for measuring fast switching transients. Conventional Rogowski coils achieve bandwidths of up to 50 MHz [152] and are therefore not suitable for measuring fast transients in the nanosecond range, as shown in Chapter 3. Current clamps achieve bandwidths of up to 120 MHz and also enable the measurement of dc currents [153]. However, current clamps are designed for the measurement of cable-carried currents. Therefore, the measurement of device currents such as the drain-source current i_{ds} is only possible with additional effort [39]. The same applies to closed-core current transformers, which achieve bandwidths of up to 250 MHz, but are also not suitable for measuring i_{ds} due to their size [154]. As with the resistive current measurement introduced in Chapter 4, multiple innovative concepts for WBG semiconductor devices have been developed in recent years.

An early innovative solution for the characterization of WBG devices was presented in [158]. The sensor developed at *Fraunhofer IZM* is based on a cylindrical coil that is inserted into an omega-shaped tube that carries the current to be measured (see Fig. 5.1a). The parasitic inductance of this technique is specified as 300 pH and, depending on the configuration, bandwidths of up to 300 MHz are possible, with a limitation being the analog integrator ciruit [155]. The concept has been adapted in various works and is therefore a suitable solution if sufficient space is available on the PCB and the lower cut-off frequency is acceptable [41], [123], [159].

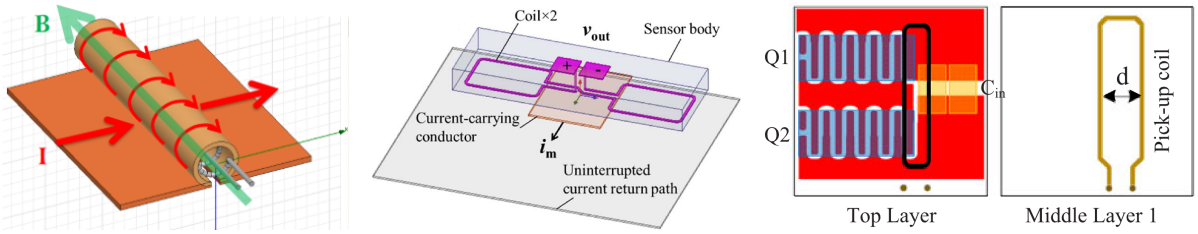

(a) *Fraunhofer IZM* current sensor [155]

(b) *Infinity Sensor* [156]

(c) Embedded pick-up coil [157]

Figure 5.1: Advanced inductive current sensors

In [156], the concept for a very compact inductive sensor known as *Infinity Sensor* was presented for the first time, which is illustrated in Fig. 5.1b. The concept from *University of Bristol* is based on two single windings, which are connected in series and pick up the magnetic field to the right and left of the conductor path to be measured. The frequency ranges from 1 MHz to 1 GHz and is therefore suitable for fast-switching WBG devices [160]. Depending on the placement of the sensor, a parasitic inductance of only 200 pH is achieved. The two series-connected windings have the advantage that external magnetic fields are canceled out to a certain extent. A challenge in the application is the post-processing of the output voltage, which consists of integration, gain correction and offset correction. Furthermore, the dc component is required to be measured externally. There are different variants of the *Infinity Sensor*, which for example are adapted to the requirements of gate-current measurement [161].

An miniaturized version for an inductive current sensor was presented in [157]. The concept specialized on LV GaN devices is shown in Fig. 5.1c and is based on a single-turn pick-up coil embedded in a multi-layer PCB. The total power loop inductance is specified as $L_{\text{loop}} = 330\,\text{pH}$ and the bandwidth is around 1 GHz. As with the *Infinity Sensor*, post-processing of the output voltage is necessary to reconstruct the current to be measured. The detailed procedure is explained in the publication and the influence of the voltage probe connected to the sensor is also taken into account. Overall, this is a promising method, but it requires a very careful and application-specific setup and has also been adapted in other works [162]. The concept may be susceptible to the coupling of external magnetic fields, as no flux-cancelling structure is used as in the *Infinity Sensor*.

In [163] another measurement technology for GaN devices is presented under the name *Piggyback Rogowski Sensor*. This is a differential coil which is embedded in a PCB and is placed as an independent component on the current-carrying conductor path, as shown in Fig. 5.2a. The parasitic inductance is given as 200 pH and a bandwidth of more than 500 MHz is specified. As with the inductive sensors presented above, post-processing of the measurement data is required. A special feature of the concept is that a shielding layer has been included to shield against external magnetic and electric fields. Although this has a negative effect on the dynamic performance of the sensor, it makes the design more robust and leads to better noise suppression.

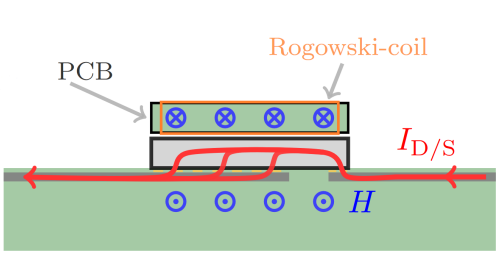

(a) *Piggyback Rogowski sensor* [163]

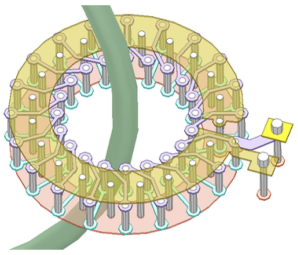

(b) *Combinational Rogowski coil* [164]

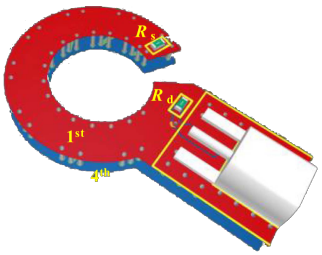

(c) *Transmission Line Rogowski Coil* [165]

Figure 5.2: Advanced inductive current sensors (continued)

The concepts presented so far were designed more for the characterization of very small GaN semiconductor devices. The method presented in [164] is intended for use with SiC modules and represents an alternative to conventional Rogowski coils. The structure shown in Fig. 5.2b corresponds to that of a traditional Rogowski coil, which is implemented in the form of a PCB. The use of shielding layers leads to improved robustness against external interference. The special feature of the concept is the associated analog signal processing circuit. This combines the differentiating and self-integrating frequency range of the coil's transfer function and gives the concept the name *Combinational Rogowski coil*. The design achieves an overall bandwidth of 300 MHz, making this solution a promising alternative to conventional Rogowski coils. In [166], a similar concept can be found, which extends a PCB-embedded Rogowski coil with an additional sensor for measuring the dc component.

Another concept was presented in [165] under the name *Transmission Line Rogowski Coil* (TL-RC). In this work, the coil is considered as a transmission line, where impedance mismatch is identified as the main limiting factor with conventional Rogowski coils. Using a matched termination resistor at both ends of the coil, a flat curve of the coil impedance is measured up to 3 GHz. The design was provided with an appropriate integrator circuit, resulting in a flat frequency response in the range 1 MHz to 1 GHz for the entire system. Due to the very small geometry for such a Rogowski coil, the application scenario of this concept is versatile. For example, the TL-RC can be used in combination with an **Ω**-shaped tube to detect the current of a conductor track, as in the concept from the *IZM Sensor* presented at the beginning in Fig. 5.1a.

It can be concluded that, as with the evaluation of the techniques for resistive current measurement in Section 4.1, there is no clear favorite for inductive current measurement. The choice of a solution depends strongly on the intended application. Besides the bandwidth and insertion impedance, the lower cut-off frequency also plays a role with inductive sensors, so that in most cases an additional measurement of the dc component is required. Compared to resistive current measurement, inductive current measurement is more susceptible to interference, as there is a risk of external coupling. In addition, the output signal must be integrated either via an analog circuit or in post-processing.

One advantage of inductive current measurement is the galvanic isolation from the DUT and the absence of ohmic losses that occur in shunt resistors. This makes this type of measurement particularly relevant for high currents.

5.2 Optimization of a Planar Pick-Up Coil

After the previous section presented different existing approaches, this section introduces a new design for an inductive current sensors. First, the basics of inductive current measurement are explained in Section 5.2.1 and a general definition of the transfer function is given. Subsequently, the design is optimized in Section 5.2.2 by varying multiple geometry and material parameters and the damping resistance. Finally, the results are evaluated in Section 5.2.3 with regard to the target variables rise time and mutual inductance and a favored design is selected.

5.2.1 Modelling of the Transfer Function

Figure 5.3a shows the principle of inductive coupling, which is the basis for all inductive current measurement techniques. The arrangement consists of a conductor that carries the current to be measured i_{sense}. Next to it is a coil which encloses part of the magnetic flux density $\vec{B}$ caused by the current i_{sense}. According to the law of induction, a change in the magnetic flux causes an induced voltage v_{ind} [167]. The electrical equivalent circuit diagram of the coil is shown in Fig. 5.3b [40], [168]. The inductive coupling of i_{sense} to the coil is expressed via the mutual inductance M. The other components are the resistance R_{s} of the windings, the series inductance L_{s} and the parasitic capacitance C_{p} between the windings. Equation (5.1) and Eq. (5.2) describe the inductive coupling between two conductors. The equations are given once in the time domain and once in the frequency domain using the Fourier transform [169]. Under no-load conditions and neglecting the parasitic capacitance C_{p}, no current flows on the secondary side and the transfer function $G(\mathrm{j}\omega)$ can be calculated according to Eq. (5.3) with the assumption $v_{\text{coil}} = v_{\text{ind}}$.

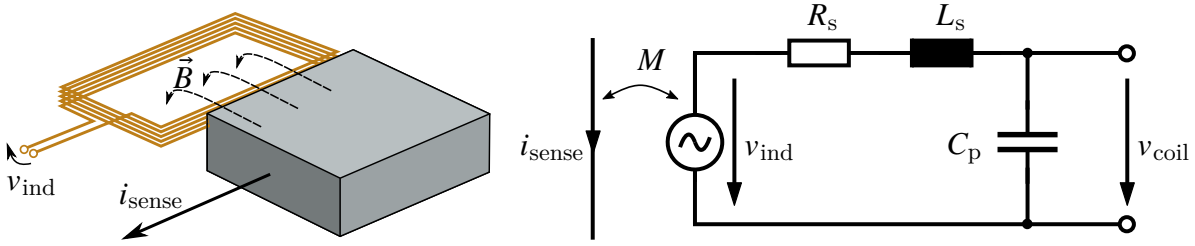

(a) Principle of inductive coupling (b) Equivalent circuit with lumped elements

Figure 5.3: Inductive coupling between coil and current carrying conductor

$$v_{\mathrm{ind}}(t) = M \cdot \frac{\mathrm{d}i_{\mathrm{sense}}(t)}{\mathrm{d}t} \circ\!\!-\!\!- \; v_{\mathrm{ind}}(\mathrm{j}\omega) = \mathrm{j}\omega M \cdot i_{\mathrm{sense}}(\mathrm{j}\omega) \tag{5.1}$$

$$i_{\mathrm{sense}} = \frac{1}{M} \cdot \int_0^t v_{\mathrm{ind}}(t)\ \mathrm{d}t \circ\!\!-\!\!- \; i_{\mathrm{sense}}(\mathrm{j}\omega) = \frac{1}{\mathrm{j}\omega M} \cdot v_{\mathrm{ind}}(\mathrm{j}\omega) \tag{5.2}$$

$$G(\mathrm{j}\omega) = \frac{v_{\mathrm{coil}}}{i_{\mathrm{sense}}} = \mathrm{j}\omega M \tag{5.3}$$

In practice, this assumption is not valid and the parasitic elements must be taken into account. As a result, a second-order system is formed with a resonant frequency caused by L_{s} and C_{p}. In the application, it is therefore common to terminate the coil on the output side with a damping resistor R_{d}, which avoids the resulting overshoot in the output voltage [170]. This resistor is dimensioned in such a way that critical damping is achieved with a damping factor $D = 1$. Equation (5.4) shows the formula for calculating R_{d} under the assumption that $R_{\mathrm{s}} \ll R_{\mathrm{d}}$ is valid.

$$R_{\mathrm{d}} = \frac{1}{2} \cdot \sqrt{\frac{L_{\mathrm{s}}}{C_{\mathrm{p}}}} \tag{5.4}$$

When simulating and measuring a coil, an assignment of the lumped elements shown in Fig. 5.3b is not always appropriate. In particular, frequency dependencies of the individual elements cannot be modeled with the simple equivalent circuit diagram. Therefore, the system, as well as the shunt resistor in Section 4.2.2, is modeled as a two-port network via the impedance matrix Z. The impedance matrix can be obtained directly from the measured or simulated S-parameters using the equations shown in Appendix A.4 without the need to know the individual component parameters. The parameter Z_{21} relevant for the transfer function is defined via Eq. (5.5).

$$Z_{21}(\mathrm{j}\omega) = \left.\frac{v_{\mathrm{coil}}(\mathrm{j}\omega)}{i_{\mathrm{sense}}(\mathrm{j}\omega)}\right|_{I_2=0\mathrm{A}} \tag{5.5}$$

To illustrate the impact of R_{d} on the transfer function, Fig. 5.5a shows the frequency-dependent sensor impedance Z_{21} for different cases. The data orginates from one of the simulations described in the following section. In the ideal case with no parasitics, a straight line with a gradient of $20\frac{\mathrm{dB}}{\mathrm{decade}}$ results, which is plotted for the example $M = 1.4\,\mathrm{nH}$ and has a constant phase of 90°. The other two curves show a response of Z_{21} with a resonance frequency of approximately 5.5 GHz. Once this is undamped and once it is damped with the damping resistor $R_{\mathrm{d}} = 200\,\Omega$.

To derive the transfer function of an inductive sensor, a further element for inductive current measurement needs to be modeled in addition to the coil and the damping resistor. Due to the differentiating behavior presented in Eq. (5.3), it is necessary to integrate the output signal v_{coil} to reconstruct the current i_{sense}. The integration can be realized in various ways [169]. The most common methods are passive integration via an RC integrator circuit, active-analog integration via an active integrator circuit using an op-

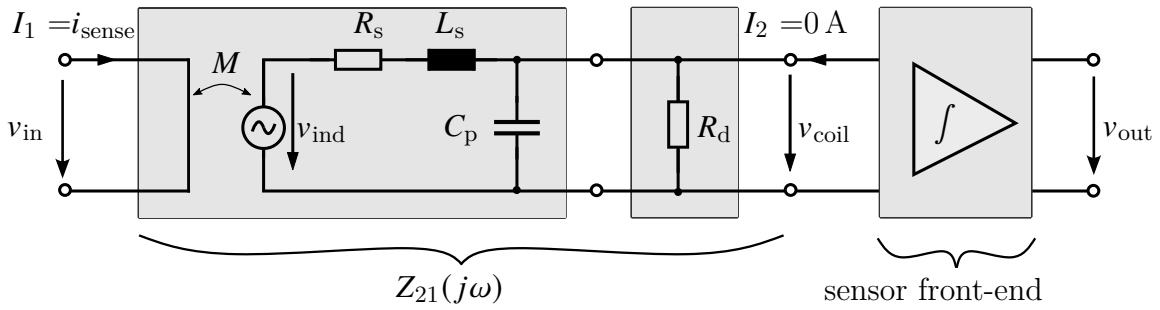

Figure 5.4: Model of the inductive measurement system consisting of coil, damping resistor and sensor front-end

amp, and digital integration via an ADC. Hybrid concepts are also possible, in which an RC circuit is combined with an op-amp integrator circuit, for example. The inductive measurement system can be represented via Fig. 5.4 [170]. The sensor described via Z_{21}, including the damping resistor, is connected to a sensor front-end that amplifies and integrates the voltage v_coil so that the output voltage v_out corresponds to the current to be measured. An ideal sensor front-end is an amplifying integrator with an infinitely high bandwidth, whose transfer function $G_\text{int}(j\omega)$ is described via Eq. (5.6). In addition to a constant gain K, an ideal front-end has an infinitely high input impedance, so that $I_2 = 0\,\text{A}$ is ensured. To obtain the total transfer function $G_\text{total}(j\omega)$, $G_\text{int}(j\omega)$ is multiplied with Z_{21} as shown in Eq. (5.7). If the condition $K = 1/M$ is fulfilled, the magnitude stays at 0 dB in the range below the cutoff frequency.

$$G_\text{int}(j\omega) = \frac{v_\text{out}}{v_\text{coil}} = \frac{K}{\text{j}\omega} \tag{5.6}$$

$$G_\text{total}(j\omega) = Z_{21}(\text{j}\omega) \cdot G_\text{int}(\text{j}\omega) = \frac{v_\text{out}}{i_\text{sense}} \cdot \frac{K}{\text{j}\omega} \tag{5.7}$$

Figure 5.5b shows the resulting total transfer functions for the case without any parasitic elements and $M = 1.4\,\text{nH}$, the undamped case ($R_\text{d} = \infty\ \Omega$) and a setup with a damping resistance of $R_\text{d} = 200\,\Omega$. To provide the relation to the physical system, the frequency in Hz is plotted on the x-axis instead of ω in $^\text{rad}/_\text{s}$. In addition, the ±3 dB corridor is plotted, which defines the cutoff frequency f_c of the measurement system. Since an ideal integration was assumed, no lower cutoff frequency is visible in the diagram. In practice, when using digital integration, this frequency depends on the vertical resolution of the ADC [171]. Low-frequency components lead to low output amplitudes, since Z_{21} is increasing with $20\frac{\text{dB}}{\text{decade}}$. Below a certain frequency, these signal components are hidden in the noise floor of the ADC and consequently cannot be integrated. A general estimate is not possible without precise specification of the hardware and the input signal. With regard to the phase response, it can be seen that the damping resistance shows a strong influence. This influence can be evaluated using the definition of group delay τ_g introduced in Section 2.3.1, which provides information about the distortion of high-frequency signal components and is relevant for deskewing.

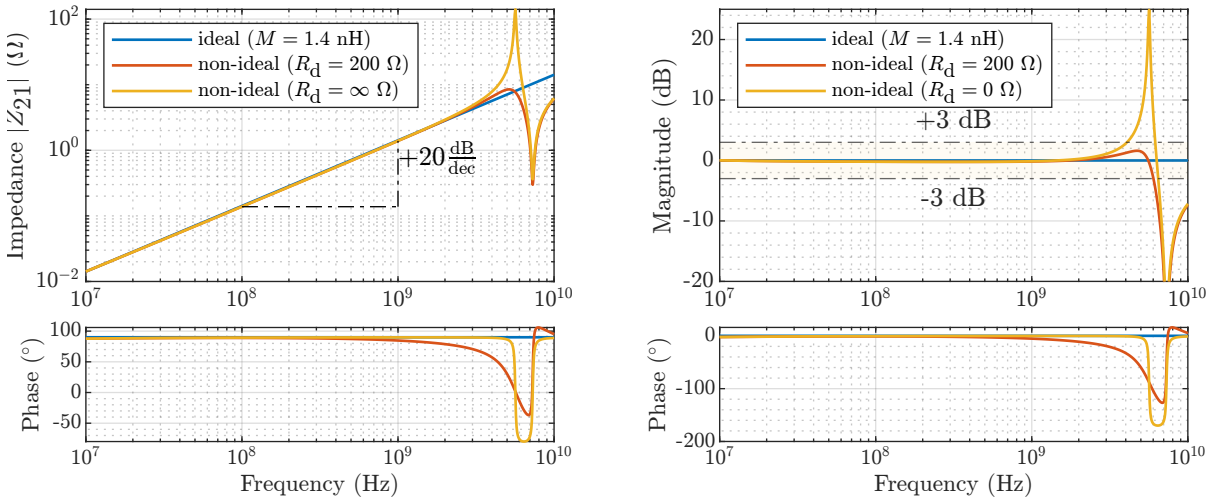

(a) Sensor impedance $Z_{21}(f)$ (b) Total transfer function $G_{\text{total}}(f)$

Figure 5.5: Bode diagrams for sensor impedance and transfer function of an examplary design

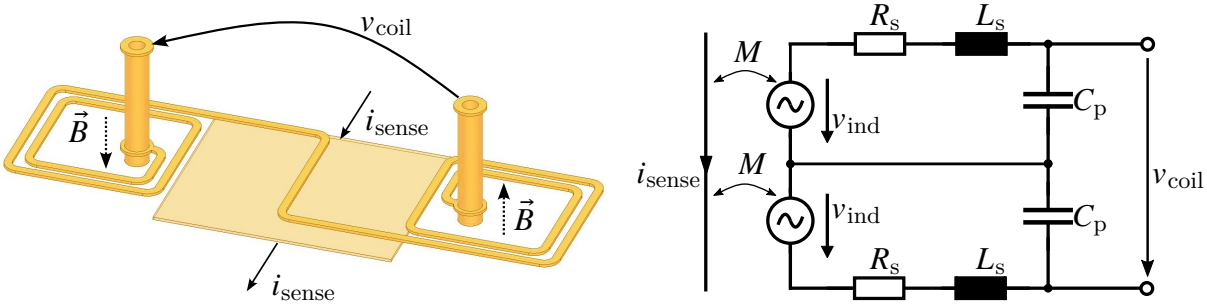

(a) 3d view of the structure (b) Equivalent circuit diagram

Figure 5.6: Concept of the planar pick-up coil

5.2.2 Setup of a Geometric Parameter Study

The inductive current sensor investigated in this work is based on the design of the *Infinity Sensor* that was presented in [156] and is shown in Fig. 5.1b. The focus of the study lies in optimizing the geometry. Additionally, the number of windings is adjusted to increase the sensor gain, as was done in the variant of the *Infinity Sensor* presented in [172] and [173]. Figure 5.6a shows the structure of the inductive current sensor to be analyzed, which will be embedded within a PCB. In the center of the arrangement is the current-carrying conductor track with the current i_{sense} to be measured. The sensor coil is located on the PCB layer above, with windings placed to the right and left of this conductor track. The magnetic flux $\vec{B}$ caused by i_{sense} passes through both windings in opposite directions. Since both windings have a different winding direction and are connected in series, the two induced voltages add up to the total voltage v_{coil}, which can be tapped

across the sensor. As discussed in [156], this approach also results in a certain suppression of the influence of external magnetic fields. If a $\vec{B}$ vector passes through both parts of the coil in the same direction, this leads to opposing induced voltages that ideally cancel out to zero. In Fig. 5.6b the equivalent circuit diagram of the configuration is shown. The sensor is modeled as a combination of two single inductively-coupled coils. Assuming that the entire sensor is symmetrical and that both sides have the same parasitic elements R_s, L_s and C_p, the equivalent circuit diagram can be simplified to the circuit shown in Fig. 5.3b.

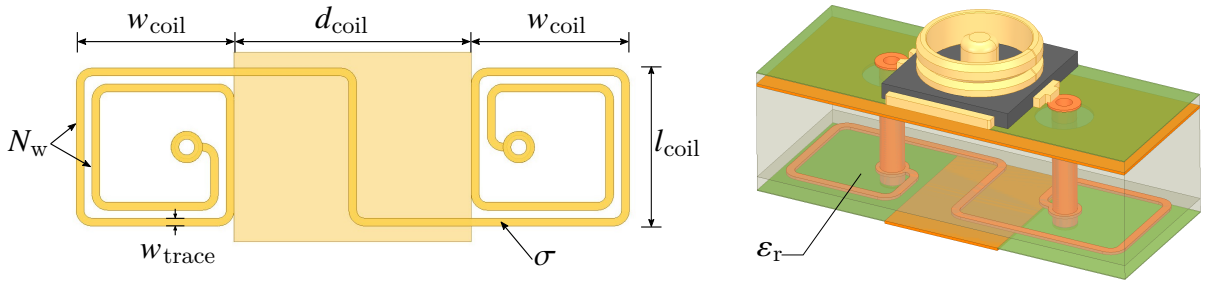

(a) Assignment of geometrical parameters

(b) View on PCB-embedded sensor

Figure 5.7: Parameteric model of the inductive sensor

Table 5.1: DoE parameter configuration for the inductive current sensor

	parameter	symbol	lower setting	upper setting
1	conductivity of winding	σ	0.058 $^{\mathrm{MS}}/_{\mathrm{m}}$	58 $^{\mathrm{MS}}/_{\mathrm{m}}$
2	length of both coils	l_coil	1.5 mm	3.0 mm
3	width of PCB trace	w_trace	100 µm	150 µm
4	width of single coil	w_coil	1.5 mm	3.0 mm
5	distance between coils	d_coil	1.5 mm	5.0 mm
6	relative permittivity of PCB	ε_r	1.0	4.0
7	number of windings per side	N_w	1	2

To adjust the geometry, the most relevant parameters are defined. Figure 5.7a shows the top view of the layout. The parameter d_coil describes the distance between the two coils, the parameter w_coil the width of a winding and l_coil the corresponding length of the winding. Other parameters are N_w, which defines the number of windings per side, and the parameter w_trace, which describes the width of the conductor track. As in Chapter 3, the DoE method is used to analyze the influence of the various design parameters. For this purpose, a lower and upper setting is defined for each parameter, which are listed in Table 5.1. In addition to the geometrical parameters, two material parameters are included in the study. These are the specific conductivity σ of the sensor winding and the relative permittivity ε_r of the dielectric material surrounding the sensor, which is shown in Fig. 5.7b. For the parameter σ, the conductivity of copper is selected for the upper value, which is $\sigma = 58\,^{\mathrm{MS}}/_{\mathrm{m}}$. The lower value corresponds to a hypothetical material that has

only 0.1 % of the conductivity of copper. With regard to ε_r, the lower value corresponds to a structure in air and the upper value to a setup in which the sensor is surrounded by a PCB material with a typical permittivity of $\varepsilon_r = 4.0$. Altogether, the design of the inductive current sensor is defined by seven parameters with two settings each, resulting in a full-factorial DoE plan with $N = 2^7 = 128$ combinations. Each of these 128 designs is simulated with the software *ANSYS Q3D Extractor* in the frequency domain. This software allows the extraction of the S-parameters and was also used in Chapter 4 to analyze the resistive current sensor.

5.2.3 Evaluation of the Simulation Results

All 128 simulated sensor variants are evaluated according to the process visualized in Fig. 5.8. The characteristics minimum rise time t_{rise} and mutual inductance M are defined as target variables. The rise time t_{rise} correlates directly with the sensor bandwidth and needs to be as low as possible so that the output signal of the sensor can also follow very short changes in the input current. The mutual inductance M, on the other hand, should be as high as possible so that the sensor delivers an output signal with a high amplitude and high SNR. As described in Section 5.2.1, inductive sensors are second-order systems that require a damping resistor R_d. This does not affect the mutual inductance M, but has a strong influence on the dynamic behavior and the resulting rise time t_{rise}. It is therefore essential for the evaluation of a sensor variant that R_d is optimally dimensioned. Since the modeling is not based on discrete components, but as a two-port network defined by the simulated S-parameters, the optimum value for R_d cannot be calculated analytically and is determined iteratively in this study.

Therefore, the basis of the evaluation is cascading the simulated S-parameters with the S-parameters of an initial damping resistor $R_d = 10\,\mathrm{M\Omega}$ that is assumed to be ideal. As in Chapter 4, cascading is performed by multiplying the chain parameters, which is achieved using the equations shown in Appendix A.4. The concatenated S-parameter matrix is then converted into Z-parameters to obtain the impedance Z_{21}, which is decisive for the transmission behavior of the sensor variant. Using the *RF Toolbox* of MATLAB, the complex transfer function Z_{21} is fitted to a rational function. This makes it possible to calculate the step response for different values of R_d, as shown in Fig. 5.9a for an exemplary sensor variant. Using the relationship shown in Eq. (5.7), the output signal of the sensor can be determined by integrating this step response. The gain K is adjusted so that the output signal reaches an amplitude of 1 A. Figure 5.9b shows the simulated output signals for different configurations of R_d. High values of R_d lead to shorter rise times of the signal, but at the same time to overshoots that are unwanted in practical use. If R_d is chosen too small, the system is overdamped and less dynamic. The relative overshoot is therefore selected as the criterion for the optimum design of R_d and the procedure described is repeated until critical damping is achieved. In the selected example, this condition is fulfilled at $R_d = 90\,\Omega$ with a rise time of $t_{rise} = 90.9\,\mathrm{ps}$.

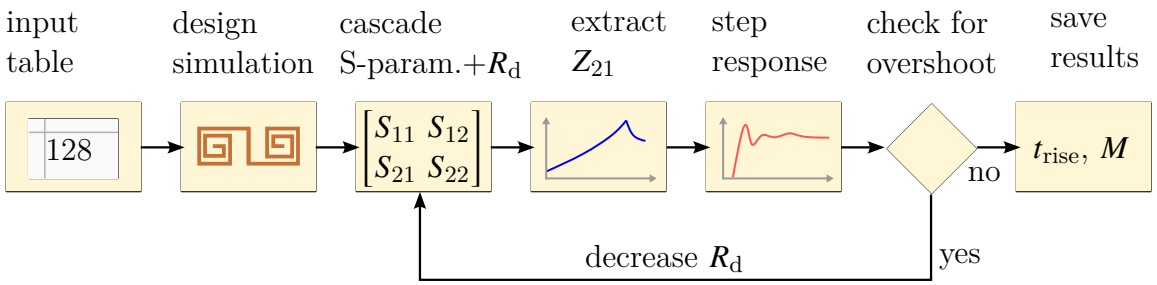

Figure 5.8: Flowchart for evaluating each sensor variant and finding optimal R_d

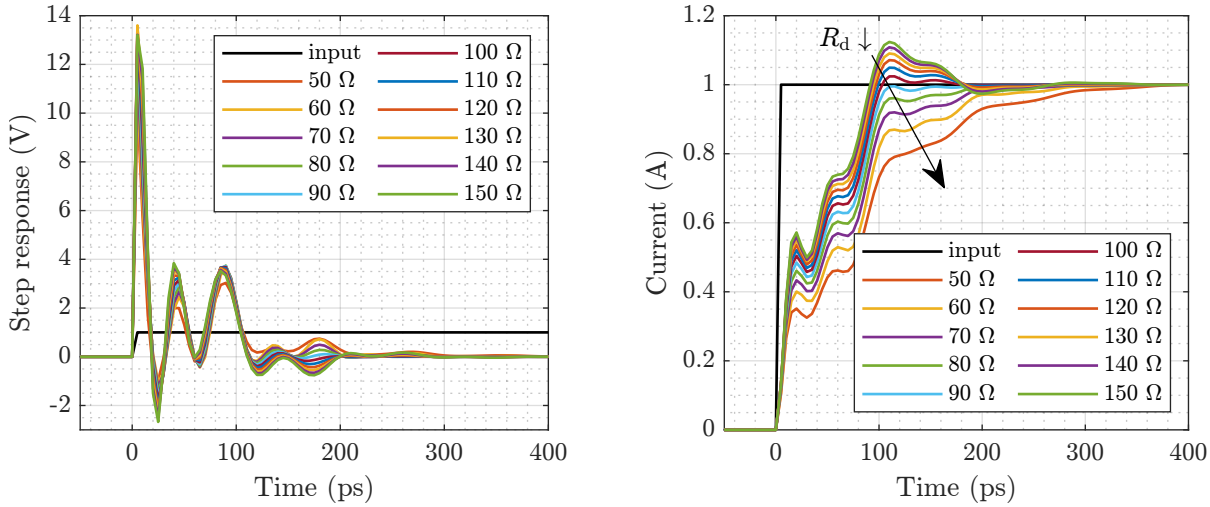

(a) Step response

(b) Integrated and rescaled step response

Figure 5.9: Evaluation of the step response of a single design with different R_d values

To enable a comparison of all 128 sensor variants, scatter diagrams are used in which the two output variables t_{rise} and M are mapped against each other (see Fig. 5.10). To evaluate the influence of the individual parameters, the data is grouped according to the setting of the respective parameter. Figure 5.10a shows the properties of all sensor variants depending on the specific conductivity σ of the winding. It was found that the variants with a regular copper coil ($\sigma = 58\,^{\mathrm{MS}}/_{\mathrm{m}}$) have on average both a shorter rise time and a higher mutual inductance than the variants with a reduced coil conductivity. A regular copper coil can therefore be used to construct the inductive sensor. With regard to the permittivity of the dielectric, Fig. 5.10b shows a clear tendency. The variants simulated in air ($\varepsilon_r = 1$) show a significantly better performance in terms of the minimum rise time t_{rise} than the variants with $\varepsilon_r = 4.0$, which is due to the increase in parasitic capacitance. However, since a regular PCB is to be used as the assembly technique of the inductive current sensor, the parameter ε_r cannot be significantly influenced in practice. The coil length l_{coil} is evaluated in Fig. 5.10c. There is a clear correlation with the mutual inductance M, which is significantly increased with a longer coil. However, a longer coil requires more space on the PCB and therefore also increases the insertion inductance of the sensor, which is why a trade-off must be made. Finally, the influence of the number of

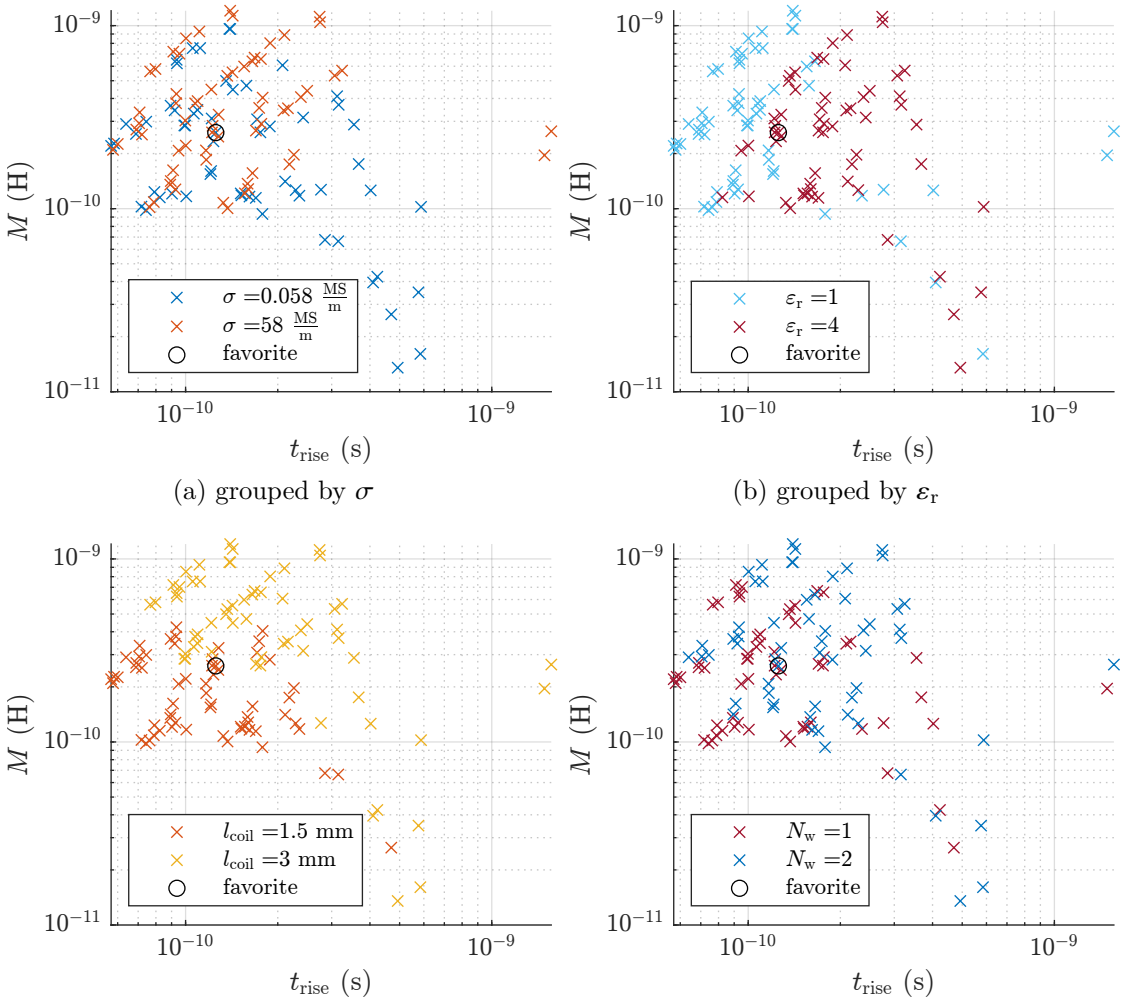

(a) grouped by σ

(b) grouped by ε_{r}

(c) grouped by l_{coil}

(d) grouped by N_{w}

Figure 5.10: Mapping of all 128 sensor variants according to the minimum rise time t_{rise} vs. mutual inductance M

turns N_{w} is examined in Fig. 5.10d. It is noticeable that the variants with a particularly high mutual inductance M always have a double winding. Otherwise, no clear pattern is recognizable. The presentation of the remaining parameters d_{coil}, w_{coil} and w_{trace} can be found in Fig. A.4 in the appendix. The parameter d_{coil} shows both a shorter rise time t_{rise} and a higher mutual inductance M at the lower setting $d_{\mathrm{coil}} = 1.5\,\mathrm{mm}$. No significant effect was determined for the parameters w_{coil} and w_{trace} using the selected method. The analysis of cross-correlations is not considered at this point, as it requires a larger number of simulations to be meaningful.

Based on the evaluation of all 128 values for t_{rise} and M, a optimal variant was selected, which is encircled in the diagrams in Fig. 5.10. This is the variant with the lowest value for t_{rise} and the highest value M, which can be implemented with regular PCB technology. The chosen variant is defined by the parameters $w_{\mathrm{coil}} = l_{\mathrm{coil}} = d_{\mathrm{coil}} = 1.5\,\mathrm{mm}$, $w_{\mathrm{trace}} =$

100 µm and $N_w = 2$. In the simulation with copper winding and regular dielectric, this configuration achieved a mutual inductance of $M = 3.84\,\text{nH}$ and a rise time of $t_{rise} = 125\,\text{ps}$ with a damping resistor of $R_d = 133\,\Omega$. Finally, the parasitic inductance of the conductor track was extracted, which is $L_{probe} = 295\,\text{pH}$. In practice, this value depends on the design and is expected to be lower, as the return path of the current causes partial flux cancellation.

5.3 Implementation and Characterization of Prototypes

After the geometry of the inductive current sensor has been optimized by simulation, the sensor is implemented on two different PCBs. The first allows measurements in the frequency domain with a VNA and the other one allows measurements in the time domain with a current pulse generator (CPG). The boards shown in Fig. 5.11 both contain different variants, with only the optimum configuration identified in Section 5.2.3 being evaluated in the following. To enable a comparison between the single and double winding in practice, the optimum configuration is implemented with both $N_w = 1$ and $N_w = 2$. As with the measurement of the shunt in Section 4.3.1, the board for frequency-domain measurements shown in Fig. 5.11a contains SOLT calibration references. Port 1 of the PCB is contacted with the current-carrying conductor path and port 2 connects to the voltage output of the coil. Using the method described in Eq. (5.7) for integration in the frequency domain, the transfer function $G(j\omega)$ is obtained from the S-parameters converted into Z-parameters.

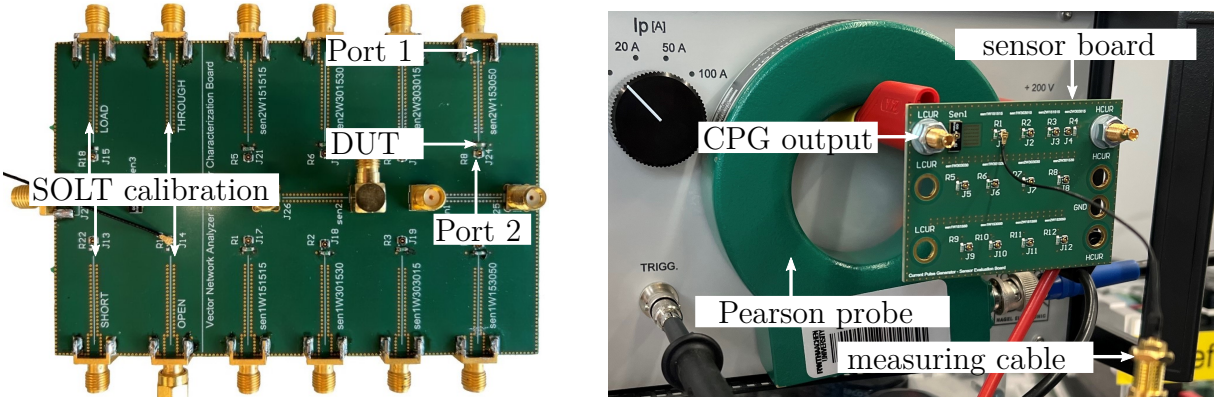

(a) Board for measurements with network analyzer

(b) Hardware setup with board for current pulse test

Figure 5.11: Experimental setups for the characterization of prototypes

Figure 5.12 shows the Bode diagrams of the measured transfer functions for the selected variant with single and double winding configuration. The measurement was repeated with different damping resistors, which shows that the bandwidth is strongly influenced

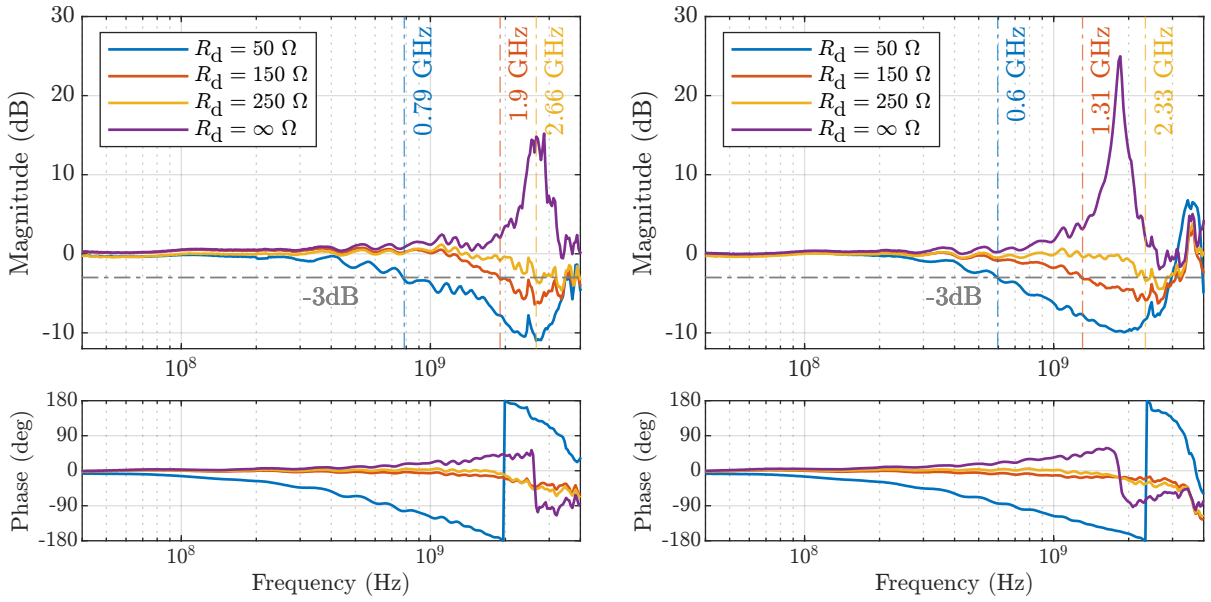

(a) $N_w = 1$ (b) $N_w = 2$

Figure 5.12: Measured transfer functions of implemented prototypes for different configurations of R_d

by R_d. The values $R_d = 50\,\Omega$ and $R_d = 150\,\Omega$ lead to overdamping in both variants, so that the maximum bandwidth cannot be utilized. For $R_d = 250\,\Omega$ the bandwidth was maximized while still suppressing the resonance. This shows that the optimum design of R_d can only be achieved in practice and that the simulated value is only suitable as a guideline. An upper cutoff frequency of $f_c = 2.66\,\text{GHz}$ was measured for the variant with $N_w = 1$ and a slightly reduced upper cutoff frequency of $f_c = 2.33\,\text{GHz}$ for the variant with $N_w = 2$. A physical interpretation could be that the variant with two windings has a higher parasitic capacitance. Both variants show a flat phase response in the frequency range below f_c.

In the second experiment, the inductive current sensor is tested in the time domain. Another board was designed for this purpose, which can be connected to a CPG, as shown in Fig. 5.11b. The CPG generates current pulses with a defined amplitude of $I_{set} = 20\,\text{A}$ and a slew rate of approximately $\mathrm{d}i/\mathrm{d}t = 1\,\text{A/ns}$. This allows the usability of the sensor to be tested in practice and the routine for post-processing to be validated. A reference measurement of the current to be measured i_{sense} is performed with a current transformer from *Pearson Electronics Inc.*, which has a bandwidth of 250 MHz and therefore provides reliable results in this specific test setup. Figure 5.13a shows the voltage v_{ind} measured at the sensor output for both tested variants. As expected, the variant with $N_w = 2$ provides a higher amplitude, which is due to the larger mutual inductance M. The input current is reconstructed according to the post-processing routine described in [156] and [160]. First, the offset voltage v_{offset} needs to be determined, with the mean value of v_{ind} being calculated in a time window of 100 ns before the switching event according to Eq. (5.8). It

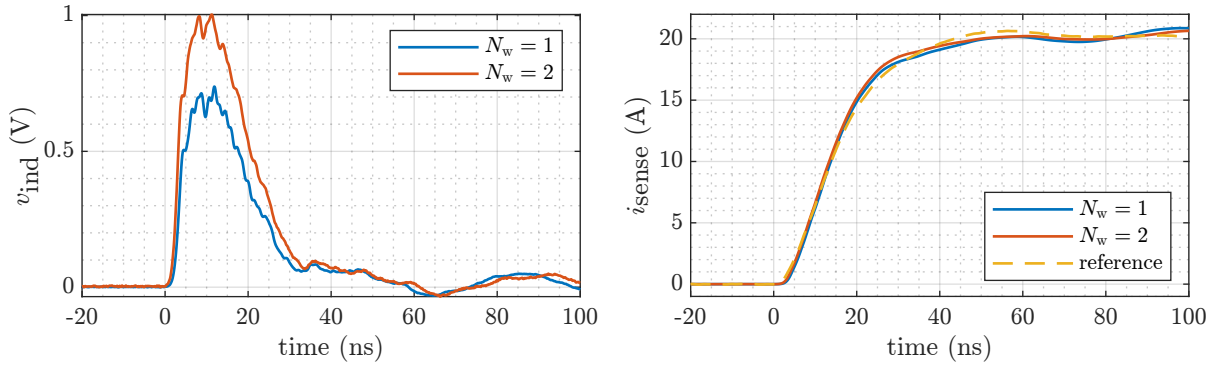

(a) Sensor output voltage

(b) Post-processed signal

Figure 5.13: Evaluation of the time domain response of the inductive sensor with a CPG for two variants with different number of windings

is noticeable that the variant with $N_{\mathrm{w}} = 2$ has a significantly larger offset voltage, which can possibly be explained by a relatively greater parasitic capacitance.

$$v_{\mathrm{offset}} = \frac{1}{100\,\mathrm{ns}} \int_{t=-100\,\mathrm{ns}}^{t=0} v_{\mathrm{ind}}(t)\ \mathrm{d}t = \begin{cases} 0.937\,\mathrm{mV} & \text{if } N_{\mathrm{w}} = 1 \\ 3.20\,\mathrm{mV} & \text{if } N_{\mathrm{w}} = 2 \end{cases} \tag{5.8}$$

Subsequently, the mutual inductance M can be calculated via Eq. (5.9). For this purpose, the integral is formed via the induced voltage v_{ind} minus the offset v_{offset} and divided by the reference amplitude I_{set}. It is noticeable that doubling N_{w} leads to an increase of the mutual inductance by 39.4 %. If offset voltage v_{offset} and mutual inductance M are identified, the current signal $i_{\mathrm{sense}}(t)$ can be reconstructed using Eq. (5.10).

$$M = \frac{1}{I_{\mathrm{set}}} \cdot \int_{t=0}^{t=100\,\mathrm{ns}} \left(v_{\mathrm{ind}}(t) - v_{\mathrm{offset}}\ \mathrm{d}t \right) = \begin{cases} 0.676\,\mathrm{nH} & \text{if } N_{\mathrm{w}} = 1 \\ 0.942\,\mathrm{nH} & \text{if } N_{\mathrm{w}} = 2 \end{cases} \tag{5.9}$$

$$i_{\mathrm{sense}}(t) = \frac{1}{M} \cdot \int_{-\infty}^{t} \left(v_{\mathrm{ind}}(t) - v_{\mathrm{offset}}\ \mathrm{d}t \right) \tag{5.10}$$

Figure 5.13b shows i_{sense} for both variants of the inductive sensor and the reference measurement via the current transformer. There is very good agreement between the signals with a measured rise time of $t_{\mathrm{rise}} = 25\,\mathrm{ns}$. In the intended application with WBG semiconductor devices, significantly shorter rise times are to be expected, but these cannot be achieved with the hardware setup used. The inductive current sensor is validated under realistic conditions in the following chapter.

5.4 Conclusion

In this chapter, an advanced design for an inductive current sensor was presented and analyzed. First, several existing concepts were evaluated and it was found that pick-up coils are preferable for the dynamic characterization of fast-switching WBG semiconductor devices, as they are very compact and achieve high bandwidths. The presented design is based on a planar pick-up coil, which is inspired by the *Infinity Sensor* and has been extended by an additional winding. A parameter study based on simulations was used to optimize the geometry of this coil. The variant with the shortest rise time and the highest mutual inductance was chosen for the assembly with a regular PCB. Subsequently, the inductive current sensor was implemented and tested both in the time and frequency domains. A high bandwidth of 2.66 GHz was experimentally validated with an parasitic inductance of approximately 295 pH. In addition, the steps required for post-processing were described, which is necessary for all inductive measurement techniques that do not include an integrator circuit. The concept of the planar pick-up coil is validated in the last chapter of this thesis in the DPT and its performance will be compared to the radial shunt resistor presented in Chapter 4.

6 Proof of Concept

In this chapter, the radial shunt resistor introduced in Chapter 4 and the inductive sensor from Chapter 5 are applied in the DPT as a proof of concept. For this purpose, a sensor evaluation board with WBG semiconductors is designed, which is presented in Section 6.1. The key element of this circuit is a half bridge with GaN HEMTs whose drain-source current i_{ds} can be measured both via the radial shunt resistor and the inductive sensor. After the switching behavior is simulated to obtain reference values for the turn-off and turn-on energies, the circuit is commissioned in Section 6.2. Section 6.3 finishes the chapter by comparing the simulation results with the results obtained from the different measurement techniques.

6.1 Design and Simulation of a Low-Inductive GaN Switching Cell

To validate the performance of the newly developed current sensors, a sensor evaluation board with a GaN half bridge was designed. To achieve fast switching transients and to be able to use both measurement techniques simultaneously, a well-planned layout is required, which is presented in Section 6.1.1. One special feature of the GaN devices used is an integrated feature to measure the current i_{ds}. This is discussed in more detail in Section 6.1.2. Finally, the simulation model and the results obtained with it are presented in Section 6.1.3.

6.1.1 Board Layout

Figure 6.1 shows the layout of the designed sensor evaluation board. The labeled elements are explained below.

Semiconductor switches The central element of the switching cell are the GaN HEMTs of type *NV6158* from the manufacturer *Navitas Semiconductor* [174]. These are connected in half bridge configuration as depicted in Fig. 6.2b ($\mathrm{S_{HS}}$ and $\mathrm{S_{LS}}$). Their rated voltage is $V_{\mathrm{DS}} = 700\,\mathrm{V}$ and the nominal current $I_{\mathrm{D}} = 12\,\mathrm{A}$, with a value of $I_{\mathrm{D,pulse}} = 24\,\mathrm{A}$ being

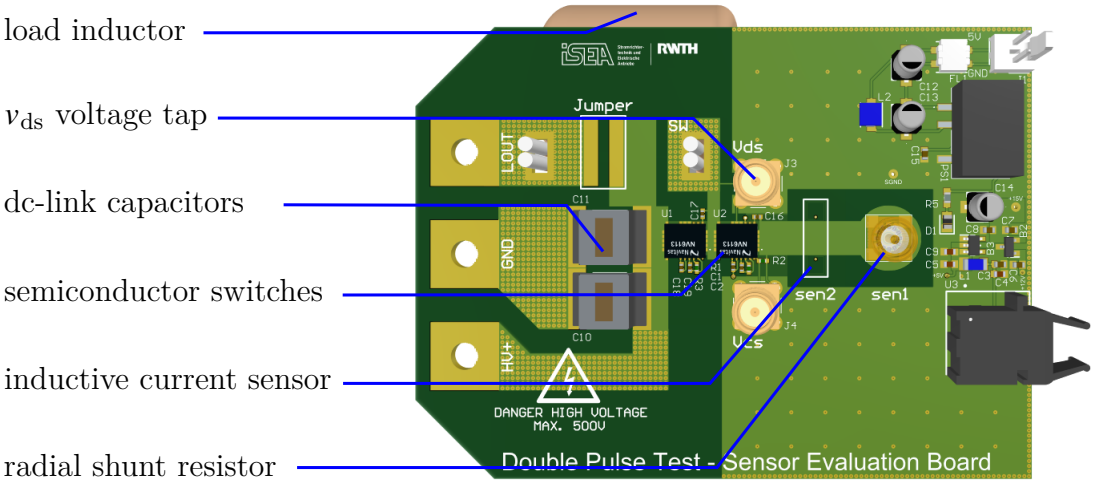

Figure 6.1: Layout of sensor evaluation board (3d view of the top layer)

specified for pulsed applications. One special feature of the selected component is an integrated driver stage. Thus, no external gate driver is required which minimizes the parasitic gate inductance. The component also has an integrated current sense feature, which is described in Section 6.1.2. The high-side switch (S_{HS}) is permanently in the turn-off state and only conducts the current in the reverse direction during the freewheeling state. The slope of the turn-on voltage transient can be controlled via an external gate resistor $R_{G,on}$. According to the recommendation in the datasheet, $R_{G,on} = 50\,\Omega$ is used. The turn-off transient is not adjustable and is set internally via a low-impedance gate resistor.

Dc-link capacitors To stabilize the dc-link voltage, two capacitors with $C_{DC} = 0.5\,\mu F$ each are used, which are multi-layer ceramic capacitors (MLCCs) from the *TDK CeraLink®* series[175]. These MLCCs are optimized for use with fast-switching power semiconductors and offer a low equivalent series inductance (ESL) and a low ESR. To save space on the board, a voltage rating of 500 V was selected, which limits the maximum operating voltage of the switching cell.

Load inductor Since the board was designed exclusively for application in the DPT, the load inductor is located directly on the backside of the PCB. The toroidal coil *HHBC24W-2R1B0065V* from *KEMET* with $L_{load} = 65\,\mu H$ was selected [176]. The used construction type has the advantage that, in contrast to a solenoid coil, the external magnetic field is reduced [18].

Radial shunt resistor To measure the drain-source current i_{ds}, the shunt resistor presented in Chapter 4 is implemented on the board. The voltage drop across the shunt

v_{shunt} is tapped via the coaxial connector of type SMA, which is connected directly to the 50 Ω input of the oscilloscope. This defines the ground potential, which is connected to the source contact of the low-side switch (S_{LS}), as shown in Fig. 6.2b.

Inductive current sensor As a further method for measuring the current i_{ds}, the inductive current sensor presented in Chapter 5 is integrated into the switching cell. It is placed in series with the shunt resistor. The voltage v_{ind} is tapped via an coaxial connector in the *MHF4* format, which is located on the backside of the PCB and has an damping resistor $R_{\text{d}} = 250\,\Omega$ connected in parallel (see Fig. 6.2a). To integrate the sensor more effectively into the low-inductive layout, the distance between the two windings was adjusted to $d_{\text{coil}} = 5\,\text{mm}$. Any other parameters have been retained and the number of windings of the implemented sensor variant is $N_{\text{w}} = 2$.

Further elements The board also contains the auxiliary power supply for the gate driver via an isolated dc-dc converter, a common mode choke (CMC) and an optical receiver that receives the logical signal s_{on} transmitted via fiber to control the low-side switch S_{LS}. To access the switching voltage v_{ds}, a coaxial connector of type SMA is located directly next to S_{LS}. To minimize the parasitic inductance L_{loop}, a 6-layer PCB is used, for which the cross-section is shown in Fig. 6.2a. The top layer (L1) contains the components of the switching cell and the radial shunt resistor. The current is returned via the first inner layer (L2), resulting in a very small current loop area, as the distance between the two layers is only 230 µm. This structure is particularly common in GaN applications [177]. The second inner layer (L3) is required to place the inductive sensor in such a way that it is as close as possible to the current-carrying conductor path. It should be noted that the magnetic field induced in the sensor is reduced by the opposing current on layer L1. This reduces the sensor gain, which must be recalibrated in the application. The inner layers L4 and L5 are unused and are connected to the ground potential of the oscilloscope. The bottom layer (L6) is used for the voltage tap of the inductive sensor and placing the damping resistor. The copper thickness on all layers is 35 µm [178].

6.1.2 Integrated Current Sensing

With GaN, there is a trend towards monolithically-integrated circuits [10]. In addition to the already described integration of a gate driver, a current sensor can also be integrated on the substrate. Possible applications are safety functions such as overcurrent protection (OCP) or closed-loop control circuits. This has the advantage that no external components are required for current measurement and potential drawbacks such as additional ohmic losses in a shunt resistor are avoided. There are various approaches for implementing a current-sensing structure, for example by integrating sense electrodes

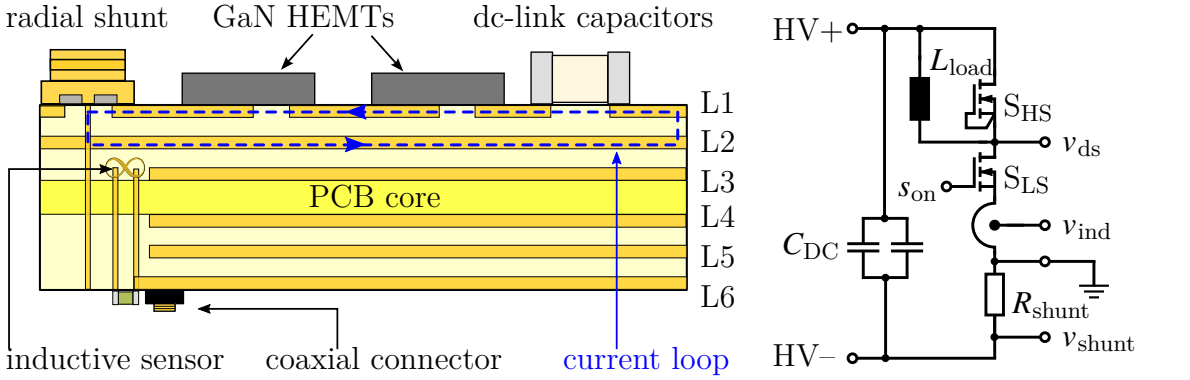

(a) Cross section of the PCB

(b) Circuit diagram of the half bridge

Figure 6.2: Structure of the sensor evaluation board

into the channel [179], using existing voltage drops within the HEMT structure [180] or integrating a magnetic pick-up coil into the footprint of the component [157].

Another approach was presented in [181] and describes an integrated current mirror. This technique uses a parallel sense FET, which has the same drain and gate contact as the main transistor, but only carries a defined fraction of the total drain current due to its reduced channel width. The advantage of this concept is that the channels of the power and the sense FET are both subject to the same temperature conditions and no additional losses are generated [182]. The current mirror technology is available in commercial devices, for example in *ICeGaN™* devices from *Cambridge GaN Devices* [183] or *GaNSense™* devices from *Navitas Semiconductors* [174]. The used device *NV6158* also offers this feature, but an external resistor R_{CS} must be connected to the source contact of the sense FET. The current $i_{ds,cs}$ through this current sense pin has a ratio of 1:4800 compared to the drain source current i_{ds}. Using this factor, R_{CS} can be dimensioned in such a way that the same voltage drop results as across the external radial shunt with $R_{shunt} = 83.3\,m\Omega$ and it follows $R_{CS} = 4800 \cdot R_{shunt} = 400\,\Omega$. To be able to evaluate the performance of the technology, the voltage across R_{CS} can be measured on the evaluation board using a coaxial connector.

Figure 6.3 shows the waveforms of the turn-off and turn-on switching events. The measurement results were generated with the setup that will be presented later in Section 6.2. When comparing the current measured via *GaNSense™* ($i_{ds,cs}$) with the current measured via the external shunt resistor ($i_{ds,shunt}$), it is noticeable that the signal $i_{ds,cs}$ reacts significantly slower and only follows the actual current i_{ds} with a certain delay. A measurement of the transients is therefore impossible and the specified bandwidth of 8 MHz is confirmed. However, the steady-state value I_{sw} immediately before the turn-off is recorded exactly. This makes the integrated current-sensing feature particularly suitable for applications in which highly dynamic detection is not necessary, such as for the control and monitoring of power electronic converters. However, in the area of highly dynamic current measurement, *GaNSense™* or similar techniques could be used as a part of an inductive

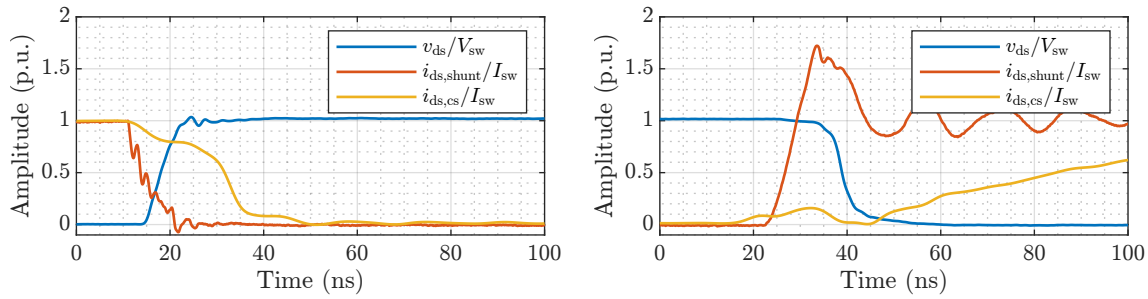

(a) turn-off (b) turn-on

Figure 6.3: Comparison of current measurement with external shunt resistor and measurement via *GaNSense™* (V_{sw} = 500 V,I_{sw} = 10 A)

current-sensing concept with a lower cutoff frequency. If no external shunt resistor is available, the dc component of the current required for calibration and reconstructing the low-frequency components can be measured in this way.

6.1.3 Simulation of the Switching Transients

To have a reference for the measurement with the shunt resistor and the measurement with the inductive sensor, the switching behavior is also investigated by means of simulation. It can be assumed that the geometry and material properties of the PCB have a non-negligible influence on the switching behavior. Therefore, the parasitic elements first need to be extracted to use them in the following circuit simulation with *LTspice*.

The parasitic elements are determined with the software *ANSYS Q3D Extractor*, which uses a combination of FEM and method of moments (MoM) solvers. The geometry shown in Fig. 6.4a is imported directly from the PCB design tool *Altium Designer*, taking into account not only the copper structure but also the dielectric materials between the layers. This allows capacitive coupling effects between the conductors to be taken into account. According to the manufacturer, the PCB core used has a relative permittivity of $\varepsilon_{r,core}$ = 4.5 and the prepregs between the individual copper layers have a relative permittivity of $\varepsilon_{r,prepreg}$ = 4.25 [178]. In addition, the solver takes into account the skin effect and the proximity effect, which leads to frequency-dependent current densities.

Each pad of the PCB relevant for the simulation was given a corresponding designator and represents a terminal as shown in Fig. 6.4a. For a pair of two terminals located on the same conductor, the software calculates the matrix RL, which represents the resistance and inductance between these two terminals [184]. in the model shown, there are a total of 10 unique conducting pairs, so that RL has the dimension 10×10. In addition, a matrix k of the same dimension is calculated, which describes the magnetic coupling between the different inductances with coupling factors. For each conductor, the entries in the

matrix CG are calculated, which contains the capacitance and conductance between the individual conductors. Since the model has a total of 4 individual conductors, CG has the dimension 4×4. The entries on the diagonal describe the capacitance in relation to the ground potential, which is defined as being at an infinite distance from the overall geometry [185]. These matrices are then used to derive the equivalent circuit of the geometry, which is based on a T-shaped equivalent circuit diagram of a transmission line and is shown in Fig. 6.4b. The complete model contains one of those equivalent circuits for each pair of terminals, which are represented by the labels T1 and T2.

Figure 6.4c shows the exported equivalent circuit diagram of the geometry, which contains the same terminal designations as Fig. 6.4a. A disadvantage of the method is that each equivalent circuit is only valid at a discrete frequency. Although the simulation can be extended to any frequency, it is not possible to model a frequency dependency in *LTspice* and other circuit simulators with discrete time steps. Hence, all entries of RL and CG are calculated for a constant frequency of 100 MHz. This means that the model is designed for a period duration of 10 ns and is therefore in a relevant order of magnitude for the simulation of switching transients. For the extraction of the power loop inductance of the entire switching cell, the model was slightly modified. Placeholder geometries were placed representing the connected components like resistors and dc-link capacitors. In this way, a closed path from LS_{drain} to LS_{source} is formed as shown in Fig. A.6 in the appendix. The inductance of this path at a frequency of 100 MHz is $L_{\mathrm{loop}} = 2.96\,\mathrm{nH}$.

In addition to the parasitic properties of the PCB, the non-ideal components must also be taken into account [74]. The used inductor has a ESR of $R_{\mathrm{s}} = 62\,\mathrm{m\Omega}$ and a specified resonant frequency of $f_0 = 8\,\mathrm{MHz}$ [176]. Using the relationship $f_0 = 1/(2\pi\sqrt{LC})$, the value of the parasitic capacitance of the coil can be calculated as $C_{\mathrm{p}} = 601\,\mathrm{pF}$. The specifications for ESR and ESL for the capacitors used can also be taken from the data sheet and equal $R_{\mathrm{s}} = 12\,\mathrm{m\Omega}$ and $L_{\mathrm{s}} = 3\,\mathrm{nH}$ [175]. It should be noted that these values are not linear and depend on both the voltage and the frequency. Furthermore, the capacitors are placed in such a way that partially flux cancellation is achieved. Since the current is returned directly underneath the component, it is assumed in the simulation that the ESL is reduced by 50 %. The manufacturer provides a behavioral model for the component *NV6158*, which is similar to the one shown in Fig. 3.2. The complete circuit model to obtain values for E_{off} and E_{on} is shown in Fig. A.5 and is based on the model of the DPT presented in chapter Chapter 3.

Figure 6.5 shows the simulated switching transients of five simulated operating points. The voltage V_{sw} is set to $V_{\mathrm{sw}} = 500\,\mathrm{V}$ and the switching current I_{sw} is varied in 4 A steps from 4 A to 20 A. It is noticeable that the turn-off transition is very fast and is completed in less than 10 ns. An exception is the turn-off transition at small current, which takes around 20 ns. The turn-on transition is subject to a uniform pattern and takes longer the greater the current I_{sw} is. It is noticeable that the slew rates $\mathrm{d}v/\mathrm{d}t$ and $\mathrm{d}i/\mathrm{d}t$ are almost constant across all operating points at turn-on. In contrast to the turn-off event, there are no significant oscillations after the turn-on and the duration varies between ranges from approximately 20 ns to 30 ns. The different speeds of turn-off and turn-on are

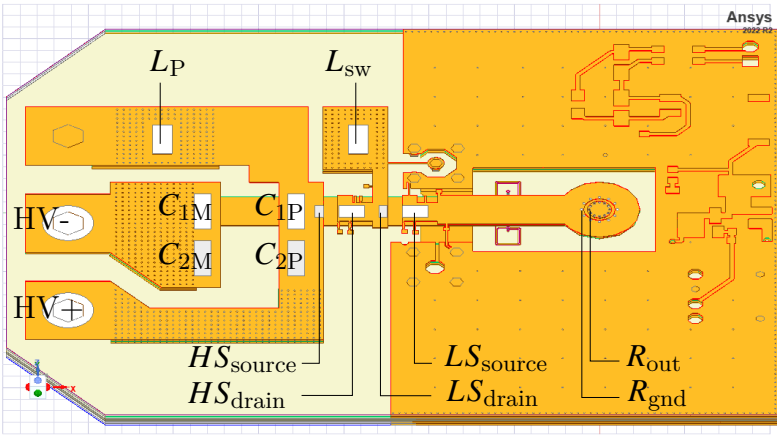

(a) PCB model with terminal definition in *ANSYS Q3D Extractor*

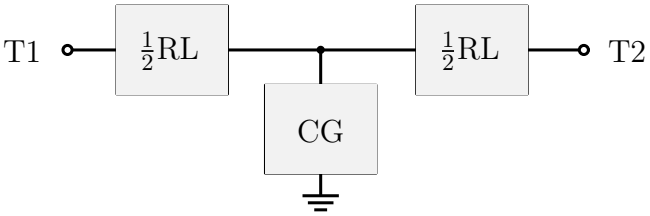

(b) Modeling of an electrical network as first-order transmission line

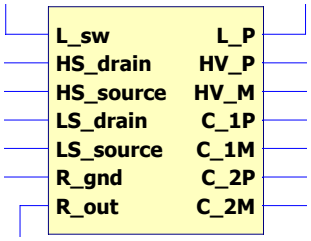

(c) Equivalent 14-terminal subcircuit in *LTspice*

Figure 6.4: Simulation and modeling of board parasitics

caused by the external gate turn-on resistance $R_{G,on} = 50\,\Omega$ and the internal gate turn-off resistance $R_{G,off} \approx 0\,\Omega$. In Appendix A.8 the same diagrams are shown for the voltage levels $V_{sw} = 300\,V$ and $V_{sw} = 400\,V$ (Fig. A.7).

Figure 6.6 shows the evaluation of the switching energy at turn-off and turn-on. Two different definitions are used to form the integral over the instantaneous power $p_{loss} = i_{ds} \cdot v_{ds}$. Firstly, the integral is formed according to the specification from *IEC 60747-8* (see Section 2.1.2) and secondly, the complete integral is calculated over the entire recorded time window. In both cases, the energies are strictly dependent on the voltage V_{sw}. With the definition according to the standard *IEC 60747-8*, the oscillation of i_{ds} and v_{ds} after turn-off is no longer taken into account as the integration stops once i_{ds} drops below 10 %. Therefore, the standardized integral for calculating E_{off} is smaller compared to the full integral. Furthermore, it is recognizable in Fig. 6.5 that the current i_{ds} falls particularly steeply at $I_{sw} = 20\,A$, resulting in the 10 % limit being reached in a very short time. Therefore, the energies according to the standard decrease for the setting $I_{sw} = 20\,A$ compared to lower settings for I_{sw}, as shown in Fig. 6.6. Using the full integral avoids these types of discontinuities.

The turn-on energy E_{on} increases continuously with increasing current I_{sw}. Since the

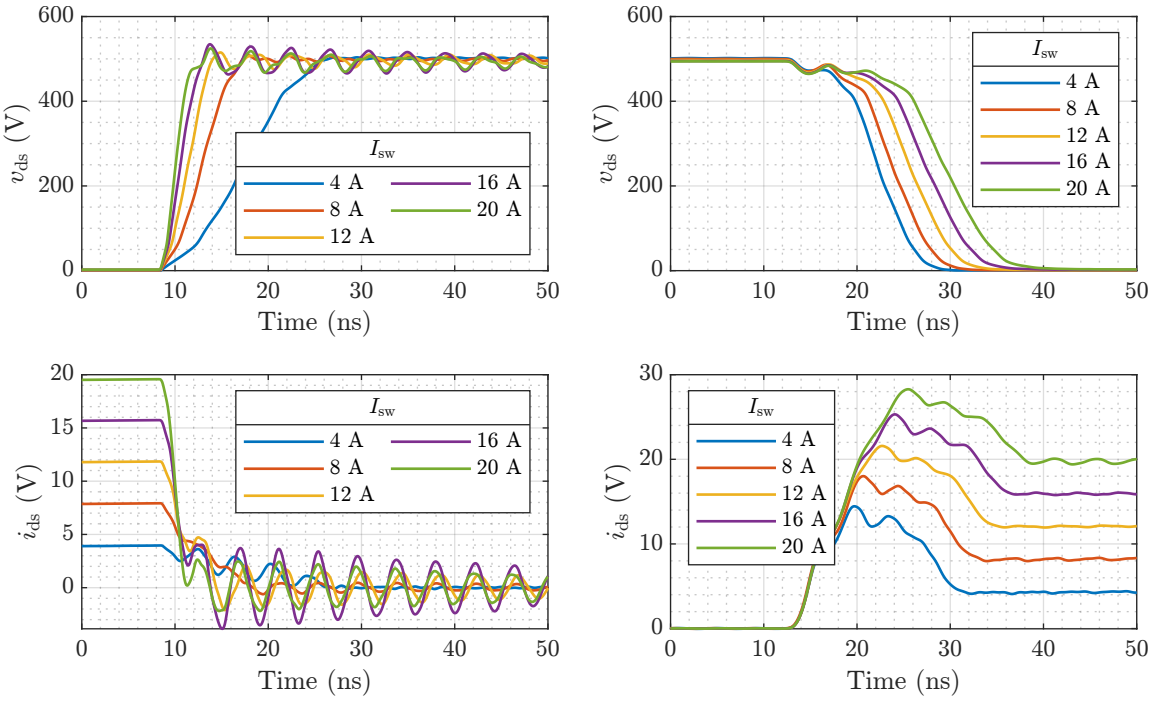

(a) turn-off (b) turn-on

Figure 6.5: Simulated switching transients for *NV6158* at different operating points (V_{sw} = 500 V, I_{sw} = 4 A ... 20 A, T_j = 25 °C)

voltage v_{ds} does not drop to 0 V after switching on but remains at $R_{DS(on)} \cdot i_{ds}$, the definition using the full integral also contains conduction losses. A significant share of E_{on} is caused by the current overshoot, which, according to the definition from the standard, is only integrated until the voltage v_{ds} has dropped to 10 %. Consequently, the full integral describes the losses caused by switching more precisely and is used in the following.

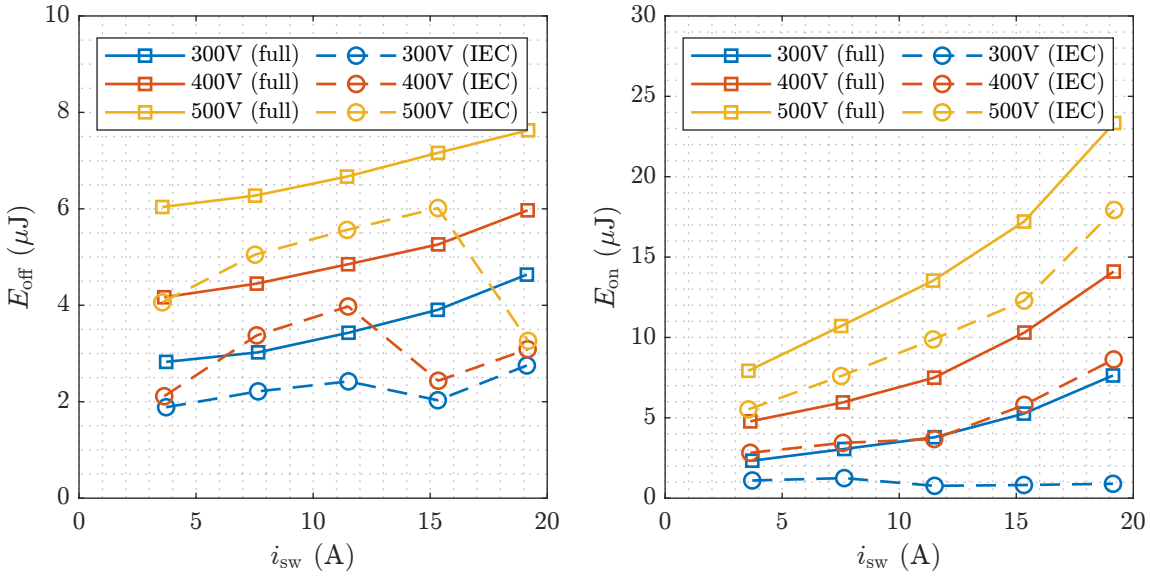

(a) turn-off (b) turn-on

Figure 6.6: Simulated switching energies for *NV6158* at 15 different operating points according to both definitions ($T_{\text{j}} = 25\,°\text{C}$)

6.2 Double-Pulse Testing

This section describes the commissioning of the previously presented sensor evaluation board. Firstly, the measurement setup is presented in Section 6.2.1 and the precautions that need to be taken for an accurate measurement are shown. The measurement results for the turn-off and turn-on switching energies are presented in Section 6.2.2. The measured values are evaluated in Section 6.3 and are compared to the previously determined simulation data.

6.2.1 Test Setup, Deskewing and Probe Compensation

Figure 6.7 shows the hardware setup for the DPT. The sensor evaluation board is connected to an existing test bench, which provides the voltage V_{sw} via large capacitors. The power supply for the driver and logic is provided by an electrically isolated laboratory power supply unit and the signal s_{on} for controlling the low-side HEMT is provided via an optical fiber cable. The voltage v_{shunt} at the shunt resistor is connected directly to the $50\,\Omega$ input of the oscilloscope *WaveRunner 8208HD* via a coaxial cable, as already described in Section 6.1. It should be noted that the maximum permissible input voltage of the oscilloscope is $V_{\text{max}} = 5\,V_{\text{rms}}$, which with a shunt resistance of $R_{\text{shunt}} = 83.3\,\text{m}\Omega$ limits the maximum permissible current to $I_{\text{max}} = \frac{V_{\text{max}}}{R_{\text{shunt}}} = 60\,\text{A}$. The voltage tap for the *GaNSense™* feature is not connected, as this has proven to be unsuitable for measuring

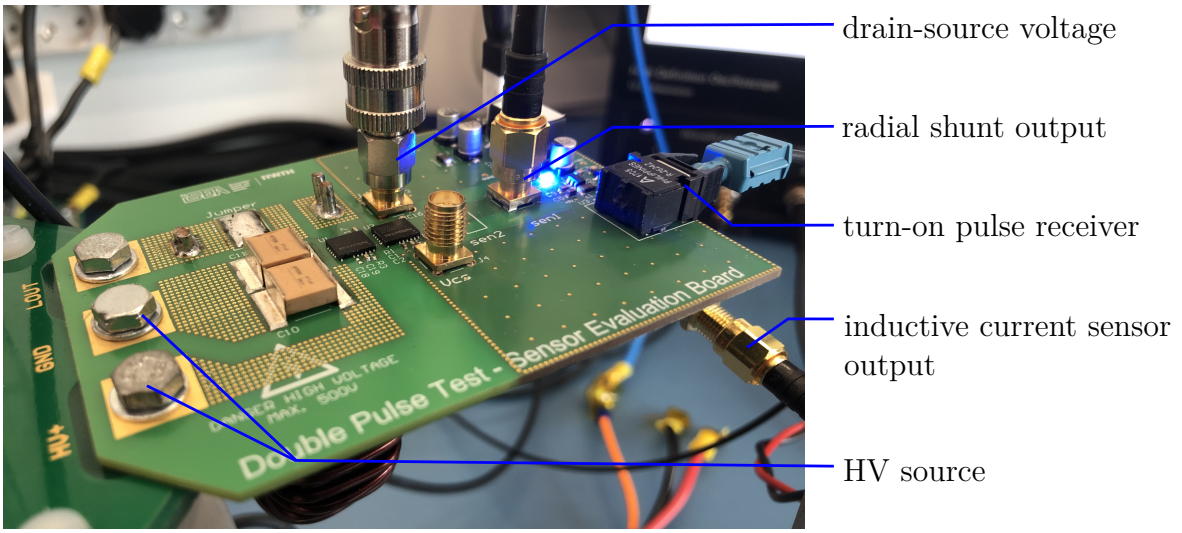

Figure 6.7: Measurement setup with sensor evaluation board

the switching transients and would form another common-mode path. The voltage v_{ds} and the voltage v_{ind} of the inductive sensor are accessed via passive probes of the type *PP018*, which are connected via coaxial connectors. These have a bandwidth of 500 MHz each, an input impedance of 10 MΩ and an attenuation ratio of 10:1 [61]. According to the analysis carried out in Chapter 3, this bandwidth is sufficient for the semiconductor class used. Directly tapping the voltage v_{ind} via the 50 Ω input of the oscilloscope has not proven to be practicable, as the terminating resistance is connected in parallel with the damping resistor R_{d} of the inductive sensor and would significantly reduce the bandwidth. The temperature is kept at around 25 °C throughout the measurement by manually controlling the air circulation in the test bench cabin.

As demonstrated in Chapter 3, the deskewing, which is the compensation of the time offset between the voltage measurement and the current measurement, plays a critical role in DPTs and is one of the major sources of error. Therefore, it is necessary to examine the transmission characteristics of the measuring equipment. The setup shown in Fig. 6.8a is used for this purpose. The oscilloscope used has an auxiliary (AUX) output, which provides a square-wave signal with a very short rise time. The square-wave signal is fed back via a cable into one oscilloscope channel (CH2), which is terminated with 50 Ω. The Y-adapter located at the input of CH2 enables a further tap of the square-wave signal. The probe or cable to be measured is connected to this adapter and to another channel (CH1). This configuration allows the time offset Δt to be determined. The accuracy of the deskewing is in the range of the sampling rate, which is $t_{\mathrm{s}} = 100\,\mathrm{ps}$. To perform deskewing at a difference that is smaller than the sampling rate, interpolation is required between the individual samples. Figure 6.9 shows the recorded waveforms and the resulting values for Δt for the passive probe *PP018* and the coaxial cable connected to the shunt resistor. The steps in the signals seen in Fig. 6.9b are caused by wave reflections on the line. The group delay, which results from the transmission behavior Z_{21} of the shunt, cannot be recorded with this procedure, but is negligible compared to the influence of the cable.

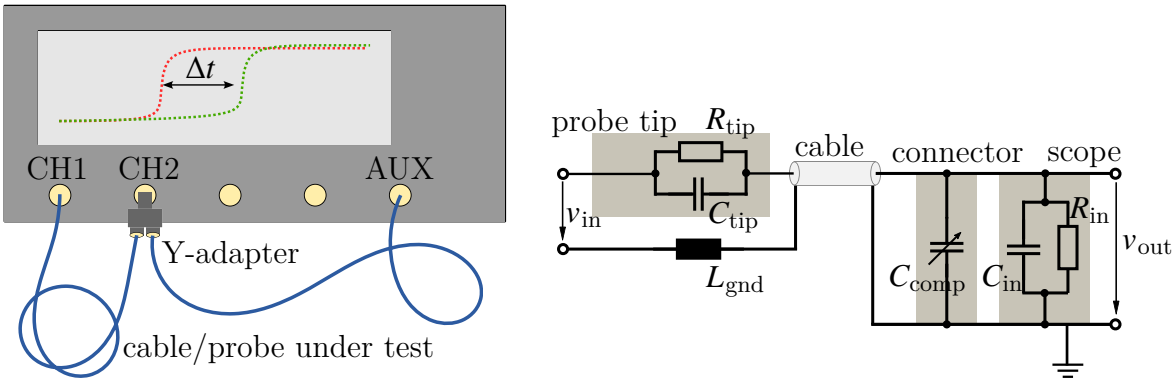

(a) Oscilloscope setup for deskewing

(b) Schematic structure of a passive voltage probe

Figure 6.8: Deskewing setup and passive voltage probe structure

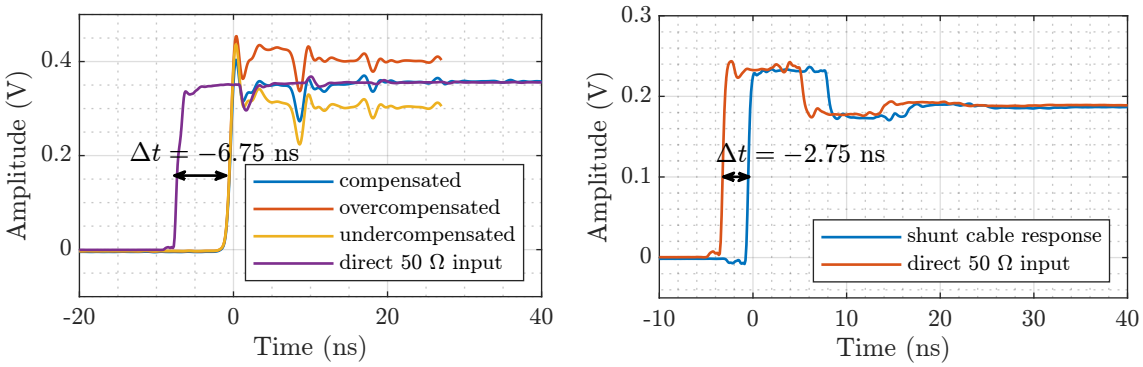

(a) Step response of *PP018* passive probe

(b) Step response of shunt cable

Figure 6.9: Deskewing of passive voltage probe and shunt

Besides deskewing, there is another characteristic of passive probes that must be taken into account. A passive probe is a resistive voltage divider that is formed from the impedance of the probe tip and the input impedance of the oscilloscope [186], [187]. Figure 6.8b shows the typical structure of a passive probe. The impedance of the probe tip for a 10:1 probe is $R_{tip} = 9\,\mathrm{M\Omega}$ and is connected in series with the input impedance of the oscilloscope, which is formed by the resistor $R_{in} = 1\,\mathrm{M\Omega}$. To avoid reflections on the cable, a specialized lossy cable made of NiCr wire is used, which represents a distributed termination system [188]. In addition, there is the parasitic capacitance of the probe tip $C_{tip} = 10\,\mathrm{pF}$ and the input capacitance $C_{in} = 19\,\mathrm{pF}$ of the oscilloscope [61], [72]. To achieve a constant dividing ratio of 10:1 over the entire frequency range, it is necessary that the two time constants τ of the probe tip and of the oscilloscope input are identical. To fulfill this condition, the additional capacitance C_{comp} is required, which is located in the connector at the oscilloscope input and can be variably adjusted with a screw. The voltage divider can then be described via Eq. (6.1) and is valid if the condition Eq. (6.2) is fulfilled.

$$\frac{v_{out}}{v_{in}} = \frac{1}{10} = \frac{R_{in}||(C_{comp} + C_{in})}{(R_{tip}||C_{tip}) + (R_{in}||(C_{comp} + C_{in}))} \tag{6.1}$$

$$\tau = R_{\text{tip}} \cdot C_{\text{tip}} \stackrel{!}{=} R_{\text{in}} \cdot (C_{\text{in}} + C_{\text{comp}}) \tag{6.2}$$

In the give setup, Eq. (6.2) is fulfilled at $C_{\text{comp}} = 71\,\text{pF}$. To set the capacitance precisely, the same setup can be used as for deskewing (see Fig. 6.8a). The different cases are shown in Fig. 6.9a. In the overcompensated case, C_{comp} was set too large and in the undercompensated case, C_{comp} was set too small. In addition to the compensation presented, there is a further high-frequency compensation for correcting overshoots. This is calibrated by default and can be adjusted as required using additional screws as described in [61]. If the properties deskewing and compensation are properly taken into account, it is possible to achieve reliable measurement results with a passive probe, as the following section will show.

6.2.2 Characterization Results

The following results were measured with the presented setup. The desired current I_{sw} was set by calculating the required turn-on period t_{ramp}. Figure 6.10 shows the measured switching transients at $V_{\text{sw}} = 500\,\text{V}$. In addition to the drain-source voltage v_{ds}, the plot shows the current i_{shunt} measured with the radial shunt and the current i_{ind} measured with the inductive sensor. The voltage v_{shunt} measured at the shunt was scaled with R_{shunt} and filtered with the filter presented in Chapter 4 to obtain the current i_{shunt}. To obtain i_{ind}, the output signal v_{ind} was integrated according to the post-processing routine explained in Section 5.3. The dc offset was determined using a time window immediately before the turn-off event and subtracted from v_{ind}. The gain factor for the integral was determined using the known amplitude of i_{shunt}. The measured switching transients for the voltage levels $V_{\text{sw}} = 300\,\text{V}$ and $V_{\text{sw}} = 400\,\text{V}$ can be found in Fig. A.8 in the appendix.

The resulting transients are very similar to those obtained in the simulation, which were shown in Fig. 6.5. As expected, the turn-off process is very fast and is completed in approximately 10 ns. Similar as in the simulation, turning off the small current $I_{\text{sw}} = 4\,\text{A}$ takes significantly longer. In addition, it is noticeable that the switching current $I_{\text{sw}} = 20\,\text{A}$ was not reached exactly. The reason for this is that the current rise during the first pulse of the DPT is non-linear and, due to frequency-dependent circuit parameters L_{load} and R_{s}, the duration t_{ramp} can only be estimated (see Appendix A.2). An exact adjustment of I_{sw} requires several iterations of the DPT and is not necessary in most cases. A further observation is the oscillation caused by the turn-off transient, which is particularly apparent in the inductive current measurement with a frequency of approximately 130 MHz. In the case of the turn-on event, very smooth waveforms were recorded with the shunt, which, as in the simulation, are characterized by a constant $\mathrm{d}i/\mathrm{d}t$. The current i_{ind} again shows an oscillation at a frequency of approximately 130 MHz. All voltage transient v_{ds} occur without significant overshoots or oscillations. This indicates a proper design of the switching cell. A precise comparison of the measured and simulated rise times is provided in Section 6.3.

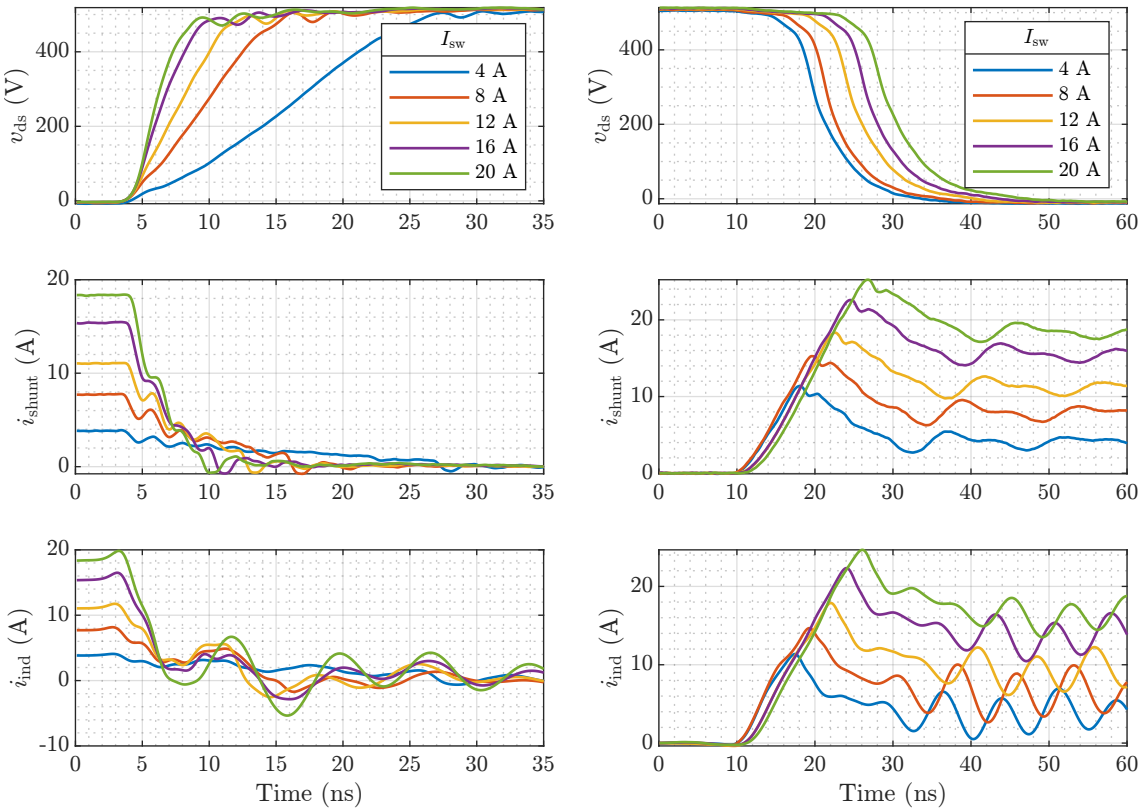

(a) turn-off (b) turn-on

Figure 6.10: Measured transients with shunt and inductive sensor at different operating points (V_{sw} = 500 V, I_{sw} = 4 A ... 20 A, T_{amb} = 25 °C)

The aim of the measurement was to determine the switching energies E_{off} and E_{on} by calculating the complete integral of p_{loss}. The time windows match the diagrams in Fig. 6.10 and have a length of 35 ns at turn-off and 60 ns at turn-on. Figure 6.11 shows the resulting switching energies E_{off} and E_{on} that were calculated from the measured waveforms of each operating point. In the case of the turn-on switching energy, there is a very close match between the measurement with shunt resistor and inductive sensor. The shape of the individual curves corresponds to the simulated values from Fig. 6.6. A detailed comparison with the simulated values is made in Section 6.3. In the case of the turn-off switching energy, it is noticeable that the measurement with the inductive current sensor leads to rather irregular results. This is due to the oscillation that can be seen when comparing i_{shunt} and i_{ind}. In Fig. A.9 in the appendix the same plot is shown for the definition of the integral via *IEC 60747-8*. In this case, there is again a high level of agreement between the two measurement methods for E_{on} and a considerable irregularity for E_{off}.

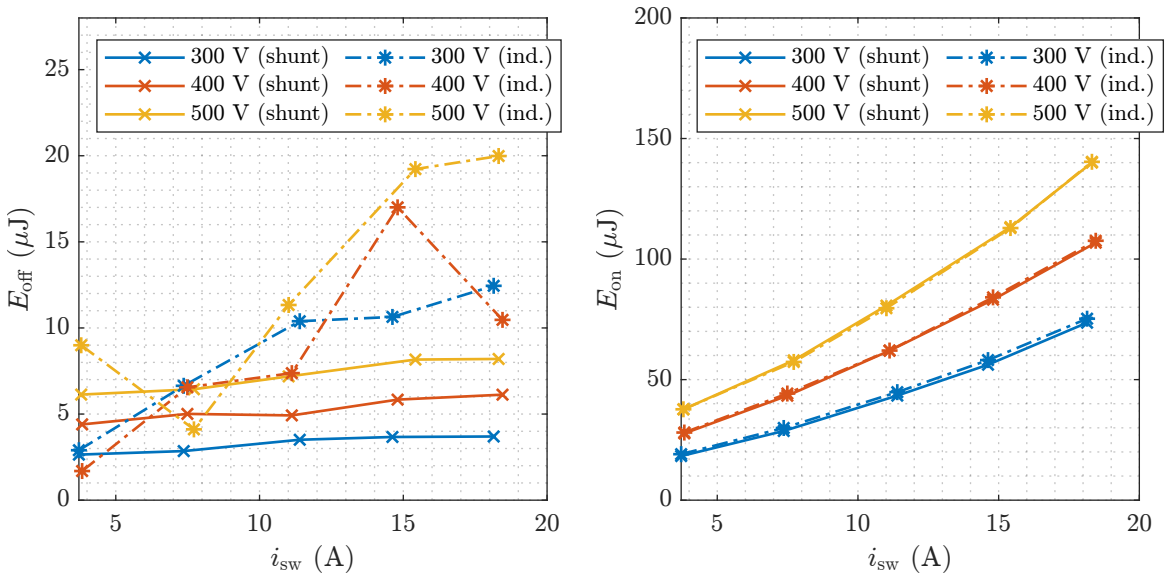

(a) turn-off switching energies

(b) turn-on switching energies

Figure 6.11: Measured switching energies with shunt and inductive sensor at different operating points ($V_{\mathrm{sw}} = 300\,\mathrm{V}$ … $500\,\mathrm{V}$, $I_{\mathrm{sw}} = 4\,\mathrm{A}$ … $20\,\mathrm{A}$, $T_{\mathrm{amb}} = 25\,^{\circ}\mathrm{C}$)

6.3 Evaluation of the Measurement Accuracy

Since the switching behavior has been analyzed both by simulation and by measurement, the measurement accuracy is evaluated by comparing the different results with each other. Fig. 6.12 shows a comparison of the simulated and measured switching transients for a single operating point. It is apparent that there is a relatively high level of agreement between the simulated transients with regard to the gradient rates $\mathrm{d}i/\mathrm{d}t$ and $\mathrm{d}v/\mathrm{d}t$ as well as the rise times. Since there are multiple operating points and the visual comparison of the waveforms is not precise, the derived dynamic characteristics are compared to each other in this section. The focus of the evaluation is on the switching energies E_{off} and E_{on}, with the rise times and fall times being considered initially.

Table 6.1 and Table 6.2 compares the rise times and fall times of the simulated and measured quantities v_{ds} and i_{ds}. In the case of v_{ds}, t_{rise} refers to the turn-off event and t_{fall} to the turn-on event. With i_{ds} this is reversed and t_{rise} is measured at the turn-on and t_{fall} at the turn-off instance. To avoid having to consider all 15 operating points, only the minimum and maximum recorded values are compared. In the case of the drain-source voltage v_{ds}, it is noticeable that the simulated transients are consistently faster than the measured ones. The highest relative deviation is for the minimum measured rise time $t_{\mathrm{rise,min}}$ and measures 41 %. This can also be transferred to the measurement of i_{ds} and indicates that either the simulation is inaccurate or the bandwidth is insufficient. According to the datasheet, the voltage probe used has a minimum rise time of $t_{\mathrm{rise}} = 700\,\mathrm{ps}$ [61]. It can therefore be assumed that the measurement accuracy is sufficient

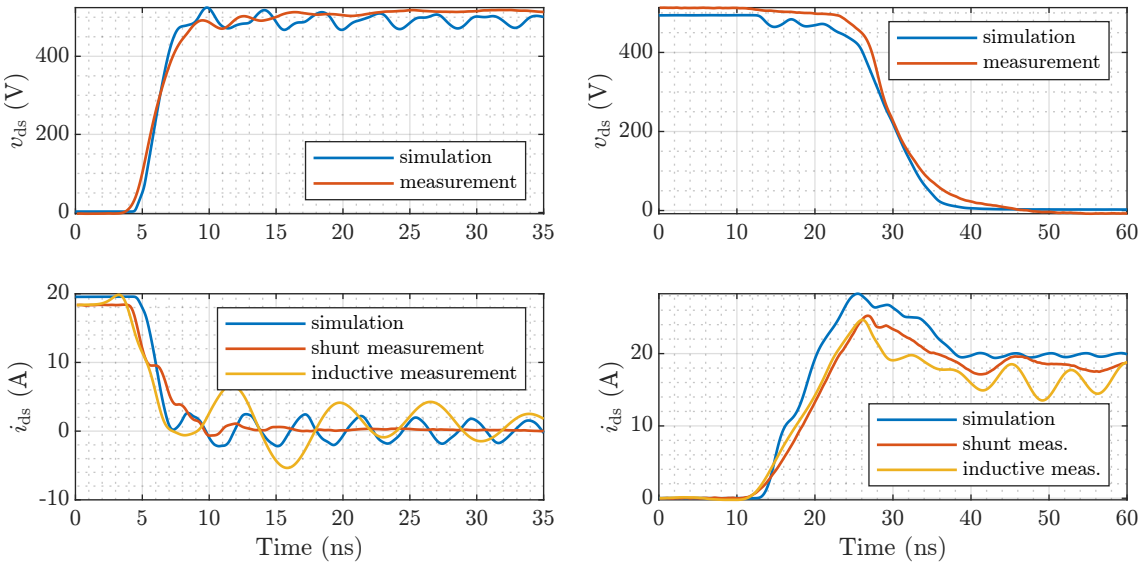

(a) turn-off (b) turn-on

Figure 6.12: Comparison of simulated and measured switching transients (V_{sw} = 500 V, I_{sw} = 20 A, T_{amb} = 25 °C)

Table 6.1: Characteristics of v_{ds}

	simulation	measurement
$t_{rise,min}$	1.56 ns	2.16 ns
$t_{rise,max}$	11.7 ns	16.5 ns
$t_{fall,min}$	6.62 ns	8.83 ns
$t_{fall,max}$	10.8 ns	11.1 ns

Table 6.2: Characteristics of i_{ds}

	simulation	shunt	inductive
$t_{rise,min}$	1.11 ns	2.30 ns	1.80 ns
$t_{rise,max}$	5.33 ns	8.03 ns	7.94 ns
$t_{fall,min}$	1.46 ns	2.64 ns	1.90 ns
$t_{fall,max}$	9.05 ns	23.0 ns	23.3 ns

and the deviation is caused by inaccuracies in the simulation. This is confirmed by the observation that the rise times of i_{ds} measured with shunt and inductive sensor are relatively consistent. The highest relative deviation between the measurement methods can be found at $t_{fall,min}$ and is 39 %.

The next comparison relates to the measurement of the switching energies E_{off} and E_{on}. To visualize deviations between the differently determined switching energies across all operating points, heatmaps are selected as a display method as shown in Fig. 6.13. Each row shows the operating points that were recorded at one specific switching voltage V_{sw}, whereas each column shows the values for on specific switching current I_{sw}. In the simulation carried out in Section 6.1.3, the switching energies were determined at the exact points I_{sw} = 4 A, 8 A, 12 A, 16 A and 20 A. The measurements carried out in Section 6.2 did not exactly match these values. To allow a more precise comparison the switching energies are interpolated to these current levels using the curves shown in Fig. 6.11a and Fig. 6.11b. This enables the switching energies to be compared at uniform settings for

four different settings of I_{sw}. With V_{sw}, no interpolation is necessary as the voltages are consistent in simulation and measurement and are set to the values 300 V, 400 V and 500 V. Above each plot, the overall mean value μ of the respective comparison is shown.

The relative percentage error between simulation and shunt measurement is shown in Fig. 6.13a and Figure 6.13b. With the exception of individual points, the relative deviation is less than 10 %, which corresponds to a high level of agreement. On average, there is a deviation of $\mu = 3.46\,\%$ for E_{off} and a deviation of $\mu = 2.97\,\%$ for E_{on} The points with the highest deviation for both E_{off} and E_{on} are at $V_{sw} = 500\,V$. Figure 6.13c and Fig. 6.13d show the comparison between simulation and measurement with the inductive current sensor. It is noticeable that the measurement of E_{off} with the inductive sensor is highly inaccurate and the relative deviation is on average 90 %. In the case of E_{on}, the deviation is significantly better and is similar to the values that resulted from the measurement via the shunt with an average relative deviation of only 1.57 %. In Fig. A.11 the same representation for the deviation between measured and simulated switching energies based on the standard *IEC 60747-8* can be found. With this definition, there is again close correlation between simulation and measurement for E_{on} across both measurement methods. E_{off}, on the other hand, deviates strongly from the simulated value for both measurement methods. The main reason for this is the oscillation after turning off.

Finally, the measurements performed with shunt and inductive sensor are compared to each other in Fig. 6.14. Figure 6.14a shows the comparison for the measurement of E_{off}. This shows a very high deviation, which is on average 84 %, from which it can be concluded that the inductive sensor is not suitable for measuring the turn-off transient. When measuring E_{on}, Fig. 6.14b shows a very high level of agreement, with an average deviation of only 1.38 %. Both comparisons are shown in Fig. A.10 using the standard *IEC 60747-8*. In this case, the relative deviation of E_{off} is slightly lower and the deviation of E_{on} remains at a very low level.

Based on the comparisons made between simulation and the two measurement methods, the following conclusions can be made:

- The inductive current sensor is not suitable for measuring the turn-off event. One possible reason is the voltage tap via the passive probe. This is not ideal because even if the passive probe has a high input impedance, it also has an input capacitance of 10 pF, which was not taken into account in the previous modeling. The oscillation of i_{ind} is less strong with i_{shunt} and is therefore assumed to be an artifact of the inductive current sensor. A possible improvement could be achieved with a high-impedance probe that has a lower input capacitance [157].

- There is a remaining deviation between simulation and measurement, which is in the single-digit percentage range and can be up to 15 % in individual cases. There are various possible explanations for the remaining uncertainty. Firstly, the simulation did not simulate any temperature influences that may exist in the measurement setup. Other effects include possible common-mode currents through the various

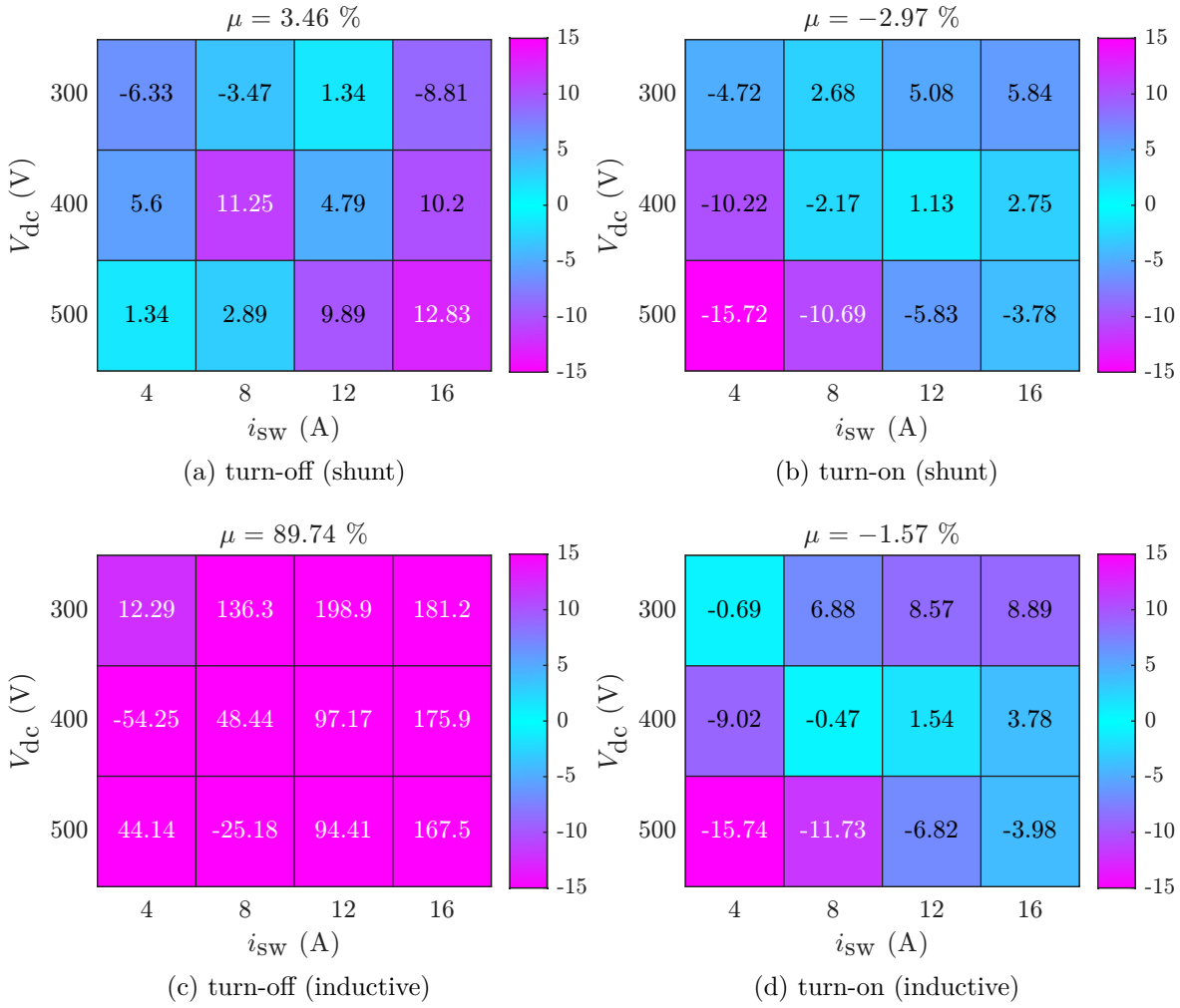

(a) turn-off (shunt)

(b) turn-on (shunt)

(c) turn-off (inductive)

(d) turn-on (inductive)

Figure 6.13: Relative percentage error between measurement and simulation at different operating points for both evaluated sensors

measurement cables, which are difficult to model, as well as the probe parasitics. In addition, there may be manufacturing tolerances in the components and the PCB as well as errors in the simulation due to frequency-dependent parameters that are not modeled in *LTspice*.

- The turn-on switching energies, which make up a major part of the total energy, were measured correctly as the two measurement methods agree very well with an average deviation of only 1.38 %. Compared to the simulation, the measurement with the shunt shows similar deviations for the turn-on and turn-off transition and it can be assumed that these were caused by inaccuracies in the simulation model and not by measurement errors. With regard to E_{on}, it makes no difference in terms of the measurement deviation whether the definition according to *IEC 60747-8* or the full integral over the switching power is used.

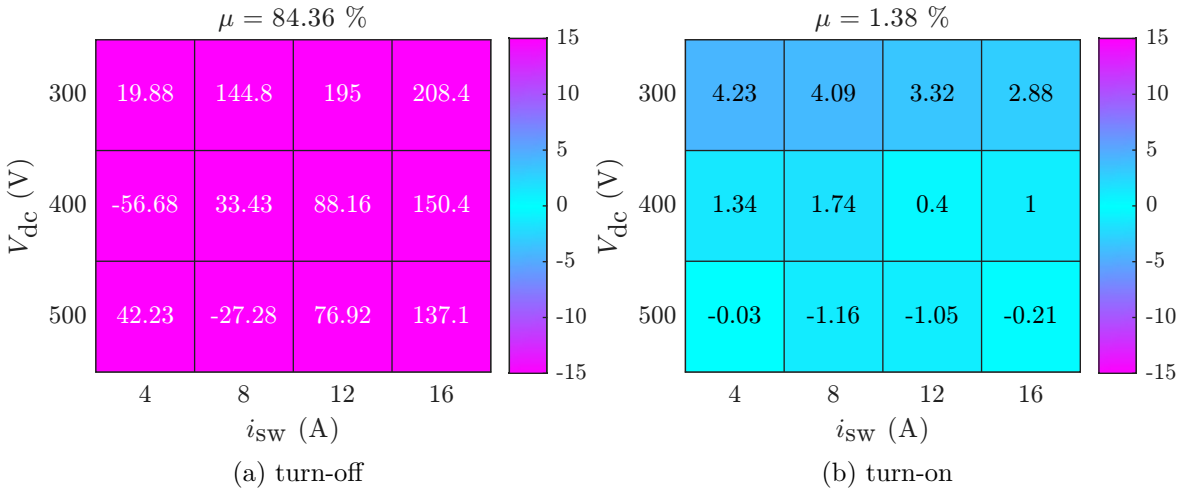

(a) turn-off (b) turn-on

Figure 6.14: Relative percentage error between shunt measurement and inductive measurement at different operating points

6.4 Conclusion

In this chapter, the two measurement methods for the drain-source current i_{ds} presented in Chapter 4 and Chapter 5 were validated. For this purpose, a corresponding sensor evaluation board was constructed, which implements the radial shunt and the inductive sensor in series and has a low power loop inductance of $L_{loop} = 2.96\,\text{nH}$. The switching behavior of this switching cell, which is based on GaN devices with a rated voltage of 700 V, was initially investigated by simulation, with special attention being given to modeling the parasitics of the PCB. After explaining the steps required in advance, such as probe compensation and deskewing, the previously simulated double-pulse tests were carried out at different voltage and current levels. The measurement error was evaluated using different comparisons. With regard to E_{off}, it was shown that measurements with the inductive sensor lead to significant deviations and the voltage tap of the inductive sensor was identified as a possible cause. When measuring E_{on}, the two measurement methods shunt and inductive sensor only deviate from each other by an average of 1.38 % and a maximum of 4.23 %. Furthermore, the shunt shows a high agreement with an average deviation of −2.97 % to the simulation. Overall, the current measurement with the radial shunt resistor has proven to be very precise and is therefore the preferred current measurement technique for the dynamic characterization of WBG semiconductor devices. Further advantages were found during implementation, such as direct voltage acquisition via a coaxial cable with the oscilloscope and no complex post-processing being required. Another advantage of the shunt is that only two layers are required on one side of the PCB core in contrast to the inductive sensor, which requires at least three layers on one side of the PCB core and is therefore more complex to implement.

7 Conclusions and Outlook

This thesis investigated the dynamic characterization of semiconductor devices, focusing high-bandwidth current-probing techniques. In the final chapter, Section 7.1 summarizes the most important findings of this work. This is followed by Section 7.2, which gives an outlook on further research.

7.1 Outcomes of This Work

The results of this work can be broken down into three main topics. The first outcome is the improved comprehension of measurement errors that occur in DPTs. The second outcome is the design and implementation of a novel shunt resistor and the third outcome the design and implementation of a novel inductive current sensor. Both techniques are suitable for measuring drain-source currents with very short rise times and have been successfully validated for switching energy measurements.

Improved Comprehension of Measurement Errors in DPTs This work has investigated which parameters influence the measurement of the switching energies in DPTs and how significant the respective effect on the measurement accuracy is. With regard to the parasitics of the probes, it was shown that the inductance of the current sensor is most significant, especially for LV GaN devices. The application of conventional coaxial shunts that have an inductance of approximately 2 nH can lead to measurement errors beyond 20 %. With regard to the input capacitance of the voltage probe, the maximum effect was found for HV SiC devices, although this effect is less pronounced. In addition, the influence of the limited bandwidths of probes was investigated. Concerning the voltage measurement, it was shown that a bandwidth of 500 MHz is sufficient for measuring the switching energies in most cases, with LV GaN devices requring a higher bandwidth as an exception. About the current measurement, it has been shown that the bandwidth should be in the range of 1 GHz to obtain accurate results. Finally, the influence of deskewing was evaluated, which is significant and an accuracy of less than 100 ps should be reached. All effects were quantified for a total of four different WBG devices. This contributed to a better assessment of the requirements and the optimization potential of DPTs.

Design and Implementation of a Novel Shunt Resistor Another key outcome is the design of a resistive current sensor. The design presented is based on a circular arrangement of thin-film resistors in a *0402* package, which are placed directly underneath a coaxial connector. Using FEM, a very low parasitic inductance of only 84.1 pF was determined. The transfer function of the radial shunt was characterized by measurements with a VNA. In combination with a matched FIR filter, a very high bandwidth of 2.17 GHz was achieved. The drawback of resistive current measurement is the thermal stress on the shunt resistors. By means of analytical calculations, a SOA was defined, which allows DPTs with an amplitude of 100 A. The concept of the radial shunt was validated in DPTs with GaN HEMTs and a high level of agreement was achieved with the simulation. In this way, a straightforward solution was introduced that fulfills the requirements for drain-source current measurement of WBG semiconductor devices. Since the design is easy to adopt, it can in many cases replace the conventional coaxial shunt, which is less dynamic and also much more cost-intensive than the proposed radial shunt.

Design and Implementation of a Novel Inductive Current Sensor A further outcome is the design of an inductive current sensor. The planar pick-up coil, which is embedded in a multi-layer PCB, allows the evaluation of the magnetic field caused by the drain-source current. A parameter study based on simulations was used to optimize the geometry of this coil, which requires a trade-off between the criteria of minimum rise time and mutual inductance. Using prototypes, a very high bandwidth of 2.66 GHz was experimentally validated with a parasitic inductance of approximately 295 pH. In addition, the steps required for post-processing were described, which is a drawback of all inductive measurement methods without integrator circuitry. In return, the advantage is that the sensor is not thermally stressed. The concept of the planar pick-up coil was validated in DPTs with GaN HEMTs and a high level of agreement was achieved with the simulation for the turn-on switching energy.

7.2 Potential for Further Research

In future work, the highly-dynamic current measurement can be further improved. With regard to resistive current measurements, there is great potential in the assembly technology. This involves overcoming the design with conventional discrete thin-film resistors and building a radial or coaxial structure with a continuous resistive thin film. This allows the component to be miniaturized even further, which reduces the parasitic inductance. As a result, the same measurement bandwidth can be achieved with lower ohmic resistance, improving the thermal performance. It is conceivable to integrate such a structure directly into a PCB or even into the package of a component. In addition to the assembly technology, the bandwidth can also be extended via compensation networks. Analog filters and operational amplifiers offer the potential to flatten the frequency response beyond 2 GHz so that even shorter rise times can be recorded precisely.

Further improvements are also possible with regard to inductive current measurement. It has been shown that very high bandwidths are possible through the miniaturization of pick-up coils. With this concept, it is also conceivable to integrate it directly into the package of a component to eliminate the need for additional space. This is a possible development of integrated current measurement, which is already available in some devices via less dynamic sense FETs. Compared to resistive current measurement, the inductive current measurement has the decisive advantage of being lossless. Nevertheless, the challenges of inductive measurement have to be solved, which primarily include noise coupling and the analog integration of the induced voltage.

Another challenge with DPTs is the issue of deskewing. The evaluation of the measurement accuracy has shown that this factor can have a very significant effect on the measurement accuracy of the switching energies. The time offset between current and voltage measurement can be determined within a few hundred picoseconds using reference measurements. However, a certain degree of uncertainty remains, as the group delay of a probe is both frequency-dependent and potentially also amplitude-dependent. For even faster-switching devices, it is therefore essential to develop new methods that allow reliable deskewing. This could be achieved using algorithms in post-processing or customized calibration techniques.

A Appendix

A.1 Relationship between Rise Time and Bandwidth of a Low-Pass System

The following equations show the relationship between rise time t_{rise} and cutoff frequency f_c of a first-order low-pass filter with the time constant $\tau = RC$ [189]. The circuit shown in Fig. A.1a is excited with a step signal with the amplitude v_{in}, which leads to the step response shown in Fig. A.1b.

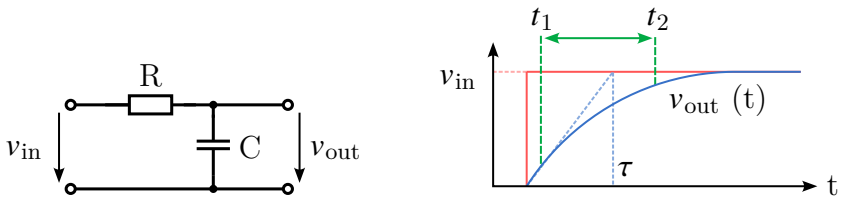

(a) 1st order RC lowpass filter (b) step response

Figure A.1: Relationship between rise time and bandwidth for a low-pass system

The output signal v_{out} follows the exponential function Eq. (A.1)

$$v_{\text{out}}(t) = v_{\text{in}} \cdot \left(1 - e^{\left(\frac{-t}{\tau}\right)}\right) \tag{A.1}$$

The relevant points t_1 and t_2 for calculating the rise time at 10 % and 90 % can be calculated using the following equations:

$$v_{\text{out}}(t_1) = 0.1 v_{\text{in}} = v_{\text{in}} \left(1 - e^{\left(\frac{-t_1}{\tau}\right)}\right) \tag{A.2}$$

$$\Rightarrow 0.1 = 1 - e^{\left(\frac{-t_1}{\tau}\right)} \tag{A.3}$$

$$\Leftrightarrow t_2 = -\ln(0.1) \cdot \tau \tag{A.4}$$

$$v_{\text{out}}(t_2) = 0.9 v_{\text{in}} = v_{\text{in}} \left(1 - e^{\left(\frac{-t_2}{\tau}\right)}\right) \tag{A.5}$$

$$\Rightarrow 0.9 = 1 - e^{\left(\frac{-t_2}{\tau}\right)} \tag{A.6}$$

$$\Leftrightarrow t_2 = -\ln(0.9) \cdot \tau \tag{A.7}$$

The difference equals the rise time t_{rise}:

$$t_{\text{rise}} = t_2 - t_1 \tag{A.8}$$

$$\Rightarrow t_{\text{rise}} = \ln\left(\frac{0.9}{0.1}\right) \cdot \tau = 2.2 \cdot \tau \tag{A.9}$$

This expression for t_{rise} is finally inserted into the definition for τ from Eq. (A.10), from which the desired relationship follows:

$$\tau = \frac{1}{2\pi f_{\text{c}}} \tag{A.10}$$

$$\Rightarrow t_{\text{rise}} = \frac{0.35}{f_{\text{c}}} \tag{A.11}$$

A.2 Calculations for the DPT with Non-linear Magnetization Phase

The following equations allow the required inductance L_{load} to be calculated for the case of a short time constant $\tau = \frac{L_{\text{load}}}{R_{\text{s}}}$ of the magnetization phase and provide an approach for calculating C_{DC} via the energy balance. In this case, the current i_{L} follows a flattening curve described by Eq. (A.12), which leads to Eq. (A.13)

$$i_{\text{L}}(t) = \frac{V_{\text{sw}}}{R_{\text{s}}}(1 - e^{-\tau t}) \tag{A.12}$$

$$\Leftrightarrow L_{\text{load}} = \frac{-R_{\text{s}}}{t_{\text{ramp}}} \ln\left(1 - \frac{R_{\text{s}} I_{\text{sw}}}{V_{\text{sw}}}\right) \tag{A.13}$$

The energy stored in the inductance in this case is equivalent to Eq. (A.14):

$$\Delta E_{\text{L}} = \frac{1}{2} L_{\text{load}} {I_{\text{sw}}}^2 = \frac{-R_{\text{s}} {I_{\text{sw}}}^2}{2 t_{\text{ramp}}} \ln\left(1 - \frac{R_{\text{s}} I_{\text{sw}}}{V_{\text{sw}}}\right) \tag{A.14}$$

The energy that is lost in the resistance R_{s} can also be calculated from Eq. (A.12):

$$\Delta E_{\text{R}} = \int_0^{t_{\text{ramp}}} R_{\text{s}} {i_{\text{L}}}^2(t) \mathrm{d}t = \frac{{V_{\text{sw}}}^2}{R_{\text{s}}} \left(\frac{e^{-2\tau t_{\text{ramp}}}(4e^{\tau t_{\text{ramp}}} - 1)}{2\tau} + t_{\text{ramp}}\right) \tag{A.15}$$

Both formulas for ΔE_{L} and ΔE_{R} can be used to calculate ΔE_{C} via the energy balance:

$$\Delta E_{\text{C}} = \Delta E_{\text{L}} + \Delta E_{\text{R}} \tag{A.16}$$

An analytical solution for C_{DC} is not provided at this point.

A.3 Extended Analysis of Simulated Switching Energies and Error Distributions

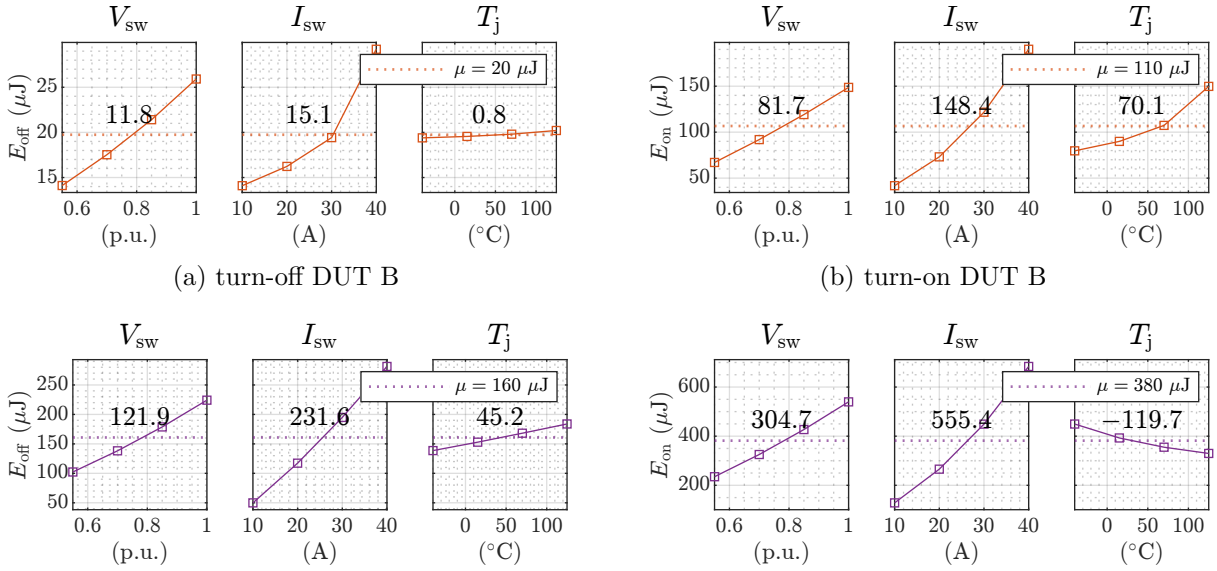

(a) turn-off DUT B

(b) turn-on DUT B

(c) turn-off DUT D

(d) turn-on DUT D

Figure A.2: Simulated main effects of switching energies (DUT B and DUT D)

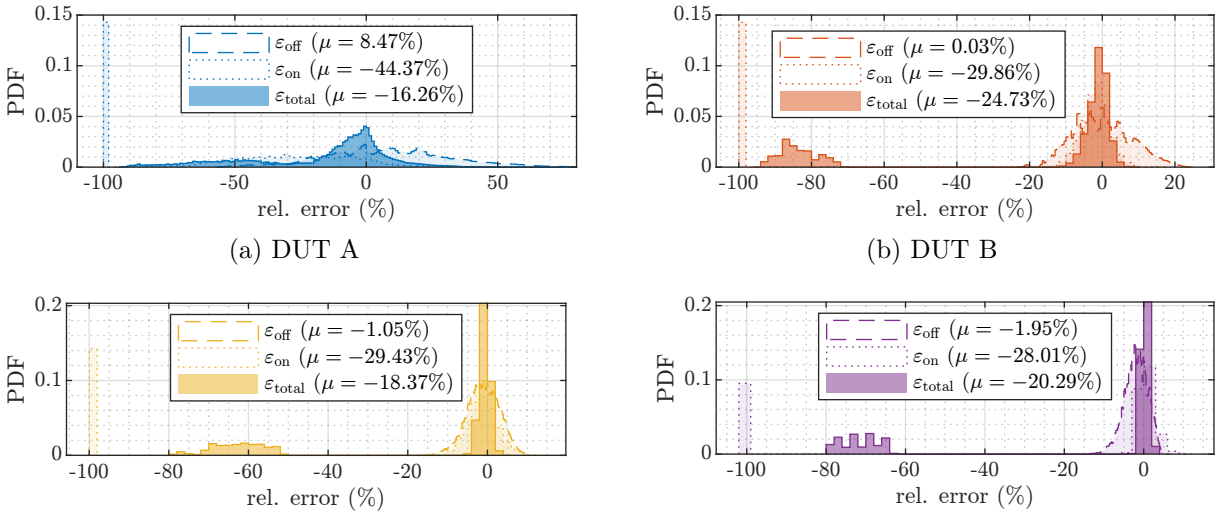

(a) DUT A

(b) DUT B

(c) DUT C

(d) DUT D

Figure A.3: Distribution of rel. errors for each DUT according to IEC standard

A.4 Conversion of Network Parameters

The following equations allow the elements of a 2-port S-parameter matrix to be converted into Z-parameters:

$$Z_{11} = \frac{((1 + S_{11})(1 - S_{22}) + S_{12}S_{21})}{\Delta_S} \cdot Z_0 \tag{A.17}$$

$$Z_{12} = \frac{2S_{12}}{\Delta_S} \cdot Z_0 \tag{A.18}$$

$$Z_{21} = \frac{2S_{21}}{\Delta_S} \cdot Z_0 \tag{A.19}$$

$$Z_{22} = \frac{((1 - S_{11})(1 + S_{22}) + S_{12}S_{21})}{\Delta_S} \cdot Z_0 \tag{A.20}$$

$$\Delta_S = (1 - S_{11})(1 - S_{22}) - S_{12}S_{21} \tag{A.21}$$

The following equations allow the elements of a 2-port S-parameter matrix to be converted into T-parameters:

$$T_{11} = \frac{-\det(S)}{S_{21}} = S_{12} - \frac{S_{11}S_{22}}{S_{21}} \tag{A.22}$$

$$T_{12} = \frac{S_{11}}{S_{21}} \tag{A.23}$$

$$T_{21} = \frac{-S_{22}}{S_{21}} \tag{A.24}$$

$$T_{22} = \frac{1}{S_{21}} \tag{A.25}$$

The following equations allow the elements of a 2-port T-parameter matrix to be converted back into S-parameters:

$$S_{11} = \frac{T_{12}}{T_{22}} \tag{A.26}$$

$$S_{12} = \frac{\det(T)}{T_{22}} = T_{11} - \frac{T_{12}T_{21}}{T_{22}} \tag{A.27}$$

$$S_{21} = \frac{1}{T_{22}} \tag{A.28}$$

$$S_{22} = \frac{-T_{21}}{T_{22}} \tag{A.29}$$

A.5 Code Snippets for Filter Design in MATLAB

```
%% Load exemplary waveform as input current
load stepDataOffset.mat     % example from MATLAB
y_in = stepOffset.Data-stepOffset.Data(1);
t = stepOffset.Time*30e-9;  % scaled time vector
ts = t(2)-t(1);             % get sample time

%% Load touchstone file with simulated or measured S-
   parameters and obtain transfer function of shunt including
    50Ohm termination
S = sparameters('shunt_measurement.s2p');
f = S.Frequencies;
S_T = cascadesparams(S,sparameters(shuntRLC('R',50),f));
Z_T = s2z(S_T.Parameters);      % converstion to Z-param.
Z21_T = squeeze(Z_T(2,1,:));    % extract Z_21
R_shunt = abs(Z21_T(1));        % get dc resistance

%% Simulate shunt response in time domain
Z21_fit = rational(f,Z21_T,'TendsToZero',false,'ErrorMetric',
   'Relative','Causal',true);
[y_out,~,~] = timeresp(Z21_fit,y_in/R_shunt,ts);

%% Design FIR lowpass filter and apply zero-phase filtering
Fs = 1/ts;      % sampling frequency of input signal

d = designfilt("lowpassfir", ...
        SampleRate= Fs, ...
        PassbandFrequency = 1.3e9, ...
        StopbandFrequency= 2.2e9, ...
        PassbandRipple = 0.1, ...
        StopbandAttenuation= 40, ...
        DesignMethod = 'equiripple');
y_comp = filtfilt(d,y_out);

%% plot input current, shunt response, filtered response
plot(t,[y_in, y_out, y_comp])
```

A.6 Additional Diagrams for the Parameter Study of the Inductive Sensor

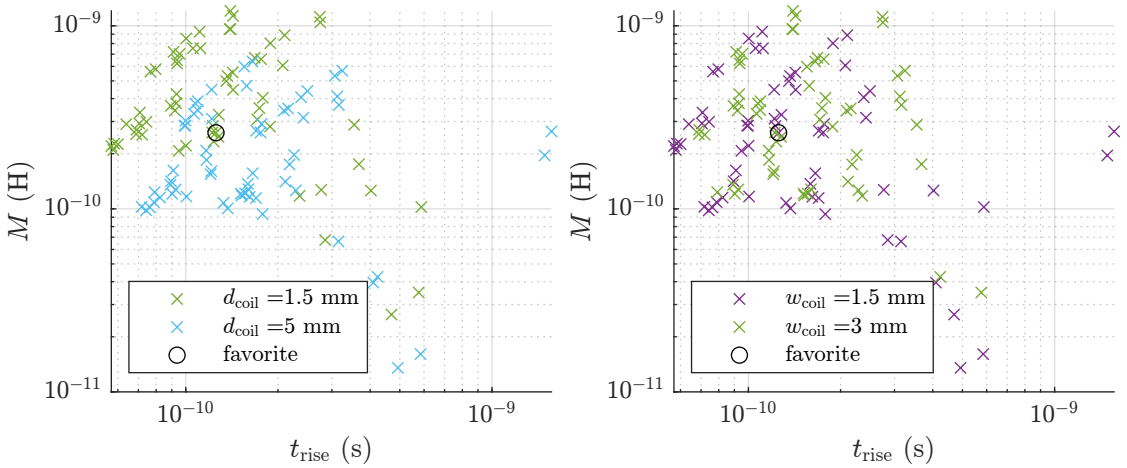

(a) grouped by d_{coil}

(b) grouped by w_{coil}

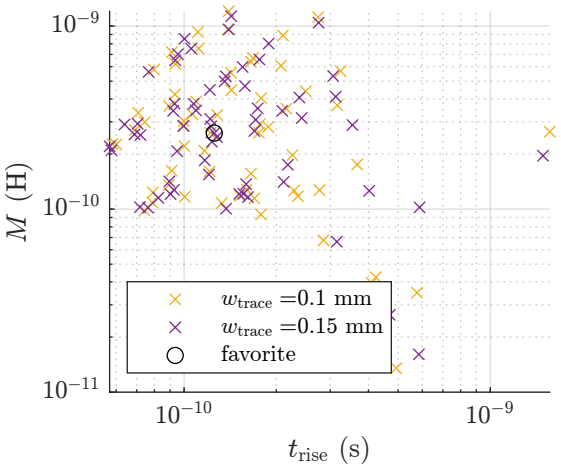

(c) grouped by w_{trace}

Figure A.4: Mapping of all 128 sensor variants according to the minimum rise time t_{rise} vs. mutual inductance M (continued)

A.7 Simulation Models of the Sensor Evaluation Board

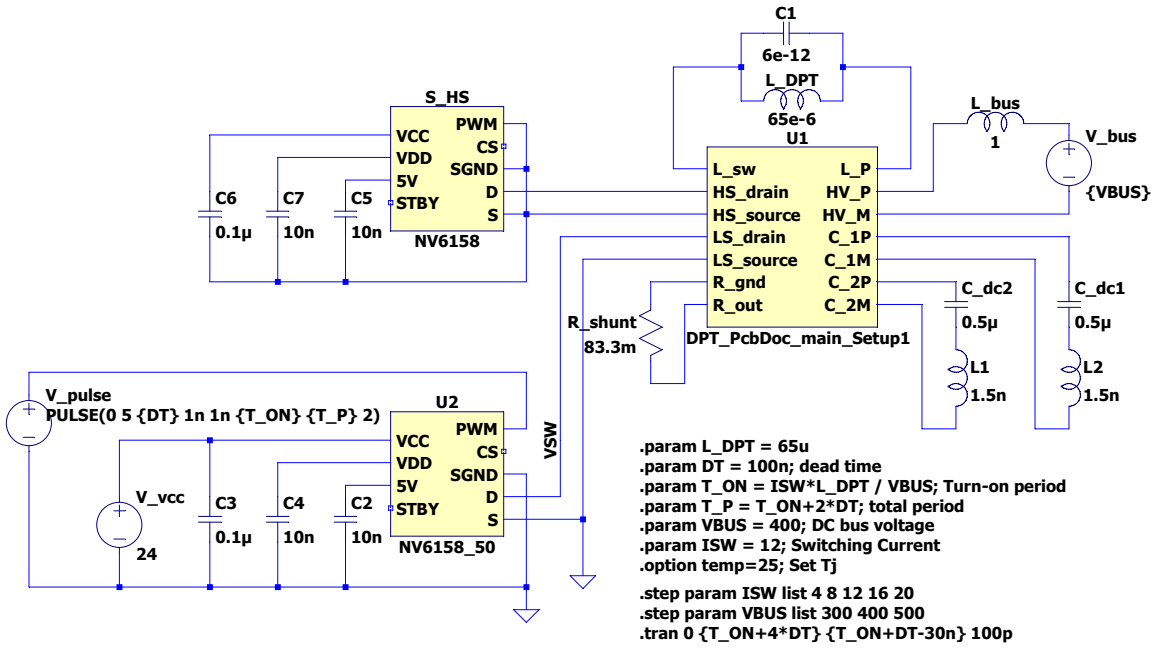

Figure A.5: *LTspice* simulation circuit with *NV6158* and PCB subcircuit

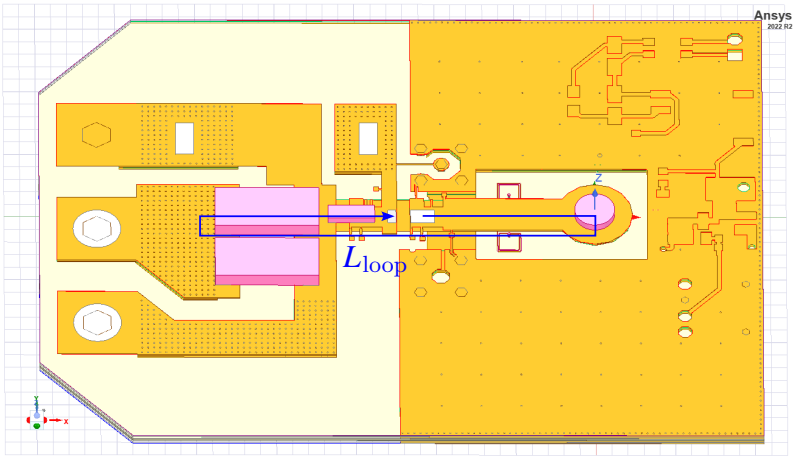

Figure A.6: Definition of the power loop inductance L_{loop} =2.96 nH in *ANSYS*

A.8 Simulated and Measured Switching Transients at 300 V and 400 V

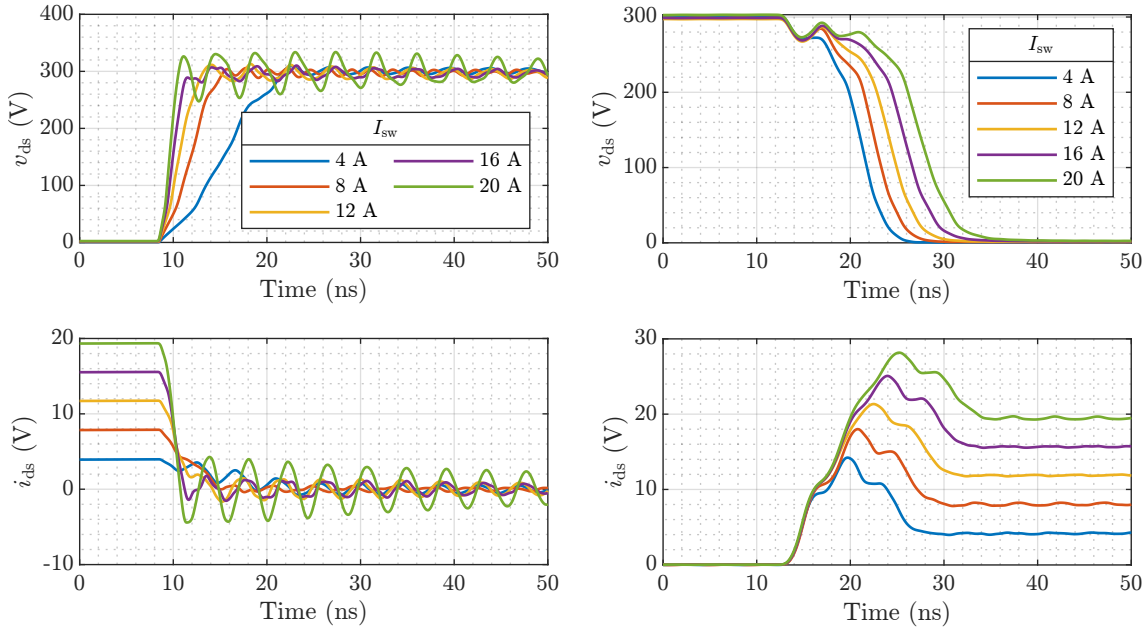

(a) turn-off, V_{sw} = 300 V (b) turn-on, V_{sw} = 300 V

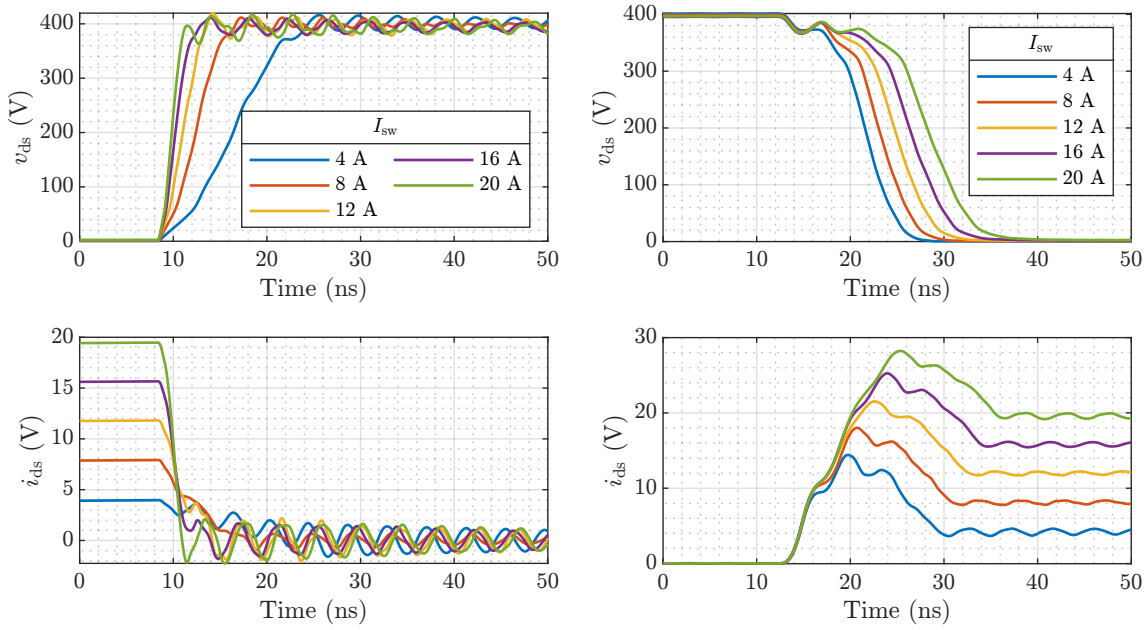

(c) turn-off, V_{sw} = 400 V (d) turn-on, V_{sw} = 400 V

Figure A.7: Simulated switching transients for *NV6158* at different operating points (V_{sw} = 300 V ... 400 V, I_{sw} = 4 A ... 20 A, T_j = 25 °C)

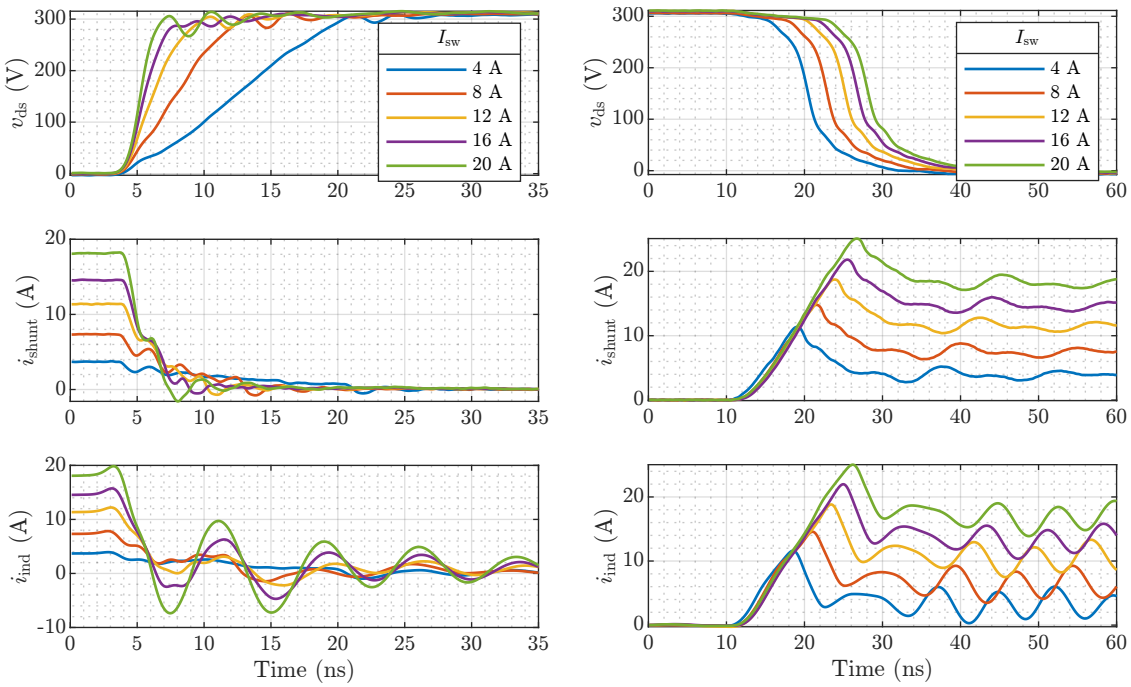

(a) turn-off, V_{sw} = 300 V

(b) turn-on, V_{sw} = 300 V

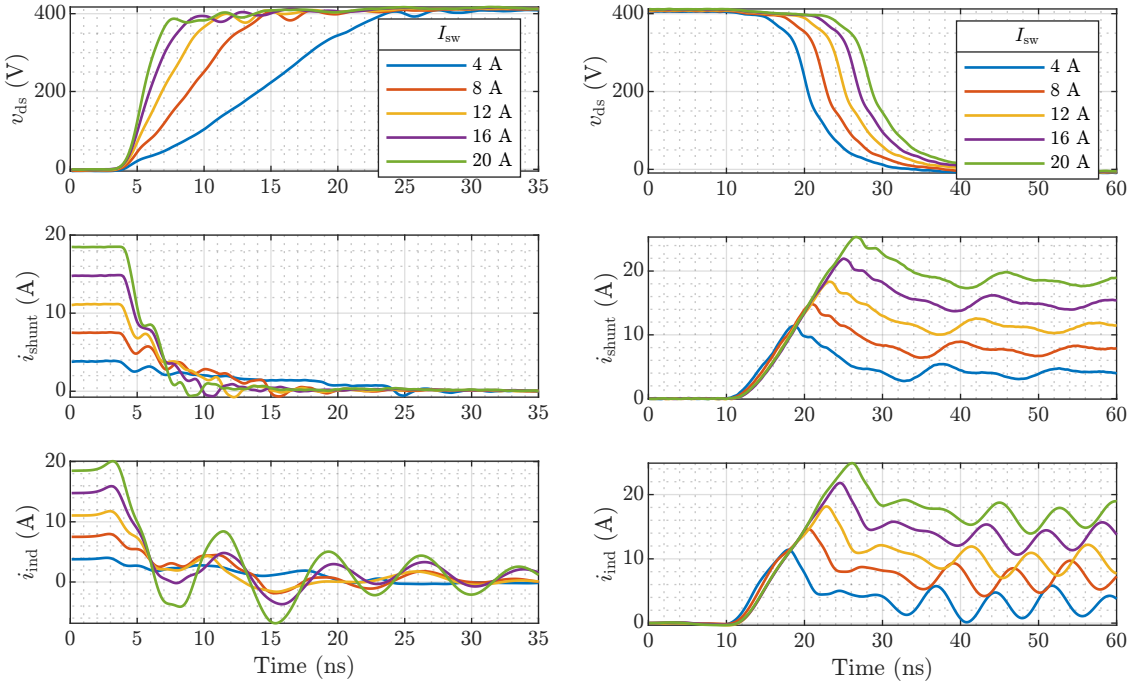

(c) turn-off, V_{sw} = 400 V

(d) turn-on, V_{sw} = 400 V

Figure A.8: Measured switching transients with shunt and inductive sensor at different operating points (V_{sw} = 300 V ... 400 V, I_{sw} = 4 A ... 20 A, T_{amb} = 25 °C)

A.9 Measured Switching Loss According to the IEC Standard

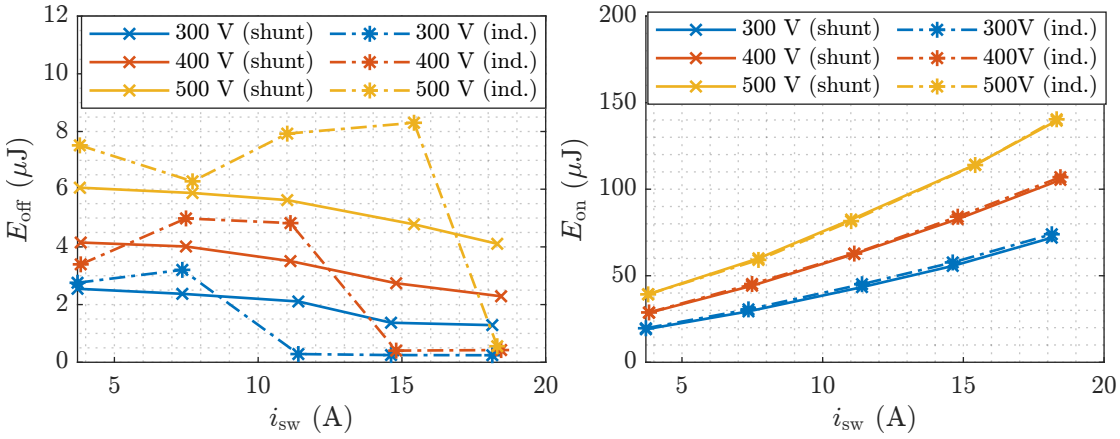

(a) turn-off (b) turn-on

Figure A.9: Measured switching loss with shunt and inductive sensor according to *IEC 60747-8* (V_{sw} = 300 V...500 V, I_{sw} = 5 A...20 A, T_{amb} = 25 °C)

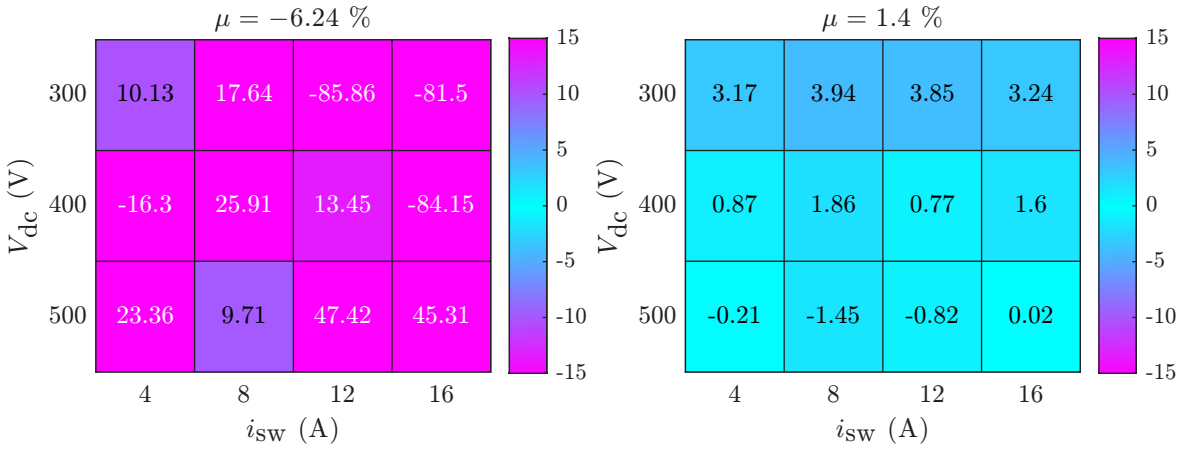

(a) turn-off (b) turn-on

Figure A.10: Relative percentage error between shunt and inductive sensor at different operating points according to the integral definition from *IEC 60747-8*

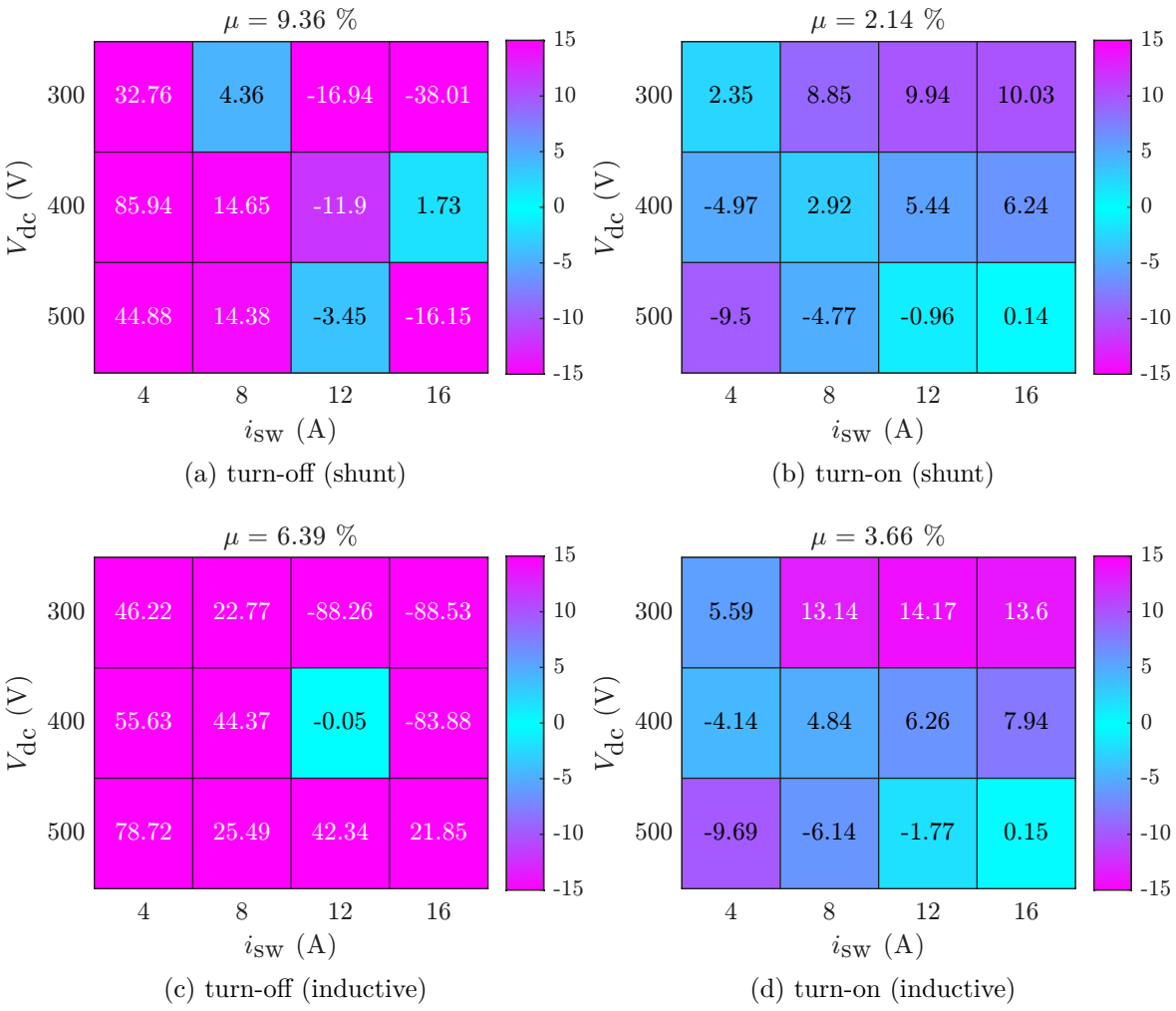

(a) turn-off (shunt)

(b) turn-on (shunt)

(c) turn-off (inductive)

(d) turn-on (inductive)

Figure A.11: Relative percentage error between measurement and simulation at different operating points according to the integral definition from *IEC 60747-8*

B Acronyms

Al_2O_3	Aluminum oxide
ADC	analog-to-digial converter
AlN	Alimunum nitride
AUX	auxiliary
BFOM	Baliga Figure of Merit
c-BN	cubic Boron nitride
CMC	common mode choke
CMRR	common mode rejection ratio
CPG	current pulse generator
DoE	design of experiments
DPT	double-pulse test
DSO	digital storage oscilloscope
DUT	device under test
EMI	electromagnetic interference
ENOB	effective number of bits
ESL	equivalent series inductance
ESR	equivalent series resistance
FEM	finite element method
FET	field-effect transistor
FIR	finite impulse response
FOCS	fibre-optic current sensor
GaN	Gallium nitride
HEMT	high-electron-mobility transistor
HV	high-voltage
IGBT	insulated-gate bipolar transistor
LV	low-voltage

MLCC	multi-layer ceramic capacitor
MoM	method of moments
MOSFET	metal-oxide semiconductor field-effect transistor
MPE	mean percentage error
Ni-P	nickel-phosphorus
NiCr	Nichrome
OCP	overcurrent protection
PCB	printed circuit board
PDF	probability density function
pp	percentage point
PWM	pulse-width modulation
SBD	Schottky barrier diode
Si	Silicon
SiC	Silicon carbide
SMA	SubMiniature version A
SMB	SubMiniature version B
SMD	surface-mounted device
SNR	signal-to-noise ratio
SOA	safe operating area
SOLT	short-open-load-thru
TCR	temperature coefficient of resistance
UWBG	ultrawide-bandgap
VNA	vector network analyzer
WBG	wide-bandgap
ZVS	zero-voltage switching

C Symbols

α_{R}	temperature coefficient of resistance (TCR)
ω	angular frequency
C_{comp}	probe compensation capacitance
C_{DC}	capacitance of DC-link capacitor
C_{DS}	drain-gate capacitance
C_{GD}	gate-drain capacitance
C_{GS}	gate-source capacitance
C_{in}	input capacitance of oscilloscope
C_{ISS}	input capacitance
σ	electrical conductivity
C_1	circuit-specific capacitance value
C_{OSS}	output capacitance
C_{p}	parasitic parallel capacitance
C_{probe}	input capacitance of voltage probe
C_{RSS}	reverse transfer capacitance
C_{sn}	capacitance of snubber circuit
C_{th}	thermal capacitance
C_{tip}	capacitance of probe tip
D	damping factor
ΔE_{C}	change of the energy stored in the capacitor
ΔE_{L}	change of the energy stored in the inductor
ΔE_{R}	ohmic energy loss
Δt	time offset between two waveforms
ΔT	temperature difference
ΔV	voltage difference
$\mathrm{d}i/\mathrm{d}t$	slew rate of current
$\mathrm{d}v/\mathrm{d}t$	slew rate of voltage
E_{bd}	breakdown field strength
E_{g}	Bandgap of a semiconductor
E_{max}	rated maximum energy
E_{off}	turn-off switching energy
$E_{\mathrm{off,meas}}$	measured turn off switching energy
E_{on}	turn-on switching energy

$E_{\mathrm{on,meas}}$	measured turn on switching energy
E_{oss}	energy stored in output capacitance
$E_{\mathrm{OSS,H}}$	energy loss due to C_{OSS} hysteresis
ε_{r}	relative permittivity
E_{qoss}	energy stored in output capacitance of high-side transistor
E_{qrr}	energy loss caused by reverse-recovery effect of high-side transistor
$\varepsilon_{\mathrm{off}}$	rel. error for turn off switching energy
$\varepsilon_{\mathrm{on}}$	rel. error for turn on switching energy
$\varepsilon_{\mathrm{total}}$	rel. error for total switching energy
E_{shunt}	energy dissipated by shunt resistor
E_{sw}	total switching energy
$E_{\mathrm{V/I}}$	energy loss caused by overlap of voltage and current
f_{c}	3 dB cutoff frequency
$f_{\mathrm{c,i}}$	cutoff frequency of current probe
$f_{\mathrm{c,v}}$	cutoff frequency of voltage probe
$\vec{B}$	magnetic flux density
f_{max}	maximum frequency
f_{s}	sampling rate
f_{sw}	switching frequency
f_0	resonance frequency
K	integrator gain
g_{m}	transconductance
c	specific heat capacity
I_{D}	nominal drain current
i_{diode}	diode current
i_{ds}	drain source current
I_{DSS}	zero gate voltage drain current
i_{gd}	gate drain leakage current
i_{g}	gate current
i_{gs}	drain source leakage current
i_{ind}	current measured with inductive sensor
i_{L}	inductor current
j	imaginary unit
I_{max}	maximum current
i_{meas}	measured current
I_{oss}	current from output capacitance
I_{qoss}	current from output capacitance of HS transistor
I_{rr}	reverse recovery current

I_{set}	amplitude of reference current
i_{sense}	current to be measured
i_{shunt}	current measured with shunt resistor
I_{sw}	switching current
I_{x}	current flowing into port x
l_{coil}	legth of coil
L_{load}	inductance of load inductor
L_{loop}	parasitic inductance of power loop
L_1	circuit-specific inductance value
L_{probe}	parasitic inductance of current probe
L_{s}	equivalent series inductance
L_{shunt}	parasitic inductance of shunt resistor
M	mutual inductance
m	mass
μ	mean value
N_{w}	winding count
ϕ	phase in radian
p_{in}	input power
p_{loss}	instantaneous power loss
P_{N}	nominal power
p_{out}	output power
Q_{G}	total gate charge
Q_{GD}	gate-drain charge
$Q_{\text{GS(pl)}}$	plateau gate charge
$Q_{\text{GS(th)}}$	threshold gate charge
Q_{OSS}	charge in output capacitance
Q_{rr}	reverse recovery charge
R_{circ}	resistance of circular resistor
R_{CS}	resistance of current sense resistor
R_{d}	resistance of damping resistor
$R_{\text{DS(on)}}$	drain-source on-resistance
$R_{\text{G,off}}$	gate turn off resistor
$R_{\text{G,on}}$	gate turn on resistor
R_{in}	input resistance of oscilloscope
R_1	circuit-specific resistance value
r_1	inner radius
R_{s}	equivalent series resistance
R_{sheet}	specific sheet resistance
R_{shunt}	resistance of shunt resistor

R_{sn}	resistance of snubber circuit
R_{T}	termination resistance
R_{th}	thermal resistance
R_{tip}	resitance of probe tip
r_2	outer radius
σ	standard deviation
$\mathrm{S_{HS}}$	high-side switch
$\mathrm{S_{LS}}$	low-side switch
s_{on}	logical turn on signal
S_{mn}	element of S-parameter matrix
T_{amb}	ambient temperature
τ_{g}	group delay
τ	time constant of an exponential function
t_{break}	turn off period between frist and second pulse
T_{c}	case temperature
λ	thermal conductivity
$t_{\mathrm{d(off)}}$	turn-off delay
$t_{\mathrm{d(on)}}$	turn-on delay
$G(\mathrm{j}\omega)$	transfer function
t_{fall}	fall time of a transient
T_{j}	junction temperature
T	chain-parameter matrix
T_{max}	maximum temperature
T_{mn}	element of T-parameter matrix
t_{off}	turn-off time
t_{on}	turn-on time
t_{12}	thickness of prepreg between layer 1 and 2
$t_{\mathrm{period,min}}$	minimum pulse period
t_{R}	thickness of discrete resistor
t_{ramp}	ramp time (duration of first pulse)
t_{rise}	rise time of a transient
t_{rr}	reverse recovery time
t_{s}	sampling time
T_{s}	settling time of system response
t_{skew}	misalignment between voltage and current waveform
t	variable point in time
$V_{\mathrm{(BR)DSS}}$	drain-source breakdown voltage
v_{coil}	output voltage of coil
V_{dc}	DC voltage
v_{diode}	diode voltage
V_{DS}	nominal drain source voltage
v_{ds}	drain source voltage

V_{F}	forward voltage drop
v_{gd}	gate drain voltage
v_{gs}	gate source voltage
$V_{\mathrm{GS,on}}$	gate turn on voltage
v_{in}	input voltage
v_{ind}	induced voltage
V_{max}	maximum voltage
v_{meas}	measured voltage
v_{offset}	offset voltage
v_{out}	output voltage
V_{rr}	reverse recovery voltage
v_{sat}	electron saturation velocity
v_{shunt}	voltage drop across shunt resistor
V_{sw}	switching voltage
$v_{\mathrm{GS(th)}}$	gate source threshold voltage
V_{x}	voltage at port x
$\vec{a}$	vector of incident wave
a_{x}	element of vector $\vec{a}$
$\vec{b}$	vector of reflected wave
b_{x}	element of vector $\vec{b}$
w_{coil}	width of coil
d_{coil}	distance between coils
w_{trace}	width of trace
Z_{in}	input impedance
$Z_{\mathrm{in,fitted}}$	input impedance (fitted)
Z_{L}	load impedance
Z	impendance-parameter matrix
Z_{mn}	element of Z-parameter matrix
Z_0	reference impedance for S-parameters
Z_{th}	thermal impedance
Z_{21}	transfer impedance

List of Figures

List of Tables

Bibliography

[1] T. Ueda, "Reliability issues in gan and sic power devices," in *2014 IEEE International Reliability Physics Symposium*, 2014, pp. 3D.4.1–3D.4.6.

[2] K. J. Chen, O. Häberlen, A. Lidow, *et al.*, "Gan-on-si power technology: Devices and applications," *IEEE Transactions on Electron Devices*, vol. 64, no. 3, pp. 779–795, 2017.

[3] N. Keshmiri, D. Wang, B. Agrawal, R. Hou, and A. Emadi, "Current status and future trends of gan hemts in electrified transportation," *IEEE Access*, vol. 8, pp. 70 553–70 571, 2020.

[4] N. Bajaj. "Unlocking a greener tomorrow: The transformative impact of gan technology." Power Electronics News, Ed. (Nov. 11, 2024), [Online]. Available: `https://www.powerelectronicsnews.com/unlocking-a-greener-tomorrow-the-transformative-impact-of-gan-technology/`.

[5] A. Elasser and T. Chow, "Silicon carbide benefits and advantages for power electronics circuits and systems," *Proceedings of the IEEE*, vol. 90, no. 6, pp. 969–986, 2002.

[6] J. Tsao, S. Chowdhury, M. Hollis, *et al.*, "Ultrawide-bandgap semiconductors: Research opportunities and challenges," *Advanced Electronic Materials*, vol. 4, Dec. 2017.

[7] M. H. Wong, O. Bierwagen, R. J. Kaplar, and H. Umezawa, "Ultrawide-bandgap semiconductors: An overview," *Journal of Materials Research*, vol. 36, no. 23, pp. 4601–4615, 2021.

[8] S. J. Pearton, J. Yang, I. Cary Patrick H., *et al.*, "A review of Ga2O3 materials, processing, and devices," *Applied Physics Reviews*, vol. 5, no. 1, p. 011 301, Jan. 2018.

[9] J. Henn, C. Lüdecke, M. Laumen, *et al.*, "Intelligent gate drivers for future power converters," *IEEE Transactions on Power Electronics*, vol. 37, no. 3, pp. 3484–3503, 2022.

[10] M. Kaufmann and B. Wicht, *Monolithic Integration in E-Mode GaN Technology* (Synthesis Lectures on Engineering, Science, and Technology). Springer International Publishing, 2022.

[11] P. Sun, M. Zou, Y. Wang, *et al.*, "Focuses and concerns of dynamic test for wide bandgap device: A questionnaire-based survey," *IEEE Transactions on Power Electronics*, vol. 38, no. 12, pp. 15 522–15 534, 2023.

[12] Z. Zeng, J. Wang, L. Wang, Y. Yu, and K. Ou, "Inaccurate switching loss measurement of sic mosfet caused by probes: Modelization, characterization, and validation," *IEEE Transactions on Instrumentation and Measurement*, vol. 70, pp. 1–14, 2021.

[13] Z. Zhang, B. Guo, F. F. Wang, E. A. Jones, L. M. Tolbert, and B. J. Blalock, "Methodology for wide band-gap device dynamic characterization," *IEEE Transactions on Power Electronics*, vol. 32, no. 12, pp. 9307–9318, Dec. 2017.

[14] W. Zhang, Z. Zhang, and F. Wang, "Review and bandwidth measurement of coaxial shunt resistors for wide-bandgap devices dynamic characterization," in *IEEE Energy Conversion Congress and Exposition (ECCE)*, Sep. 2019, pp. 3259–3264.

[15] Z. Xin, H. Li, Q. Liu, and P. C. Loh, "A review of megahertz current sensors for megahertz power converters," *IEEE Transactions on Power Electronics*, vol. 37, no. 6, pp. 6720–6738, 2022.

[16] A. Wintrich, U. Nicolai, W. Tursky, S. I. GmbH, and T. Reimann, *Application Manual Power Semiconductors*. ISLE-Verlag, 2011.

[17] *Semiconductor devices - Discrete devices - Part 8: Field-effect transistors (IEC 60747-8:2010)*, International Electrotechnical Commission, Dec. 2010.

[18] N. Mohan, T. Undeland, and W. Robbins, *Power Electronics: Converters, Applications, and Design* (Power Electronics: Converters, Applications, and Design). John Wiley & Sons, 2003.

[19] K. Li, P. L. Evans, and C. M. Johnson, "Characterisation and modeling of gallium nitride power semiconductor devices dynamic on-state resistance," *IEEE Transactions on Power Electronics*, vol. 33, no. 6, pp. 5262–5273, 2018.

[20] Y. Cai, A. J. Forsyth, and R. Todd, "Impact of gan hemt dynamic on-state resistance on converter performance," in *2017 IEEE Applied Power Electronics Conference and Exposition (APEC)*, 2017, pp. 1689–1694.

[21] E. A. Jones and A. Pozo, "Hard-switching dynamic rds,on characterization of a gan fet with an active gan-based clamping circuit," in *2019 IEEE Applied Power Electronics Conference and Exposition (APEC)*, 2019, pp. 2757–2763.

[22] G. Zu, H. Wen, Y. Zhu, *et al.*, "Review of pulse test setup for the switching characterization of gan power devices," *IEEE Transactions on Electron Devices*, pp. 1–11, 2022.

[23] J. Fedison and M. Harrison, "Coss hysteresis in advanced superjunction mosfets," in *2016 IEEE Applied Power Electronics Conference and Exposition (APEC)*, 2016, pp. 247–252.

[24] Z. Tong, J. Roig-Guitart, T. Neyer, J. D. Plummer, and J. M. Rivas-Davila, "Origins of soft-switching coss losses in sic power mosfets and diodes for resonant converter applications," *IEEE Journal of Emerging and Selected Topics in Power Electronics*, vol. 9, no. 4, pp. 4082–4095, 2021.

[25] JEDEC Solid State Technology Association. "Test Methods for Switching Energy Loss Associated with Output Capacitance Hysteresis in Semiconductor Power Devices (JEP200)." (Jun. 2024), [Online]. Available: `https://www.jedec.org/standards-documents/docs/jep200`.

[26] K. Puschkarsky, H. Reisinger, T. Aichinger, W. Gustin, and T. Grasser, "Threshold voltage hysteresis in sic mosfets and its impact on circuit operation," in *2017 IEEE International Integrated Reliability Workshop (IIRW)*, 2017, pp. 1–5.

[27] D. Peters, T. Aichinger, T. Basler, G. Rescher, K. Puschkarsky, and H. Reisinger, "Investigation of threshold voltage stability of sic mosfets," in *2018 IEEE 30th International Symposium on Power Semiconductor Devices and ICs (ISPSD)*, 2018, pp. 40–43.

[28] J. Schweickhardt, K. Hermanns, and M. Herdin. "Application Note - Tips & Tricks on Double Pulse Testing." Rohde & Schwarz GmbH & Co. KG, Ed. (Mar. 2021), [Online]. Available: `https://scdn.rohde-schwarz.com/ur/pws/dl_downloads/dl_application/application_notes/gfm347/GFM347_1e_Double_Pulse_Testing.pdf`.

[29] J. Gottschlich, M. Kaymak, M. Christoph, and R. W. De Doncker, "A flexible test bench for power semiconductor switching loss measurements," in *2015 IEEE 11th International Conference on Power Electronics and Drive Systems*, Jun. 2015, pp. 442–448.

[30] K. Fujii, P. Koellensperger, and R. W. De Doncker, "Characterization and comparison of high blocking voltage igbts and iegts under hard- and soft-switching conditions," in *2006 37th IEEE Power Electronics Specialists Conference*, 2006, pp. 1–7.

[31] D. Garrido, I. Baraia-Etxaburu, J. Arza, and M. Barrenetxea, "Simple and affordable method for fast transient measurements of sic devices," *IEEE Transactions on Power Electronics*, vol. 35, no. 3, pp. 2933–2942, 2020.

[32] K. Johnson and D. Maliniak, "Oscilloscope probes for power electronics: Be sure to choose the right probe for accurate measurements," *IEEE Power Electronics Magazine*, vol. 5, no. 1, pp. 37–44, 2018.

[33] P. S. Niklaus, D. Bortis, and J. W. Kolar, "Next generation measurement systems with high common-mode rejection," in *2018 IEEE 19th Workshop on Control and Modeling for Power Electronics (COMPEL)*, Jun. 2018, pp. 1–8.

[34] "IEEE Standard for Terminology and Test Methods for Circuit Probes," *IEEE Std 1696-2013*, pp. 1–65, Feb. 2014.

[35] S. Sprunck, M. Koch, C. Lottis, and M. Jung, "Suitability of voltage sensors for the measurement of switching voltage waveforms in power semiconductors," *IEEE Open Journal of Power Electronics*, pp. 1–12, 2022.

[36] L. Hoffmann and J. Friebe, "Characterisation of wide-bandgap semiconductors in double pulse testing using optically isolated probes," in *PCIM Europe 2024; International Exhibition and Conference for Power Electronics, Intelligent Motion, Renewable Energy and Energy Management*, Jun. 11, 2024.

[37] H. Lutzen, J. Müller, and N. Kaminski, "A review of current sensors in power electronics: Fundamentals, measurement techniques and components to measure the fast transients of wide bandgap devices," in *2023 25th European Conference on Power Electronics and Applications (EPE'23 ECCE Europe)*, 2023, pp. 1–11.

[38] P. Poulichet, F. Costa, and E. Laboure, "A new high-current large-bandwidth dc active current probe for power electronics measurements," *IEEE Transactions on Industrial Electronics*, vol. 52, no. 1, pp. 243–254, 2005.

[39] S. Yin, Y. Wu, M. Dong, J. Lin, and H. Li, "Design of current transformer for in situ switching current measurement of discrete sic power devices," *IEEE Journal of Emerging and Selected Topics in Industrial Electronics*, pp. 1–1, 2022.

[40] M. H. Samimi, A. Mahari, M. A. Farahnakian, and H. Mohseni, "The rogowski coil principles and applications: A review," *IEEE Sensors Journal*, vol. 15, no. 2, pp. 651–658, Feb. 2015.

[41] T. Zhang, E. Shelton, L. Shillaber, and P. Palmer, "High current, high bandwidth current measurement techniques," in *2020 IEEE Energy Conversion Congress and Exposition (ECCE)*, 2020, pp. 3464–3470.

[42] S. Sprunck, C. Lottis, F. Schnabel, and M. Jung, "Suitability of current sensors for the measurement of switching currents in power semiconductors," *IEEE Open Journal of Power Electronics*, vol. 2, pp. 570–581, 2021.

[43] H. Dymond, Y. Wang, S. Jahdi, and B. Stark, "Probing techniques for gan power electronics: How to obtain 400+ mhz voltage and current measurement bandwidths without compromising pcb layout," in *PCIM Europe 2022*, Aug. 2022, pp. 1–10.

[44] ABB Switzerland Ltd. "ABB FOCS - Fiber-Optic Current Sensors." (2004), [Online]. Available: `https://library.e.abb.com/public/d5dd4fe92316ebe4c1257b130056e110/3BHS208968E01_REV-_ABB%20FOCS%20Brochure.pdf`.

[45] S. Sprunck, M. Muench, and P. Zacharias, "Transient current sensors for wide band gap semiconductor switching loss measurements," in *Proceedings of the PCIM Europe, Nuremberg, Germany*, May 2019, pp. 1–8.

[46] Iwatsu Electric Co., Ltd. "Opical probe Electric Current Sensor (OpECS)." (May 2024), [Online]. Available: `https://www.iwatsu.com/wp-content/uploads/2024/05/OpECS_Catalog_EN_202405.pdf`.

[47] C. New, A. N. Lemmon, B. T. DeBoi, M. R. Hontz, A. J. Sellers, and R. Khanna, "Comparison of methods for switching loss estimation in wbg systems," in *2019 IEEE Electric Ship Technologies Symposium (ESTS)*, Aug. 2019, pp. 569–576.

[48] Q. Yang, A. Nabih, R. Zhang, Q. Li, and Y. Zhang, "A converter based switching loss measurement method for wbg device," in *2023 IEEE Applied Power Electronics Conference and Exposition (APEC)*, 2023, pp. 8–13.

[49] H. Wen, Y. Zhang, D. Jiao, and J.-S. Lai, "A new method of switching loss evaluation for gan hemts in half-bridge configuration," in *IEEE Applied Power Electronics Conference and Exposition (APEC)*, Mar. 2020, pp. 647–651.

[50] K. Rigbers, S. Schroder, R. de Doncker, P. Lurkens, M. Wendt, and U. Boke, "High-efficient soft-switching converter for three-phase grid connections of renewable energy systems," in *2005 International Conference on Power Electronics and Drives Systems*, vol. 1, 2005, pp. 246–250.

[51] J. R. A. Da Cruz, W. B. Correia, D. De S. O. Junior, and A. M. O. Silva, "Design of a double-jacket closed-type calorimeter for power loss measurement of power electronic devices," in *2023 IEEE 8th Southern Power Electronics Conference and 17th Brazilian Power Electronics Conference (SPEC/COBEP)*, 2023, pp. 1–5.

[52] S. Bolte, L. Keuck, J. K. Afridi, N. Fröhleke, and J. Böcker, "Calorimetric measurements with compensating temperature control," in *2017 IEEE 26th International Symposium on Industrial Electronics (ISIE)*, 2017, pp. 636–639.

[53] D. Neumayr, M. Guacci, D. Bortis, and J. W. Kolar, "New calorimetric power transistor soft-switching loss measurement based on accurate temperature rise monitoring," in *2017 29th International Symposium on Power Semiconductor Devices and IC's (ISPSD)*, 2017, pp. 447–450.

[54] J. Weimer, D. Koch, R. Schnitzler, and I. Kallfass, "Determination of hard- and soft-switching losses for wide bandgap power transistors with noninvasive and fast calorimetric measurements," in *2021 33rd International Symposium on Power Semiconductor Devices and ICs (ISPSD)*, 2021, pp. 327–330.

[55] J. Weimer, R. Schnitzler, D. Koch, and I. Kallfass, "Thermal impedance calibration for rapid and non-invasive calorimetric soft-switching loss characterization," *IEEE Transactions on Power Electronics*, pp. 1–14, 2023.

[56] S. Ramo, J. R. Whinnery, and T. Van Duzer, *Fields and waves in communication electronics*. John Wiley & Sons, 1994.

[57] C. Mittermayer and A. Steininger, "On the determination of dynamic errors for rise time measurement with an oscilloscope," *IEEE Transactions on Instrumentation and Measurement*, vol. 48, no. 6, pp. 1103–1107, 1999.

[58] W. M. Leach Jr, "The differential time-delay distortion and differential phase-shift distortion as measures of phase linearity," *Journal of the Audio Engineering Society*, vol. 37, no. 9, pp. 709–715, 1989.

[59] C. Lottis, S. Sprunck, B. Sah, and M. Jung, "Compensation techniques for bandwidth-distorted measurementsof fast transients in double pulse tests," in *PCIM Europe 2024; International Exhibition and Conference for Power Electronics, Intelligent Motion, Renewable Energy and Energy Management*, Jun. 11, 2024.

[60] H. K. Schoenwetter, "High-accuracy settling time measurements," *IEEE Transactions on Instrumentation and Measurement*, vol. 32, no. 1, pp. 22–27, 1983.

[61] Teledyne LeCroy, Inc. "User Manual PP017 and PP018 Passive Probes." (May 2021), [Online]. Available: `https://cdn.teledynelecroy.com/files/manuals/pp017-pp018-user-manual.pdf`.

[62] G. Engelmann, N. Fritz, C. Lüdecke, *et al.*, "Impact of the different parasitic inductances on the switching behavior of sic mosfets," in *2018 IEEE 18th International Power Electronics and Motion Control Conference (PEMC)*, 2018, pp. 918–925.

[63] J. Lautner and B. Piepenbreier, "Impact of current measurement on switching characterization of gan transistors," in *2014 IEEE Workshop on Wide Bandgap Power Devices and Applications*, 2014, pp. 98–102.

[64] Gan Systems, Inc. "GS61004B 100V enhancement mode GaN transistor (Datasheet)." (Dec. 1, 2022), [Online]. Available: `https://gansystems.com/wp-content/uploads/2020/04/GS61004B-DS-Rev-221201.pdf`.

[65] Teledyne LeCroy, Inc. "DCS025 Deskew Calibration Source (Datasheet)." (2017), [Online]. Available: `https://cdn.teledynelecroy.com/files/pdf/dcs025-datasheet.pdf`.

[66] P. M. Gaudo and C. Bernal, "Phase shift deskew of oscilloscope current and voltage sensing probes by means of energy balance," in *2008 71st ARFTG Microwave Measurement Conference*, 2008, pp. 1–4.

[67] S. Yin, Y. Liu, Y. Gu, *et al.*, "Automatic v - i alignment for switching characterization of wide band gap power devices," in *2018 1st Workshop on Wide Bandgap Power Devices and Applications in Asia (WiPDA Asia)*, May 2018, pp. 75–78.

[68] M. Dong, H. Li, S. Yin, Y. Wu, and K. Y. See, "A postprocessing-technique-based switching loss estimation method for gan devices," *IEEE Transactions on Power Electronics*, vol. 36, no. 7, pp. 8253–8266, 2021.

[69] D. A. R. Fulton. "Oscilloscope Fundamentals Primer." Rohde & Schwarz USA, Inc., Ed. (Jul. 19, 2012), [Online]. Available: `https://ethz.ch/content/dam/ethz/special-interest/chab/chab-dept/research/documents/LPC/oscilloscopefundamentals.pdf`.

[70] P. J. Pupalaikis. "Random Interleaved Sampling (RIS)." LeCroy Corporation, Ed. (Sep. 25, 2003), [Online]. Available: `https://cdn.teledynelecroy.com/files/whitepapers/wp_ris_102203.pdf`.

[71] W. Kester and Analog Devices, Inc., *Data Conversion Handbook* (Analog Devices series). Elsevier Science, 2005.

[72] Teledyne LeCroy, Inc. "WaveRunner 8000HD (Datasheet)." (2023), [Online]. Available: `https://cdn.teledynelecroy.com/files/pdf/waverunner-8000hd-datasheet.pdf`.

[73] R. De Doncker, "Zero-voltage crossing detector for soft-switching devices," US5166549A, Nov. 24, 1992.

[74] N. Förster, D. Urbaneck, B. Kohlhepp, D. Kübrich, O. Wallscheid, and F. Schafmeister, "Pitfalls and their avoidability in the double-pulse test," in *PCIM Europe 2024; International Exhibition and Conference for Power Electronics, Intelligent Motion, Renewable Energy and Energy Management*, Jun. 11, 2024.

[75] G. Sergentanis, Y. R. De Novaes, L. De Lillo, L. Empringham, and M. C. Johnson, "Dynamic characterization of 650v gan hemt transistors," in *2023 IEEE 8th Southern Power Electronics Conference and 17th Brazilian Power Electronics Conference (SPEC/COBEP)*, 2023, pp. 1–7.

[76] J. Xu, Y. Qiu, D. Chen, J. Lu, R. Hou, and P. Di Maso. "An experimental comparison of gan e-hemts versus sic mosfets over differentoperating temperatures." GaN Systems Inc., Ed. (Oct. 17, 2017), [Online]. Available: `https://gansystems.com/wp-content/uploads/2018/01/An-Experimental-Comparison-of-GaN-E-HEMTs-versus-SiC-MOSFETs-over-Different-Operating-Temperatures.pdf`.

[77] R. Hou, J. Xu, and D. Chen, "A multivariable turn-on/turn-off switching loss scaling approach for high-voltage gan hemts in a hard-switching half-bridge configuration," in *2017 IEEE 5th Workshop on Wide Bandgap Power Devices and Applications (WiPDA)*, 2017, pp. 171–176.

[78] R. Hou, J. Lu, and D. Chen, "Parasitic capacitance eqoss loss mechanism, calculation, and measurement in hard-switching for gan hemts," in *2018 IEEE Applied Power Electronics Conference and Exposition (APEC)*, Mar. 2018, pp. 919–924.

[79] M. Guacci, M. Heller, D. Neumayr, *et al.*, "On the origin of the C_{oss} -losses in soft-switching gan-on-si power hemts," *IEEE Journal of Emerging and Selected Topics in Power Electronics*, vol. 7, no. 2, pp. 679–694, 2019.

[80] JEDEC Solid State Technology Association. "Guidelines for Representing Switching Losses of SIC Mosfets in Datasheets (JEP187)." (Dec. 2021), [Online]. Available: `https://www.jedec.org/standards-documents/docs/jep187`.

[81] N. Zhang, Z. Lin, L. Hong, Y. Tang, and H. Ma, "An improved analytical model of gan hemt in cascode configuration during turn-on transition," in *2015 IEEE 24th International Symposium on Industrial Electronics (ISIE)*, 2015, pp. 233–238.

[82] S. Klever and R. W. De Doncker, "A simulative study of measurement errors during double pulsetesting of gan devices," in *PCIM Europe 2024; International Exhibition and Conference for Power Electronics, Intelligent Motion, Renewable Energy and Energy Management*, Jun. 11, 2024.

[83] D. Martin, P. Killeen, W. A. Curbow, B. Sparkman, L. E. Kegley, and T. McNutt, "Comparing the switching performance of sic mosfet intrinsic body diode to additional sic schottky diodes in sic power modules," in *2016 IEEE 4th Workshop on Wide Bandgap Power Devices and Applications (WiPDA)*, 2016, pp. 242–246.

[84] Gan Systems, Inc. "GS66508T Top-side cooled 650 V E-mode GaN transistor (Datasheet)." (Apr. 2, 2020), [Online]. Available: https://gansystems.com/wp-content/uploads/2020/04/GS66508T-DS-Rev-200402.pdf.

[85] Rohm Semiconductor. "SCT4045DW7 N-channel SiC power MOSFET (Datasheet)." (Aug. 23, 2023), [Online]. Available: https://fscdn.rohm.com/en/products/databook/datasheet/discrete/sic/mosfet/sct4045dw7-e.pdf.

[86] Rohm Semiconductor. "SCT4062KW7 N-channel SiC power MOSFET (Datasheet)." (Aug. 23, 2023), [Online]. Available: https://fscdn.rohm.com/en/products/databook/datasheet/discrete/sic/mosfet/sct4062kw7-e.pdf.

[87] Rohm Semiconductor. "SCS210KE2SiC Schottky Barrier Diode (Datasheet)." (May 6, 2022), [Online]. Available: https://fscdn.rohm.com/en/products/databook/datasheet/discrete/sic/sbd/scs210ke2-e.pdf.

[88] GaN Systems Inc. "GN001 Application Note - Design with GaN Enhancement mode HEMT." (Apr. 2018), [Online]. Available: https://cn.gansystems.com/wp-content/uploads/2018/01/91096_GaNSystems__GN001_Design_with_GaN_EHEMT_Rev3_20161007.pdf.

[89] GaN Systems Inc. "GN012 Application Note - Gate Driver Circuit Designwith GaN E-HEMTs." (Mar. 2022), [Online]. Available: https://gansystems.com/wp-content/uploads/2022/03/GN012_Gate-Driver-Design-with-GaN-E-HEMTs_220308.pdf.

[90] K. Wang, M. Tian, H. Li, F. Zhang, X. Yang, and L. Wang, "An improved switching loss model for a 650v enhancement-mode gan transistor," in *2016 IEEE 2nd Annual Southern Power Electronics Conference (SPEC)*, 2016, pp. 1–6.

[91] K. Wang, X. Yang, H. Li, H. Ma, X. Zeng, and W. Chen, "An analytical switching process model of low-voltage egan hemts for loss calculation," *IEEE Transactions on Power Electronics*, vol. 31, no. 1, pp. 635–647, Jan. 2016.

[92] J.-W. Shin and J. Shin, "Simulating Wide Bandgap FET Models in LTspice," in *2022 International Power Electronics Conference (IPEC-Himeji 2022- ECCE Asia)*, 2022, pp. 1952–1958.

[93] GaN Systems Inc. "GN006 Application Note - SPICE model for GaN HEMT - usage guidelines and example." (Aug. 2016), [Online]. Available: https://gansystems.com/wp-content/uploads/2018/01/GN006_SPICE-model-for-GaN-HEMT-usage-guidelines-and-example-v10.pdf.

[94] ROHM Co., Ltd. "Application Note - How to Use LTspice Models." (Jan. 2024), [Online]. Available: https://fscdn.rohm.com/en/products/databook/applinote/common/how_to_use_ltspice_models_an-e.pdf.

[95] A. Hu and J. Biela, "An analytical switching loss model for a sic mosfet and schottky diode half-bridge based on nonlinear differential equations," in *2021 23rd European Conference on Power Electronics and Applications (EPE'21 ECCE Europe)*, Sep. 2021, P.1–P.11.

[96] GaN Systems Inc. "LTspice Model User Guide." (2017), [Online]. Available: https://gansystems.com/wp-content/uploads/2018/05/LTspice-Model-User-Guide.pdf.

[97] Transphorm Inc. "Application Note 0009 - Recommended External Circuitry for Transphorm GaN FETs." (2018), [Online]. Available: https://www.transphormusa.com/en/document/recommended-external-circuitry-transphorm-gan-fets/.

[98] GaN Systems Inc. "GN008 Application Note - GaN Switching Loss Simulation using LTSpice." (Mar. 2022), [Online]. Available: https://gansystems.com/wp-content/uploads/2022/03/GN008-GaN_Switching_Loss_Simulation_LTspice_220308.pdf.

[99] J. Antony, *Design of Experiments for Engineers and Scientists*. Elsevier Science, 2023.

[100] Component Technical Committee. "AEC-Q101 - Failure Mechanism Based Stress Test Qualification For Discrete Semiconductors In Automotive Applications." (Mar. 1, 2021), [Online]. Available: http://www.aecouncil.com/Documents/AEC_Q101_Rev_E_Base_Document.pdf (visited on 02/05/2024).

[101] Teledyne LeCroy, Inc. "Oscilloscope Probes and Accessories (Catalog)." (Dec. 5, 2023), [Online]. Available: https://cdn.teledynelecroy.com/files/pdf/oscilloscope_probe_catalog.pdf.

[102] P. Velleman and D. Hoaglin, *Applications, Basics, and Computing of Exploratory Data Analysis* (Duxbury series in statistics and decision sciences). Duxbury Press, 1981.

[103] J. Devore and K. Berk, *Modern Mathematical Statistics with Applications*. Thomson Brooks/Cole, 2007.

[104] G. Leroy, "Understanding main and interaction effects," in *Designing User Studies in Informatics*. London: Springer London, 2011, pp. 113–123.

[105] R. Ren, H. Gui, Z. Zhang, *et al.*, "Characterization of 650 v enhancement-mode gan hemt at cryogenic temperatures," in *2018 IEEE Energy Conversion Congress and Exposition (ECCE)*, 2018, pp. 891–897.

[106] R. Hou, Y. Shen, H. Zhao, H. Hu, J. Lu, and T. Long, "Power loss characterization and modeling for gan-based hard-switching half-bridges considering dynamic on-state resistance," *IEEE Transactions on Transportation Electrification*, vol. 6, no. 2, pp. 540–553, Jun. 2020.

[107] J. Qi, K. Tian, Z. Mao, *et al.*, "Dynamic performance of 4h-sic power mosfets and si igbts over wide temperature range," in *2018 IEEE Applied Power Electronics Conference and Exposition (APEC)*, 2018, pp. 2712–2716.

[108] B. N. Torsæter, S. Tiwari, R. Lund, and O.-M. Midtgård, "Experimental evaluation of switching characteristics, switching losses and snubber design for a full sic half-bridge power module," in *2016 IEEE 7th International Symposium on Power Electronics for Distributed Generation Systems (PEDG)*, 2016, pp. 1–8.

[109] C. Johnson, "Current measurement using compensated coaxial shunts," in *1991 IEE Colloquium on Measurement Techniques for Power Electronics*, 1991, pp. 7/1–7/4.

[110] T&M Research Products, Inc. "Current Viewing Resistors." (Mar. 2022), [Online]. Available: https://www.tandmresearch.com/index.php?page=products.

[111] T. Wickramasinghe, B. Allard, C. Buttay, *et al.*, "A study on shunt resistor-based current measurements for fast switching gan devices," in *IECON 2019 - 45th Annual Conference of the IEEE Industrial Electronics Society*, vol. 1, 2019, pp. 1573–1578.

[112] W. Zhang, Z. Zhang, F. Wang, E. V. Brush, and N. Forcier, "High-bandwidth low-inductance current shunt for wide-bandgap devices dynamic characterization," *IEEE Transactions on Power Electronics*, vol. 36, no. 4, pp. 4522–4531, Apr. 2021.

[113] E. V. Bedareva, E. I. Tsimbalist, A. A. Epifanova, and N. A. Gavrilenko, "Consideration of complementary error during design of the alternating current coaxial shunts," in *2015 International Conference on Mechanical Engineering, Automation and Control Systems (MEACS)*, 2015, pp. 1–4.

[114] H. Lutzen, V. Polezhaev, K. B. Rawal, K. Ahmmed, T. Huesgen, and N. Kaminski, "Temperature compensated m-shunts for fast transient and low inductive current measurements," in *CIPS 2022; 12th International Conference on Integrated Power Electronics Systems*, 2022, pp. 1–7.

[115] H. Lutzen, J. Müller, V. Polezhaev, T. Huesgen, and N. Kaminski, "Reducing the impact of skin effect induced measurement errors in m-shunts by deliberate field coupling," in *2022 24th European Conference on Power Electronics and Applications (EPE'22 ECCE Europe)*, 2022, P.1–P.11.

[116] M. Adelmund, C. Bödeker, and N. Kaminski, "Optimisation of shunt resistors for fast transients," in *PCIM Europe 2016; International Exhibition and Conference for Power Electronics, Intelligent Motion, Renewable Energy and Energy Management*, 2016, pp. 1–8.

[117] F. Yang, Z. Liang, Z. J. Wang, and F. Wang, "Design of a low parasitic inductance sic power module with double-sided cooling," in *2017 IEEE Applied Power Electronics Conference and Exposition (APEC)*, 2017, pp. 3057–3062.

[118] P. Ziegler, J. Haarer, P. Marx, M. Eckstein, A. Haspel, and J. Roth-Stielow, "Evaluation of a low-cost wide bandwidth current shunt for characterization of wide bandgap semiconductor devices," in *2023 25th European Conference on Power Electronics and Applications (EPE'23 ECCE Europe)*, 2023, pp. 1–9.

[119] L. Shillaber, Y. Jiang, L. Ran, and T. Long, "Ultrafast current shunt (ufcs): A gigahertz bandwidth ultra-low-inductance current sensor," *IEEE Transactions on Power Electronics*, vol. 37, no. 12, pp. 15 493–15 504, 2022.

[120] E. Shelton, N. Hari, X. Zhang, T. Zhang, J. Zhang, and P. Palmer, "Design and measurement considerations for wbg switching circuits," in *2017 19th European Conference on Power Electronics and Applications (EPE'17 ECCE Europe)*, 2017, P.1–P.10.

[121] M. Meissner, J. Schmitz, F. Weiss, and S. Bernet, "Current measurement of gan power devices using a frequency compensated smd shunt," in *PCIM Europe 2019; International Exhibition and Conference for Power Electronics, Intelligent Motion, Renewable Energy and Energy Management*, 2019, pp. 1–8.

[122] E. V. B. IV, N. M. Forcier, F. F. Wang, Z. Zhang, and W. Zhang, "Test Fixture for Observing Current Flow through a Set of Resistors (US 10,884,023 B2)," EN, U.S. Patent US10884023B2, Jan. 5, 2021.

[123] S. Klever, A. Thönnessen, and R. W. De Doncker, "Characterization of conventional and advanced current measurement techniques suitable for wbg semiconductor devices," in *2022 24th European Conference on Power Electronics and Applications (EPE'22 ECCE Europe)*, 2022, P.1–P.10.

[124] Y. Wang, Z. Zeng, T. Long, P. Sun, L. Wang, and M. Zou, "Impedance-matching shunt: Current sensor with ultrahigh bandwidth and extremely low parasitics for wide-bandgap device," *IEEE Transactions on Power Electronics*, vol. 37, no. 10, pp. 11 528–11 533, 2022.

[125] S. Klever and R. W. De Doncker, "A high-bandwidth and low-inductive sensor for measuring the commutation current of wbg devices," in *2023 25th European Conference on Power Electronics and Applications (EPE'23 ECCE Europe)*, 2023, pp. 1–8.

[126] U. Pogliano, G. C. Bosco, and D. Serazio, "Coaxial shunts as ac–dc transfer standards of current," *IEEE Transactions on Instrumentation and Measurement*, vol. 58, no. 4, pp. 872–877, 2009.

[127] A. Joannou and D. Pentz, "Miniature integrated co-axial current shunt for high frequency switching power electronics," *Group on Electronic Energy Processing (GEEP), Dept. of Electrical and Electronic EngineeringScience, Corner of University Road and Kingsway Road, University of Johannesburg, Johannesburg*, 2013.

[128] A. J. L. Joannou, D. C. Pentz, J. D. van Wyk, and A. S. de Beer, "Some considerations for miniaturized measurement shunts in high frequency power electronic converters," in *2014 16th European Conference on Power Electronics and Applications*, 2014, pp. 1–7.

[129] J. D. Jackson, *Classical electrodynamics*. American Association of Physics Teachers, 1999.

[130] S. Babic, C. Akyel, S. Salon, and S. Kincic, "New expressions for calculating the magnetic field created by radial current in massive disks," *IEEE Transactions on Magnetics*, vol. 38, no. 2, pp. 497–500, 2002.

[131] C. Akyel, S. Kincic, and S. Babic, "Fast calculation of the magnetic field in the system with radial current-carrying using thin sheet inductors," in *CCECE 2003 - Canadian Conference on Electrical and Computer Engineering. Toward a Caring and Humane Technology (Cat. No.03CH37436)*, vol. 1, 2003, 279–283 vol.1.

[132] H. Kong, F. Yang, C. Yang, *et al.*, "A highly integrated gan power module with low parasitic inductance and high thermal performance," in *2022 IEEE Energy Conversion Congress and Exposition (ECCE)*, 2022, pp. 1–7.

[133] B. Sun, Z. Zhang, and M. A. Andersen, "Research of low inductance loop design in gan hemt application," in *IECON 2018 - 44th Annual Conference of the IEEE Industrial Electronics Society*, Oct. 2018, pp. 1466–1470.

[134] P. V. Oorschot and J. Pustjens, "The resistor guide - the complete guide to the world of resistors," in D. Wilson, I. Hahn, R. Belviz, and PhilipCandole, Eds., 2nd ed. EETech Media, LLC., 2022, ch. 3.8 - Thin and Thick Film Resistors, pp. 72–76.

[135] Vishay Intertechnology, Inc. "Frequency Response of Thin Film Chip Resistors (Technical Note 60107)." (Feb. 2019), [Online]. Available: `https://www.vishay.com/docs/60107/freqresp.pdf`.

[136] N.-C. Chuang, J.-T. Lin, T.-C. Chang, T.-M. Tsai, K.-C. Chang, and C.-W. Wu, "The film thickness effect on electrical conduction mechanisms and characteristics of the ni–cr thin film resistor," *IEEE Journal of the Electron Devices Society*, vol. 4, no. 6, pp. 441–444, 2016.

[137] T. Garami and O. Krammer, "Investigating the mechanical effect of the solder joint thickness with simulation," in *2013 IEEE 19th International Symposium for Design and Technology in Electronic Packaging (SIITME)*, 2013, pp. 259–262.

[138] D. Pozar, *Microwave Engineering*. Wiley, 2011.

[139] Times Microwave Systems. "LMR 100A Flexible Low Loss Communications Coax (Datasheet)." (Mar. 2024), [Online]. Available: `https://timesmicrowave.com/wp-content/uploads/2022/03/lmr-100a-coax-cables-datasheet.pdf`.

[140] C. D. New, A. N. Lemmon, and B. T. DeBoi, "Sensitivities in high-bandwidth, high-current shunt measurements for silicon-carbide multi-chip power modules," in *2022 IEEE Applied Power Electronics Conference and Exposition (APEC)*, 2022, pp. 1658–1663.

[141] F. Isen, *DSP for MATLAB and LabVIEW: Digital filter design* (DSP for MATLAB and LabVIEW). Morgan & Claypool Publishers, 2008.

[142] F. Gustafsson, "Determining the initial states in forward-backward filtering," *IEEE Transactions on Signal Processing*, vol. 44, no. 4, pp. 988–992, 1996.

[143] B. Friedlander and B. Porat, "The modified yule-walker method of arma spectral estimation," *IEEE Transactions on Aerospace and Electronic Systems*, vol. AES-20, no. 2, pp. 158–173, 1984.

[144] Bourns, Inc. "CRT Series - Thin Film Precision Chip Resistors (Datasheet)." (Mar. 2020), [Online]. Available: `https://www.bourns.com/docs/Product-Datasheets/crt.pdf`.

[145] Vishay Intertechnology, Inc. "MCS 0402, MCT 0603, MCU 0805, MCA 1206 - Professional Thin Film Chip Resistors (Datasheet)." (May 4, 2023), [Online]. Available: `https://www.vishay.com/docs/28705/mcx0x0xpro.pdf`.

[146] JLC Electromet Pvt. Ltd. "Property Table of Nickel Chromium Alloys." (2023), [Online]. Available: `https://www.nickel-alloys.net/article/nichrome-nickel-chrome-alloys.html`.

[147] Bourns, Inc. "Material Declaration Sheet CRT0402." (Jun. 2012), [Online]. Available: `https://www.bourns.com/docs/Product-MDS/crt0402_mds.pdf`.

[148] L. Shillaber, L. Ran, Y. Shen, and T. Long, "Gigahertz current measurement for wide band-gap devices," in *2020 IEEE Energy Conversion Congress and Exposition (ECCE)*, 2020, pp. 2357–2363.

[149] J. Andresakis, P. Pramanik, D. Brandler, and D. Nong, "Novel substrate with combined embedded capacitance and resistance for better electrical performance and higher integration," in *56th Electronic Components and Technology Conference 2006*, 2006, 4 pp.

[150] H. Chammas, "Embedded passive technology - materials, design and process," *Quantic Ticer Publications*, vol. 32, pp. 30–35, Jan. 2015.

[151] Ohmega Technologies, Inc. "OhmegaPly Design (Presentation Slides)." (Sep. 2017), [Online]. Available: `https://quanticohmega.com/wp-content/uploads/Ohmega-Design-Version-2.1.pdf`.

[152] PEM UK - Power Electronic Measurements Ltd. "CWTMini50HF (Datasheet)." (Feb. 2020), [Online]. Available: `https://www.pemuk.com/Userfiles/cwtmini50hf/CWT_Mini50HF_DS_Feb_2020.pdf`.

[153] Tektronix, Inc. "30A AC/DC Current Probe TCP0030A (Datasheet)." (Aug. 28, 2017), [Online]. Available: `https://download.tek.com/datasheet/TCP0030A-Current-Probe-Datasheet-51W1904210.pdf`.

[154] Pearson Electronics, Inc. "Pearson Current Monitor Model 6585." (2019), [Online]. Available: `https://www.pearsonelectronics.com/products/wideband-current-monitors`.

[155] K. Klein and E. Hoene, "High speed current measurements for ultra low inductance power modules," in *ECPE Workshop: Current Measurement for Power Electronics Applications and in Lab Scale*, Oct. 2017.

[156] J. Wang, M. Hedayati, D. Liu, *et al.*, "Infinity sensor: Temperature sensing in gan power devices using peak di/dt," in *2018 IEEE Energy Conversion Congress and Exposition (ECCE 2018)*, United States, Dec. 2018, pp. 884–890.

[157] K. Wang, X. Yang, H. Li, L. Wang, and P. Jain, "A high-bandwidth integrated current measurement for detecting switching current of fast gan devices," *IEEE Transactions on Power Electronics*, vol. 33, no. 7, pp. 6199–6210, 2018.

[158] E. Hoene, A. Ostmann, B. Lai, C. Marczok, A. Müsing, and J. Kolar, "Ultra-low-inductance power module for fast switching semiconductors," *Proceedings of the PCIM Europe, Nuremberg, Germany*, pp. 198–205, Jan. 2013.

[159] A. Stippich, "Exploiting the full potential of silicon carbide devices via optimized highly integrated power modules," Dissertation, Rheinisch-Westfälische Technische Hochschule Aachen, Aachen, 2021.

[160] University of Bristol. "Datasheet for the Infinity Sensor V2." (Aug. 2022), [Online]. Available: `https://www.infinitysensor.com/resources`.

[161] Y. Wang, Q. Wang, M. Appleby, *et al.*, "'infinity gate sensor': A differential magnetic field sensor formeasuring gate current of sic power transistors," in *PCIM Europe 2024; International Exhibition and Conference for Power Electronics, Intelligent Motion, Renewable Energy and Energy Management*, Jun. 11, 2024.

[162] D. Koch, T. Fink, J. Nuzzo, K. M. Barón, and I. Kallfass, "Pcb-integrated pickup-coil for overcurrent detection in high-current, paralleled gan hemts," in *2024 IEEE Applied Power Electronics Conference and Exposition (APEC)*, 2024, pp. 555–560.

[163] D. Koch, H. Bantle, J. Acuna, P. Ziegler, and I. Kallfass, "Design methodology for ultra-compact rogowski coils for current sensing in low-voltage high-current gan based dc/dc-converters," in *2021 23rd European Conference on Power Electronics and Applications (EPE'21 ECCE Europe)*, 2021, P.1–P.9.

[164] W. Zhang, S. B. Sohid, F. Wang, H. Cui, and B. Holzinger, "High-bandwidth combinational rogowski coil for sic mosfet power module," *IEEE Transactions on Power Electronics*, vol. 37, no. 4, pp. 4397–4405, 2022.

[165] Y. Wang, T. Long, M. Zou, *et al.*, "Transmission line rogowski coil: Isolated current sensor with bandwidth exceeding 3 ghz for wide-bandgap device," *IEEE Transactions on Power Electronics*, vol. 38, no. 11, pp. 13 599–13 605, 2023.

[166] S. B. Sohid, X. Tian, N. Jia, *et al.*, "Pcb rogowski coil with dc sensing for double pulse test applications," *IEEE Transactions on Power Electronics*, pp. 1–9, 2023.

[167] M. Faraday, "Experimental researches in electricity, vol. 1," *Philosophical Transactions of the Royal Society of London*, vol. 122, pp. 125–162, 1832.

[168] N. Fritz, C. Neeb, and R. W. de Doncker, "A PCB Integrated Differential Rogowski Coil for Non-Intrusive Current Measurement Featuring High Bandwidth and dv/dt Immunity," in *Tagungsband zum Power and Energy Student Summit 2015*, Dortmund, Jan. 13, 2015.

[169] Y. Shi, Z. Xin, P. C. Loh, and F. Blaabjerg, "A review of traditional helical to recent miniaturized printed circuit board rogowski coils for power-electronic applications," *IEEE Transactions on Power Electronics*, vol. 35, no. 11, pp. 12 207–12 222, 2020.

[170] T. Funk and B. Wicht, *Integrated Wide-Bandwidth Current Sensing*. Springer International Publishing, 2020.

[171] G. D'Antona, M. Lazzaroni, R. Ottoboni, and C. Svelto, "Ac current-to-voltage transducer based on digital processing of rogowski coils signal," in *2nd ISA/IEEE Sensors for Industry Conference*, 2002, pp. 72–77.

[172] M. H. Hedayati, J. Wang, H. C. P. Dymond, D. Liu, and B. H. Stark, "Overtemperature protection circuit for gan devices using a di/dt sensor," *IEEE Transactions on Power Electronics*, vol. 36, no. 7, pp. 7417–7428, 2021.

[173] A. P. Sirat, H. Niakan, and B. Parkhideh, "Ultra-wideband surface current sensor topology for wide-bandgap power electronics applications," in *2023 IEEE 10th Workshop on Wide Bandgap Power Devices and Applications (WiPDA)*, 2023, pp. 1–6.

[174] Navitas Semiconductor. "NV6158 GaNFast Power IC with GaNSense Technology (Datasheet)." (Apr. 13, 2022), [Online]. Available: `https://www.mouser.com/datasheet/2/1451/NV6158_2520datasheet_2520FINAL_252004_13_22-3076939.pdf`.

[175] TDK Electronics AG. "CeraLink - Capacitor for fast-switching semiconductors." (Mar. 2023), [Online]. Available: `https://www.tdk-electronics.tdk.com/inf/20/10/ds/B58031_LP.pdf`.

[176] KEMET Electronics Corporation. "Differential Mode Coils, HHBC Series (Fe-Si) (Datasheet)." (Oct. 8, 2023), [Online]. Available: `https://content.kemet.com/datasheets/KEM_LF0050_HHBC.pdf`.

[177] B. Sun, Z. Zhang, and M. A. Andersen, "Research of pcb parasitic inductance in the gan transistor power loop," in *2019 IEEE Workshop on Wide Bandgap Power Devices and Applications in Asia (WiPDA Asia)*, May 2019, pp. 1–5.

[178] Multi Circuit Boards Ltd. "Defined Layer Buildup / Layout Examples for Impedance." (2024), [Online]. Available: `https://www.multi-circuit-boards.eu/fileadmin/pdf/leiterplatten_lagenaufbau/Multi-CB_Definierter_Lagenaufbau_Impedanzen_en.pdf`.

[179] R. Sun, Y. C. Liang, Y.-C. Yeo, and C. Zhao, "Au-free algan/gan mis-hemts with embedded current sensing structure for power switching applications," *IEEE Transactions on Electron Devices*, vol. 64, no. 8, pp. 3515–3518, 2017.

[180] S. Moench, R. Reiner, P. Waltereit, R. Quay, O. Ambacher, and I. Kallfass, "Integrated current sensing in gan power ics," in *2019 31st International Symposium on Power Semiconductor Devices and ICs (ISPSD)*, 2019, pp. 111–114.

[181] J. Roberts, G. Klowak, D. Chen, and A. Mizan, "Drive and protection methods for very high current lateral gan power transistors," in *2015 IEEE Applied Power Electronics Conference and Exposition (APEC)*, 2015, pp. 3128–3131.

[182] V.-S. Nguyen, R. Escoffier, S. Catellani, M. FaYolle-Lecocq, and J. Martin, "Design, implementation and characterization of an integrated current sensing in gan hemt device by using the current-mirroring technique," in *2022 24th European Conference on Power Electronics and Applications (EPE'22 ECCE Europe)*, 2022, pp. 1–9.

[183] F. Udrea, M. Arnold, L. Efthymiou, *et al.*, "The smart icegantm platform with sensing and protection functions for both enhanced ease of use and gate reliability," in *2022 IEEE 34th International Symposium on Power Semiconductor Devices and ICs (ISPSD)*, 2022, pp. 41–44.

[184] ANSYS, Inc. "ANSYS Q3D Getting Started - Module 2 - Q3D Workflow." (2020), [Online]. Available: `https://courses.ansys.com/wp-content/uploads/2021/07/Q3D_GS_2020R1_EN_LE02_Workflow.pdf`.

[185] ANSYS, Inc. "ANSYS Q3D Getting Started - Module 4 - Q3D Capacitance Matrix Reduction." (2020), [Online]. Available: `https://courses.ansys.com/wp-content/uploads/2021/07/Q3D_GS_2020R1_EN_LE04_Cap_Matrix.pdf`.

[186] Tektronix, Inc. "ABCs of Probes." (Feb. 2018), [Online]. Available: `https://download.tek.com/document/ABCs%20of%20Probes%2060W-6053-15.pdf`.

[187] Z. Qi, Y. Pei, L. Wang, *et al.*, "A high-bandwidth and easy-to-integrate parasitics-based switching current measurement method for fast gan devices," *IEEE Transactions on Power Electronics*, vol. 38, no. 1, pp. 447–459, 2023.

[188] Teledyne LeCroy, Inc. "10x Passive Probes and Cable Reflections." (Nov. 28, 2018), [Online]. Available: `https://blog.teledynelecroy.com/2018/11/10x-passive-probes-and-cable-reflections.html`.

[189] Thorlabs, Inc. "Technical Resources - Relationship Between Rise Time and Bandwidth for a Low-Pass System." (Apr. 1, 2019), [Online]. Available: `https://www.thorlabs.com/images/TabImages/Rise_Time_3dB_Bandwidth_Relationship_Lab_Fact.pdf`.

Curriculum Vitae

Severin Klever

Personal Information

Date of birth	January 6, 1993
Place of birth	Langenfeld (Rhld.), Germany
Nationality	German

Education

10/2016–12/2018	Studies for Master's Degree in Electrical Engineering, Information Technology and Technical Computer Science at RWTH Aachen University, Aachen, Germany
10/2012–09/2016	Studies for Bachelor's Degree in Electrical Engineering, Information Technology and Technical Computer Science at RWTH Aachen University, Aachen, Germany
08/2003–05/2012	Abitur (German High School Diploma) at Marienschule Opladen, Leverkusen, Germany

Work Experience

03/2019–05/2024	Research Associate in the Research Group for Power Electronics at the Institute for Power Electronics and Electrical Drives (ISEA) of RWTH Aachen University under the Supervision of Professor Rik W. De Doncker, Aachen, Germany
10/2017–03/2018	Internship in the R&D Department for Drives Technology and Power Electronics at Robert Bosch GmbH, Renningen, Germany

ABISEA Band 1
Eßer, Albert
Berührungslose, kombinierte Energie- und Informationsübertragung für bewegliche Systeme
1. Aufl. 1992, 129 S.
ISBN 3-86073-046-0

ABISEA Band 2
Vogel, Ulrich
Entwurf und Beurteilung von Verfahren zur Hochausnutzung des Rad-Schiene-Kraftschlusses durch Triebfahrzeuge
1. Aufl. 1992, 131 S.
ISBN 3-86073-060-6

ABISEA Band 3
Reckhorn, Thomas
Stromeinprägendes Antriebssystem mit fremderregter Synchronmaschine
1. Aufl. 1992, 128 S.
ISBN 3-86073-061-4

ABISEA Band 4
Ackva, Ansgar
Spannungseinprägendes Antriebssystem mit Synchronmaschine und direkter Stromregelung
1. Aufl. 1992, 137 S.
ISBN 3-86073-062-2

ABISEA Band 5
Mertens, Axel
Analyse des Oberschwingungsverhaltens von taktsynchronen Delta - Modulationsverfahren zur Steuerung von Pulsstromrichtern bei hoher Taktzahl
1. Aufl. 1992, 178 S.
ISBN 3-86073-069-X

ABISEA Band 6
Geuer, Wolfgang
Untersuchungen über das Alterungsverhalten von Blei-Akkumulatoren
1. Aufl. 1993, 97 S.
ISBN 3-86073-097-5

ABISEA Band 7
Langheim, Jochen
Einzelradantrieb für Elektrostraßenfahrzeuge
1. Aufl. 1993, 213 S.
ISBN 3-86073-123-8
(vergriffen)

ABISEA Band 8
Fetz, Joachim
Fehlertolerante Regelung eines Asynchron-Doppelantriebes für ein Elektrospeicherfahrzeug
1. Aufl. 1993, 136 S.
ISBN 3-86073-124-6
(vergriffen)

ABISEA Band 9
Schülting, Ludger
Optimierte Auslegung induktiver Bauelemente für den Mittelfrequenzbereich
1. Aufl. 1993, 126 S.
ISBN 3-86073-174-2
(vergriffen)

ABISEA Band 10
Skudelny, H.-Ch.
Stromrichtertechnik
4. Aufl. 1997, 259 S.
ISBN 3-86073-189-0

ABISEA Band 11
Skudelny, H.-Ch.
Elektrische Antriebe
3. Aufl. 1997, 124 S.
ISBN 3-86073-231-5

ABISEA Band 12
Schöpe, Friedhelm
Batterie-Management für Nickel-Cadmium Akkumulatoren
1. Aufl. 1994, 148 S.
ISBN 3-86073-232-3
(vergriffen)

ABISEA Band 13
v. d. Weem, Jürgen
Schmalbandige aktive Filter für Schienentriebfahrzeuge am Gleichspannungsfahrdraht
1. Aufl. 1995, 126 S.
ISBN 3-86073-233-1

ABISEA Band 14
Backhaus, Klaus
Spannungseinprägendes Direktantriebssystem mit schnelllaufender geschalteter Reluktanzmaschine
1. Aufl. 1995, 146 S.
ISBN 3-86073-234-X
(vergriffen)

ABISEA Band 15
Reinold, Harry
Optimierung dreiphasiger Pulsdauermodulationsverfahren
1. Aufl. 1996, 107 S.
ISBN 3-86073-235-8

ABISEA Band 16
Köpken, Hans-Georg
Regelverfahren für Parallelschwingkreisumrichter
1. Aufl. 1996, 125 S.
ISBN 3-86073-236-6

ABISEA Band 17
Mauracher, Peter
Modellbildung und Verbundoptimierung bei Elektrostraßenfahrzeugen
1. Aufl. 1996, 192 S.
ISBN 3-86073-237-4

ABISEA Band 18
Protiwa, Franz-Ferdinand
Vergleich dreiphasiger Resonanz-Wechselrichter in Simulation und Messung
1. Aufl. 1997, 178 S.
ISBN 3-86073-238-2

ABISEA Band 19
Brockmeyer, Ansgar
Dimensionierungswerkzeug für magnetische Bauelemente in Stromrichteranwendungen
1. Aufl. 1997, 175 S.
ISBN 3-86073-239-0

Aachener Beiträge des ISEA

ABISEA Band 20
Apeldoorn, Oscar
Simulationsgestützte Bewertung von Steuerverfahren für netzgeführte Stromrichter mit verringerter Netzrückwirkung
1. Aufl. 1997, 134 S.
ISBN 3-86073-680-9

ABISEA Band 21
Lohner, Andreas
Batteriemanagement für verschlossene Blei-Batterien am Beispiel von Unterbrechungsfreien Stromversorgungen
1. Aufl. 1998, 126 S.
ISBN 3-86073-681-7

ABISEA Band 22
Reinert, Jürgen
Optimierung der Betriebseigenschaften von Antrieben mit geschalteter Reluktanzmaschine
1. Aufl. 1998, 153 S.
ISBN 3-86073-682-5

ABISEA Band 23
Nagel, Andreas
Leitungsgebundene Störungen in der Leistungselektronik: Entstehung, Ausbreitung und Filterung
1. Aufl. 1999, 140 S.
ISBN 3-86073-683-3

ABISEA Band 24
Menne, Marcus
Drehschwingungen im Antriebsstrang von Elektrostraßenfahrzeugen - Analyse und aktive Dämpfung
1. Aufl. 2001, 169 S.
ISBN 3-86073-684-1

ABISEA Band 25
von Bloh, Jochen
Multilevel-Umrichter zum Einsatz in Mittelspannungs-Gleichspannungs-Übertragungen
1. Aufl. 2001, 137 S.
ISBN 3-86073-685-X

ABISEA Band 26
Karden, Eckhard
Using low-frequency impedance spectroscopy for characterization, monitoring, and modeling of industrial batteries
1. Aufl. 2002, 137 S.
ISBN 3-8265-9766-4

ABISEA Band 27
Karipidis, Claus-Ulrich
A Versatile DSP/ FPGA Structure optimized for Rapid Prototyping and Digital Real-Time Simulation of Power Electronic and Electrical Drive Systems
1. Aufl. 2001, 164 S.
ISBN 3-8265-9738-9

ABISEA Band 28
Kahlen, Klemens
Regelungsstrategien für permanentmagnetische Direktantriebe mit mehreren Freiheitsgraden
1. Aufl. 2002, 154 S.
ISBN 3-8322-1222-1

ABISEA Band 29
Inderka, Robert B.
Direkte Drehmomentregelung Geschalteter Reluktanzantriebe
1. Aufl. 2003, 182 S.
ISBN 3-8322-1175-6

ABISEA Band 30
Schröder, Stefan
Circuit-Simulation Models of High-Power Devices Based on Semiconductor Physics
1. Aufl. 2003, 123 S.
ISBN 3-8322-1250-7

ABISEA Band 31
Buller, Stephan
Impedance-Based Simulation Models for Energy Storage Devices in Advanced Automotive Power Systems
1. Aufl. 2003, 138 S.
ISBN 3-8322-1225-6

ABISEA Band 32
Schönknecht, Andreas
Topologien und Regelungsstrategien für das induktive Erwärmen mit hohen Frequenz-Leistungsprodukten
1. Aufl. 2004, 157 S.
ISBN 3-8322-2408-4

ABISEA Band 33
Tolle, Tobias
Konvertertopologien für ein aufwandsarmes, zweistufiges Schaltnetzteil zum Laden von Batterien aus dem Netz
1. Aufl. 2004, 148 S.
ISBN 3-8322-2676-1

ABISEA Band 34
Götting, Gunther
Dynamische Antriebsregelung von Elektrostraßenfahrzeugen unter Berücksichtigung eines schwingungsfähigen Antriebsstrangs
1. Aufl. 2004, 157 S.
ISBN 3-8322-2804-7

ABISEA Band 35
Dieckerhoff, Sibylle
Transformatorlose Stromrichterschaltungen für Bahnfahrzeuge am 16 2/3Hz Netz
1. Aufl. 2004, 147 S.
ISBN 3-8322-3094-7

ABISEA Band 36
Hu, Jing
Bewertung von DC-DC-Topologien und Optimierung eines DC-DC-Leistungsmoduls für das 42-V-Kfz-Bordnetz
1. Aufl. 2004, 148 S.
ISBN 3-8322-3201-X

ABISEA Band 37
Detjen, Dirk-Oliver
Characterization and Modeling of Si-Si Bonded Hydrophobie Interfaces for Novel High-Power BIMOS Devices
1. Aufl. 2004, 135 S.
ISBN 3-8322-2963-9

ABISEA Band 38
Walter, Jörg
Simulationsbasierte Zuverlässigkeitsanalyse in der modernen Leistungselektronik
1. Aufl. 2004, 121 S.
ISBN 3-8322-3481-0

ABISEA Band 39
Schwarzer, Ulrich
IGBT versus GCT in der Mittelspannungsanwendung - ein experimenteller und simulativer Vergleich
1. Aufl. 2005, 170 S.
ISBN 3-8322-4489-1

ABISEA Band 40
Bartram, Markus
IGBT-Umrichtersysteme für Windkraftanlagen: Analyse der Zyklenbelastung, Modellbildung, Optimierung und Lebensdauervorhersage
1. Aufl. 2006, 185 S.
ISBN 3-8322-5039-5

ABISEA Band 41
Ponnaluri, Srinivas
Generalized Design, Analysis and Control of Grid side converters with integrated UPS or Islanding functionality
1. Aufl. 2006, 163 S.
ISBN 3-8322-5281-9

ABISEA Band 42
Jacobs, Joseph
Multi-Phase Series Resonant DC-to-DC Converters
1. Aufl. 2006, 185 S.
ISBN 3-8322-5532-X

ABISEA Band 43
Linzen, Dirk
Impedance-Based Loss Calculation and Thermal Modeling of Electrochemical Energy Storage Devices for Design Considerations of Automotive Power Systems
1. Aufl. 2006, 185 S.
ISBN 3-8322-5706-3

ABISEA Band 44
Fiedler, Jens
Design of Low-Noise Switched Reluctance Drives
1. Aufl. 2007, 176 S.
ISBN 978-3-8322-5864-1

ABISEA Band 45
Fuengwarodsakul, Nisai
Predictive PWM-based Direct Instantaneous Torque Control for Switched Reluctance Machines
1. Aufl. 2007, 141 S.
ISBN 978-3-8322-6210-5

ABISEA Band 46
Meyer, Christoph
Key Components for Future Offshore DC Grids
1. Aufl. 2007, 187 S.
ISBN 978-3-8322-6571-7

ABISEA Band 47
Fujii, Kansuke
Characterization and Optimization of Soft-Switched Multi-Level Converters for STATCOMs
1. Aufl. 2008, 199 S.
ISBN 978-3-8322-6981-4

ABISEA Band 48
Carstensen, Christian
Eddy Currents in Windings of Switched Reluctance Machines
1. Aufl. 2008, 179 S.
ISBN 978-3-8322-7118-3

ABISEA Band 49
Bohlen, Oliver
Impedance-based battery monitoring
1. Aufl. 2008, 190 S.
ISBN 978-3-8322-7606-5

ABISEA Band 50
Thele, Marc
A contribution to the modelling of the charge acceptance of lead-acid batteries - using frequency and time domain based concepts
1. Aufl. 2008, 165 S.
ISBN 978-3-8322-7659-1

ABISEA Band 51
König, Andreas
High Temperature DC-to-DC Converters for Downhole Applications
1. Aufl. 2009, 154 S.
ISBN 978-3-8322-8489-3

ABISEA Band 52
Dick, Christian Peter
Multi-Resonant Converters as Photovoltaic Module-Integrated Maximum Power Point Tracker
1. Aufl. 2010, 182 S.
ISBN 978-3-8322-9199-0

ABISEA Band 53
Kowal, Julia
Spatially resolved impedance of nonlinear inhomogeneous devices: using the example of lead-acid batteries
1. Aufl. 2010, 203 S.
ISBN 978-3-8322-9483-0

ABISEA Band 54
Roscher, Michael Andreas
Zustandserkennung von LiFeP04-Batterien für Hybrid- und Elektrofahrzeuge
1. Aufl. 2011, 186 S.
ISBN 978-3-8322-9738-1

ABISEA Band 55
Hirschmann, Dirk
Highly Dynamic Piezoelectric Positioning
1. Aufl. 2011, 146 S.
ISBN 978-3-8322-9746-6

ABISEA Band 56
Rigbers, Klaus
Highly Efficient Inverter Architectures for Three-Phase Grid Connection of Photovoltaic Generators
1. Aufl. 2011, 244 S.
ISBN 978-3-8322-9816-9

ABISEA Band 57
Kasper, Knut
Analysis and Control of the Acoustic Behavior of Switched Reluctance Drives
1. Aufl. 2011, 205 S.
ISBN 978-3-8322-9869-2

Aachener Beiträge des ISEA

ABISEA Band 58
Köllensperger, Peter
The Internally Commutated Thyristor - Concept, Design and Application
1. Aufl. 2011, 214 S.
ISBN 978-3-8322-9909-5

ABISEA Band 59
Schoenen, Timo
Einsatz eines DC/DC-Wandlers zur Spannungsanpassung zwischen Antrieb und Energiespeicher in Elektro-und Hybridfahrzeugen
1. Aufl. 2011, 128 S.
ISBN 978-3-8440-0622-3

ABISEA Band 60
Hennen, Martin
Switched Reluctance Direct Drive with Integrated Distributed Inverter
1. Aufl. 2012, 141 S.
ISBN 978-3-8440-0731-2

ABISEA Band 61
van Treek, Daniel
Position Sensorless Torque Control of Switched Reluctance Machines
1. Aufl. 2012, 144 S.
ISBN 978-3-8440-1014-5

ABISEA Band 62
Bragard, Michael
The Integrated Emitter Turn-Off Thyristor. An Innovative MOS-Gated High-Power Device
1. Aufl. 2012, 164 S.
ISBN 978-3-8440-1152-4

ABISEA Band 63
Gerschler, Jochen B.
Ortsaufgelöste Modellbildung von Lithium-Ionen-Systemen unter spezieller Berücksichtigung der Batteriealterung
1. Aufl. 2012, 334 S.
ISBN 978-3-8440-1307-8

ABISEA Band 64
Neuhaus, Christoph R.
Schaltstrategien für Geschaltete Reluktanzantriebe mit kleinem Zwischenkreis
1. Aufl. 2012, 133 S.
ISBN 978-3-8440-1487-7

ABISEA Band 65
Butschen, Thomas
Dual-ICT- A Clever Way to Unite Conduction and Switching Optimized Properties in a Single Wafer
1. Aufl. 2012, 168 S.
ISBN 978-3-8440-1771-7

ABISEA Band 66
Plum, Thomas
Design and Realization of High-Power MOS Turn-Off Thyristors
1. Aufl. 2013, 113 S.
ISBN 978-3-8440-1884-4

ABISEA Band 67
Kiel, Martin
Impedanzspektroskopie an Batterien unter besonderer Berücksichtigung von Batteriesensoren für den Feldeinsatz
1. Aufl. 2013, 226 S.
ISBN 978-3-8440-1973-5

ABISEA Band 68
Brauer, Helge
Schnelldrehender Geschalteter Reluktanzantrieb mit extremem Längendurchmesserverhältnis
1. Aufl. 2013, 192 S.
ISBN 978-3-8440-2345-9

ABISEA Band 69
Thomas, Stephan
A Medium-Voltage Multi-Level DC/DC Converter with High Voltage Transformation Ratio
1. Aufl. 2014, 226 S.
ISBN 978-3-8440-2605-4

ABISEA Band 70
Richter, Sebastian
Digitale Regelung von PWM Wechselrichtern mit niedrigen Trägerfrequenzen
1. Aufl. 2014, 126 S.
ISBN 978-3-8440-2641-2

ABISEA Band 71
Bösing, Matthias
Acoustic Modeling of Electrical Drives - Noise and Vibration Synthesis based on Force Response Superposition
1. Aufl. 2014, 188 S.
ISBN 978-3-8440-2752-5

ABISEA Band 72
Waag, Wladislaw
Adaptive algorithms for monitoring of lithium-ion batteries in electric vehicles
1. Aufl. 2014, 232 S.
ISBN 978-3-8440-2976-5

ABISEA Band 73
Sanders, Tilman
Spatially Resolved Electrical In-Situ Measurement Techniques for Fuel Cells
1. Aufl. 2014, 126 S.
ISBN 978-3-8440-3121-8

ABISEA Band 74
Baumhöfer, Thorsten
Statistische Betrachtung experimenteller Alterungsuntersuchungen an Lithium-Ionen Batterien
1. Aufl. 2015, 157 S.
ISBN 978-3-8440-3423-3

ABISEA Band 75
Andre, Dave
Systematic Characterization of Ageing Factors for High-Energy Lithium-Ion Cells and Approaches for Lifetime Modelling Regarding an Optimized Operating Strategy in Automotive Applications
1. Aufl. 2015, 196 S.
ISBN 978-3-8440-3587-2

ABISEA Band 76
Merei, Ghada
Optimization of off-grid hybrid PV-wind-diesel power supplies with multi-technology battery systems taking into account battery aging
1. Aufl. 2015, 184 S.
ISBN 978-3-8440-4148-4

ABISEA Band 77
Schulte, Dominik
Modellierung und experimentelle Validierung der Alterung von Blei-Säure Batterien durch inhomogene Stromverteilung und Säureschichtung
1. Aufl. 2016, 165 S.
ISBN 978-3-8440-4216-0

ABISEA Band 78
Schenk, Mareike
Simulative Untersuchung der Wicklungsverluste in Geschalteten Reluktanzmaschinen
1. Aufl. 2016, 126 S.
ISBN 978-3-8440-4282-5

ABISEA Band 79
Wang, Yu
Development of Dynamic Models with Spatial Resolution for Electrochemical Energy Converters as Basis for Control and Management Strategies
1. Aufl. 2016, 188 S.
ISBN 978-3-8440-4303-7

ABISEA Band 80
Ecker, Madeleine
Lithium Plating in Lithium-Ion Batteries:
An Experimental and Simulation Approach
1. Aufl. 2016, 154 S.
ISBN 978-3-8440-4525-3

ABISEA Band 81
Zhou, Wei
Modellbasierte Auslegungsmethode von Temperierungssystemen für Hochvolt-Batterien in Personenkraftfahrzeugen
1. Aufl. 2016, 175 S.
ISBN 978-3-8440-4589-5

ABISEA Band 82
Lunz, Benedikt
Deutschlands Stromversorgung im Jahr 2050
Ein szenariobasiertes Verfahren zur vergleichenden Bewertung von Systemvarianten und Flexibilitätsoptionen
1. Aufl. 2016, 187 S.
ISBN 978-3-8440-4627-4

ABISEA Band 83
Hofmann, Andreas G.
Direct Instantaneous Force Control: Key to Low-Noise Switched Reluctance Traction Drives
1. Aufl. 2016, 228 S.
ISBN 978-3-8440-4715-8

ABISEA Band 84
Budde-Meiwes, Heide
Dynamic Charge Acceptance of Lead-Acid Batteries for Micro-Hybrid Automotive Applications
1. Aufl. 2016, 157 S.
ISBN 978-3-8440-4733-2

ABISEA Band 85
Engel, Stefan P.
Thyristor-Based High-Power On-Load Tap Changers Control under Harsh Load Conditions
1. Aufl. 2016, 156 S.
ISBN 978-3-8440-4986-2

ABISEA Band 86
Van Hoek, Hauke
Design and Operation Considerations of Three-Phase Dual Active Bridge Converters for Low-Power Applications with Wide Voltage Ranges
1. Aufl. 2017, 231 S.
ISBN 978-3-8440-5011-0

ABISEA Band 87
Diekhans, Tobias
Wireless Charging of Electric Vehicles - a Pareto-Based Comparison of Power Electronic Topologies
1. Aufl. 2017, 151 S.
ISBN 978-3-8440-5048-6

ABISEA Band 88
Lehner, Susanne
Reliability Assessment of Lithium-Ion Battery Systems with Special Emphasis on Cell Performance Distribution
1. Aufl. 2017, 184 S.
ISBN 978-3-8440-5090-5

ABISEA Band 89
Käbitz, Stefan
Untersuchung der Alterung von Lithium-Ionen-Batterien mittels Elektroanalytik und elektrochemischer Impedanzspektroskopie
1. Aufl. 2016, 258 S.
DOI: 10.18154/RWTH-2016-12094

ABISEA Band 90
Witzenhausen, Heiko
Elektrische Batteriespeichermodelle: Modellbildung, Parameteridentifikation und Modellreduktion
1. Aufl. 2017, 266 S.
DOI: 10.18154/RWTH-2017-03437

ABISEA Band 91
Münnix, Jens
Einfluss von Stromstärke und Zyklentiefe auf graphitische Anoden
1. Aufl. 2017, 171 S.
DOI: 10.18154/RWTH-2017-01915

ABISEA Band 92
Pilatowicz, Grzegorz
Failure Detection and Battery Management Systems of Lead-Acid Batteries for Micro-Hybrid Vehicles
1. Aufl. 2017, 212 S.
DOI: 10.18154/RWTH-2017-09156

ABISEA Band 93
Drillkens, Julia
Aging in Electrochemical Double Layer Capacitors:
An Experimental and Modeling Approach
1. Aufl. 2017, 179 S.
DOI: 10.18154/RWTH-2018-223434

Aachener Beiträge des ISEA

ABISEA Band 94
Magnor, Dirk
Globale Optimierung netzgekoppelter PV-Batteriesysteme unter besonderer Berücksichtigung der Batteriealterung
1. Aufl. 2017, 210 S.
DOI: 10.18154/RWTH-2017-06592

ABISEA Band 95
Iliksu, Merve
Elucidation and Comparison of the Effects of Lithium Salts on Discharge Chemistry of Nonaqueous Li-O_2 Batteries
1. Aufl. 2018, 160 S.
DOI: 10.18154/RWTH-2018-223782

ABISEA Band 96
Schmalstieg, Johannes
Physikalisch-elektrochemische Simulation von Lithium-Ionen-Batterien: Implementierung, Parametrierung und Anwendung
1. Aufl. 2017, 168 S.
DOI: 10.18154/RWTH-2017-04693

ABISEA Band 97
Soltau, Nils
High-Power Medium-Voltage DC-DC Converters: Design, Control and Demonstration
1. Aufl. 2017, 176 S.
DOI: 10.18154/RWTH-2017-04084

ABISEA Band 98
Stieneker, Marco
Analysis of Medium-Voltage Direct-Current Collector Grids in Offshore Wind Parks
1. Aufl. 2017, 144 S.
DOI: 10.18154/RWTH-2017-04667

ABISEA Band 99
Masomtob, Manop
A New Conceptual Design of Battery Cell with an Internal Cooling Channel
1. Aufl. 2017, 167 S.
DOI: 10.18154/RWTH-2018-223281

ABISEA Band 100
Marongiu, Andrea
Performance and Aging Diagnostic on Lithium Iron Phosphate Batteries for Electric Vehicles and Vehicle-to-Grid Strategies
1. Aufl. 2017, 222 S.
DOI: 10.18154/RWTH-2017-09944

ABISEA Band 101
Gitis, Alexander
Flaw detection in the coating process of lithium-ion battery electrodes with acoustic guided waves
1. Aufl. 2017, 109 S.
DOI: 10.18154/RWTH-2017-099519

ABISEA Band 102
Neeb, Christoph
Packaging Technologies for Power Electronics in Automotive Applications
1. Aufl. 2017, 132 S.
DOI: 10.18154/RWTH-2018-224569

ABISEA Band 103
Adler, Felix
A Digital Hardware Platform for Distributed Real-Time Simulation of Power Electronic Systems
1. Aufl. 2017, 156 S.
DOI: 10.18154/RWTH-2017-10761

ABISEA Band 104
Becker, Jan
Flexible Dimensionierung und Optimierung hybrider Lithium-Ionenbatterie-speichersysteme mit verschiedenen Auslegungs-zielen
1. Aufl., 2017, 157 S.
DOI: 10.18154/RWTH-2017-09278

ABISEA Band 105
Warnecke, Alexander J.
Degradation Mechanisms in NMC Based Lithium-Ion Batteries
1. Aufl. 2017, 158 S.
DOI: 10.18154/RWTH-2017-09646

ABISEA Band 106
Taraborrelli, Silvano
Bidirectional Dual Active Bridge Converter using a Tap Changer for Extended Voltage Ranges
1. Aufl. 2017, 94 S.
DOI: 10.18154/RWTH-2018-228242

ABISEA Band 107
Sarriegi, Garikoitz
SiC and GaN Semiconductors: The Future Enablers of Compact and Efficient Converters for Electromobility
1. Aufl. 2017, 106 S.
DOI: 10.18154/RWTH-2018-227548

ABISEA Band 108
Senol, Murat
Drivetrain Integrated Dc-Dc Converters utilizing Zero Sequence Currents
1. Aufl. 2017, 134 S.
DOI: 10.18154/RWTH-2018-226170

ABISEA Band 109
Kojima, Tetsuya
Efficiency Optimized Control of Switched Reluctance Machines
1. Aufl. 2017, 142 S.
DOI: 10.18154/RWTH-2018-226697

ABISEA Band 110
Lewerenz, Meinert
Dissection and Quantitative Description of Aging of Lithium-Ion Batteries Using Non-Destructive Methods Validated by Post-Mortem-Analyses
1. Aufl. 2018, 139 S.
DOI: 10.18154/RWTH-2018-228663

ABISEA Band 111
Büngeler, Johannes
Optimierung der Verfügbarkeit und der Lebensdauer von Traktionsbatterien für den Einsatz in Flurförderfahrzeugen
1. Aufl. 2018, 171 S.
DOI: 10.18154/RWTH-2018-226569

ABISEA Band 112
Wegmann, Raphael
Betriebsstrategien und Potentialbewertung hybrider Batteriespeichersysteme in Elektrofahrzeugen
1. Auflage 2018, 184 S.
DOI: 10.18154/RWTH-2018-228833

ABISEA Band 113
Nordmann, Hannes
Batteriemanagementsysteme unter besonderer Berücksichtigung von Fehlererkennung und Peripherieanalyse
1. Aufl. 2018, 222 S.
DOI: 10.18154/RWTH-2018-228763

ABISEA Band 114
Engelmann, Georges
Reducing Device Stress and Switching Losses Using Active Gate Drivers and Improved Switching Cell Design
1. Aufl. 2018, 195 S.
DOI: 10.18154/RWTH-2018-228973

ABISEA Band 115
Klein-Heßling, Annegret
Active DC-Power Filters for Switched Reluctance Drives during Single-Pulse Operation
1. Aufl. 2018, 166 S.
DOI: 10.18154/RWTH-2018-231030

ABISEA Band 116
Burkhart, Bernhard
Switched Reluctance Generator for Range Extender Applications - Design, Control and Evaluation
1. Aufl. 2018, 194 S.
DOI: 10.18154/RWTH-2019-00025

ABISEA Band 117
Biskoping, Matthias
Discrete Modeling and Control of a versatile Power Electronic Test Bench with Special Focus on Central Photovoltaic Inverter Testing
1. Aufl. 2018, 236 S.
DOI: 10.18154/RWTH-2019-03346

ABISEA Band 118
Schubert, Michael
High-Precision Torque Control of Inverter-Fed Induction Machines with Instantaneous Phase Voltage Sensing
1. Aufl. 2019, 221 S.
DOI: 10.18154/RWTH-2018-231364

ABISEA Band 119
Van der Broeck, Christoph
Methodology for Thermal Modeling, Monitoring and Control of Power Electronic Modules
1. Aufl. 2019, 290 S.
DOI: 10.18154/RWTH-2019-01370

ABISEA Band 120
Hust, Friedrich Emanuel
Physico-chemically motivated parameterization and modelling of real-time capable lithium-ion battery models – a case study on the Tesla Model S battery
1. Aufl. 2019, 203 S.
DOI: 10.18154/RWTH-2019-00249

ABISEA Band 121
Ralev, Iliya
Accurate Torque Control of Position Sensorless Switched Reluctance Drives
1. Aufl. 2019, 154 S.
DOI: 10.18154/RWTH-2019-03071

ABISEA Band 122
Ayeng'o, Sarah Paul
Optimization of number of PV cells connected in series for a direct-coupled PV system with lead-acid and lithium-ion batteries
1. Aufl. 2019, 114 S.
DOI: 10.18154/RWTH-2019-01843

ABISEA Band 123
Koschik, Stefan Andreas
Permanenterregte Synchronmaschinen mit verteilter Einzelzahnsteuerung - Regelkonzepte und Betriebsstrategien für hochintegrierte Antriebssysteme
1. Aufl. 2019, 158 S.
DOI: 10.18154/RWTH-2019-03446

ABISEA Band 124
Farmann, Alexander
A comparative study of reduced-order equivalent circuit models for state-of-available-power prediction of lithium-ion batteries in electric vehicles
1. Aufl. 2019, 214 S.
DOI: 10.18154/RWTH-2019-04700

ABISEA Band 125
Mareev, Ivan
Analyse und Bewertung von batteriegetriebenen, oberleitungsversorgten und brennstoffzellengetriebenen Lastkraftwagen für den Einsatz im Güterfernverkehr in Deutschland
1. Aufl. 2019, 158 S.
DOI: 10.18154/RWTH-2019-04698

ABISEA Band 126
Qi, Fang
Online Model-predictive Thermal Management of Inverter-fed Electrical Machines
1. Aufl. 2019, 154 S.
DOI: 10.18154/RWTH-2019-08304

ABISEA Band 127
Kairies, Kai-Philipp
Auswirkungen dezentraler Solarstromspeicher auf Netzbetreiber und Energieversorger
1. Aufl. 2019, 140 S.
DOI: 10.18154/RWTH-2019-06706

Aachener Beiträge des ISEA

ABISEA Band 128
Fleischer, Michael
Traction control for Railway Vehicles
1. Aufl. 2019, 162 S.
DOI: 10.18154/RWTH-2019-10570

ABISEA Band 129
Teuber, Moritz
Lifetime Assessment and Degradation Mechanisms in Electric Double-Layer Capacitors
1. Aufl. 2019, 150 S.
DOI: 10.18154/RWTH-2019-10071

ABISEA Band 130
Bußar, Christian
Investigation of Optimal Transformation Pathways towards 2050 for the Successful Implementation of a Sustainable Reduction of Carbon Emissions from Power Generation
1. Aufl. 2019, 204 S.
DOI: 10.18154/RWTH-2019-09975

ABISEA Band 131
Wienhausen, Arne Hendrik
High Integration of Power Electronic Converters enabled by 3D Printing
1. Aufl. 2019, 146 S.
DOI: 10.18154/RWTH-2019-08746

ABISEA Band 132
Kwiecien, Monika
Electrochemical Impedance Spectroscopy on Lead-Acid Cells during Aging
1. Aufl. 2019, 138 S.
DOI: 10.18154/RWTH-2019-09480

ABISEA Band 133
Titiz, Furkan Kaan
A Three-phase Low-voltage Grid-connected Current Source Inverter
1. Aufl. 2019, 128 S.
DOI: 10.18154/RWTH-2020-00458

ABISEA Band 134
Wünsch, Martin
Separation der Kathoden-alterung in Lithium-Ionen-Batteriezellen mittels elektrochemischer Impedanzspektroskopie
1. Aufl. 2019, 177 S.
DOI: 10.18154/RWTH-2019-11017

ABISEA Band 135
Badeda, Julia
Modeling and Steering of Multi-Use Operation with Uninterruptible Power Supply Systems - utilizing the example of lead-acid batteries
1. Aufl. 2020, 282 S.
DOI: 10.18154/RWTH-2020-05456

ABISEA Band 136
Kleinsteinberg, Björn
Energy Efficiency Increase of a Vanadium Redox Flow Battery with a Power-Based Model
1. Aufl. 2020, 163 S.
DOI: 10.18154/RWTH-2020-06092

ABISEA Band 137
Cai, Zhuang
Optimization of dimension and operation strategy for a wind-battery energy system in German electricity market under consideration of battery ageing process
1. Aufl. 2020, 144 S.
DOI: 10.18154/RWTH-2020-06525

ABISEA Band 138
Sabet, Pouyan Shafiei
Analysis of Predominant Processes in Electrochemical Impedance Spectra and Investigation of Aging Processes of Lithium-Ion Batteries with Layered Oxide Cathodes and Graphitic Anodes
1. Aufl. 2020, 136 S.
DOI: 10.18154/RWTH-2020-07683

ABISEA Band 139
Angenendt, Georg
Operation, Optimization and Additional Market Participation of Households with PV Battery Storage System and Power-to-Heat Application
1. Aufl. 2020, 221 S.
DOI: 10.18154/RWTH-2020-05200

ABISEA Band 140
Oberdieck, Karl Friedrich
Measurement and Mitigation of Electromagnetic Emissions of Propulsion Inverters for Electric Vehicles
1. Aufl. 2020, 181 S.
DOI: 10.18154/RWTH-2020-09215

ABISEA Band 141
Bubert, Andreas Martin
Optimierung des elektrischen Antriebsstrangs von Elektrofahrzeugen mit Betrachtung parasitärer Ströme innerhalb der elektrischen Maschine
1. Aufl. 2020, 215 S.
DOI: 10.18154/RWTH-2020-09556

ABISEA Band 142
Fleischer, Christian Georg
Model-Driven Software Development and Verification Solutions for Safety Critical Battery Management Systems
1. Aufl. 2021, 356 S.
DOI: 10.18154/RWTH-2021-00436

ABISEA Band 143
Arzberger, Arno
Thermografische Methoden zur zerstörungsfreien Messung der anisotropen Wärmeleitfähigkeit von Lithium-Ionen Zellen
1. Aufl. 2020, 131 S.
DOI: 10.18154/RWTH-2021-00479

ABISEA Band 144
Lange, Tobias
Oberwellenbasierte Modellierung, Regelung und Auslegung von Permanentmagnet- und Reluktanz-Synchronmaschinen
1. Aufl. 2020, S.
DOI: 10.18154/RWTH-2021-02537

ABISEA Band 145
Weiss, Claude
Fault Tolerant Switched Reluctance Machines with Distributed Inverters – Modeling and Control
1. Aufl. 2020, S.
DOI: 10.18154/RWTH-2021-02327

ABISEA Band 146
Huck, Moritz
Modelling the Transient Behaviour of Lead-Acid Batteries: Electrochemical Impedance of Adsorbed Species
1. Aufl. 2020, 151 S.
DOI: 10.18154/RWTH-2020-08362

ABISEA Band 147
Willenberg, Lisa
Volumenausdehnung und ihre Auswirkungen auf die Alterung einer zylindrischen Lithium-Ionen-Batterie
1. Aufl. 2020, S.
DOI: 10.18154/RWTH-2021-01906

ABISEA Band 148
Rogge, Matthias
Electrification of Public Transport Bus Fleets with Battery Electric Busses
1. Aufl. 2020, 161 S.
DOI: 10.18154/RWTH-2021-02146

ABISEA Band 149
Münderlein, Jeanette
Numerische Methodik zur Auslegung eines Hybriden Speichersystems mit Multinutzen“
1. Aufl. 2020, 221 S.
DOI: 10.18154/RWTH-2021-00867

ABISEA Band 150
Merten, Michael
Participation of Battery Storage Systems in the Secondary Control Reserve Market
1. Aufl. 2020, 187 S.
DOI: 10.18154/RWTH-2021-01029

ABISEA Band 151
Ge, Lefei
Performance Enhancement of Switched Reluctance Machines for High-speed Back-up Generators
1. Aufl. 2020, 152 S.
DOI: 10.18154/RWTH-2020-11546

ABISEA Band 152
Neubert, Markus
Modeling, Synthesis and Operation of Multiport-Active Bridge Converters
1. Aufl. 2020, 227 S.
DOI: 10.18154/RWTH-2020-10814

ABISEA Band 153
Schülting, Philipp
Optimierte Auslegung von hochintegrierten und bidirektionalen Onboard GaN-Ladegeräten
1. Aufl. 2020, 158 S.
DOI: 10.18154/RWTH-2020-09771

ABISEA Band 154
Sewergin, Alexander
Design Challenges and Solutions for the Practical Application of SiC Power Moduls – Exemplified by an Automotive DC-DC Converter. 1. Aufl. 2021, 154 S.
DOI: 10.18154/RWTH-2021-04498

ABISEA Band 155
Stippich, Alexander
Exploiting the Full Potential of Silicon Carbide Devices via Optimized Highly Integrated Power Modules
1. Aufl. 2021, 188 S.
DOI: 10.18154/RWTH-2021-08122

ABISEA Band 156
Gottschlich, Jan
Hilfsspannungsversorgungskonzepte für Mittelspannungs-DC/DC-Wandler
1. Aufl. 2021, 178 S.
DOI: 10.18154/RWTH-2021-11881

ABISEA Band 157
Hollstegge, Philipp
Injektion raumzeigerzerlegter Stromharmonischer zur Minderung tonaler Geräuschanteile in asymmetrisch sechsphasigen Permanentmagnetsynchronmaschinen
1. Aufl. 2021, 191 S.
DOI: 10.18154/RWTH-2021-11040

ABISEA Band 158
Grau, Vivien
Development of a Test Bench to Investigate the Impact of Steep Voltage Slopes on the Lifetime of Insulation Systems for Coil Windings
1. Aufl. 2021, 182 S.
DOI: 10.18154/RWTH-2021-09577

ABISEA Band 159
Ringbeck, Florian
Optimized Charging of Lithium-Ion Batteries with Physico-Chemical Models
1. Aufl. 2021, 174 S.
DOI: 10.18154/RWTH-2021-11038

ABISEA Band 160
Bank, Thomas
Performance and Aging Analysis of High-Power Lithium Titanate Oxide Cells for Low-Voltage Vehicle Applications
1. Aufl. 2021, 148 S.
DOI: 10.18154/RWTH-2021-10369

Aachener Beiträge des ISEA

ABISEA Band 161
Aupperle, Felix
Realizing High-Performance Silicon-Based Lithium-Ion Batteries
1. Aufl. 2022, 138 S.
DOI: 10.18154/RWTH-2022-05155

ABISEA Band 162
Schröer, Philipp A.
Entwicklung einer adaptiven Leistungsprognosefunktion für Starterbatterien mit Lithium-Titanat-Oxid-Anode als Grundlage zur sicheren Energieversorgung im Fahrzeug
1. Aufl. 2021, 187 S.
DOI: 10.18154/RWTH-2021-10819

ABISEA Band 163
Dechent, Philipp
Simulation and Real-Life assessment of cell-to-cell variation of ageing lithium-ion batteries
1. Aufl. 2022, 149 S.
DOI: 10.18154/RWTH-2022-09298

ABISEA Band 164
Li, Weihan
Battery Digital Twin with Physics-Based Modeling, Battery Data and Machine Learning
1. Aufl. 2022, 234 S.
DOI: 10.18154/RWTH-2022-02292

ABISEA Band 165
Thien, Tjark G. C.
Optimaler Betrieb von stationären Hybrid-Batterie-speichern am Beispiel des Projekts M5BAT
1. Aufl. 2022, 172 S.
DOI: 10.18154/RWTH-2022-00997

ABISEA Band 166
Lüdecke, Christoph
Compensating Asymmetries of Parallel-Connected SiC MOSFETs Using Intelligent Gate Drivers
1. Aufl. 2022, 166 S.
DOI: 10.18154/RWTH-2022-09587

ABISEA Band 167
Rahe, Christiane
Untersuchung von Batterieelektroden mit optischen Verfahren
1. Aufl. 2022, 214 S.
DOI: 10.18154/RWTH-2022-08794

ABISEA Band 168
Weber, Felix Martin
Stability of lithium electrolyte interphase enabling rechargeable lithium-metal batteries
1. Aufl. 2023, 168 S.
DOI: 10.18154/RWTH-2023-03565

ABISEA Band 169
Henn, Jochen
Gate Driver Integrated Closed-Loop Control for Electromagnetic Emissions and Switching Losses of Wide Bandgap Power Electronic Converters
1. Aufl. 2023, 169 S.
DOI: 10.18154/RWTH-2023-07726

ABISEA Band 170
Quabeck, Stefan
Modeling of Parasitic Currents and Fault Detection in Electrical Traction Drives
1. Aufl. 2023, 133 S.
DOI: 10.18154/RWTH-2023-10920

ABISEA Band 171
Hecht, Christopher
Usage overview, prediction, and siting optimization for electric vehicles public charging infrastructure with machine learning and big data methods
1. Aufl. 2023, 185 S.
DOI: 10.18154/RWTH-2024-01156

ABISEA Band 172
Kuipers, Matthias L. U.
Development of a Virtual Cell Design Tool for Objective Comparisons between State-of-the-Art Battery Cells and Next Generation Technologies
1. Aufl. 2023, 203 S.
DOI: 10.18154/RWTH-2023-11897

ABISEA Band 173
Brieske, Daniel Martin
Anwendungsbezogene Modellierung und Zustandsbestimmung von Lithium-Schwefel-Batterien
1. Aufl. 2023, 146 S.
DOI: 10.18154/RWTH-2023-10905

ABISEA Band 174
Teichert, Philipp
Einfluss der Degradation von nickelreichen $Li[Ni_xMn_yCo_z]O_2$ (NMC) Elektroden (mit $x \geq 0.6$) auf Vollzellalterung von Lithium-Ionen-Zellen
1. Aufl. 2023, 159 S.
DOI: 10.18154/RWTH-2024-01059

ABISEA Band 175
Kühnle, Hannes Sebastian
Optical and electrochemical investigations of fundamental lithium metal deposition processes on lithium surfaces
1. Aufl. 2023, 218S.
DOI: 10.18154/RWTH-2024-05806

ABISEA Band 176
Epp, Alexander
Multiphysical Models and Optimization for Conceptual Design of High-Voltage Battery Systems
1. Aufl. 2024, 256 S.
DOI: 10.18154/RWTH-2024-00430

ABISEA Band 177
Figgener, Jan
Data-driven battery aging analysis of home storage systems based on high-resolution field measurements
1. Aufl. 2024, 208 S.
DOI: 10.18154/RWTH-2024-10709

ABISEA Band 178
Meishner, Fabian
Untersuchung eines direktnetzgekoppelten stationären LTO-Speichersystems in einem 750 V DC Stadtbahnnetz
1. Aufl. 2024, 116 S.
DOI: 10.18154/RWTH-2024-06358

ABISEA Band 179
Frambach, Tobias
Anwendungsgerechte Dimensionierung und Betriebsstrategien von 48 V Plug-In-Hybridfahrzeugen
1. Aufl. 2024, 154 S.
DOI: 10.18154/RWTH-2024-03411

ABISEA Band 180
Goldbeck, Rafael
Model-Based Control of Three-Phase Dual-Active Bridge Converters for Dynamic Operation and Adaptive Compensation of Parameter Deviations
1. Aufl. 2024, 194 S.
DOI: 10.18154/RWTH-2025-00288

ABISEA Band 181
Götz, Georg Tobias
Bidirectional DC-to-DC Converter with Integrated Switched Reluctance Generator
1. Aufl. 2024, 192 S.
DOI: 10.18154/RWTH-2024-03854

ABISEA Band 182
Harries, Martin
Aktive Reduzierung der Vibrationen von Permanentmagnet-Synchronmaschinen durch adaptive Regler
1. Aufl. 2024, 144 S.
DOI: 10.18154/RWTH-2025-00626

ABISEA Band 183
Börner, Martin Florian
Ein prozessbasiertes Modell zur Berechnung der Kosten von Lithium-Ionen-Batteriezellen
1. Aufl. 2024, 163 S.
DOI: 10.18154/RWTH-2024-07853

ABISEA Band 184
Bihn, Stephan
Automatic Parameterisation of Electrical Equivalent Circuit Models for Virtual Battery Cell Design
1. Aufl. 2024, 226 S.
DOI: 10.18154/RWTH-2024-10636

ABISEA Band 185
Xu, Huihui
Thermal Modeling and Control of an Oil-Cooled Permanent Magnet Synchronous Machine: Initialization, Nonlinearity, and Controllability
1. Aufl. 2025, S.
DOI: 10.18154/RWTH-

ABISEA Band 186
Fritz, Niklas
Generalized Control Methodology for Modular DC-DC Converters
1. Aufl. 2025, S.
DOI: 10.18154/RWTH-

ABISEA Band 187
Kalker, Sven
Toward Robust Monitoring of Power Electronic Devices: Challenges and Efficient Solutions
1. Aufl. 2025, S.
DOI: 10.18154/RWTH-

ABISEA Band 188
Wasylowski, David
Accelerating Battery Cell Design, Manufacturing, and Testing through Ultrasound Imaging
1. Aufl. 2025, S.
DOI: 10.18154/RWTH-

ABISEA Band 189
Steininger, Valentin
Aging analysis of lithium-ion batteries with field data
1. Aufl. 2025, S.
DOI: 10.18154/RWTH-

ABISEA Band 190
Jacqué, Kevin
Analyse der Belastungsprofile, der Alterung und der Wirtschaft-lichkeit eines Batteriespeichers im Primärregelleistungsmarkt aus realen Feldmessdaten
1. Aufl. 2025, S.
DOI: 10.18154/RWTH-

ABISEA Band 191
Hamzelui, Niloofar
Investigation of active materials and polymeric binders in silicon-based negative electrodes for lithium-ion batteries
1. Aufl. 2025, S.
DOI: 10.18154/RWTH-

The continuous demand for higher efficiency and power density drives the development of modern power electronics, particularly in mobile applications. Wide-bandgap (WBG) semiconductors are key enablers, offering high switching speeds and low losses. Accurate dynamic characterization via the double-pulse test is essential to optimize these devices.

It has been verified that the parasitic inductance and the limited bandwidth of the current probe are among the most critical variables for achieving reliable measurement results. Common solutions, such as coaxial shunts with an inductance of approx. 2 nH, are unsuitable for measuring very fast switching transients, as they introduce significant disturbances. This dissertation introduces a novel shunt resistor based on radially arranged thin-film resistors. The design minimizes the inductance to below 100 pH and offers a usable bandwidth beyond 2 GHz. Additionally, an inductive sensor is designed as a reference. It is based on a planar pick-up coil embedded in a multilayer circuit board and achieves a similar bandwidth. Both methods were validated with a low-inductive Gallium Nitride switching cell.

The results demonstrate that the radial shunt resistor outperforms existing solutions for the dynamic characterization of WBG semiconductors. Its high accuracy, combined with an innovative design and an easy-to-reproduce assembly technique, makes it a valuable tool for advancing power electronics. This work establishes a new standard for high-frequency current measurements, pushing the boundaries of precision in WBG semiconductor characterization.

ISSN 1437-675X